AE3200 – Design Synthesis Exercise

Hyperion 4 – Final Report

Group 16

July 3, 2018

Faculty of
Aerospace Engineering

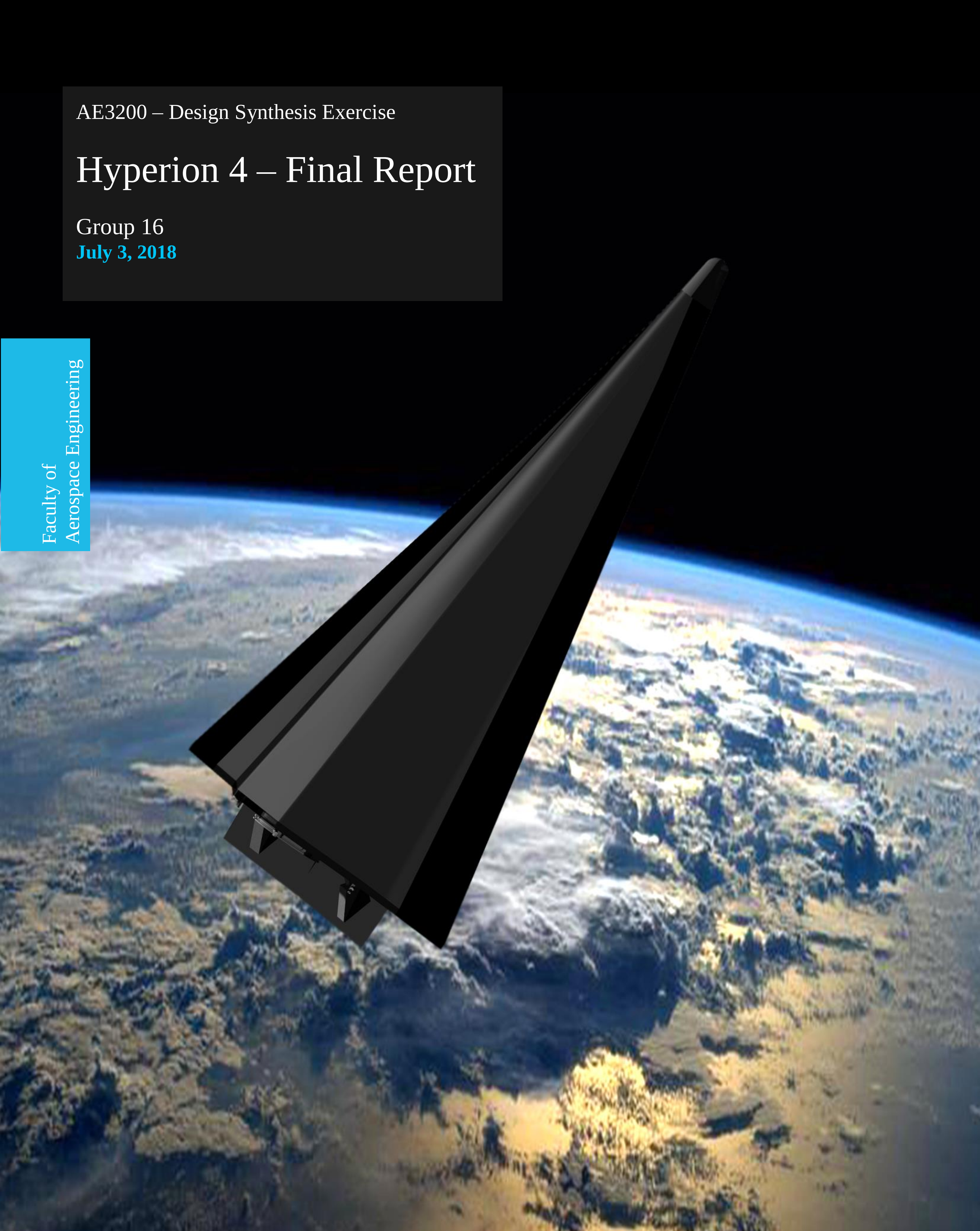

TU Delft
Delft
University of
Technology

Challenge the future

Hyperion 4 - Final Report

Design and Development of a Hypersonic Re-entry Vehicle

AE3200 Design Synthesis Exercise

Group 16
Jonas Amend
Bavly Barsom
Michaela Brchnelova
Giulio Dacome
Bardienus Duisterhof
Andrea Levoni
Louis Lischwe
Ericka Matsuda-Martin
Jacopo Sem
Douwe Sonneveldt

July 3, 2018

Supervisors:
Dr. ir. Erwin Mooij
ir. Kees Sudmeijer

—— Version 1.0 ——

Executive Summary

The principal aim of the final report is to present the process and outcome of the work completed by the group, starting from the mission definition, leading into the conceptual phase, and concluding with the preliminary design stage. This includes the identification and structuring of tasks through work-flow diagrams, work breakdown structures and Gantt charts, but also several models used to simulate and asses the performance of the vehicle and its subsystems. The key vehicle characteristics are outlined including justification for critical design decisions. Moreover, the plans for the organization of the upcoming stages of design, manufacture and operations are outlined.

Mission Profile

The vehicle will be launched from French Guiana in the European Vega rocket, a proven design, which meets the ΔV and accuracy requirements. Vehicle injection will occur at 120 km, leaving the vehicle in a suborbital trajectory, with a velocity of 7.32 km/s at separation (aligned with the local horizontal). Upon initial reentry into the atmosphere, the vehicle performs multiple skips, peaking around 260 km altitude, which dramatically improves the range of the vehicle. After the last skip, reentry into the atmosphere begins, during which the vehicle follows the maximum heat-load constraint, imposed on the trajectory by the thermal protection and cooling system's capacity. Consequent to intersection with the g-load constraint, the vehicle follows this more critical boundary, attempting to maintain a constant deceleration of 4g. Experiments are conducted starting at an altitude of 40 km, lasting approximately 18.5 seconds. Ensuing the completion of the experiments, the vehicle further progresses in its reentry, with velocity falling below the Mach barrier prior to parachute ejection and deployment. It is projected that at an altitude of 10 km, the vehicle will have decelerated to around 180 m/s (Mach 0.6), at which point a drogue chute will be ejected from the rear of the vehicle, aiding in further reduction of speed. The main chute is also released soon thereafter. The vehicle is recovered by mid-air retrieval and returned to the Guiana Space Centre by a helicopter.

System Characteristics

Since the submission of the mid-term report, the group has focused on further developing the various elements of the selected concept. Throughout this section the various constituents of the vehicle are presented and their main performance characteristics outlined. The present design was found to meet most top-level user requirements. However, compliance with the requirements concerning the reusability and cost of the vehicle cannot be confirmed at this stage of design. Other requirements such as those on the trajectory, the mass and the experiments are projected to be met based on simulations and preliminary vehicle configuration.

Geometrical and Aerodynamic Characteristics

The outcome of the aerodynamic iteration process, the vehicle's exterior shape, is shown in Figure 9.7. The nose radius was fixed at 40 mm and the leading edge radius, thanks to a sweep angle of 72 degrees, could be lowered to 7.5 mm without violating heat flux constraints. The vehicle length, from nose tip to back-frame (excluding elevons), is 2840 mm with a maximum height of 480 mm at the rear of the vehicle. Modifications to the upper surface geometry were seen to have little to no impact on performance in consequence to this region being shadowed at nominal conditions (high angle of attack). The maximum lift to drag ratio occurs at an altitude of approximately 40 km, attaining values in proximity to 3.5 when flying at Mach 10.

Figure 1: Render of the vehicle in-flight

Thermal Protection System

The material selection for the thermal protection system can be divided into three geometric zones based on the predicted heat loads from the aerothermodynamic model. The critical condition for the nose tip and leading edges is expected to occur when the cooling system is switched off, resulting in equilibrium temperatures around 3000 and 1725 K respectively. The maximum temperature experienced by the lower surface is 1600 K, whereas the upper surface is only required to endure around 1000 K. For the nose tip, literature offered sufficient evidence that a porous silicon carbide doped carbon-carbon ceramic can offer the necessary qualities to survive the extreme environment. This nose tip utilizes transpiration cooling to locally combat the extreme stagnation temperatures. For the lower surface and leading edge, no cooling system is used; instead Toughened Uni-Piece Fibrous Reinforced Oxidation-Resistant Composite (TUFROC) is used as a heat-shield. The upper surface is least critical in terms of the temperature and so Surface Protected Flexible Insulation (SPFI), a material flight tested by ESA, was chosen.

An alternative nose tip has been developed in parallel to the principal design. The feasibility of a film-cooled Tungsten nose tip coated with Al_2O_3 has been investigated. Though promising, large uncertainties still persist, particularly concerning the reactivity of the material in case of a cooling system failure. A Technology Readiness Level (TRL) development plan, outlining the various steps necessary to further evaluate the feasibility of such as a system, is presented. This will help in gaining further certainty about the future of such a system.

Internal Subsystems

A variety of systems are necessary for reliable operation of the Hyperion IV vehicle. The core systems include the thermal protection system (including active cooling pumps and tanks), the communication subsystem, which consists of an antenna and an amplifier, the thruster attitude control subsystem, including tanks and thrusters, and the primary flight computer. The parachute and electric power subsystem also occupy a large fraction of the vehicle's internal volume.

Electrical Power Subsystem

Electrical power is supplied by an array of 100 Li-Ion polymer batteries, which can be stepped down using two DC-DC converters, capable of supplying up to 500 W each. The requirement on the electronic power subsystem's capacity mainly arises as a result of the electrical actuators for the control surfaces, the main flight-computer and the active cooling pumps. It is important to note that there are a multitude of items which are only activated in certain instances and do not require permanent power. Moreover, certain items such as pyrotechnic valves, pyro bolts and the parachute mortar are only fired once during the flight. Thus, in the unlikely event of failure of a single DC-DC converter, the vehicle can still be operated with restricted functionality to ensure safe return to the ground.

Structural Subsystem

The structure features seven longitudinal beams located at the kinks in the core structure. These beams run along the full length of the structure, converging to the base of the nosecone. A total of 11 frames are placed at equal intervals along the vehicle's length, enhancing the overall stiffness of the structure. In between the longerons, shear webs are employed to transfer shear loads throughout the structure. All relevant load cases, from launch to recovery were considered, with the structure found to be capable of sustaining them all. The vibrational analysis concluded that all natural frequencies were above the required minimums.

Control Subsystem

A similar configuration as that flown on the Intermediate eXperimental Vehicle (IXV), employing flaperons, is used to control the vehicle during the atmospheric segments of the trajectory. Each flaperon has dimensions of 0.6×0.4 m, resulting in sufficient area to both resist the destabilizing moments and offer headroom to manoeuvre the vehicle to perform attitude changes. The system works in conjunction with a reaction control system consisting of 6 Triad model 50-820 cold gas thrusters, which allow for attitude changes in the absence of air. The system can also be used to assist the flaperons during atmospheric flight, though their relative effectiveness in resisting aerodynamic moments scales with the reciprocal of the dynamic pressure.

It was found that obtaining an open-loop directionally stable vehicle was not possible with the current internal configuration. The addition of vertical control surfaces and/or the investigation of artificial stabilization with thrusters should be considered in the upcoming stages of design.

Telemetry and Avionics

The flight computer controls the vehicle trajectory, monitors subsystem performance & health, and manages the transition between different operatives modes over the course of the mission. Besides the electrical power subsystem, it is the only fault tolerant element of the vehicle. The avionics also include an inertial measurement unit, two GPS receivers and a radar altimeter. A dedicated set of payload data handling and acquisition systems is employed. It can store up to 224 GB of telemetry data, sensor readings and infra-red camera images on solid state storage devices. To ensure that the data is not lost in the case of catastrophic failure, the most critical data streams are also transmitted throughout the flight with a high temperature antenna, whenever possible. The link budget was found to close at a Signal to Noise ratio of 15 dB when using the Vector-Aydin T-300 transmitter at a nominal transmission rate of 15 Mbps via Binary Phase Shift Keying (BPSK).

Recovery

The concept chosen for recovery is mid-air retrieval by helicopter. Other concepts such as skids, landing gear or floaters were discarded due to excessive increases in weight or insufficient confidence in the reliability of the system. An important characteristics of mid-air retrieval is its negligible impact from a structural perspective. Moreover the method places less stringent requirements on the accuracy of the trajectory whilst allowing for "landing" practically anywhere within the retrieval vehicle's range. Helicopters are preferred over aircraft as their ability to hover makes them more suitable for reattempt after a failed "catch". Based on the desired terminal velocity, a preliminary study of the required parachute surface was executed, yielding a mass of 18.6 kg, occupying a volume equivalent to a cube with a side of 29 cm. The canopy will be manufactured out of Kevlar®281, a high specific strength aramid fibre based fabric.

Budget Overview

The estimated mass and power budgets required for each subsystem are listed in Table 1. A significant amount of uncertainty still persists in the power consumption of the control surfaces (flaps), resulting in a conservative estimate of 200 W.

Table 1: Preliminary design mass and power budget

Subsystem	Mass [kg]	Power [W]
Structures	51.53	0
Thermal Protection	93.07	100
Thruster Attitude Control	21.27	72
Flap Attitude Control	25.45	200
Power System	14.3	0
Telemetry	0.44	60
Avionics	28.12	299.05
Instrumentation	21	69.7
Ballasts	8.16	0
Recovery	34.5	75.5
Harness	23.82	70.1
Total wet mass/Total Power	321.69	946.35

Onboard Experiments

The study of hypersonics remains a topic of central importance in present developments of re-entry vehicles. To further strengthen understanding of complex phenomena, the payload includes a boundary layer transition module. The exterior of the vehicle's upper side is lined with roughness patches to trigger transition. A boundary layer shockwave interaction experiment is also on board: the control surfaces at the rear of the vehicle act as a ramp when deflected, such that data on the flow can be collected for various conditions. The present configuration, sweeps across the Reynolds number range in approximately 18.5 seconds.

A hypersonic test vehicle offers rare opportunities for materials testing in conditions representative of reentry. Though plasma tunnels and hypersonic wind tunnels may be used to independently assess material reactivity and thermal performance under extreme conditions, the modular interface, which the vehicle will be equipped with, achieves realistic conditions for evaluating material suitability for reentry applications.

Once the vehicle is shown to operate reliably under nominal conditions, various control and guidance experiments can be conducted. Fuzzy Control Logic has been successfully implemented in various UAVs for autonomous control of flight. The applications of nonlinear dynamic inversion control will also be investigated.

The active cooling system is at the core of both the experiments as well as the thermal protection system: its operation will pioneer the technology necessary for further development of reusable reentry vehicles. The low TRL of active cooling is also the principal reason why the nose tip is designed to survive in case of a failure. This technology demonstration is key milestone to the development of reusable manned high glide-ratio vehicles.

Electromagnetic wave communication has historically been a problem during reentry, preventing data transmission and reception. The ionized particles tend to absorb the electromagnetic radiation locally such that antennae become ineffective. The plasma sheath channel seeks to pioneer blackout prevention in-flight by matching the transmission frequency with a radio-transparent wavelength.

Pressure ports, thermocouples, heat flux sensors will be placed at multiple locations on the surface of the vehicle to monitor the aerodynamic, cooling and material experiments. Moreover, internal sensors such as strain gauges are used to monitor structural performance. A RAFLEX sensor is used to evaluate freestream conditions whereas an Infrared (IR) camera is placed at the back of the vehicle to monitor the temperature distribution on the control surfaces.

Simulation of Vehicle Performance

The prediction of aerodynamic forces and moments is of critical importance for the stability and trajectory analysis of the vehicle. For the preliminary design stage, computational fluid dynamics were deemed too resource intensive, resulting in slow iterations. Instead, a modified Newtonian inclination method is used to predict the aerodynamic body forces and moments. The model makes use of triangular surface mesh elements which can be imported and processed starting from a stereolithographic (STL) file. The accuracy of the model was determined to be sufficient by comparison of its output to the results of the solution of the Euler Equations at various angles of attack. Moreover, the model was enhanced with an option for viscous drag estimation for both laminar, turbulent and transitioning boundary layers. A scaling factor based correction method was formulated starting from data of similar missions, allowing for estimation of the vehicle's performance at supersonic and subsonic velocities, where the underlying assumptions of the modified Newtonian model no longer hold. Through estimation of the various aerodynamic performance parameters, the program could be used to substantiate critical design decisions. Furthermore, the model was also later used to determine aerodynamic coefficients of the current design throughout the course of the mission.

The aerothermodynamic model allows for determination of the stagnation point heat flux through equations found in literature. Moreover, the heat flux at all other points on the vehicle's lower surface can be determined for both turbulent and laminar flow based on another set of empirical formulas. An iterative method is used to determine the equilibrium wall temperature based on the heat flux induced by: the hypersonic flow, radiative heat dissipation, and cooling systems. The models for stagnation point heat flux have already been validated in the original articles by Detra et al. (1957) and Scott et al. (1985), whereas the model for the body surface temperature was validated by comparison to Space Shuttle and Buran flight data. The model's accuracy in presence of cooling fluxes was confirmed through comparison with the article published by Sudmeijer et al. (2007b). The temperatures of the upper surface were estimated based on past mission data.

The flight dynamics model numerically integrates the full non-linear equations of motion in an Earth Centered, Earth Fixed coordinate frame, by means of a 5th order accurate explicit Runge-Kutta time stepping scheme. Individual sub-components of the simulation, such as the international standard atmospheric model and the integration scheme were verified by a combination of unit tests. Moreover, generic trajectories were compared to analytical solutions of an atmosphere-free Earth for verification purposes. The model output was also found to produce very similar trajectories as the commercial software ASTOS, when initialized with the same parameters. The complete model was validated by comparison to a simulation of the reentry of the Apollo capsule by Hirschel and Weiland (2009), achieving remarkable likeness in the predicted trajectory.

A highly adaptive design philosophy was adopted for conception and optimization of the trajectory. Through a combination of proportional-integral-derivative software based control and analytical guidance equations, α (angle of attack) and σ (roll angle) modulation were implemented successfully to control the vehicle's reentry path. To guarantee that the necessary attitude changes can be performed and maintained, the vehicle's closed loop response to flap deflections was investigated in the scope of the control model.

The final stage of flight, starting from the ejection of the drogue parachute is covered by an independent model. The equations of motion presented in Mooij (2017a) are numerically integrated, yielding the velocity as a function of time as well as the oscillation angle. The model was also used to size the parachute, whose area is mainly dictated by the required terminal velocity for recovery, whilst oversizing results in excessive additional mass, volume and g-load upon deployment.

The structural model is used to ascertain whether the aerodynamic and resulting acceleration loads experienced during the launch, flight and recovery can effectively be sustained by the preliminary structural concept. The continuum structure is discretized into a boom and shear web structure, yielding a low order model, which is of adequate accuracy for the present stage of design. Failure is assessed based on the von Mises yield criterion, with a target safety factor of 3. Moreover, boom elements in compression are further surveyed with Euler's critical load buckling theory. Thermal expansion and its importance in the structure is briefly touched upon, followed by a vibrational analysis for a multi mass, multiple degree of freedom (MDF) systems, which is used to design the stiffness of the structure.

Risk Analysis

Risks were identified by looking at individual subsystems and analyzing the functional flow diagrams. After discovery, each risk was assigned a unique identifier and filled into the risk map according to its likelihood and impact. Mitigation strategies are proposed for the most critical risks.

The high sensitivity of the trajectory to the injection accuracy was found to represent a significant risk. If separation occurs at a too low altitude, the total energy will be insufficient to achieve the required range. The proposed mitigation strategy is to supply more energy than required to guarantee that the vehicle does not fall short of its trajectory requirements. However, the additional energy will have to be dissipated in a similar timeframe, resulting in more severe heat loads. The nose tip material is also known to be relatively brittle, such that particle impacts could result in potentially fatal damage during flight. The risk will be alleviated by frequent inspection of the exterior surface integrity as well as x-ray scans, as outlined in the inspection and maintenance schedule. Active risk monitoring is used to ensure that new risks are identified and old ones are being updated as the design evolves.

Market Opportunities

Several additional entities have been identified as potential customers in addition to the European Space Agency (ESA). Aerodynamic research centres are expected to be the main customer of the boundary layer transition and boundary layer shockwave interaction experiments. However, companies developing numerical simulation tools may also be interested in this data to validate their models.

The vehicle also offers opportunities for testing of thermal protection systems, which are the key to advancing reusable reentry systems technology. The necessity for an active cooling system also arises as a result of the sharp nose and leading edge radius, which in turn is required for achieving the high lift-to-drag ratio stipulated by the top-level user requirements. High glide-ratio vehicles are likely to be of increasing importance for sustainable and cost effective spaceflight in the upcoming age of space tourism.

Finally, it is undeniable that a hypersonic reentry vehicle could also be re-purposed for military applications. Though a potentially lucrative market, it is still unclear whether a co-operation with ESA will hinder military exploitation and/or funding.

Cost

The cost of the project may be broken down into costs relating to the materials and manufacture, the development cost, the operations and maintenance cost and finally the cost of disposal. The total project cost, including the technology readiness level development plan, is predicted to be approximately 266 M€. At the prospect of a reduced launch cost for the first flight, the operation of the vehicle is projected to cost 10 M€for the first flight, with all following flights estimated at 28.5 M€.

Future Development

The definition of subcontractors has been completed, assigning the detailed definition to companies specialized in the individual disciplines. The subsequent testing of individual components and subsystems has also been briefly outlined. Moreover, manufacturing, system testing and nominal operational protocols have been drafted. Guidelines for vehicle disposal are also proposed, largely in a context of recycling valuable materials and subsystems.

A rigorous reliability, availability, maintainability and safety (RAMS) analysis was executed, to ensure that the vehicle fulfills its requirements throughout its life cycle. Furthermore, the various logistical concepts, qualification tests and operational procedures are briefly outlined. Finally, the sustainability of each individual mission element is evaluated such that the mission complies with top-level user requirements.

Contents

List of Acronyms

Acronym	**Full Name**
AAOS	Active Anti-Oxidation System
AC	Active cooling
AR	Acceptance Review
ARA	Ablative Laboratory
BL	Boundary layer
CAD	Computer-aided design
CDR	Critical Design Review
CFD	Computational Fluid Dynamics
CIRA	Centro Italiano Ricerche Aerospaziali
CMC	Ceramic Matrix Composite
COTS	Component off the shelf
CSG	Centre Spatiale Guiannais
DLR	Deutsches Zentrum für Luft- und Raumfahrt
DOT	Design Options Tree
EADS	European Aeronautic Defence and Space Company
EPCU	Ensemble de Preparation des Charges Utiles
EPS	Electrical Power System
ESA	European Space Agency
ESOC	European Space Operations Centre
ESTEC	European Space Research and Technology Centre
FAA	Federal Aviation Administration
FEM	Finite Element Method
FLC	Fuzzy Logic Control
FMEA	Failure Mode Effect Analysis
FRR	Flight Readiness Review
FTC	Fault Tolerant Computer
GNC	Guidance, Navigation and Control
HEG	High Enthalpy Shock Tunnel Göttingen
HETC	High Efficiency Tantalum-based Ceramic Composite
IABG	Industrieanlagen-Betriebsgesellschaft mbH
ISA	International Standard Atmosphere
ISRO	Indian Space Research Organization
LEAF	Large European Acoustic Facility
LQR	Linearized Quadratic Regulator
LVA	Launch Vehicle Adapter
MDF	Multiple Degrees of Freedom
NDI	Nonlinear Dynamic Inversion
ORR	Operational Readiness Review
PD	Proportional-Derivative
PDR	Project Design Review
PID	Proportional–Integral–Derivative
QR	Qualification Review
RAM	Random-access memory
RAMS	Reliability, Availability, Maintainability and Safety
RCS	Reaction Control System
ROCCI	Refractory Oxidation-resistant Ceramic Carbon Insulation
SPFI	Surface Protected Flexible Insulation
SSR	Solid State Recorder
TPS	Thermal Protection System
TRL	Technology Readiness Level
TT&C	Telecommunications, Telemetry and Command
TUFROC	Toughened Uni-Piece Fibrous Reinforced Oxidation-Resistant Composite
VPDHS	VECTRONIC Payload Data Handling System

List of Symbols

Symbol	Meaning, Unit
A_{nose}	Nose area, m^2
a_x, a_z	Acceleration in x- or z-direction respectively (body-frame), m/s^2
B_n	Area of nth boom, m^2
C_D	Drag coefficient, -
C_{D_p}	Parachute drag coefficient, -
C_{D_v}	Vehicle drag coefficient, -
C_f	Friction coefficient, -
C_L	Lift coefficient, -
C_m	Moment coefficient, -
C_p	Pressure coefficient, -
c_p	Specific heat for constant pressure, J/kg K
c_{p_∞}	Freestream specific heat for constant pressure, J/kg K
c_v	Specific heat for constant volume, J/kg K
D	Drag force, N
D_0	Canopy diameter, m
D_p	Parachute drag force, N
D_v	Vehicle drag force, N
DR	Data bit rate, bit/s
E	Internal energy, J/kg
F_{rt}	Radial strength, N
F_{sl}	Suspension line strength, N
F_x, F_y, F_z	Force along the x-, y- or z-axis respectively, N
G_r	Ground station antenna gain, -
G_t	Vehicle antenna gain, -
g	gravitational acceleration, m/s^2
g_0	gravitational acceleration at sea level, m/s^2
$H_{t,current}$	Total enthalpy, J
h	Altitude, m
h_e	Entry altitude, m
$h_{w,current}$	Wall enthalpy, J
I_{xx}, I_{yy}, I_{zz}	Area moment of inertia about the x-, y- or z-axis respectively, m^4
K_{fq}	Pitch thrust controller gain, -
$K_{f\alpha}$	Body flap controller gain, -
K_n	Knudsen number, -
K_{yq}	Pitch thrust controller gain, -
$K_{y\alpha}$	Body flap controller gain, -
k	Roughness height, m Column effective length factor, -
k_{eff}	Effective roughness height, m
L	Lift force, N
L_a	Atmospheric attenuation, -
L_n	Length of nth boom, m
L_S, L_t	Space loss, - , Cable loss, -
l	Coolant latent heat, $\frac{J}{kg \cdot K}$
l_{sl}	Length of suspension lines, m
M_e	Boundary layer edge Mach number, -
M_p	Parachute mass, kg
M_{ref}	Reference Mach number, -
ΔM_{T_y}	Moment increment due to pitch thruster, Nm
M_x, M_y, M_z	Moment about the x-, y- or z-axis, Nm
M_∞	Freestream Mach number, -
N_{gores}	Number of gores, -
N_{sl}	Number of suspension lines, -
$\vec{n}$	Normal vector, -
$n_{g,max}$	Maximum load factor
P	Transmitter power, W
ΔP	Pressure difference between reservoir pressure and outside pressure, Pa
P_{cr}	Axisymmetrical buckling load for thin-walled conical shells, N
P_{crit}	Buckling load, N
P_p	Pump power, W
P_r	Prandtl number, -
p_n	Pressure force on inclined surface, Pa
q	Heat flux, $\frac{MW}{m^2}$, pitch rate, m/s
$\bar{q}$	Dynamic pressure, N/m^2
q_{cool}	Heat flux decrease due to cooling mechanism, MW/m^2
q_s	Shear flow, N/m
q_{target}	Target heat flux, MW/m^2
q_w	Wall heat flux, MW/m^2
R	Gas constant for air, J/kg K
R	Resultant aerodynamic force, N
Re	Reynolds number, -
Re_T	Transition Reynolds number, -
Re_x	Reynolds number at a distance x from the leading edge, -
R_{nose}	Nose radius, mm
r	position vector, m
S	Reference area, m^2
S_0	Canopy reference area, m^2
S_p	Parachute reference area, m^2
S_v	Vehicle reference area, m^2
S_z	Total shear force in z-direction, N
$S_{z,w}$	Shear force carried by the web, N
SNR	Signal-to-Noise ratio, -
St_∞	Stanton number, -
T	Temperature, K
T_r	Recovery temperature, K
T_s	System noise temperature, K
$T_{w,current}$	Wall temperature, K
t_D	Thickness of the webs, m
u_0	Wall component of velocity, m/s
u_θ	Velocity normal to material after deflection θ, m/s
u_∞	Freestream velocity, m/s
V	Velocity, m/s
V_c	Circular velocity, m/s
V_e	Entry velocity, m/s
V_g	Velocity for flying under g-load constraint, m/s
V_n	Freestream velocity normal component, m/s
V_q	Velocity for flying under heat flux constraint, m/s
V_∞	Freestream velocity, m/s
ΔV_j	Velocity Ejection velocity, m/s
W	Weight, N
x_k	Roughness location, m
x_{ref}	Reference x-coordinate, m
y_{ref}	Reference y-coordinate, m
z_n	z-coordinate of nth boom, m

List of Greek Symbols

Symbol	**Meaning, Unit**
α	Angle of attack, rad
$\alpha_{(L/D)_{max}}$	Angle of attack at maximum L/D, rad
β	Angle of sideslip, rad
β	Angle between the diagonal side and the horizontal plane of a thin-walled conical shell, rad
γ	Ratio of specific heats, -
γ	Flight path angle, rad
$\dot{\gamma}$	Flight path angle angular velocity, rad/s
γ_e	Entry flight path angle, rad
δ	Geocentric latitude, rad
$\dot{\delta}$	Geocentric latitude angular velocity, rad/s
δ_f	Flap deflection, rad
δ/x	Boundary layer thickness, -
ϵ	Emissivity, -
η	Efficiency, -
θ	Deflection angle, rad
θ_j	Ejection angle, rad
Λ	Sweep angle, rad
λ_r	Antenna efficiency, -
μ	Aerodynamic roll angle, rad
ν	Poisson's ratio, -
ρ	Density, kg/m^3
ρ_{eq}	Density for equilibrium glide condition, kg/m^3
ρ_g	Density for flying under g-load constraint, kg/m^3
ρ_∞	Freestream density, kg/m^3
σ	Stefan Boltzmann constant, $J/s\,m^2\,K^4$
σ_{n_n}	Normal stress of nth boom, N/m^2
σ_v	von Mises stress, N/m^2
σ_{yield}	Yield strength, N/m^2
τ	Geocentric longitude
τ	Shear stress, N/m^2
$\dot{\tau}$	Geocentric longitude angular velocity, rad/s
ϕ	Roll angle, rad
$\dot{\phi}$	Roll angle angular velocity, rad/s
$\ddot{\phi}$	Roll angle angular acceleration, rad/s^2
χ	Geocentric heading, rad
$\dot{\chi}$	Geocentric heading angular velocity, rad/s
Ω_t	Rotation rate of the Earth, rad/s

1 Project Objective & Organization

Driven by strong struggles in finding a breakthrough for the field of hypersonic research and re-entry vehicles, a project named Hyperion IV was set up to design an experimental hypersonic testbed with the priorities being low mass, proper reusability and low cost. Instead of using a single-use hypersonic vehicle, the reusability requirement shall guarantee to reduce future cost on the use of hypersonic vehicles for various objectives. The challenges faced by the design group ranges from the dangers of aerothermodynamics, such as high-temperature gas flows, to problems regarding shockwave-related phenomena, as well as material and performance aspects.

The Hyperion IV main purpose is to achieve a hypersonic flight ($M > 10$) and maintain the predetermined Mach number. Hyperion IV will collect data about various experiments including but not limited to the shockwave boundary-layer interaction and the boundary layer transition. Hyperion IV will also illustrate and test the functionality of an active cooling system. The need for these tests comes from the fact that the effects of hypersonic flight cannot be fully tested in ground-test facilities and not all phenomena are properly understood, which leads to the mission statement:

Mission Need Statement: To bridge the gap between ground-based estimations of hypersonic flow and hypersonic performance in flight.

To realize this need, the design team set its own objective combining its own needs with the customer needs. The primary objective statement is as follows:

Project Objective Statement: To design an unmanned experimental hypersonic testbed within 10 weeks with a group of 10 students with the additional goal of winning the Anthony Fokker prize.

In Chapter 2, an explanation is provided on what system engineering elements are incorporated in this project, how these were viewed by the group and these deliverables were made. Following in Chapter 3, the complete set of user requirements is introduced together with the derived critical user requirements, as well as the identification of top level user requirements. Chapter 4 a complete description of the market analysis is given, concerning the different parties which may potentially benefit from this project. Also, in the same chapter the return of investment is discussed. The outline on the different functions for the Hyperion IV is shown in Chapter 5, in the form of a functional flow and functional breakdown. Here, the functions of the Hyperion IV are shown in both a chronological and overarching manner, respectively. Going to a more technical stance, Chapter 6 discusses how the team managed to pick the final concept starting from the design option tree and performing a decent trade-off. After performing all of the different analyses, Chapter 7 shows the final design with the different budgets and a complete vehicle specification description. In Chapter 8, all experiments thought of by the design group per department are mentioned and discussed, in addition to an explanation on the methodology per experiment. Then in Chapter 9, an elaborate discussion is provided on how the Hyperion IV was analyzed from an aerodynamic perspective. The trajectory followed by the Hyperion IV is explained in Chapter 10. The controllability of the vehicle is fully discussed in Chapter 11. Moving to Chapter 12, the complete recovery part of the mission is discussed. Also, Chapter 13 considers the Hyperion IV from a structural perspective. Moreover, Chapter 14 considers the aerothermodyanmic phenomena which have to accounted for during hypersonic flight. The different approaches on designing a Thermal Protection System (TPS) are discussed in Chapters 15, 16, 17 and 18. To know how data onboard the vehicle is stored and transmitted, Chapter 19 provides a description on how the Telemetry, Tracking & Command subsystem is organized. Accompanying the latter, Avionics and Data management is explained in Chapter 20. The electric side of vehicle is fully described in Chapter 21. Coming to the more systems engineering side of the project, Chapter 22 discusses how the project is divided in different phases and what happens in each phase. For knowing the unprecedented flaws of the design, a risk analysis was performed and can be found in Chapter 23. The RAMS analysis of this project was documented in Chapter 24. To deem the Hyperion IV feasible in all regards, Chapter 25 discusses the sustainability analysis performed considering vehicle. To summarize on wether the Hyperion IV met all requirements, a requirement compliance matrix was set up in Chapter 26 to verify wether all requirements were was met. To encourage future research regarding the critical subsystems of the design, a TRL development plan was established and documented in Chapter 27. This TRL development plan is then included amongst others in the vehicle cost assessment, which can be found in Chapter 28. Finally, this report is ended with a conclusion written in Chapter 29 together with a brief recap on the major recommendations mentioned throughout the report.

2 Systems Engineering Approach

The systems engineering approach was a crucial part of the Hyperion IV design. Due to the time and manpower constraints on the project, it was mainly thanks to the use of system engineering tools that the work could be distributed efficiently among the team and that the design could be developed within 10 weeks such that it complies with the user requirements.

First, the systems engineering philosophy according to which the project was conducted is presented. Afterwards, the systems engineering tools applied throughout the project are discussed.

2.1 The Systems Engineering Philosophy

For the Hyperion IV mission, an ESA inspired systems engineering approach was followed throughout the project. The schematics of the approach, further described below, is shown on Figure 2.1.

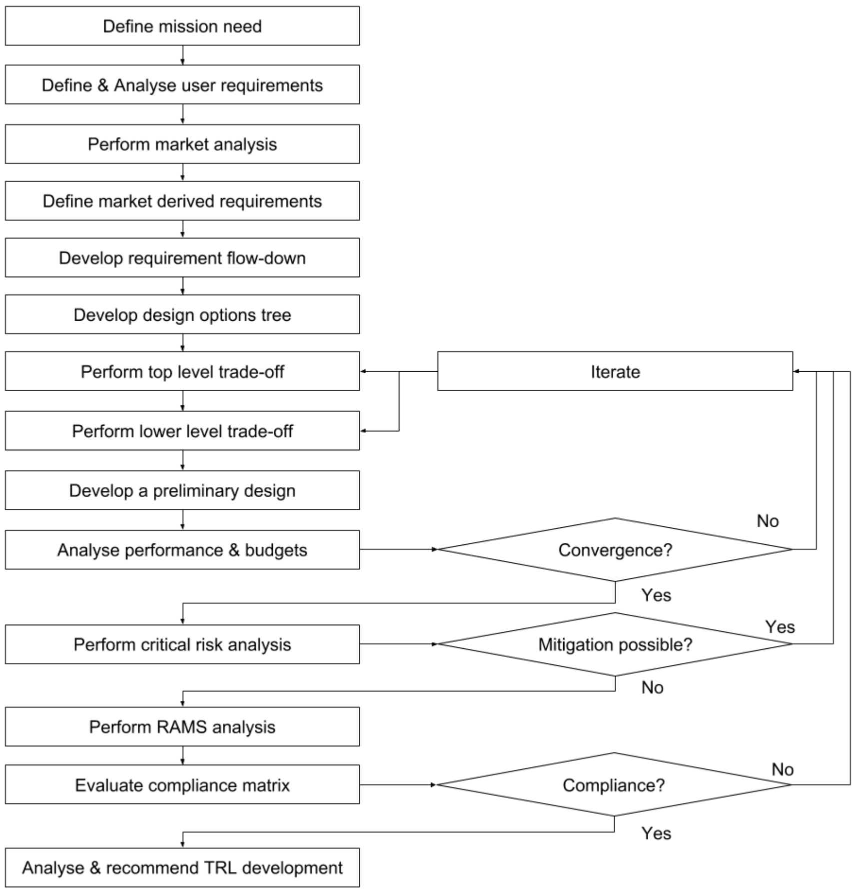

Figure 2.1: Schematic view the systems engineering approach to the design of Hyperion IV

Firstly, the mission need was determined and the user requirements analyzed. Afterwards, a thorough market analysis was performed to derive another set of user requirements with the purpose of increasing the vehicle's market value. The user requirements were then translated into system requirements, and a requirements discovery tree was made to show the effects of these requirements on the subsystem design.

With the requirements analyzed, several vehicle concepts were developed and documented in the design options tree (DOT). The DOT was filtered out by removing unfeasible concept branches, and the final concepts entered a trade-off process. After the trade-off of the main concepts, several trade-offs were performed on a lower level. For the most suitable concept, a preliminary design was made, and its performance was evaluated. In case this performance complied with the requirements and its interfaces could be satisfied by the rest of the subsystems, the concept was kept. Usually however, the performance was insufficient or there was found to be a conflict with other subsystems, and thus iteration was necessary. Due to size and time constraints, the lower level iterations are not included in the report.

Once convergence was found, risk assessment was performed. If critical risks were found, mitigation strategies were proposed. If these strategies were feasible and could be readily included in the design, another iteration was performed with the most critical risks mitigated. Afterwards, the RAMS (Reliability, Availability, Maintainability, Safety) analysis along with a sustainability study was developed. The design was then checked for the compliance with all the user requirements using the compliance matrix. In case compliance was not satisfactory (requirements not met or verified) and if sufficient time was available for re-design, the design was iterated again.

Once convergence was achieved, the technology readiness level development was analyzed. With this step, the analysis was completed for this phase of the project.

2.2 Systems Engineering Tools

As mentioned in the paragraphs above, several tools have been used during the project to pursue the systems engineering philosophy. Such tools were:

- Scheduling and organizational tools: Work breakdowns, Flow diagrams, Gantt charts, Organograms
- Project design tools: Requirements discovery tree, Design options tree, Return of Investment analysis, Trade-off tables, Sensitivity analysis
- Interface control tools: N2 charts, Interface documents and excel sheets
- Risk and feasibility control tools: Risk maps, RAMS analysis, Compliance matrix, Sustainability questionnaires

The interface documents and sheets along with the sustainability questionnaires were developed specifically for this project to enhance the level of systems engineering and to promote sustainability of the mission. The tools above were used throughout the project and will be presented in the rest of the report.

2.3 Project Organization & Scheduling

Preceding the technical work, the working group was split into several divisions such that concurrent engineering is possible. For that purpose, an organogram was created to distinguish the responsibilities in the team. The organogram was updated each time when resources had to be redistributed.

Furthermore, the project was split into 4 separate phases with the following reviews:

- Baseline review, 7th May 2018 at TU Delft
- Midterm review, 29th May 2018 at TU Delft
- Final review, 28th June 2018 at ESTEC, Noordwijk

A Gantt chart was made to plan the tasks until every scheduled review, and was kept as a living document to monitor the progress of the project.

The phases along with a short description of their content, their respective reviews and other deliverables are shown in Figure 2.2. It is also shown during which phases the design iteration and the tool development processes took place, and that systems engineering was an integral part of every stage of the project. As indicated in Figure 2.1, the definition of the mission objective was followed by the requirement analysis, which is presented in the next chapter.

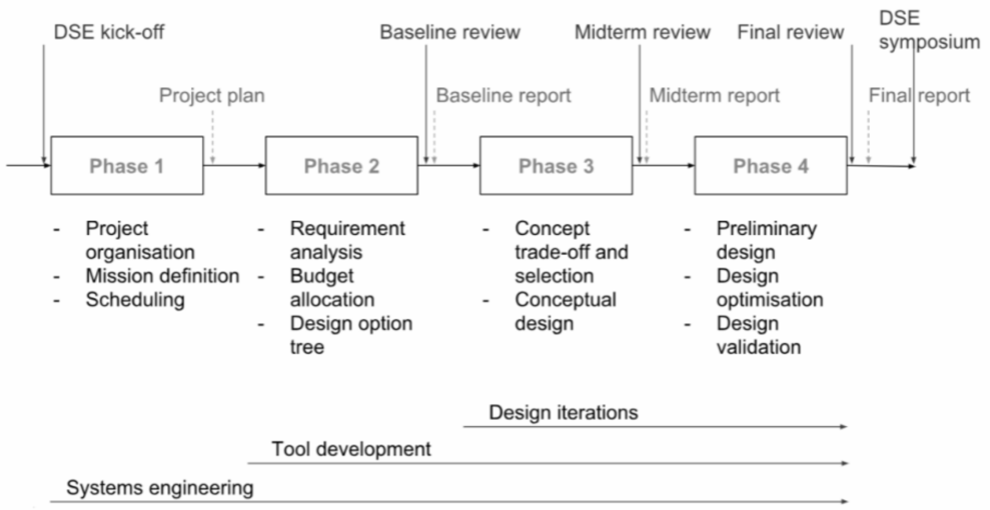

Figure 2.2: Schematic view the systems engineering approach to the design of Hyperion IV

3 Requirement Analysis

This chapter describes the given user requirements for the project leading to the system requirements used as a benchmark for the respective subsystem design described subsequent. The user requirements are elaborated as top level mission requirements and revised.

3.1 User Requirements

The following user requirements were specified by the customer:

- **US.REQ.01 A vehicle shall be designed that can serve as test bed for, amongst other, hypersonic experiments.**
- **US.REQ.02 The cost of the vehicle including operations shall not exceed M€120.**
- **US.REQ.03 A launcher vehicle shall be selected and a design of the interface with the launcher shall be included.**
- **US.REQ.04 The launch cost shall be minimal; the negotiation of a free launch is encouraged.**
- **US.REQ.05 The maximum mass of the vehicle shall be 250 kg.**
- **US.REQ.06 The design of the recovery system shall be included in this exercise.**
- **US.REQ.07 The vehicle shall be reusable for at least 20 times.**
- **US.REQ.08 The use of toxic materials shall be avoided.**
- **US.REQ.09 Testing shall be minimized (without violating reliability) to not waste resources.**
- **US.REQ.10 Landing and recovery shall not pose a hazard to environment and personnel.**
- **US.REQ.11 End-of-life strategy of the vehicle shall be defined.**
- **US.REQ.12 The vehicle's trajectory shall remain sub-orbital.**
- **US.REQ.13 During reentry the vehicle shall be able to fly (at least) the next trajectories.**
  a. Flying at a constant pre-selected Mach number (M $>$ 10) with a Reynolds number variation: 500,000 $<$ Re $<$ 2,000,000 (per meter).
  b. Flying at a constant pre-selected stagnation point, with a heat load: 1 MW/m^2 $< q_{nose} <$ 6 MW/m^2.
- **US.REQ.14 The L/D shall be as high as possible, if needed wings are allowed.**
- **US.REQ.15 Launch site, trajectory and landing site shall be determined.**
- **US.REQ.16 The vehicle shall land within 100 km of the launch site.**
- **US.REQ.17 The vehicle must be fully autonomous to complete its mission.**
- **US.REQ.18 Onboard experiments include (but are not limited to):**
  a. Active cooling systems.
  b. Exposure of heat materials to a hot hypersonic flow.
  c. Boundary layer transition experiments.
  d. Shockwave boundary-layer interactions.
- **US.REQ.19 Market analysis shall identify potential experiments and customers.**
- **US.REQ.20 Easy reconfiguration of the vehicle interfaces shall allow for installing different passenger experiments in between flights.**
- **US.REQ.21 It shall be possible to reconstruct the trajectory post-flight.**
- **US.REQ.22 Temperature and pressure shall be measured at critical locations at a TBD frequency.**
- **US.REQ.23 It shall be possible to reconstruct the boundary-layer transition (post-flight).**

User requirements 02, 04, 05, 07, and 09 concern the minimization of resources and a lean project. ESA as a public supranational organization has to treat each project under high budget constraints. As the project is standing on the shoulder of giants, it is important to provide additional scientific value for the society. This shall be done by the means of experiments, and the raising of TRL of promising technology. User requirements 01, 12, 13, 16, 17, 18, 19, 20, 21, 22, and 23 were given under this consideration. In times of scarce resources paired with natural and society environmental issues, it is important to design a sustainable project. This is expressed in requirements 10 and 11. In the next step, top level mission requirements are derived from the introduced user requirements.

3.2 Top Level Mission Requirements

The user requirements given and introduced in section 3.1 are analyzed and condensed in this section. Multiple user requirements are merged in one mission level requirement to enable the derivation of initial system level requirements and constraints. This step is vital in the design process, as it determines the direction of the project.

- **SYS.F.1 The vehicle shall be reusable 20 times.**
- **SYS.F.2 The vehicle shall follow a suborbital trajectory.**
- **SYS.F.3 It shall be possible to reconstruct the trajectory post-flight with an accuracy smaller than 1 m.**
- **SYS.F.4 The landing site shall be within 100 km from the launch site.**
- **SYS.F.5 The vehicle shall be fully autonomous.**
- **SYS.F.6 The trajectory shall ensure a constant Mach > 10 and a variable Re of 5e5 < Re < 2e6.**
- **SYS.F.7 The trajectory shall ensure a phase of constant stagnation point heat flux of 1 MW/m^2 < q < 6 MW/m^2.**
- **SYS.F.8 Active cooling systems shall be included in the mission design as an experiment.**
- **SYS.F.9 Material experiments shall be included in the mission design.**
- **SYS.F.10 Aerodynamic experiments shall be included in the mission design.**

In addition to the functional mission requirements, the following mission constraints were defined:

- **SYS.C.1 The cost shall not exceed M€120.**
- **SYS.C.2 Safety shall be ensured throughout the project.**
- **SYS.C.3 Use toxic material shall be avoided.**
- **SYS.C.4 All aspects of the project shall comply with national and international laws.**
- **SYS.C.5 Maximum mass of the wet S/C shall be below 250 kg.**

The mission level constraints paired with the system level requirement 1 enforce a tight design corridor on the project, limiting resources and imposing a challenging number of reusability when comparing with mission heritage. The experimental phase is closer defined by the mission requirements 6, 9, and 10. Further, mission level requirements 2, 4, 5, and 8 suggest the design of a long range mission, extending experimental time as far as possible. As driving requirements mission requirement 1, 2, 4, 6, 7, and 9 were identified, as they point the design in a specific direction not achievable otherwise. As critical requirements, and maybe in a later stage identified as killer requirements, requirement 1, and constraint 1 and 5 were identified. In a next step, alteration of the top level mission requirements, if identified as killer requirements, is described.

3.3 Requirements Negotiation

During the early design process it became obvious that it was not possible to achieve a design fulfilling all of the critical requirements. The critical requirements on their own are already challenging, but a combination of them, and paired with the driving requirements, would lead to an unfeasible design. Based on internal communication with the supervisors and the customer, it was decided to challenge SYS.C.1, SYS.C.5, and SYS.F.1.

After negotiation with the customer, the requirement SYS.C.5 was changed to a target value of 400 kg, including a margin of 50 kg. Furthermore, it was decided to design for two distinct design cases with different combinations of cost and reusability. The total cost for a vehicle that can be flown at least one time should not overshoot M€156. The total cost for a mission of 20 times reusability should be lower than M€267. The increase of total cost to M€267 ensures a proper development program to increase the TRL to meet the 20 times reusability in light of a responsible risk management. The TRL development plan covers the development program for a metallic nose tip only, as a program for all subsystems is beyond the scope of this report. The new top level mission requirements and constraints read as follows.

- **SYS.C.1 The cost in combination of a one time use or 20 times reusability shall not exceed the following:**
  a. M€156 for a vehicle flown once.
  b. M€267 for a vehicle that is 20 times reusable.
- **SYS.C.5 Maximum mass of the wet S/C shall be below 400 kg.**

3.4 Derived Critical System Requirements

The top level mission requirements define an encompassing set of mission parameters to be satisfied. These parameters naturally lead to more specific requirements, both at the system and subsystem level. While the subsystem requirements are individually analyzed in each separate subsystem chapter, the system ones will be mentioned and reviewed in the following section.

- **SYS.CR.1 The vehicle shall withstand any loads imposed on it during the mission**: Stemming from various system requirements, it is rather clear that the vehicle should not experience significant damage due to unexpected loads or impacts. This requirement will be mostly tackled by the structures housing the internal components of the vehicle.
- **SYS.CR.2 The vehicle shall be designed such to protect the internal subsystems**: Following the above requirement, it is necessary for the vehicle to provide housing and protection for subsystems. This includes, but is not limited to, high volumetric efficiency as well as specifically positioned holes within the structural webs to house all components.
- **SYS.CR.3 The vehicle shall be designed to ensure reliability and reusability**: Stemming directly from US.REQ.07, the vehicle shall have specifically designed subsystems to withstand 20 flights. This not only includes the structures and TPS, but also redundancy of most flight components.
- **SYS.CR.4 The vehicle shall provide means of guidance & navigation**: The vehicle shall be able to receive signals and to navigate to the experiment "location".
- **SYS.CR.5 The vehicle shall provide means of control**:This requirement implies the 3-dimensional movement of the vehicle by various means; however more specific requirements will be set by subsystems themselves.
- **SYS.CR.6 The vehicle shall have an L/D ratio higher than 3**: This requirements is meant to satisfy US.REQ.14, while giving it a coherent figure.
- **SYS.CR.7 The vehicle shall have an active cooling system** Not only due to user requirements, but also to aerothermodynamic effects, the presence of such a cooling system is required.
- **SYS.CR.8 The vehicle shall provide a platform for experimental testing** Since the whole mission is built around the experiments, the vehicle needs a physical platform to place them on. This can be assembled on either side, but it needs to be considered with the placement of thermocouples and other sensors.
- **SYS.CR.9 The vehicle shall allow for dis-assembly** Due to its reusability and accessibility requirements, the vehicle's inside needs to be accessed for data collection and hardware replacement purposes.
- **SYS.CR.10 The vehicle shall transmit data through communication link with speeds of 15Mbit/s** Due to redundancy requirements, the vehicle will need to transmit data to the ground stations at all times except the blackout phase. This will allow for the data to be stored remotely in case of vehicle failure.
- **SYS.CR.11 The vehicle shall be able to store 100 GB data on board** During the blackout phase, when hot plasma makes communication impossible, data will need to be stored within the vehicle.
- **SYS.CR.12 The vehicle shall be able to transfer all gathered data upon vehicle retrieval** Stemming from the requirement above, the data collected will need to be retrieved from hard drives and moved to a ground facility for analysis.

Further requirements can be derived from the market analysis, which is discussed in the next chapter.

4 Market Value and Investment of Return

Hyperion IV is certainly the first craft to maintain a constant hypersonic flight, vehicles like the HTV-2, X-51, and IXV have tried before. To understand the need for such vehicles can be better understood if one identifies the main groups of interests and identifies what more Hyperion IV has to offer. The groups considered are aerothermodynamic research centers, the military and the space industry. Each interest group will be covered in their own section. Each section will describe why this group is particularly interested, what Hyperion IV has to offer to fulfill this interest and what experiments increase its market value. When considering a vehicle that will preform 20 flights, it is expected that after one flight the desired aerothermodynamic data would have been collected. To make the other 19 flights appealing, besides demonstrating reusability, other tests are considered. Most of these tests will concern testing of new technologies, something that aligns with the philosophy of the craft as a testbed.

4.1 Aerodynamic Research

Despite decades of research and testing, much is still unknown regarding hypersonic boundary layer transition phenomena. The understanding of boundary layer transition is critical for hypersonic flight vehicles, as the state of the boundary layer dictates much of the vehicle design and even the mission profile. Therefore vehicle design is often left to hypersonic wind tunnels and plasma wind tunnels test, which unfortunately lack the ability to correctly imitate all conditions during hypersonic flight. Hyperion IV aims to deliver valuable data which will allow researchers to better understand the hypersonic flight regime, and with this, better predict and model hypersonic aerodynamic phenomenon. Hyperion IV will do this by allowing the recreation of both the laminar an turbulent boundary layer under different Reynolds and Mach numbers. Also tiles can be replaced with different materials which allows for the study of the stability of the boundary layer. For later flights it might be possible to add new aerodynamic devices or sensors. This was partly why straight and relatively easy manufacturable plates were chosen. Experiments can be integrated in those plates and easily switched between flights. It is therefore suggested that if opted for case 2, a proper interface should be designed which allows the integration of many modular experiments. Examples of these sensors are optical pressure sensors and high-response sensors. The former uses infrared waves to study the pressure and therefore does not interact with the boundary layer, producing more accurate data. The latter is a tube that sticks out which has a very high sample rate and is therefore able to do short wavelength acoustic and shock wave measurements, making the study of second mode instability possible.

4.2 Thermal Protection Research

A thermal protection system is one of the hardest systems to develop for reentry and hypersonic vehicles. It is for this reason that a truly reusable vehicle has not been developed to date. The Space Shuttle was officially a reusable craft, however after every flight the entire TPS had to be inspected and many parts had to be replaced. Even the new Dragon capsule from SpaceX, with a design driven by reusability, replaces its TPS. Hyperion IV aims to develop a fully reusable TPS which also operates at critical conditions without compromising the vehicle integrity. It aims to achieve this by using an active cooling system, thus reducing the critical conditions at the surface and by considering materials with a high ablative damage tolerance. The latter is applicable when an Al2O3-W nose tip is chosen (described in Ch. 18). Note that a better understanding of the boundary layer results in more accurate predictions of the heat load therefore the thermal protection system can be designed more effectively. The craft will allow, through its modular panel construction, the analysis of TPS materials of which the behavior has to be studied under different reentry conditions. It will be possible to connect the researched material to the inside through the TURFOC such that accurate sensor data can be extracted.

4.3 Military

Currently military organizations are the biggest investors for hypersonic vehicles, examples are the X-43, X-51 and most recently the HTV-2. Applications of military hypersonic technology vary from fast extractions of personnel to surveillance, projects similar to ones ran in the 80s. Although military would be a lucrative investor, its impact on the project should be properly discussed with ESA and the other parties involved. Since ESA is a cooperation between governments, military influence might be undesired. It is also necessary to consider that military specifications generally vary greatly from civilian ones, something that could drive up the development cost to the utmost extent.

4.4 The Space Industry

Ever since the first launch, this industry has been struggling with the enormous cost that comes with putting something in space. It was due to this reason that as early as the 60s, spaceplane concepts emerged. The feasible development of spaceplanes, however, requires huge technological steps concerning various subsystems such as propulsion, thermal protection, lift and stability & controllability, also known as milestones. Although it was not part of Hyperion IV's initial mission, some additional requirements were found to be valuable to contribute to these big steps (4.6) and thus increase both the vehicle's scientific and commercial value. Hyperion IV can accomplish this by demonstrating the use of an active TPS. This is a promising answer to the reusable TPS problem and by allowing the study of controllability in all flight regimes, subsonic to hypersonic.

Hyperion IV will primarily generate value by reducing the development cost for spaceplanes by reducing their uncertainty. Hyperion IV also offers the testing of a couple of new GNC software, namely Fuzzy Logic and nonlinear dynamic inversion control, which are described in Section 8.6. Hyperion will also explore communication during reentry which is normally disturbed by the plasma. If successful it will allow future vehicles to send their data during reentry, resulting in a safer system. On the other hand communication with ground control, during landing, will be crucial when spaceplanes enter the transportation sector. Other experiments may be included under the philosophy of modular plates. Examples could include infrared optical guidance sensors, which aims to look past the plasma and such can be guided and stirred to a destination. Such experiments and the modular capabilities can and will be studied in later iterations.

4.5 Return on Investment

Due the testbed nature of Hyperion IV, it is impossible to perform a conventional return on investment analysis. The return is therefore namely in the scientific data and milestones it aims to overcome. As has been mentioned before, a modular integration in the next phase might offer a way for commercial and non-commercial organizations to buy experimental space. With the selling of experimental space it might be feasible to accumulate a budget (37.1M€) such that a "free" launch can be achieved. The amount that organizations are willing to pay is very uncertain since there is currently no market that offer the same flight conditions. The closest comparable systems are plasma shock wind tunnels however with expensive operational cost and limited Mach numbers that can be researched at a constant Reynolds number. Being such a unique project, therefore, can greatly help Hyperion IV generating much more return on investment than only science data gathering. Now, in the next chapter the functional baseline will be discussed. It was developed to understand all mission functions prior to the conceptual design.

4.6 Derived User Requirements

Hyperion IV has a the potential to contribute a significant amount of scientific value to the space industry, however for this to happen the following derived requirements had to be considered throughout the design process. These Four requirement might not seem very driving on the surface, but in reality it drives Hyperion IV to tackle the three of the four primary milestones of spaceplane development. Unfortunately due to the mass constrain a spaceplane propulsion system could not be included. Every derived requirement includes a small explanation why it was set.

- **DUS.REQ.01 The vehicle shall be able generate compression and pressure lift** For a spaceplane to work it has be able to fly though the 4 sonic regimes, it therefore needs to produce lift throughout the 4 sonic regimes.
- **DUS.REQ.02 The vehicle shall fly at an altitude such that the hypersonic boom does not disturb civil life, when flying over civilian areas.** One of the major reason the Concorde became economically unfeasible, was its limited application, due the regulation that prevented flying over land. For spaceplanes to thrive, they have to show that their hypersonic boom is not disturbing to civil life.
- **DUS.REQ.03 The vehicle shall have a minimum constant hypersonic flight of at least 11.3 seconds.** This requirement was set based on the Hypersonic constant flight record, set by X-43. Even though this craft had the primary purpose of proving the feasibility of scramjets. Secondarily, it was also used to research the flight conditions during constant hypersonic flight. Hyperion IV who primary purpose is to research the hypersonic flight conditions should therefore at least preform better at this task than the X-43.
- **DUS.REQ.04 The vehicle shall allow the study of stability & controllability during hyper-, super-, tran-, and subsonic conditions** The stability and especially the controllability are still major issues for hypersonic vehicle development, illustrated by DARPA's HTV-2 and the X vehicles 43 and 51. All either lost control or were disregarded the moment they left the hypersonic regime. Hyperion aims to create a better understanding on this phenomenon.

5 Functional Baseline

As a part of the system engineering approach, the functional baseline was developed for the mission prior to conceptual design analysis such that all the functions of the mission are understood and considered. Firstl a three level functional flow diagram (FFD) was generated, outlying the main functions and responsibilities of the vehicle systems. Three levels were chosen as they could provide sufficient detail about the function to make decisions about the design. They lead to the definition of high level functional requirements, while also not violating the clarity of the diagram. Afterwards, the functional breakdown structure (FBS) was constructed based on the FFD to elaborate on the tasks to a higher level of detail. The FBS included four levels of functional breakdown.

5.1 Functional Flow

The FFD was split into two parts. First, Figure 5.1 shows the phases of testing, transportation, refurbishment and end of life (EOL) phases of the mission. The mission operations (OPS), including the flow from C to OPS END, will be discussed later.

The first functionality considered is the vehicle testing. From the perspective of the vehicle, it should be designed such that it is possible to attach it to transportation systems and such that it withstands the transportation and handling loads. Moreover, it should allow for assembly and disassembly in case the subsystems and components can be tested together as well as separately. For the transportation to the launch site, the same transportation functions already mentioned hold. In addition, the vehicle shall also be able to survive the storage conditions for prolonged period of time in case the launch is delayed. If the launch delay is too large, testing might need to be performed again to verify that the vehicle still operates properly, which is indicated by the dashed arrow back coming back to testing.

Once at the launch site, the OPS block indicates that the flight phase takes place. The OPS phase is shown in Figure 5.2, which shows the flight part of the mission, starting from launch to performing of the experiment. The end of the OPS block, the recovery and the refurbishment, are shown back on the bottom of Figure 5.1. The launch functionality focuses mostly on pre-flight system testing and checks. Once the proper functioning of the systems is confirmed and memory is cleared, updating of the battery and tank statuses is performed. The crucial flight software (FTC stands for flight computer and VPDHS for the data handling unit, for more information refer to Chapter 20) is then properly initialized for the launch and the vehicle is integrated with the launch vehicle through its launch vehicle adapter.

The mission proceeds with the separation from the launch vehicle. The separation switch allowing for recovery is activated and the rest of the on board systems is initialized. The GPS signal is obtained, leading to the evaluation of the attitude and position, based on which the first maneuvers can take place.

During the next phase of the flight, the trajectory is precisely maintained while the experiments are performed and the transmission and deceleration to the recovery conditions occurs. During the trajectory maintenance, the inputs from the GPS and IMU are constantly processed. Just before recovery at 10 km, data from the altimeter is also included. The attitude, position and velocity of the vehicle can be thus computed. This data is compared to the nominal trajectory and the required moment and force changes are determined. Based on the required deflections and freestream conditions, it is decided which method of reaction control is the most optimum for usage, and the appropriate flap deflections or thruster firing is executed to achieve the changes in attitude and velocity. The precise chain of control can be found in Chapter 11.

The experiments which can be found in Chapter 8 are performed by processing the data from the sensors, first through the payload data acquisition and handling units (VPDHS), and secondly through the flight computer (FTC). To provide data backup, the data is stored in both the payload handling units and the flight computer. In addition, the data is also down linked to ground stations once the Mach is below Mach 10 and the plasma layer does no longer pose a significant problem for the signal transmission. A net of several ground stations was developed as described in Chapter 19 and based on the vehicle's position, a ground station will be picked for connection. Based on the available transmission power and the ground station characteristics, the gains of the transmitter and amplifiers will be adjusted to provide for sufficiently low bit error rate (BER), as explained in Chapter 19. Once all the Mach-dependent experiments are finished, the hypersonic regime is aborted, and the vehicle starts deceleration to perform recovery.

The recovery along with the end of the mission are shown on the bottom of Figure 5.1. A signal is sent to the recovery circuit, which fires the pyro bolt through a pyrotechnic charge. This activates the mortar and releases the parachute. Location is broadcasted through the transmitter once again to assist the retrieval, after which most of the sensors and instruments apart from the main computer are turned off to prevent harm and resulting data loss during the recovery operations. After sufficient stabilization and deceleration of the vehicle is achieved thanks to the parachute, mid-air retrieval is performed by helicopters. More information on the retrieval can be found in Chapter 12. After recovery, the vehicle is refurbished. The main functions of the vehicle are then to provide both physical and data access to its subsystems for maintenance activities. This concludes the flight phase of the FFD. From Figure 5.1, it can be seen that after each flight the vehicle is again transported back and possibly tested if needed. Once 20 flights are performed, the EOL phase begins. During EOL, the memory is cleared, the vehicle shuts down completely and allows for a safe disassembly.

The functional flow diagram serves mainly to analyse the roles of different subsystems during the mission, and to derive functional system requirements.

5.2 Functional Breakdown

Based on the FFD, the functional breakdown was made. The tasks of the vehicle were categorized to distinct groups and collected. Afterwards, they were broken down to the fourth level of detail. This was done such that it is easier to gather all the functionalities required for a given subsystem, and thus easier derivation of the subsystem requirements.

Figure 5.3 shows the FFD derived tasks related to the categories of Guidance and Control, Navigation, Command and Control and finally, Testing and Transportation. It is indicated that all the Command and Control related tasks are performed by the flight computer or by the payload data handling unit and thus those instruments are no longer mentioned in the separate tasks in that category.

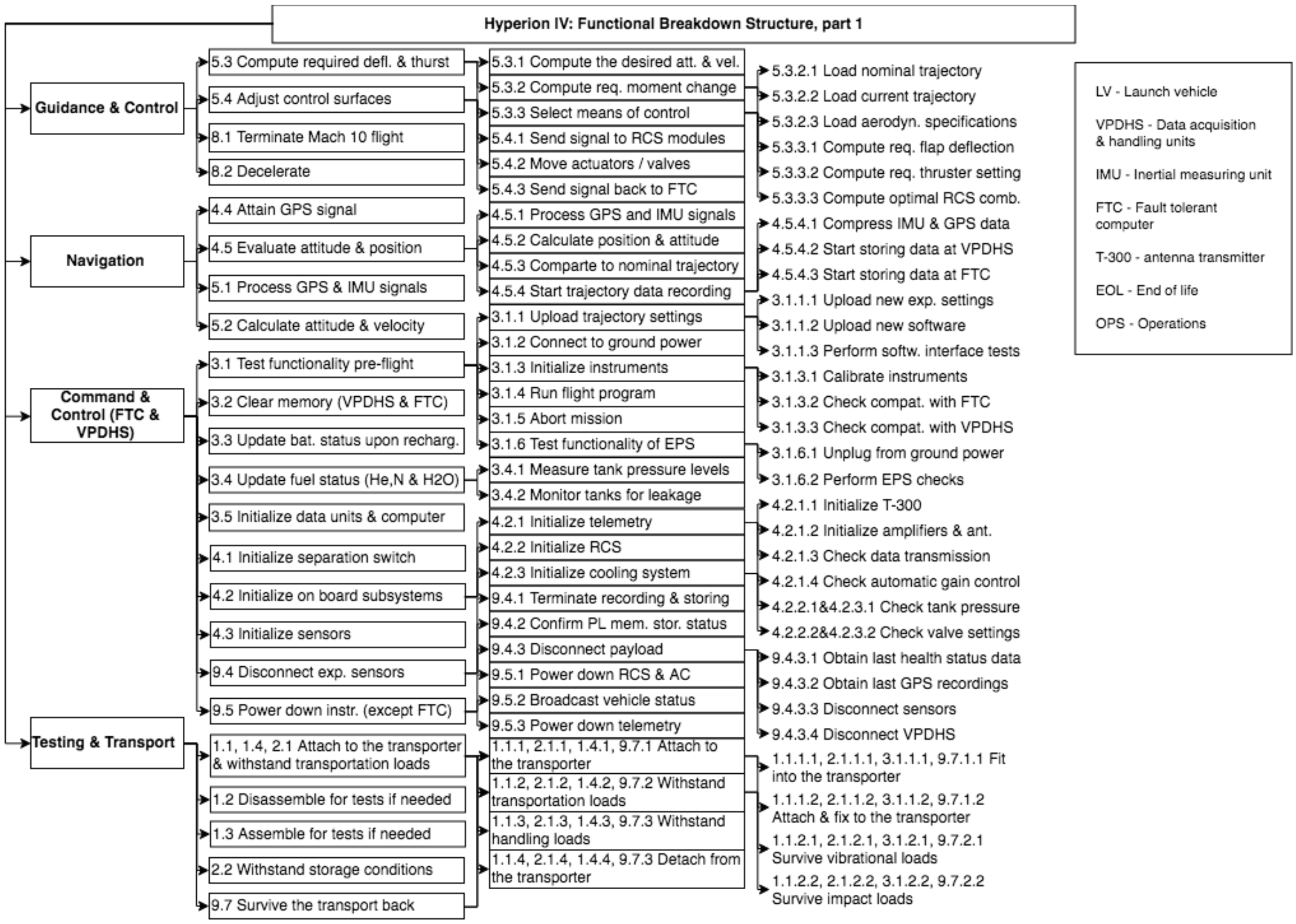

Figure 5.3: First part of the Functional Breakdown Structure

The second part of the FBS is shown on Figure 5.4. This part includes that tasks regarding the Launch Vehicle Integration, the In-flight Data Handling, In-flight Data Transmission, Landing with Recovery and lastly, the Maintenance and End of Life. In-flight data handling is performed mainly by the payload data handling unit, while the transmission is conducted by the transmitter, amplifier and the antenna.

At the end of the design process, the FBS should be revisited to ensure that all the above mentioned tasks can be performed. Just like several other system engineering tools, the FFD and FBS are living documents and thus it is possible to update these charts during all the design iterations to reflect the mission profile with better accuracy.

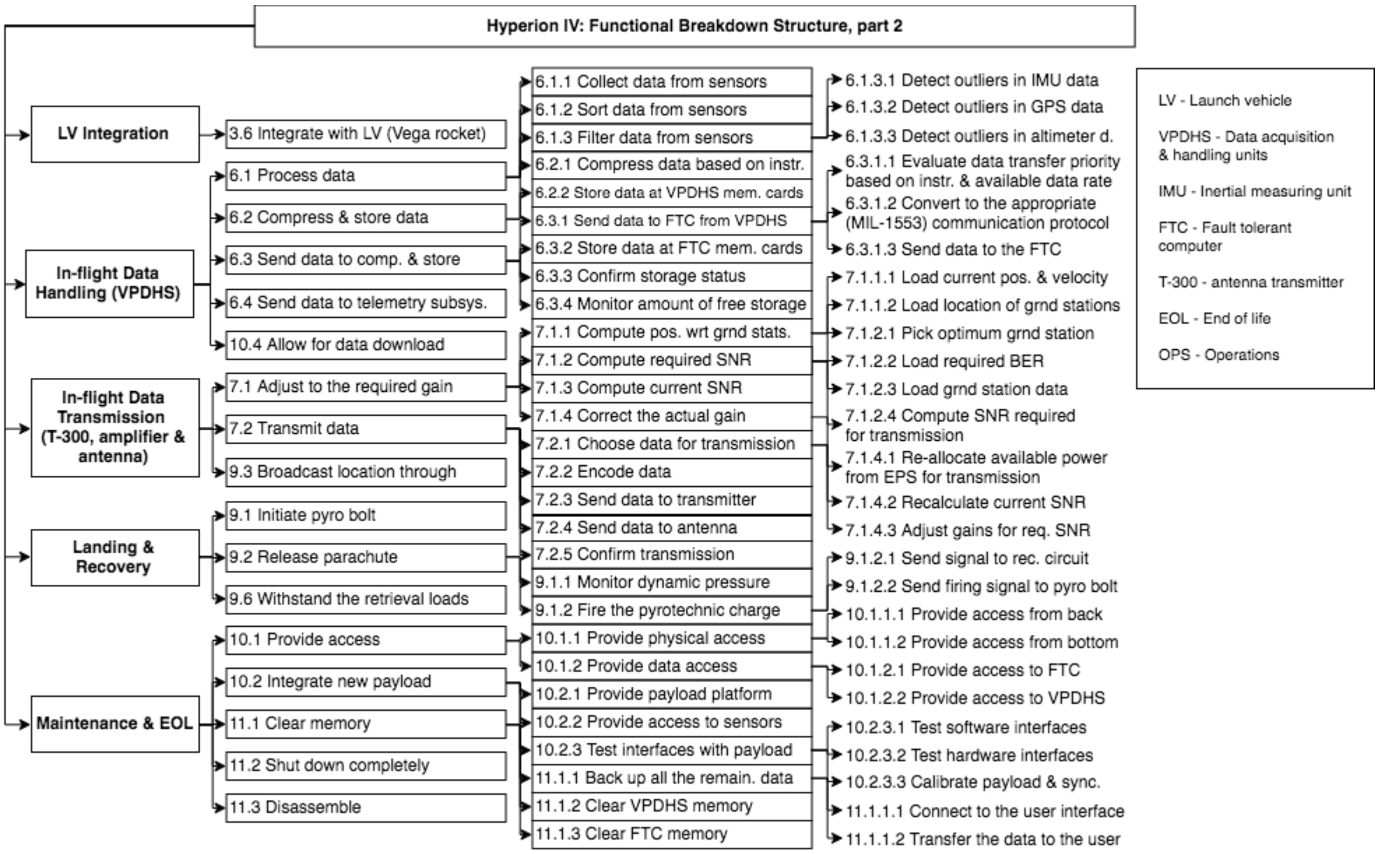

Figure 5.4: Second part of the Functional Breakdown Structure

After the functional baseline was defined, the conceptual design development was performed, through which the options were explored and a trade-off was made and which is described in the next chapter.

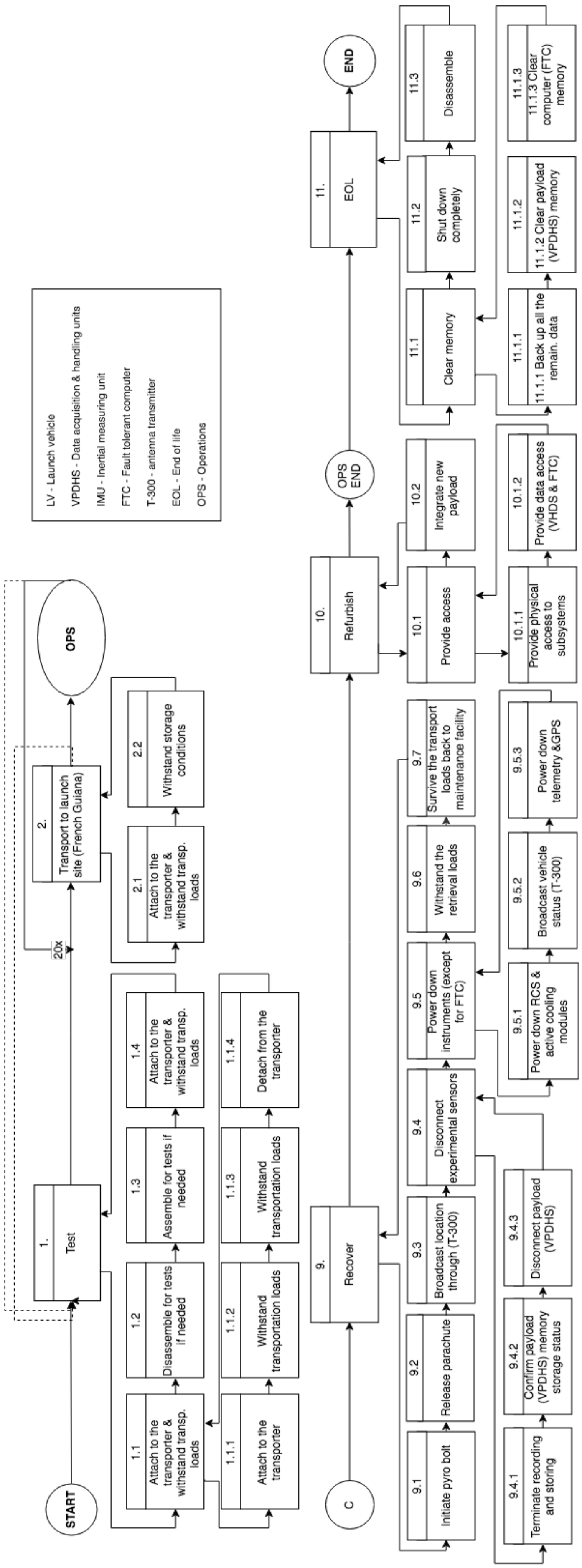

Figure 5.1: Functional Flow Diagram with the testing, transportation, refurbishment and EOL functions

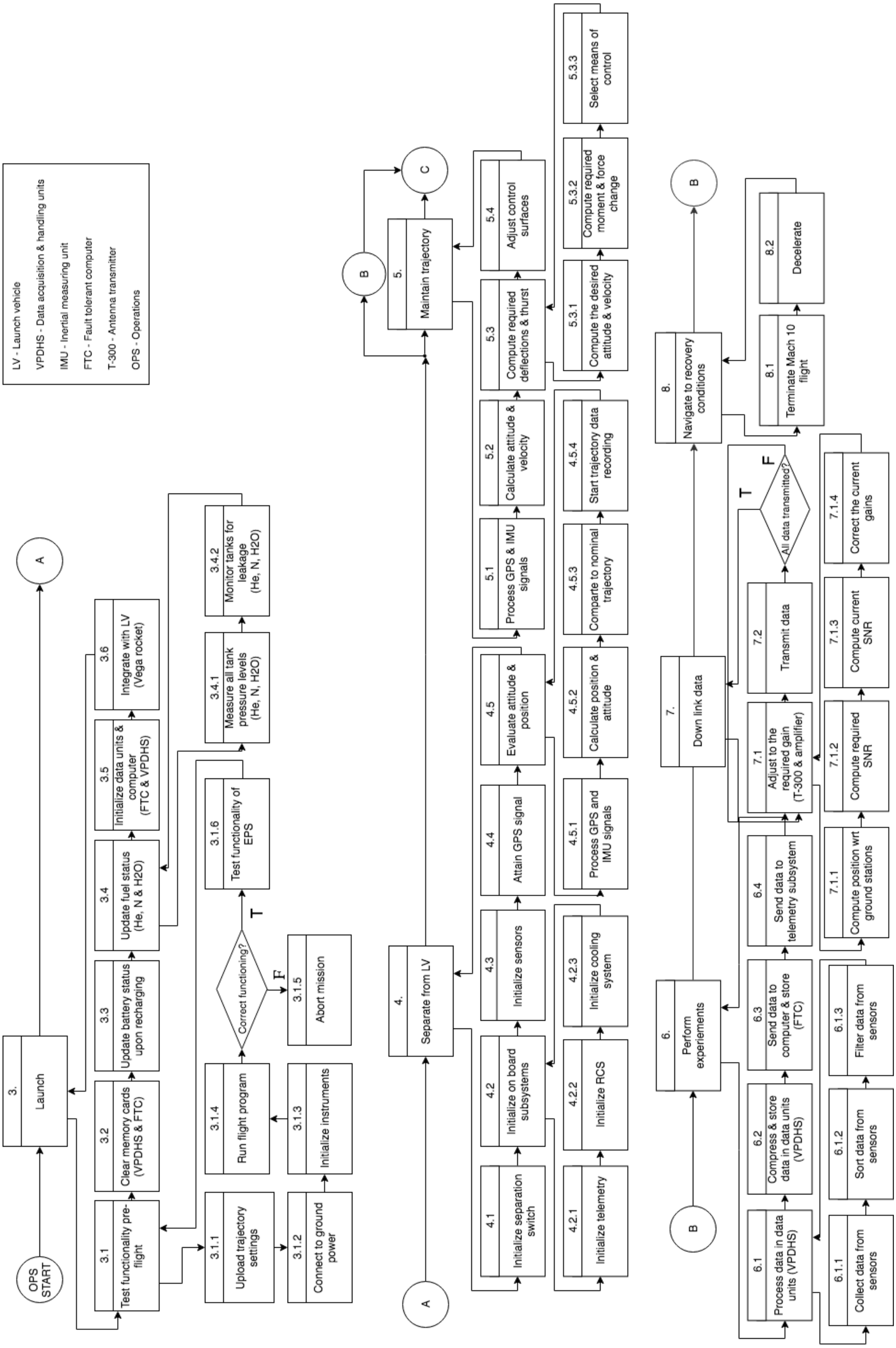

Figure 5.2: Functional Flow Diagram with the functions derived for the flight phases

6 Conceptual Design Development

Decisions on the initial vehicle configurations had to be made before preliminary design could be developed for further analysis. For that purpose, at first, a design options tree (DOT) was developed based on an extensive literature study. Secondly, after the unfeasible branches of the DOT were removed as a result of in-depth requirement analysis, concepts were generated to enter the trade-off. Finally, trade-off of the concepts was performed and a conceptual design was selected which proceeded to the preliminary design phase. This chapter discusses this process in more detail, starting with the DOT.

6.1 Design Options Tree

Based on the literature study and analysis of past missions, a DOT was generated to select a preliminary vehicle concept. The main objective of developing the DOT was to select a preliminary shape of the vehicle, since the rest of the vehicle aspects could be traded off on a lower, subsystem level. The categories examined within the DOT were as follows:

- Launch
- Propulsion
- Materials
- Shape
- Control
- Flight path
- Recovery

It was discovered that several of the categories, such as recovery, launch, control or materials were not significantly dependent on the concept shape, and thus it was decided to trade off these categories on a subsystem level. In addition, it was found that that due to the mass constraints, including propulsion was not possible. Moreover, due to the requirements of landing within 100 km and due to the fact that propulsion was not possible, the skipping flight path had to be selected. The remaining category that was considered for the concept design was thus the shape of the vehicle and was expanded as follows:

- Number of control surfaces (only flaps only versus ailerons and rudders)
- Winged, non-winged versus lifting body design
- Curved edges and surfaces versus or round edges and surfaces

The final four concepts that entered the trade-off are shown on Figure 6.1.

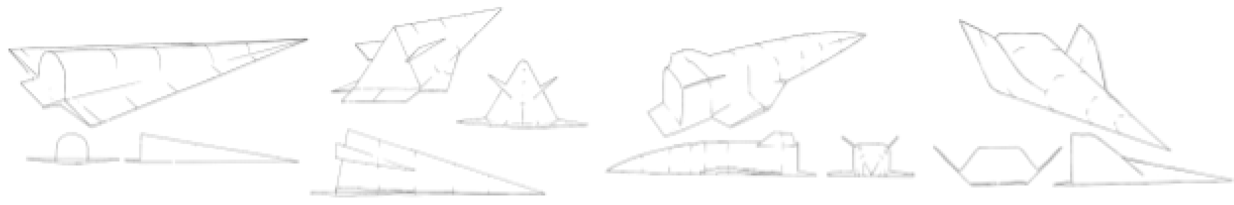

Figure 6.1: Four initial concepts

The subsystem level trade-offs, such as the recovery system, launch system, material design and others are briefly discussed in the sections of the respective subsystems later in the report.

6.2 Top Level Trade-Off Summary

After the design options were analyzed, trade-off was performed. During the trade-off, first the criteria were identified and weights were assigned to each criterion. The weights were given on a scale from 1 to 5, with 5 being the highest weight and 1 the lowest. The weight 1 stands for minimal relevance, 2 for marginal relevance, 3 for significant relevance, 4 for critical relevance and 5 for essential relevance. To each criterion, a grade was given. These grades were 1 for Sufficient, 2 for Good and 3 for Excellent. An Insufficient grade received -10 points to account for the partial unfeasibility. The option that had the most points, given by the product of the weight and the grade, was considered the most suitable option.

For the concept trade-off, the criteria evaluated were the structural feasibility, maximum L/D, possible area of experimental platforms, accessibility and the volumetric efficiency. The total structural feasibily grade consisted of the criteria based on heating, manufacturability and expected structural mass.

Table 6.1: Trade summary table

Criteria	Weights	Concept 1	Concept 2	Concept 3	Concept 4	Concept 5
Structures Total	5	27 [G]	26 [S]	19 [I]	25 [I]	40 [E]
Max L/D	5	5.44 at 3.8 [deg] [E]	2.61 at 14.3 [deg] [I]	2.25 at 16.6 [deg] [I]	1.98 at 16.6 [deg] [I]	4.23 at 5.7 [deg] [S]
Experiments Platform	5	Double Curved Top [I]	Pyramid like Top [G]	Flat Top but Curvature towards the front [G]	Flat Top [E]	Flat Top [E]
Accessibility Constraints	3	Small Back [S]	Wide access at back [G]	Square hatches possible in the back [G]	Wide access at back [G]	Wide access at back [G]
Volumetric Efficiency	2	0.086 [S]	0.109 [S]	0.119 [G]	0.105 [S]	0.087 [S]
Total Points		21	13	0	3	43

Based on the trade-off of the original four concepts presented in Table 6.1, it was found out that neither of the concepts were feasible, since the only concept having a sufficient L/D to satisfy the requirement of landing within 100 km, concept 1, could not provide platform for experiments, thus violating another critical requirement. Therefore, concepts 1 and 4 were merged to combine a good L/D while having flat surfaces for experiments, and resulted in the final concept 5, which was selected for the mission.

The concept selected for the preliminary design is shown on Figure 6.2. It can be seen that there is sufficient amount of flat surfaces to provide platform for experiments while there is also a sufficient projected area with sharp edges for the maximum L/D of 4.23 at Mach 10. Leading edges and nose are sharp to also satisfy the user requirement regarding the heat flux and the wing sweep is large to prevent the wings from excessive heating. Wing dihedral is added to improve stability, and the curved upper surface provides sufficient volumetric performance.

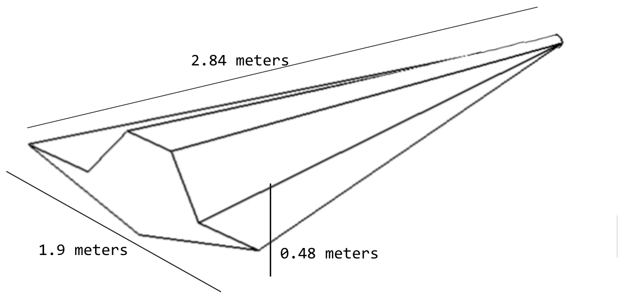

Figure 6.2: Selected concept shape with associated dimensions

The basic parameters of all of the preliminary concepts are documented in Table 6.1. Based on the trade-off results, it is obvious that the new vehicle concept 5 presented above is the only feasible one without violating any user requirements. Once the final concept has been selected, the concept entered the preliminary design phase, which was the final stage of the project. The results of this phase are documented in the following chapters.

7 Final Design Presentation

This chapter summarizes the main results of the vehicle design to give an initial overview of the design. The detailed derivation can be found following in the respective chapters.

7.1 Mission Budgets

Table 7.1 summarizes the top level cost, link budget, and data storage mission budgets for Hyperion IV. The derivation and a detailed view of the budgets is found in Chapter 28 for cost, Chapter 19 for the link budget, and Chapter 20 for the data storage budget. The cost budget is split up into a case a, which represents the cost for a single flight mission, and case b, which summarizes the cost for a mission with 20 flights. The different development steps leading to case b are described throughout the text, especially in Chapter 8 elaborating on the experiments, Chapter 16 and 18 describing the feasibility of a metal nose tip, and Chapter 27 depicting the TRL development program..

Table 7.1: Final cost, link, and data storage budget

Cost budget [M€]	Link budget [dB]	Data storage budget [GB]
a. 156/ b. 266.2	15	224

Table 7.2 describes the final mass and power budget, split up into subsystem contributions, derived in more detail at the end of each subsystem related chapter. The EPS providing the power needed and provided is described in 21. As pictured in the table the biggest mass contributions are structures, thermal protection, and avionics. The total wet mass is 321.7 kg, staying within the defined budget by SYS.C.5. The largest power consumers are Avionics, flap attitude control, and thermal protection. The total power needed is 946.4 W. Volume budget is presented where relevant.

Table 7.2: Final mass and power budget

Subsystem	Mass [kg]	Power [W]
Structures	51.5	0
Thermal Protection	93.1	100
Thruster Attitude Control	21.3	72
Flap Attitude Control	25.5	200
Power System	14.3	0
Telemetry	0.4	60
Avionics	28.1	299.1
Instrumentation	21	69.7
Ballasts	8.2	0
Recovery	34.5	75.5
Dry Mass/Net Power	286	876.3
Wet Mass/Net Power	297.9	876.3
Harness	23.8	70.1
Total Dry Mass/Total Power	309.8	946.4
Total wet mass/Total Power	321.7	946.4

7.2 Performance Overview

Though a detailed coverage of the individual models' output is already outlined in the respective sections along with a sensitivity analysis, this section aims to summarize the key performance parameters in a single place. Table 7.3 summarizes the cornerstones of the calculated trajectory and aerodynamic performance of the vehicle. A description of the models can be found in Chapters 9 and 10. The parameters are the main input for the detailed design of the vehicle.

Hyperion IV is to be launched with the Vega launch system from Guiana Space Center. The mission profile consists of four main guidance phases after launch: skipping, heat flux tracking, g-load in the gsptracking and the experimental phase. The vehicle will then reach the recovery interface at an altitude of 10 km with a velocity of 180 m/s. The mission profile is displayed in Figure 7.1.

Table 7.3: Performance Overview

Separation altitude [km]	Apogee [km]	Initial velocity [km/s]	Flight time [min]
120	250	7.32	100
Experimental time [sec]	Maximum load [g]	Maximum heat flux [MW/m^2]	Recovery altitude [km]
18.45	6	4.01	10
Integrated heat flux [MJ/m^2]	C_{L_α} [1/rad]	C_{m_α} [1/rad]	C_{n_β} [1/rad]
5,909.73	3.17	0.37	-0.107

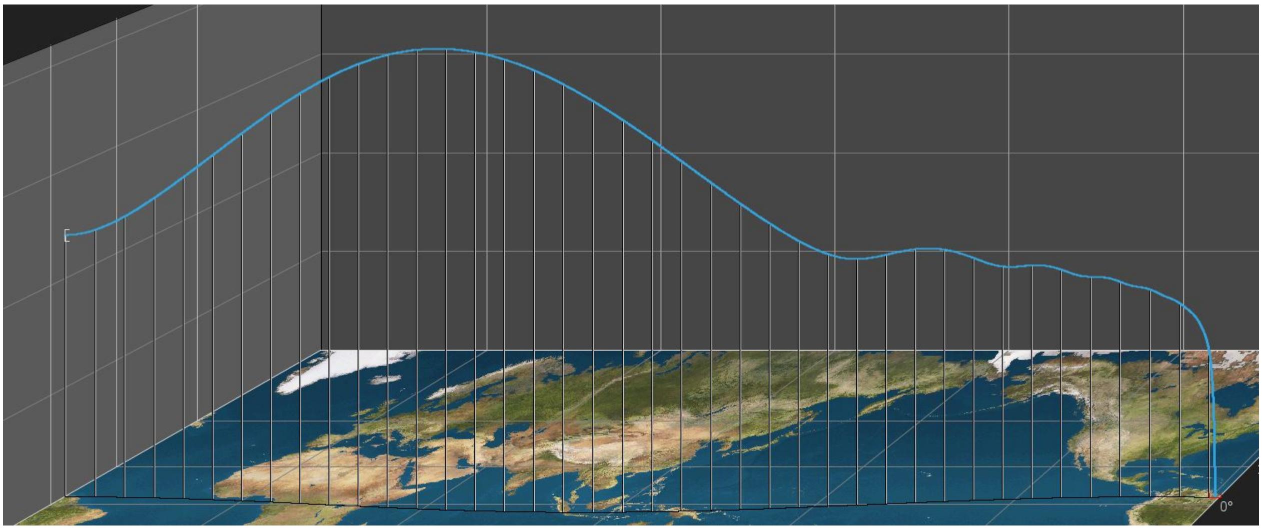

Figure 7.1: Mission profile of Hyperion IV produced with ASTOS 9.2.0

7.3 Configuration Layout

The inside view of the vehicle, the configuration layout including the structure can be seen in figure 7.2. Due to clarity, the figure only shows the biggest and most important items, neglecting amongst others the experimental instrumentation and harness. All heavy and voluminous items are placed on the line of symmetry, to limit the use of control systems to counteract an offset of centre of gravity. Computer and electronic devices are placed further to the back, making use of the extended volume and reduced temperature. The computer system is encompassed by a pressurized box. The parachute system at the back and the cooling tanks at the front are placed to facilitate their use. The GPS receiver is attached at the top to be able to receive the signal. Contrary, the antenna is placed at the bottom over the radio transparent tile. The back plate features modular tiles to assess the interior and conduct repairs. A pressure venting systems accounts for the large pressure differences during the flight. The approximated usable volume is 0.3 m^3, which generously hosts the configuration layout.

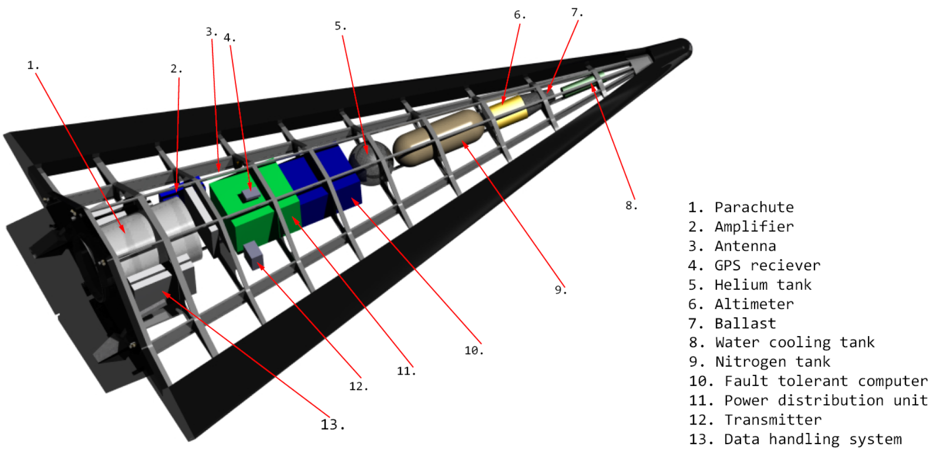

Figure 7.2: Configuration layout

8 Experiments

8.1 Requirements on Experiments

The requirements on experiments, or any relevant requirements described in Chapter 3 are the following:

- **SYS.F.9 Material experiments shall be included in the mission design.**
- **SYS.F.10 Aerodynamic experiments shall be included in the mission design.**
- **SYS.CR.8 The vehicle shall provide a platform for experimental testing**.

These requirements were kept in mind when designing the on-board experiments which will be presented in this chapter.

8.2 Summary of Trade-Off

A substantial part of the vehicle design trade-off was the capability to house modular experiments in a straight plate on top of the vehicle. The winning design features 3 straight top plates being able to house the desired experiments. There has not been a trade-off regarding different experiments.

8.3 Aerodynamic Experiments

In this section the boundary layer transition and shock wave boundary layer interaction experiments are described.

8.3.1 Boundary Layer Transition

Boundary layer transition is in general a highly complicated topic, even more in the hypersonic regime. First theoretical explanations were done by Lord Rayleigh (1887). Prandtl (1921) confirmed and expanded the findings of a boundary layer instability theory. The theory was summarized by Schlichting (1979). The line of thought is, that the velocity and pressure components of the Navier-Stokes equations consist of a mean and disturbance component. The mean velocity components are influenced by disturbances in the form of a wave, which propagates through the boundary layer. The stability of the laminar boundary layer can then be described as an eigenvalue problem. More elaborate analysis was done by Reshotko (1976) and Mack (2010). The degree and sign of wave amplification on the instability waves differs for each flow parameter. A thorough overview of the topic was provided by Stetson (1990). A general statement is often hard to make, as the effect on the layer stability depends on the combination of flow characteristics and the range of the parameter. That the topic is theoretically still not fully understood is confirmed by the writings of Anderson (2006) and Arnal and Délery (2004). Usually, a very simplified empirical relationship for the transition Reynolds number is used as shown by Bowcutt et al. (1987), given by Equation 9.17. To sum up, a lot of research is still to be done. Therefore, experimental data gathered during the mission is of tremendous value, both profit and scientific research wise.

The experiment is placed on the top plate of the vehicle. Temperature sensors and pressure sensors capturing the mentioned effects, as well as the effect of the Reynolds number sweep which is suggested by Mulaert et al. (2009). To gather data for a clean comparison, temperature and pressure sensors are additionally placed on the inclined plates of the upper surface. To ensure, that the boundary layer transition certainly takes place during the experimental phase, the tripping height, k, needs to be sufficient. The required k is calculated with the van Driest Blumer criterion explained by Arnal and Délery (2004), shown in Eq. (8.1) which is mainly applicable for spherical roughness heights, also used by the EXPERT vehicle experiment setup (Mulaert et al., 2009).

$$Rk_{eff} = 33.4[1 + \frac{\gamma - 1}{2} {M_e}^2] {R_{x_k}}^{0.25} \tag{8.1}$$

The equation is simplified by assuming an adiabatic wall temperature to account for the limited available data. As this represents the worst case for an intentional boundary layer transition, k is going to be over designed. The roughness location x_k is taken as 0.9 m, trading-off temperature at the tripping height and sufficient length to capture as much of the boundary layer as possible, as pointed out by Scott et al. (2000). γ is assumed to stay constant at 1.4. The free-stream Reynolds number R varies from 500,000 to 2,500,000, as required for the Reynolds sweep. The boundary layer edge Mach number M_e at the top surface is calculated using the required free-stream Mach number of 10 and the Prandtl-Mayer Expansion equation over a varying angle of attack from 6 to 10 degree, as depicted by Anderson (2017). As Anderson (2006) shows, as the Mach number increases the transition Reynolds number increases as well. Therefore, the highest Mach number calculated for the experimental phase with 11.95 is used, to account for the worst case scenario. Solving for the required effective roughness height k_{eff} a maximum value of 5.11 cm is proposed. The maximum height seems reasonable if compared to the tripping height of the X-43 wind tunnel experiments summarized by Scott et al. (2000). To measure three dimensional effects, the spherical roughness elements of 5.11 cm height are distributed over the entire width of the top plate.

It is suggested to use off the shelf thermocouples to measure the temperature and characterize the transition. The thermocouples are connected to the inside of the outer shell to measure the temperature. The measured temperature has to be corrected by the heat flux of the outer shell material. A high temperature N type platinum thermocouple as the one offered by Omega would be ideal. It can measure a temperature range of -270 to 1300 C and has a connection rating up to 1650 C. It features good accuracy at high temperatures with a tolerance range of 1.1 C. The cost is €920 per thermocouple[1].

A high accuracy pressure transducer especially manufactured for the aerospace sector with a cost of €650 is proposed[2] As the temperatures directly at the surface are too high, an extension tube has to be used, approximately 10 cm long. It has to be mentioned, that the boundary layer properties can only be deduced from the pressure and temperature measurements. If one wants more elaborate data on the boundary layer, pressure and temperature rakes should be used. As they are exposed to the high temperatures directly, they need to be designed and manufactured for the mission needs[3]. The detailed design of those devices is beyond the scope of this report.

Based on visual inspection of the sketched boundary layer phases shown by Anderson (2017) a thermocouple and pressure transducer placed every 10 cm, 3 apart, starting behind the roughness height is a reasonable trade-off between cost and data density. The sample rate is going to be 20 Hz. The sensors are delivering data during the whole flight time.

8.3.2 Shock Wave Boundary Layer Interaction

Shock wave boundary interaction in the hypersonic flight regime is of high importance for the aerodynamic performance of the vehicle. In general, one can distinguish between two types of effects, performance alteration due to adverse pressure gradient, and shock wave impingement onto the boundary layer.

The hypersonic boundary layer is substantially thicker than in other flight regimes, adhering to Equation 8.2, as described by Anderson (2017). The thicker boundary layer displaces the inviscid streamlines outside, therefore creating a bow like shock wave. The shock wave on the contrary imposes an adverse pressure gradient onto the boundary layer, and thereby, squeezing it. By that, the velocity gradient increases noticeable, causing higher friction coefficients as explained by Anderson (2017). The described effect varies along the boundary layer and can be split into strong and weak shock wave boundary layer interaction. The strong interaction is present upstream beginning right behind the shock wave. In the strong interaction region the pressure rise and disturbance of the inviscid flow is severe. Further downstream the effects weaken and the boundary layer growth is small. Therefore, interaction effects are negligible.

$$\frac{\delta}{x} = \frac{{M_e}^2}{\sqrt{Re_x}} \tag{8.2}$$

A shock wave impingement onto the boundary layer will trigger local separation of the boundary layer due to the adverse pressure gradient as described by Anderson (2017) and Schlichting (1979). The separation itself triggers multiple expansion shock waves, as well as a shock wave accompanying the reattachment. The triggered shock waves and local adverse pressure gradients can cause severe local hot spots, imposing challenges for the TPS design.

Numerical simulations as conducted by Reinatz and Ballmann (2016) can predict a few of the described effects. Nevertheless, because of the large number of different interactions, it is hard to catch all effects, and therefore, experiments have to be conducted as shown by Pasha and Sinha (2012). Therefore, conducting the shock wave boundary layer interaction experiment is of high importance to generate reliable scientific data concerning this topic.

To catch the pressure and friction effects of the strong and weak shock wave boundary layer interaction, pressure and temperature sensors are placed behind the nose cone distributed along the bottom of the vehicle. The same sensors as used for the active cooling system experiment can be used. On the top of the vehicle the same type of sensors are proposed to be placed from the beginning of the nose cone till the roughness

[1] `https://www.omega.nl/pptst/RAT-QD.html#description`, last access on 08/06/2018
[2] `https://www.omega.com/pptst/PX409_SERIES.html`, last access on 11/06/2018
[3] Discussion with supervisors on 11/06/2018

height elements. Those measurements can provide additional insight, as here an expansion wave boundary layer interaction can be observed during most of the flight time. Following the same reasoning as above, 7 sensors placed 10 cm apart are placed.

Based on the experiment proposed for the EXPERT vehicle, the needed body flap is exploited to trigger shock waves at the end of the bottom surface of the vehicle. Pressure and temperature measurements are taken to characterize the local flow. Figure 8.1 shows the expected pressure change around the inclined body flap. Following the colour change from light blue to green, green to light blue again, and finally a change to red, one can identify the described changes over the initial shock wave, expansion waves, and reattachment waves, in this order. Figure 8.2 clearly shows the boundary layer separation and the risk of hot spots at the reattachment shock wave. It follows, that the body flaps also need to be equipped with TPS tiles both, at the upper and lower side. Based on experiments conducted for the EXPERT vehicle, which planned to conduct the same experiment, the maximum expected temperature due to the reattachment of the flow is 1300 C as shown by Rösgen et al. (2012). The estimations are based on a compressible solution of viscous Navier-Stokes using CFD in Ansys. Based on those estimations, a thermocouple and pressure transducer every 5 cm is sufficient to capture all effects, starting 0.3 m before the body flap, and placing 3 next to each other to capture 3D effects. The sample rate is proposed to be 20 Hz for all sensors used to gather data every Reynolds number step of 5500, which was deemed sufficient detail. The sensors are delivering data during the whole flight time.

The same thermocouple and pressure transducer as used for the boundary layer transition experiment can be used as proposed for the EXPERT vehicle shown by Mulaert et al. (2009). Additionally, an infrared camera measuring the temperature range of the rear body flap is proposed. The infrared camera will allow for a neat documentation of the reattachment heat fluxes around the body flap.

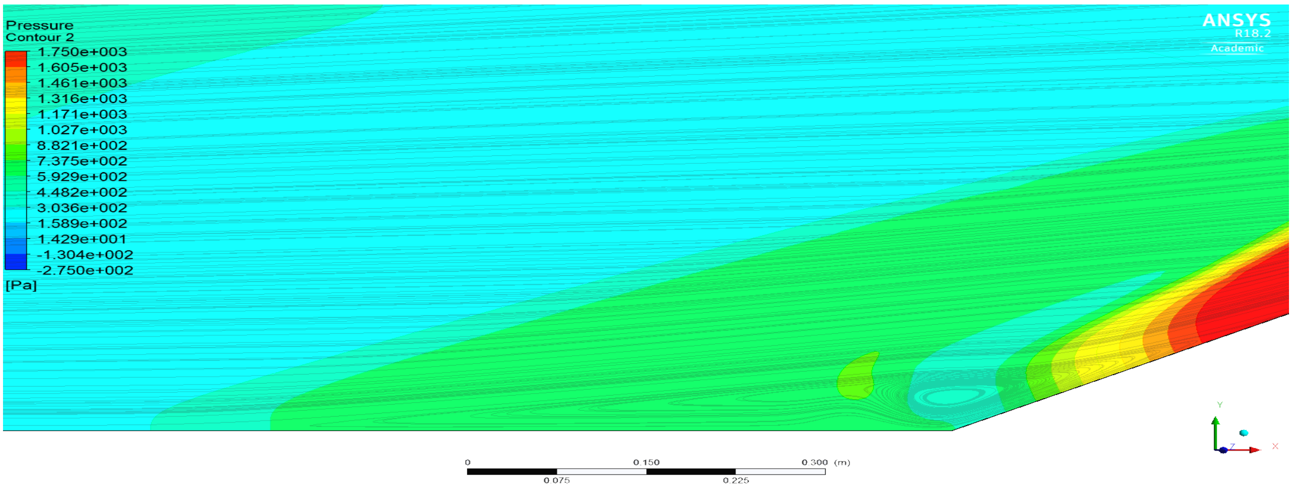

Figure 8.1: Boundary layer interaction pressure change

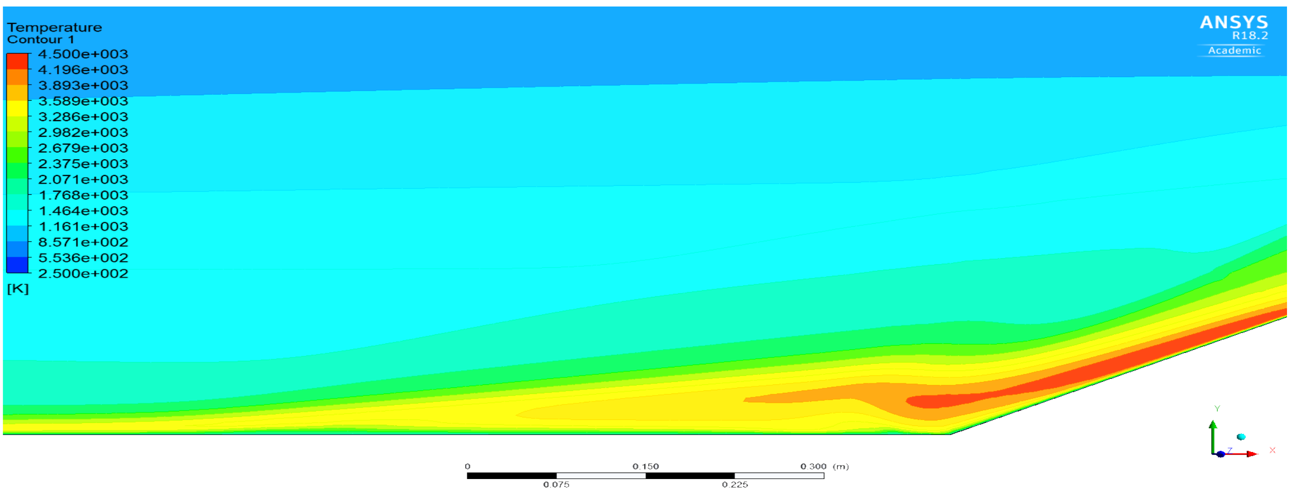

Figure 8.2: Boundary layer interaction temperature change

8.4 Material Experiments

A platform for customer material experiments is provided on the bottom or upper side of the vehicle, depending on the desired testing conditions. This platform should be of sufficient size to catch the necessary detail in the material behaviour during the testing. For example, if ablative material is used, it should be large enough to not completely ablate away during the flight for a post flight analysis. On the other hand, the material should not create an aerodynamic disturbance to the extent that the thermal protection system could be damaged as a result.

For example, if the material is too rough and too large, transition or complete detachment of the boundary layer may occur prematurely, leading to much higher heat transfer rates to the vehicle TPS behind the sample. It might also affect the flow such that aerodynamic experiments, if located behind it, are no longer possible or reliable.

For this reason, the material sample shall be positioned as aft as possible on the vehicle surface and its size should be limited to minimize the contamination of the boundary layer. Assuming that ceramic tiles will be tested, which are typically of the size of 15 x 15 x 7.5 cm as inspired by NASA (2010). As material testing is one of the primary objectives of the mission, at least this area should be provided on the platform.

To monitor the temperatures, the material are exposed to 5 thermocouples which should be used below or inside the material and also on the surfaces surrounding it. The same should be done with heat flux measurements and heat flux sensors.

According to Thiele et al. (2011a), heat flux sensors, thermocouples and pressure ports are used for material in-flight testing. The pressure ports will be included in the TPS and the rest of the vehicle skin, hence deeming only one pressure port dedicated for the experiment sufficient. In Thiele et al. (2011a), 5 thermocouples are used per panel, installed from the back side of the tile. Based on the expected temperatures, the thermocouples will likely either be Type S or K (Thiele et al., 2011b). In addition, one heat flux measurement sensor will be placed on the surface of the tile.

8.5 Active Cooling Experiments

An active cooling subsystem will have to be implemented as an integral and critical part of the vehicle design at the nose tip, as described in Chapter 16. Even though it is an integral part of the vehicle design, it will be regarded as an experiment, since it has never been flight tested before. Treating it as an experiment will allow the design to focus on proper monitoring of both the conditions the system is under and its functioning during service.

Additional active cooling experiments can also be placed on the vehicle, but should not be considered as a part of the vehicle design. This can be done by using a platform that is provided at the lower part of the vehicle or by placing the active cooling system on the leading edges to expose it to even higher heat fluxes and relieve the thermal stresses on the structures. Certain coolant injection rates can lead to a boundary layer transition, and if that is the case for a particular experiment, it shall use the platform at the aft of the vehicle (as was the case with the material experiments).

To measure the temperature drop and heat flux drop achieved by the cooling system, a set of S- or K-type thermocouples and heat flux measurement sensors will be placed at the source of the coolant injection and along the path of the coolant flow. To measure the lateral coolant flow dispersion, the tensors can be placed in a square matrix on the surface behind the injection of the coolant. If a square or a rectangular measurement matrix is used, 25 thermocouples can be used from the backside of the tiles. Since heat flux sensors are larger and require piercing through the tiles, only 5 will be used along the length of the coolant flow over the surface.

8.6 Guidance, Navigation & Control Experiments

For the guidance, navigation and control, different algorithms can be tested to validate the control theory in real flight. In this report, two algorithms namely the fuzzy logic control system and the dynamic inversion control will be introduced. The algorithms are proposed to run in parallel with the nominal guidance systems, to be able to switch back to the tested system if too large deviations occur.

Fuzzy Logic Control System for Flight Control Recently, the number and variety of applications of fuzzy logic control (FLC) have significantly increased, including the area of aerospace engineering. FLCs were developed for automatic flight control in aircraft and UAVs (Luo and Lan, 1995), satellite image processing, small satellite attitude determination (Pietra et al., 2005), and also for attitude control system for the atmospheric reentry spacecraft X-38. With the use of FLC, an enhanced safety and reliability of the vehicle, together with reduced cost of the ground station due to the automated configuration can be expected. Its ability to tackle problems in a simple and human-oriented way makes FLC a suitable candidate for innovative spacecraft control application, and therefore it is the interest of the mission experiment. FLC will be applied as an attitude controller, which will be constructed based on the attitude errors and their derivatives (Wu et al., 2000). This type of FLC was developed for X-38 vehicle and various simulation has been already conducted. Testing this control system in the real flight HYPERION IV mission will allow validation and promising future of this technology. Note that it will be necessary to have the nominal control system on-board together with the FLC to ensure a backup system in case of failure.

Nonlinear Dynamic Inversion Control Complex flight conditions, large airspace, strong coupling and nonlinear characteristics of a reentry vehicle is not adaptive to traditional linear control method which assumes small perturbation theory (Wen-Tao et al., 2005). Nonlinear Dynamic Inversion (NDI) control provides robustness and is able to reduce dependency on model information for nonlinear control systems.

Given a nonlinear open loop system, the NDI creates a closed loop system that behaves like a linear system. The two main advantages of this closed loop system rising from the NDI concept are: the unnecessity of controllers scheduling and also that the controllers are flexible (daCosta et al., 2003). NDI can also reduce the need of parameter tuning for different missions, contributing to increasing the flexibility of tracking different reference trajectories. This can be very beneficial for the HYPERION IV mission, where the user requirement stated that the vehicle should be 20 times reusable. With the use of NDI, variety of trajectories can be flexibly tested with ease every flight.

This field is also a great interest of Delft University of Technology. This system has already been tested in the TU Delft Cessna Citation II fly-by-wire aircraft. According to the university, the TRL of this control system has reached a level of 6 [4] and it can be expected to collaborate closely together with the research team if this option is chosen to be pursued.

8.7 Plasma Sheath Channel for Blackout Prevention

During reentry, the vehicle is covered in a layer of plasma due to its chemical reaction with the surrounding atmosphere at high Mach numbers. This plasma is opaque to the radio signal and hence causes blackout in the communication, which thus also means that no data can be transferred by the vehicle while travelling at high Mach numbers and measuring experiments.

Progress has been made on how to make this plasma transparent to the signal and prevent the communication blackout. It was found that there are several relatively transparent frequency windows in which the signal could propagate even at high Mach numbers. The results are discussed in Shi et al. (2012).

An on-board experiment can thus be made during which the frequency of the transmitting antenna will be altered, and the data will be attempted to be sent during the blackout phase. Based on Figures 8.3a and 8.3b, sufficient Bit Error Rate (ideally below 1e-3) can be achieved below Mach 12 using 40 GHz frequency, resulting in 40 dB signal.

If this experiment proves to be successful during the first flights, an antenna can be developed based on this research and the data can be also transmitted to the ground during the blackout. This will result in the possibility to generate more data on-board during the tests, as more data can be transmitted.

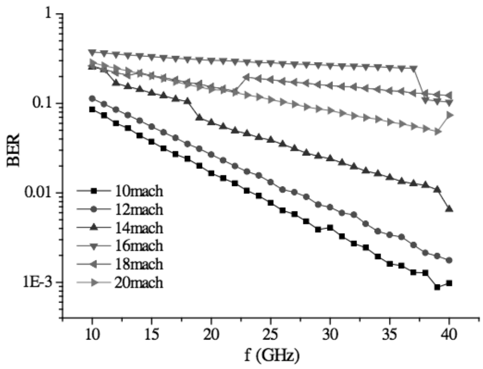

(a) The dependency of the Bit Error Rate on the signal frequency and Mach number, according to Shi et al. (2012)

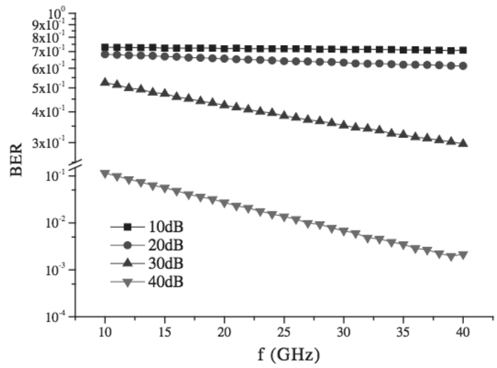

(b) The dependency of the Bit Error Rate on the signal frequency and Signal to Noise Ratio, according to Shi et al. (2012)

Figure 8.3: Bit Error Rate dependency

[4] https://www.tudelft.nl/technology-transfer/development-innovation/research-exhibition-projects/dynamic-inversion-control/ last access on 12/06/2018

8.8 Experiment of Metallic Nose Tip

As was mentioned before in Chapter 18 a metallic nose should be developed for a fully reusable craft. However if a one time use vehicle is chosen, ESA should still include a material test with the $W-Al_2O_3$ locate as far to the tip as possible. This is not to just test the metallic TPS, but rather to test the functionality and the effectiveness of the active anti-oxidation system (AAOS). The AAOS is based on the capacitive coupling already wildly used on earth today. The principal works as follow, oxidation is a redox reaction were the metal offer one of its electrons to the oxidizer, most commonly oxygen. so by giving the metal an excessive amount of electrons, the oxidizer can take these instead. This is achieved by turning the exposed metal into an capacitor. With a small potential of a couple of MeV, oxidation is significantly reduced. Now the Idea here is that at very low pressures the oxygen can penetrate the alumina and directly react with the tungsten. Now for a one time use this is a negligible amount, but over the course of many flights the oxide can accumulate. The experiment would work the following First a model is made predict the amount of oxidation that should happen due the low pressures, The material is flown and retrieved after which with ultrasounds the oxidation is checked. The difference between the model and the experiment will give an conclusion about the effectiveness and functionality. Alternatively two W-Al2O3 experiments could be mounted, one with the AAOS and the other without. The amount of potential that has to be created has still to be determined and should be done in future iteration, due to time constrains this could not be done in this report.

8.9 Summary of Instrumentation, Budget, and Recommendations

To conduct all the experiments described in this chapter, certain instrumentation such as sensors, ports and cameras are required. In this section, a summary of these instruments together with a detailed explanation of several important sensors will be provided. Additionally, the required link and storage budget is derived. Finally an outlook on further recommended experiments is given.

Table 8.1: Summary of Experimental Instruments

Type of Experiment	Instrument	Number of items	Parameters	Sample rate (Hz)	Duration (s)	Bits per data (bits)	Total bits (Mbits)
GNC	GPS	2	7	100	5980.8	64	535.88
	IMU	1	6	100	5980.8	64	114.83
Aerodynamics	Pressure port	54	1	20	5293	64	413.39
	Thermocouple	54	1	20	5980.8	64	413.39
	IR Camera	1	1	25	5980.8	880128	131596.74
TPS	Thermocouple	10	1	20	5980.8	64	76.55
Inner Structure Monitoring	Strain gauge	20	1	16	5980.8	64	122.49
	Thermocouple	20	1	16	5980.8	64	122.49
Materials	Thermocouple	15	1	16	5980.8	64	91.86
	Heat flux	1	1	200	5980.8	64	76.55
Active cooling	Pressure ports	11	1	100	5980.8	64	421.05
	Pressure ports	5	1	200	5980.8	64	191.39
Body Measurements	Heat flux	5	1	200	5980.8	64	382.77
	Thermocouple	25	1	16	5980.8	64	153.11
	Thermocouple	5	1	20	5980.8	64	38.28
	Pressure ports	5	1	20	5980.8	64	38.28
Total							134712.5

8.9.1 Instrumentation Budget

Table 8.1 shows the summary of required experimental instruments. The total required storage is 134712 Mbits. When including a 20 % margin, total required storage sums up to 20.2 GB. This is way lower than the 224 GB available shown in Chapter 20. However, the limiting factor for the gathered data is the transmission window described in Chapter 19. Therefore, if there is no need to transmit the data, to make sure they are received in case of failure, much more experimental data can be stored. The arrangement of all mentioned instruments are shown in figure 8.4 as described in the respective section, starting with the top view, bottom view, and back view. Blue points represent a combination of thermocouples and pressure transducer. The red wavy lines indicate the position of the roughness height. The yellow rectangle shows the position of the infrared camera at the back of the vehicle observing the temperature on the bodyflaps. The two red rectangles define the position of the material experiments and their respective sensors. Four RAFLEX sensors determining the attitude are marked by green stars. Finally, heat flux sensors are indicated as black diamonds, and single thermocouples as pink triangles. Instruments placed to measure interior parameters are not shown in the figure.

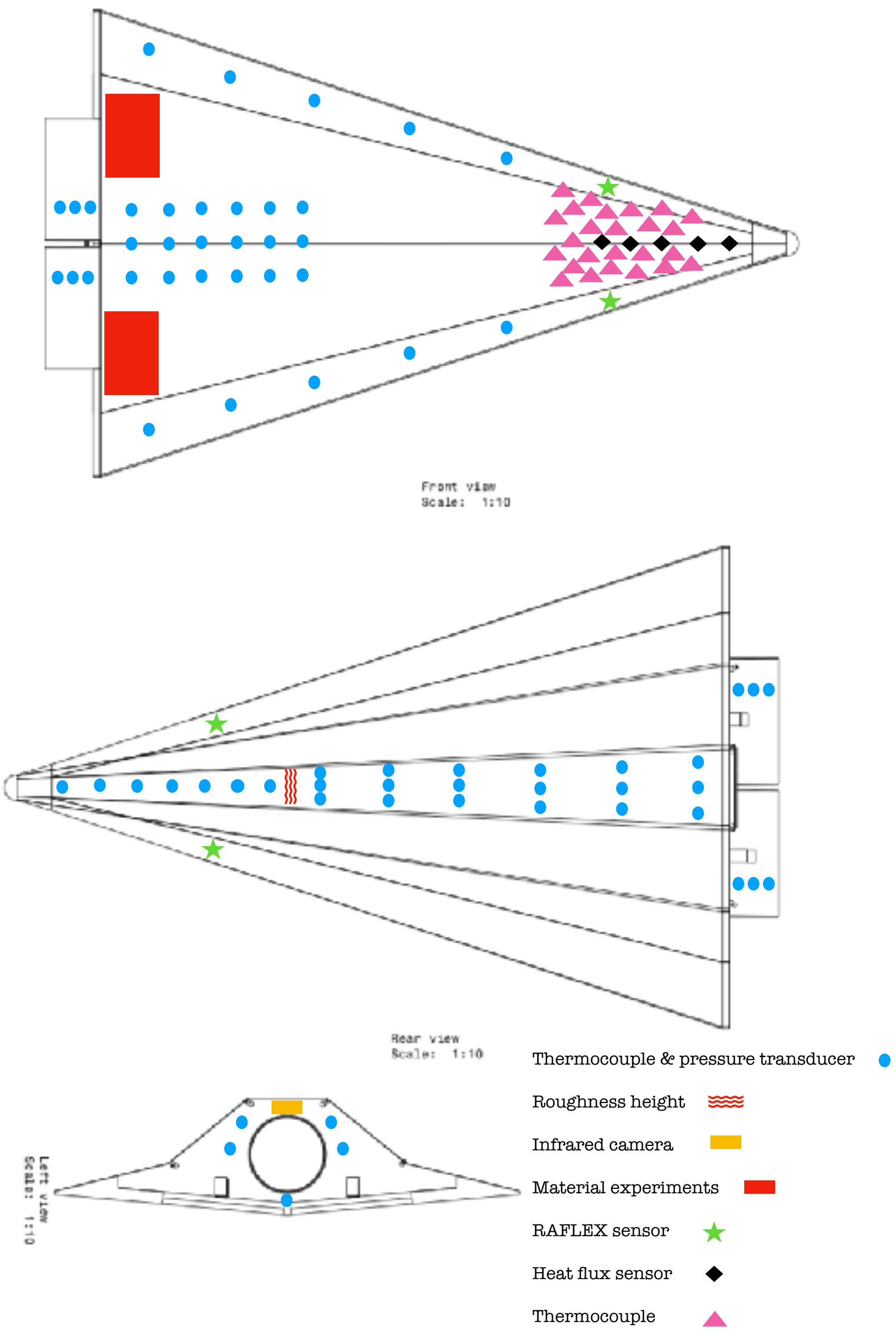

Figure 8.4: Arrangement of outboard experimental instruments

8.9.2 RAFLEX Sensors

The Reentry Aerodynamic Flow Experiment RAFLEX was first developed for the EXPRESS mission in the years 1993 to 1995, and was further developed for the MIRKA mission outputting successful results. This sensor was designed to measure the free stream flow condition for the whole reentry until the landing. To achieve this, the particle flux and the heat flux must be measured in the free molecular and the the transitional region. Furthermore, dynamic pressure, the surface pressure and the heat flux must be measured in the continuum flow. Therefore based on these mission heritage, four RAFLEX sensors shall be installed; one dynamic pressure probe in the geometric stagnation point and three identical combined flux probes in a 48 degree angle to the stagnation point. Note that this combination of probes also allows the analysis of the dynamic motion of the vehicle.

8.9.3 Infrared Camera

The infrared (IR) camera will be placed on the back surface so that the thermal evolution of the rear flap can be monitored throughout the flight. Furthermore it could optically track the flap positions. The IR camera was chosen based on its resistance to heat and its capability to detect the very high temperature on the control surface. The IR camera, "ThermoIMAGER" from MICRO-EPSILON is chosen as the best candidate for this mission. It weighs 320 g and it has a maximum field of view of 20 x 15 degrees at 382 x 288 pixels. Heat shielding jackets are also optionally available to increase its resistance to heat.

8.9.4 Recommendations

The described experiments cover the most important aspects of the hypersonic flight regime. Nevertheless, more further experiments during the the mission life could be conducted, including ablation experiments and gathering data about the chemical composition inside and outside the hypersonic shock as described for the EXPERT mission by Mulaert et al. (2009). Also, it has to be mentioned, that the active cooling system might contaminate the boundary layer, and therefore, trigger transition earlier. To understand possible contamination, more research has to be done.

9 Aerodynamic Model

Though the full, steady, compressible Navier Stokes and energy equations are certainly suitable candidates for evaluating the performance of the design iterations, their solution is computationally expensive. They are hence rarely used during the preliminary design stage. Among conceivable alternatives are the small-disturbance Euler equations (inviscid flow) and local inclination methods (Anderson, 2006). Though the inviscid formulation of the Navier Stokes equations requires a less fine grid to satisfy convergence than the viscous variant, the resources required to produce meaningful results are still significant, particularly due time consuming meshing activities. Hence, it is evident that the only viable option at this stage of design are local inclination methods, which make use of surface meshes instead of volume meshes. This significantly reduces the time required for mesh generation such that a more rapid iteration cycle time may be achieved.

9.1 Modified Newtonian Method

The modified Newtonian method is a local inclination formulation for the impact side of the vehicle. It assumes that all momentum of the flow component, which is parallel to a surface normal, is transferred to that surface. All deflected flow is assumed to have a velocity orthogonal to the surface normal (parallel to the surface). This means that an infinitesimally thin plate will generate zero lift and zero drag when the plate surface is aligned with the flow whereas when the plate normal is aligned with the flow, all momentum of the flow will be transferred to the plate.

On an inclined surface (see Figure 9.1), the impacting fluid particles change direction and thus transfer their normal momentum to the surface. The time rate of change in this momentum flux results in a pressure force on the inclined surface, given by Equation (9.1).

$$p_n = \rho V_n^2 = \rho(V_\infty \sin\theta)^2 \tag{9.1}$$

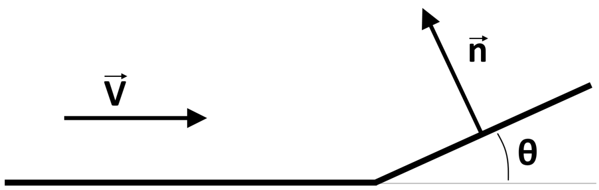

Figure 9.1: Normal vector and flow vector for an inclined surface

The flow deflection angle θ can be determined from a dot product between the velocity vector and the normal vector. This is demonstrated in Equation (9.2).

$$\theta = \frac{\pi}{2} + \frac{\mathbf{V} \bullet \mathbf{n}}{|\mathbf{V}||\mathbf{n}|} \tag{9.2}$$

However, in the actual code the angle itself is insignificant; instead the sine squared of the angle is obtained through the dot product in combination with the Pythagorean identity. This reduces the overhead of the calculation. The pressure coefficient on each individual surface can be evaluated with Equation (9.3).

$$C_p = C_{p_{max}} sin^2\theta = C_{p_{max}} \left[1 - \left(\frac{\mathbf{V} \bullet \mathbf{n}}{|\mathbf{V}||\mathbf{n}|}\right)^2\right] \tag{9.3}$$

A corrected maximum pressure coefficient seen in Equation (9.4) may be derived from the Rayleigh Pitot tube formula (Anderson, 2006), which takes into account the loss of total pressure across a normal shockwave. It expresses the maximum pressure coefficient as a function of the gas' ratio of specific heats γ and the freestream Mach number, M_∞.

$$C_{p_{max}} = \frac{2}{\gamma M_\infty^2} \left\{ \left[\frac{(\gamma+1)^2 M_\infty^2}{4\gamma M_\infty^2 - 2(\gamma-1)}\right]^{\frac{\gamma}{\gamma-1}} \left[\frac{1-\gamma+2\gamma M_\infty^2}{\gamma+1}\right] - 1 \right\} \quad [5] \tag{9.4}$$

9.1.1 Impact and Shadow Detection

Local inclination methods separate the surface mesh into two distinct types regions. The impact zone and a shadow zone. The shadow zone is the region which the velocity "rays" do not reach, typically at the aft side of the vehicle. All cells which are outside of the shadow region(s) are in an impact region. Whereas the pressure coefficient in most shadowed regions is unknown, the formula proposed by Jorgensen (1973) can be used to estimate the base pressure (back-side of the vehicle). Base pressure coefficients are set according to Equation (9.5); all other shadow region elements have their pressure coefficient set to zero. The pressure coefficient of each element in an impact zone is calculated using Equation (9.3).

$$C_{p_{base}} = \frac{2}{\gamma M_\infty^2}\left[\left(\frac{2}{\gamma+1}\right)^{1.4}\left(\frac{1}{M_\infty}\right)^{2.8}\left(\frac{2\gamma M_\infty^2-(\gamma-1)}{\gamma+1}\right)-1\right] \qquad [32] \tag{9.5}$$

The zones are currently classified according to the following algorithm: if the dot product between the velocity vector and the normal vector is less than 0, then the corresponding element is part of the impact region. If the normalized dot product between the velocity and normal vector is greater than 0.8, the element's pressure is set to the base pressure corresponding to the Mach number and gas properties, according to Equation (9.5). In all other cases, $C_p = 0$. Extensions to this basic functionality are proposed at the end of the chapter.

9.1.2 Surface Meshing

The surface mesh, necessary for running the modified Newtonian local inclination method, consists of triangular surface elements, stored in the form of a stereolithographic file (STL). Each element is represented as a combination of the vertex locations in Cartesian coordinates and the surface normal unit vector. Unfortunately CATIA V5 offers little control over both the size of the mesh elements and the direction of the normal vector. This means that to ensure that all vectors are pointing outwards, an intermediate processing step in Blender[1] is required to correct normal vectors which are inward pointing. Furthermore, even though the large number of mesh elements currently merely results in increased processing times, the anisotropy (high aspect ratio) of current elements is expected to cause problems if ray-tracing methods are to be employed for shadow zone detection, particularly in non-uniform freestream flow fields.

9.1.3 Calculation of Forces and Moments

Once the pressure coefficient on each element has been determined, the forces and moments may be integrated to yield their net contribution to the vehicle translational and rotational accelerations. Force integration does not make use of an advanced interpolation scheme to determine the distribution of pressure on an individual element. Instead, the pressure coefficient is multiplied by the mesh element area and the freestream dynamic pressure (Equations (9.6-9.8)). This may be justified by the fact that the surface inclination with respect to the local incoming flow is the only parameter which has an impact on the pressure coefficient. Hence, for the planar elements used in the present implementation, the integration method does not lead to any error.

$$dF_{x_i} = qS_iC_{p_i}\mathbf{i}_i \qquad F_x = \sum dF_{x_i} \tag{9.6}$$

$$dF_{y_i} = qS_iC_{p_i}\mathbf{j}_i \qquad F_x = \sum dF_{y_i} \tag{9.7}$$

$$dF_{z_i} = qS_iC_{p_i}\mathbf{k}_i \qquad F_x = \sum dF_{z_i} \tag{9.8}$$

Similarly the moments can be integrated by assuming all forces to be located at the geometrical centroid of the triangular mesh elements as shown in Equations (9.9-9.11) (again a valid assumption, as modified Newtonian theory is being used).

$$M_x = \mathbf{i}_i \sum (y_i - y_{ref})dF_{z_i} - (z_i - z_{ref})dF_{y_i} \tag{9.9}$$

$$M_y = \mathbf{j}_i \sum (z_i - z_{ref})dF_{x_i} - (x_i - x_{ref})dF_{z_i} \tag{9.10}$$

$$M_z = \mathbf{k}_i \sum (x_i - x_{ref})dF_{y_i} - (y_i - y_{ref})dF_{x_i} \tag{9.11}$$

[1] https://www.blender.org/

9.2 Model Verification and Validation

As to confirm that the modified Newtonian model is correctly implemented, and attains sufficient accuracy under hypersonic conditions, the model has to be verified. The chosen verification method is a comparison to the results produced by an established computational fluid dynamics (CFD) suite. A generic extruded (constant profile) geometry, designed to test all aspects of the modified Newton method, was investigated in both ANSYS Fluent and with the in-house modified Newton method. The setup of the computational fluid dynamics simulation will be discussed in the following sections. Finally, results from both methods are compared to draw a conclusion on the performance of the modified Newtonian model in the hypersonic flight regime.

9.2.1 Test Geometry

The generic test geometry is shown in Figure 9.2. The geometry was designed to trigger all important features of the modified Newtonian implementation: a surface on which the flow impacts at positive angles of attack, a surface which is shadowed under normal operating conditions, and a base pressure region.

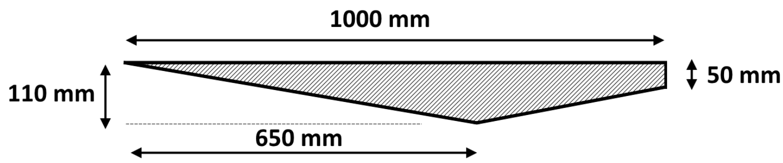

Figure 9.2: Geometry used for model acceptance testing

9.2.2 Mathematical Model

Modeling the flow as a continuum may be justified by considering the Knudsen number: at conditions representative of the flow conditions, $Kn = 3 \times 10^{-5}$. At Knudsen numbers above 0.01 the flow starts to behave similar to a molecular flow (and significant non-zero slip velocities may occur).

The pair of complete Navier-Stokes as well as the continuity and energy equations are simplified to their inviscid and steady form, yielding Equations (9.12-9.15), also commonly referred to as the Euler equations. The omission of the viscous term may be justified by the fact that it scales by the reciprocal of the Reynolds number, which is very high in the relevant flow case. No turbulence model is employed due to the more stringent requirements on the mesh element size. Finally, the equation system is completed with the equation of state for an ideal gas.

$$\frac{\partial(\rho u)}{\partial x} + \frac{\partial(\rho v)}{\partial y} = 0 \tag{9.12}$$

$$u\frac{\partial(\rho u)}{\partial x} + v\frac{\partial(\rho u)}{\partial y} = -\frac{\partial p}{\partial x} \tag{9.13}$$

$$u\frac{\partial(\rho u)}{\partial x} + v\frac{\partial(\rho u)}{\partial y} = -\frac{\partial p}{\partial x} \tag{9.14}$$

$$\frac{\partial \rho u E}{\partial x} + \frac{\partial \rho v E}{\partial y} = -p\left(\frac{\partial u}{\partial x} + \frac{\partial v}{\partial y}\right) + k\left(\frac{\partial^2 T}{\partial x^2} + \frac{\partial^2 T}{\partial x^y}\right) \tag{9.15}$$

$$p = \rho RT \qquad\qquad E = c_v T \tag{9.16}$$

In the above equations, ρ is the density, u the velocity in x direction, v the velocity in y direction, p the static thermodynamic pressure, E the specific internal energy, k the gas' thermal conductivity and T its temperature. The specific heat for constant volume is kept assumed constant; $c_v = 719.43$ J/kg K.

The equations are discretized using second order accurate schemes in combination with a pressure which is fully coupled to the velocity. This type of pressure-velocity coupling is "robust and efficient for single phase implementation for steady-state flows" ANSYS. (2017). All cases were solved using 24 processors on a machine with 64 GB of RAM, resulting in each case requiring about 10 minutes of CPU time.

9.2.3 Computational Domain, Mesh and Boundary Conditions

Figure 9.3 shows the computational domain, with the two boundary surfaces highlighted in red and blue (not to scale). The chosen method of boundary condition specification is to set the Mach number, gauge pressure, and static temperature at the inlet and outlet boundaries. Though arguably the problem is ill-posed from a momentum-conservation perspective, the shockwave and the large domain size contribute to a physically accurate solution in the vicinity of the test geometry. Depending on the desired angle of attack, the inlet/outlet velocity components can be adjusted. In all flow cases, the u velocity component is positive, with v accommodating the various angles of attack required for model verification.

The pressure farfield boundary condition is set to a Mach number of 10, a gauge pressure of 70 Pa and a static temperature of 250 K. The operating conditions are set to 0 Pa static pressure; the actual static pressure is enforced using gauge pressure specification.

The employed meshing strategy attempts to save computational resources by applying a coarse mesh in the regions which are distant from the shockwave features. In the region containing the largest gradients, mainly due to shockwaves (no boundary layers present), the mesh is refined to improve stability. Finally, an inflation layer is added near the wall. This is not to capture the (non-existant) viscous sublayer, but rather to better resolve the pressure and temperature gradients induced by shockwaves. The resulting mesh has approximately 425,000 cells.

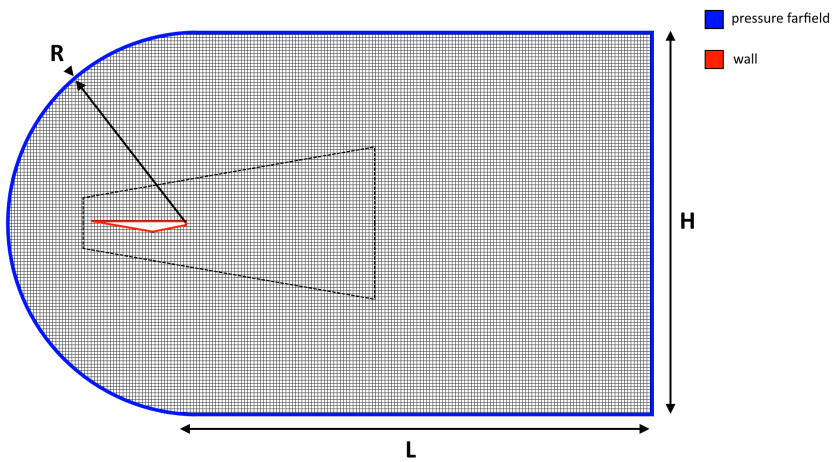

Figure 9.3: Computational domain for CFD (not to scale: $R = 7$ m, $L = 24$ m)

9.2.4 Mesh Independence Study and Residuals

All residuals of the x-momentum, y-momentum and energy equations of the final flowfield are below 10^{-7}. The continuity equation flattens out around 10^{-3}. This should not be mistaken for an un-converged solution: since the residual is normalized by the initial value, only marginal improvement will be witnessed if the initial (guessed) flowfield is similar to the final one.

Table 9.1: Mesh independence study: normal/tangential force N

α [rad]	-0.15	-0.10	-0.05	0.0	0.1	0.2
Original mesh	-342.18/10.38	-134.52/18.78	51.77/31.86	232.11/50.36	626.47/102.71	1134.59/172.65
Refined mesh	-342.98/10.64	-136.40/18.95	50.68/32.06	231.54/50.62	626.85/103.40	1136.38/173.65
Percent change	+0.24/+2.49	+1.40/+0.91	-2.10/+0.64	-0.24/+0.52	+0.06/+0.67	+0.16/+0.58

A mesh independence study was also conducted to verify that the solution is converged. Its results can be found in Table 9.1. In most cases, less than one percent variation in the forces, which were chosen as control variables, was witnessed. This is sufficient for the present application. All results presented hereafter correspond to the solution on the original mesh.

9.2.5 Results

Figure 9.4 shows that appreciable likeness between the modified Newtonian inclination method and CFD is achieved, particularly at low angles of attack. At larger angles of attack, both positive and negative, the

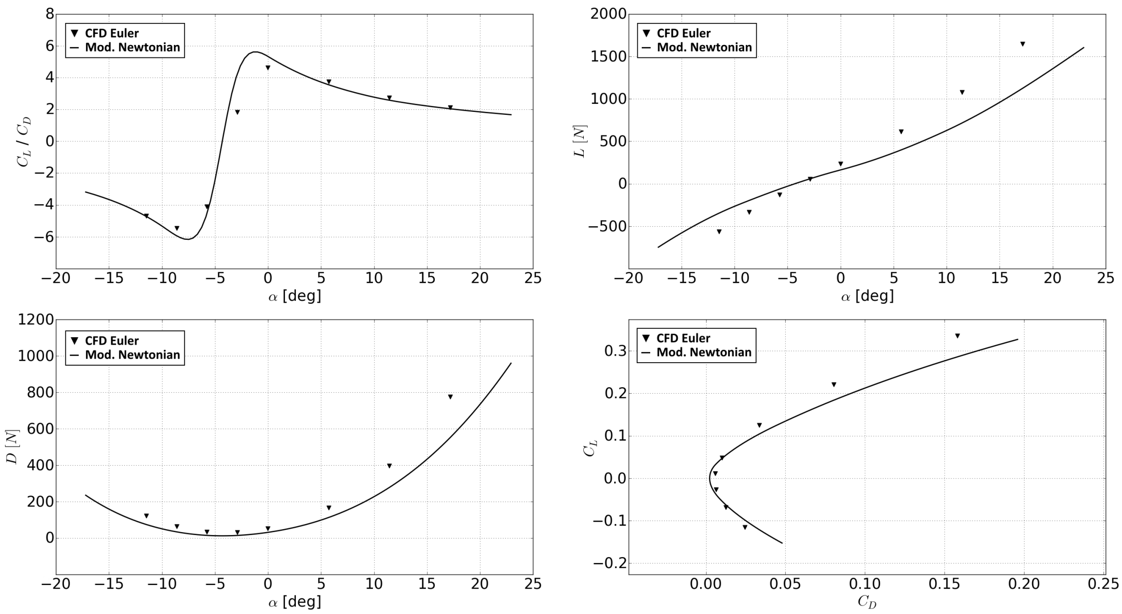

Figure 9.4: Comparison of modified Newton method (line) and CFD (triangles), $\beta = 0°$, $M = 10$

Euler equations predict both higher lift (in the absolute sense) and higher drag. The main reason for this discrepancy is the oversimplification of complex phenomena in the modified Newtonian method, which are particularly prominent at high angles of attack, where non-linearities become more important.

9.3 Skin Friction Model

As part of the final report, the inviscid model was enhanced with a skin friction coefficient model to obtain a more realistic estimate of the aerodynamic performance. An important aspect of the study of boundary layer flows is the transition from laminar to turbulent flow. The transition Reynolds number, Re_T, was estimated using Equation (9.17) (Bowcutt and Anderson, 1987). The transition location relative to the leading edge can then be used to determine whether a laminar or turbulent model should be used to determine the viscous drag. Though the methods presented in this section are primarily intended for the transition of flows over flat plates, the various planar elements of which the vehicle is comprised.

$$Re_T = 10^{6.421 \, exp(1.209 \cdot 10^{-5} M^{2.641})} \tag{9.17}$$

When Re is below the critical Reynolds number, the flow is laminar and may be approximated by Blasius' flat plate boundary layer solution (Equation (9.18). The equation predicts an infinite skin friction coefficient at the leading edge. When the Reynolds number based on the distance from the leading edge, Re_x, is in excess of the transition Reynolds number, Re_T, then the turbulent skin friction coefficient model (Equation (9.19)) proposed by Schlichting (1979) is employed. Moreover, the resulting friction of each of the models is corrected according to Eckert's reference temperature method presented in Anderson (2017). The edge temperature was set to freestream conditions whilst the wall temperature was taken from the aerothermodynamic model.

$$C_f = \frac{0.664}{\sqrt{Re_x}} \tag{9.18}$$

$$C_f = \frac{0.0576}{\sqrt[5]{Re_x}} \tag{9.19}$$

The frictional force is assumed to point to the same direction as a vector, which is the projection of the velocity vector onto the surfaces in question. Though this may not be representative of the true direction of local frictional force, it is consistent with the assumptions of the modified Newtonian method. The skin friction model could not be verified with computational fluid dynamics because these more sophisticated methods assume either a fully turbulent or a fully laminar flow, whereas the model above includes an empirical estimation of the transition location. Nevertheless, it was established that the response of the model is consistent with what is expected. For example, decreasing the Reynolds number was seen to be beneficial for increasing the glide ratio at first (as this results in fully laminar flow on the vehicle), but further reduction (in Re) resulted in a decrease in performance due to the gradual increase in the skin friction coefficient at lower Reynolds numbers. Moreover, when increasing the Reynolds number such that a large fraction of the vehicle is turbulent, an increase in Reynolds number (reduction in altitude) was seen to improve the performance due to the inverse-fifth-root relationship between Re and the (turbulent) skin friction coefficient.

9.4 Recommendations

A more sophisticated shadow detection method is expected to lead to improvement in the accuracy of the moment distribution. Especially when calculating the pressure distribution due to angular rates, the current shadow detection method is expected to result in significant errors. A ray tracing method, with particles initialized on the element's centroids could be implemented in a future version of the program. Moreover, to achieve greater accuracy, the reference x-coordinate for computing Re_x could be estimated on a spanwise basis. With such a modification, the cells towards the lateral extremities would be more likely to experience a laminar boundary layer than the surfaces in proximity to the vehicle's symmetry plane. However, this also means that the leading edges would experience high friction coefficients (due to the singularity at the leading edge). The model was implemented and tested but the automatic detection of the equation corresponding to the leading edge was problematic due to a finite nosetip radius. Future stages of design are likely to involve more sophisticated numerical prediction methods.

9.5 Auxiliary Aerodynamic Models

When the Hyperion IV completes its experiments and any other mission objectives, the next phase will be the recovery phase. As the goal of a re-entry is to bring the vehicle to a standstill in a controlled manner starting from hypersonic conditions, the Hyperion IV will evidently pass through supersonic, transonic and subsonic conditions during the re-entry phase. Therefore, this section will discuss how the Hyperion IV is modelled for supersonic velocities ranging between transonic ($M = 1.2$) to highly supersonic ($M = 5$).

9.5.1 Supersonic Model

For modelling the aerodynamic characteristics of the Hyperion IV at supersonic velocities, it was deemed too sophisticated to use proper models, such as in (Prasad and Srinivas, 2012) and Adamov et al. (2015), due to high computational cost. Taking into account that the main focus of the current project lies within the hypersonic flight regime, only rough supersonic data is sufficient for this project. Therefore, it was decided to have a look into mission heritage and carefully choose appropriate data from any past re-entry vehicle, which would have essential similarities in both mission profile and vehicle characteristics to the Hyperion IV vehicle. Data for the HORUS-2B7 Mooij (2017a) was used to construct the scaling factors, with the choice of this vehicle motivated primarily by the availability of data across a wide range of Mach numbers. For this vehicle, the reference velocity was chosen to be $M_{ref} = 10$. For the model, data was collected for a velocities between $1.2 < M < 5$ whilst considering the HORUS-2B7 based on lift coefficient C_L, drag coefficient C_D and the lift-over-drag ratio L/D. After finding the above aerodynamic values, the data was normalized to the reference value (associated with M_{ref}) to obtain the scaling factor between hypersonic and supersonic values. The range for the of angle of attack based on which aerodynamic data was collected ranges between $0° < \alpha < 45°$. Table 9.2 provides more information on how the HORUS-2B7 data was used.

Table 9.2: Data points of HORUS-2B7 for the supersonic model

	HORUS-2B7
Angle of Attack Range (°)	$0 < \alpha < 45$
Analyzed parameters	C_L, C_D, L/D
Analyzed Mach numbers	$M = 1.2, 1.5, 2, 3, 5$

To determine the scaling factor in the supersonic regime based on the Mach and α ranges provided in Table 9.2, linear interpolation was applied in which the Mach number and angle of attack were considered variables. Based on this procedure, a programming script was written in which a function was created. This function generates the scaling factor based on an input on both the Mach number and the angle of attack. The range of input possibilities on the Mach number and angle of attack are the same ranges stated in Table 9.2.

9.5.2 Subsonic Model

Before the vehicle is recovered, a brief part of the approach of the Hyperion IV will take place in the transonic and finally also in the subsonic realms. To model these two phases, the same approach was applied as already explained in Section 9.5. The only difference though is that for this model sub and transonic data is used, instead of supersonic data, to determine the scaling factors. The reference vehicle for this model was chosen to be the PHOENIX (Germany). Data was used for Mach numbers ranging in between $M = 0.2$ and

$M = 1.33$. The aerodynamic data for this vehicle is documented in Weiland (2014). Table 9.3 provides more information on the implementation of the PHOENIX for this model.

Table 9.3: Data points of PHOENIX (Germany) for the (mainly) subsonic model

	PHOENIX
Angle of Attack Range (°)	$0 < \alpha < 25$
Analyzed parameters	C_L, C_D, L/D
Analyzed Mach numbers	$M = 0.2, 0.5, 0.8, 1.1, 1.33$

9.5.3 Verification of Auxiliary Models

As was mentioned before, only rough data was used from mission heritage to determine scaling factors for both subsonic and supersonic flight regimes. However, as this method is potentially prone to large errors, the methodology applied for this part of the aerodynamic analysis should be carefully verified.

For verification, the scaling factors acquired were multiplied with the absolute Hyperion IV coefficients at $M_{ref} = 10$, as it was explained before. The values obtained in this way were then compared to the actual flight data belonging to the respective reference vehicle belonging to either the subsonic realm (PHOENIX) or the supersonic realm (HORUS 2B7).

For the supersonic regime, verification was done at a Mach number of $M = 3$. Here, the lift and drag coefficients obtained for the Hyperion IV were compared graphically with the HORUS 2B7 data, which is documented in Mooij (2017a). Doing so results in the graph shown in Figure 9.5. The highest error for C_L is encountered at $\alpha = 45°$, which estimated to be 18 %. For the C_D, the highest error occurs at $\alpha = 45°$ and is estimated to be 17 %. The maximum errors found for both coefficients is found to be reasonable.

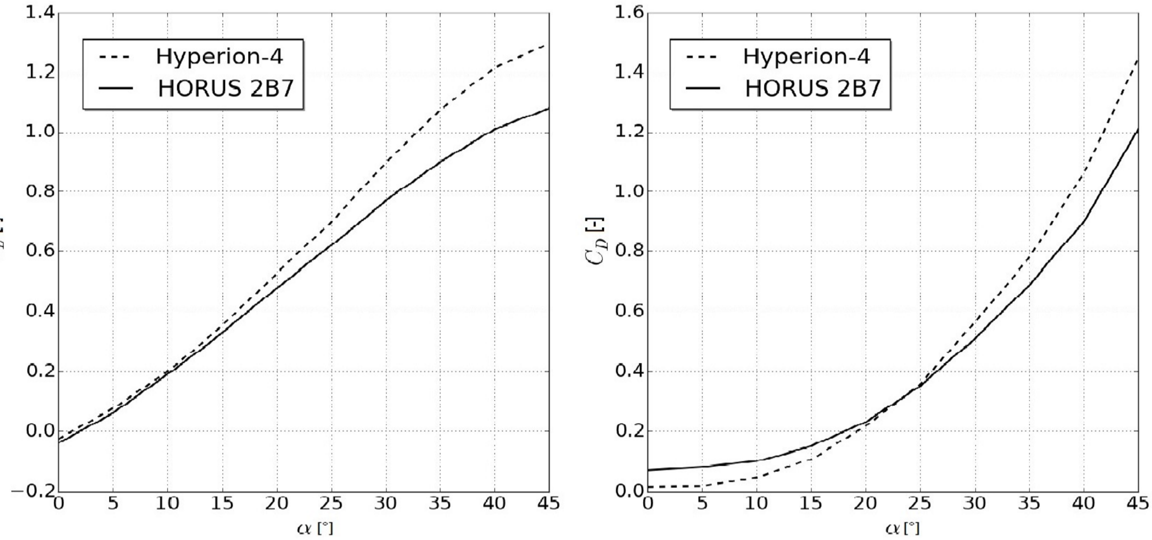

Figure 9.5: Verification of the supersonic model at $M = 3$

Similarly, the subsonic model can also be verified with the reference vehicle. The highest error both the C_L and C_D was found to be significant. One of the causes for the large errors, is that there are extensive differences in configuration between the PHOENIX and the Hyperion IV. Whereas the PHOENIX has a blunt nose and a vertical tail, the Hyperion IV has a sharp nose and no vertical control surfaces. Consequently, the Hyperion IV team recommends the development of a subsonic aerodynamic model, to be used for evaluation of the performance during the final moments of each flight.

9.6 Design Iteration & Sensitivity Analysis

This section offers a qualitative perspective on the sensitivity of the vehicle's aerodynamic performance with regard to variables such as the nosetip radius, leading edge radius and vehicle length, starting from the design selected in the midterm report. The conclusions were used to tune the aerodynamic characteristics as to meet top-level user requirements pertaining to the vehicle glide ratio and range.

It is key to initially define the inter-relation between the different design parameters. For example, with increasing leading edge sweep, the leading edge radius, which would otherwise be constrained by thermal considerations, can be reduced. Moreover, the vehicle's projected mass is heavily dependent on the volume of the vehicle, hence any increase in any dimension will likely result in an overall increase in vehicle mass. It is noted once again that the ideal geometry for hypersonic flight, from a purely aerodynamic point of view, is a flat plate, which is of course unfeasible from both a thermal and structural standpoint. In addition, with the introduction of the viscous model, the shape of the vehicle is no longer the single determining parameter, but the Reynolds number (proportional to the absolute length) becomes important as well.

Various nose radii were investigated to determine the degree of dominance of this design parameter. Moreover the effect of leading edge sweep as well as leading edge (not nose) radius was quantified. The sweep was found to have only a minor effect when switching between 60, 70, and 80 degrees. The conclusion drawn from this was that the nose radius in relation to the vehicle length (when keeping other dimensions such as height constant) was the most relevant to obtaining a higher glide ratio.

Table 9.4: Sensitivity of lift-to-drag ratio to nosetip radius

R_{nose} [mm]	L/D_{max} [N/A]	$\alpha_{L/D_{max}} [rad]$
25	3.04	0.158
50	2.71	0.174
75	2.37	0.221
100	2.08	0.253

Table 9.4 shows the variation in lift-to-drag ratio as a result of a change in nose radius. The benchmark was conducted at an altitude of 40 km at a Mach number of ten. The geometry corresponds to the selected concept at mid-term, with leading edges rounded to a radius of 15 mm.

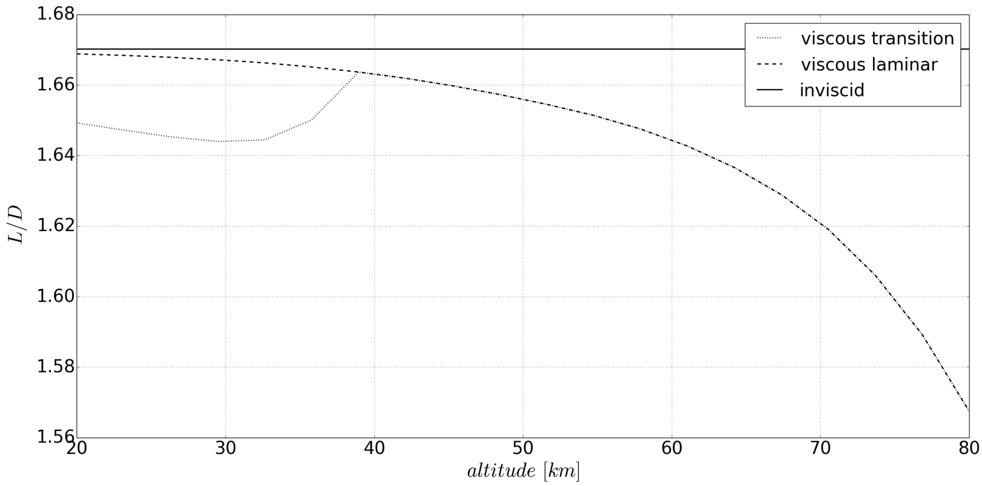

Figure 9.6: Sensitivity of glide ratio at $M = 10$, $\alpha = 0.5$ rad

Figure 9.6 displays the variation in predicted lift-to-drag ratio at an angle of attack of 0.5 rad at $M = 10$ using various of the aerodynamic model's settings. Unsurprisingly, under inviscid conditions, the lift to drag is independent of the Reynolds number. Moreover, the model including transition can be seen to coincide with the laminar model at higher altitudes, where the transition model predicts a laminar flow. As most of the uncertainty (aside from the modified Newtonian assumption) originates from the choice of viscous model, particularly at low angles of attack where viscous drag is important, the range of predicted values can be used as error bounds, due to the uncertainty of the transition behavior.

9.7 Aerodynamic Performance Analysis

The outcome of the iteration process, the vehicle's exterior shape, is shown in Figure 9.7. The nose radius was fixed at 40 mm whereas the leading edge radius, as a consequence of a sweep angle of 72 degrees, could be lowered to 7.5 mm without violating heat flux constraints. The vehicle length, from nosetip to back-frame (excluding elevons) is 2840 mm with a maximum height of 480 mm, at the rear of the vehicle. Modifications to the upper surface geometry were seen to have little to no impact on performance in consequence to this region being shadowed at nominal conditions (high angle of attack).

Figure 9.7: Vehicle exterior shape after design iteration

The vehicle's performance was investigated over a wide range of flight conditions. As previously discussed, the altitude can be used to set reference ambient temperature and density, which in combination with the Mach number yields the Reynolds number, the principal parameter for the viscous drag. Figure 9.8 shows the variation in the aerodynamic behavior of the vehicle at various altitudes. Both the drag polar and the lift-to-drag ratio plot indicate that performance is optimal around 40 km. This behavior is likely a result of the travel of the predicted transition location (Equation 9.17). At 40 km, the transition is predicted to occur 3.74 m aft of the leading edge, which corresponds to a location behind the vehicle. This means that the flow over the vehicle is entirely laminar. In contrast, the Reynolds number at an altitude of 30 km is far greater, resulting in a transition at only 77 cm behind the leading edge. The large fraction of the vehicle experiencing a turbulent boundary layer will hence experience a higher drag, in contrast to the situation where the flow over the vehicle is fully laminar. The decrease in performance at higher altitudes (lower Re) may be attributed to a different mechanism. For example, at 70 km, transition is projected to occur at 61 vehicle lengths aft of the leading edge, owing to the extremely low Reynolds number. In this instance, the inverse-root relationship of the laminar skin-friction coefficient results in a dramatic increase in the viscous drag, ultimately lowering the glide ratio. Finally, upon further inspection of the graph it may be noted that performance at high angles of attack is relatively similar due to the dominance of pressure drag.

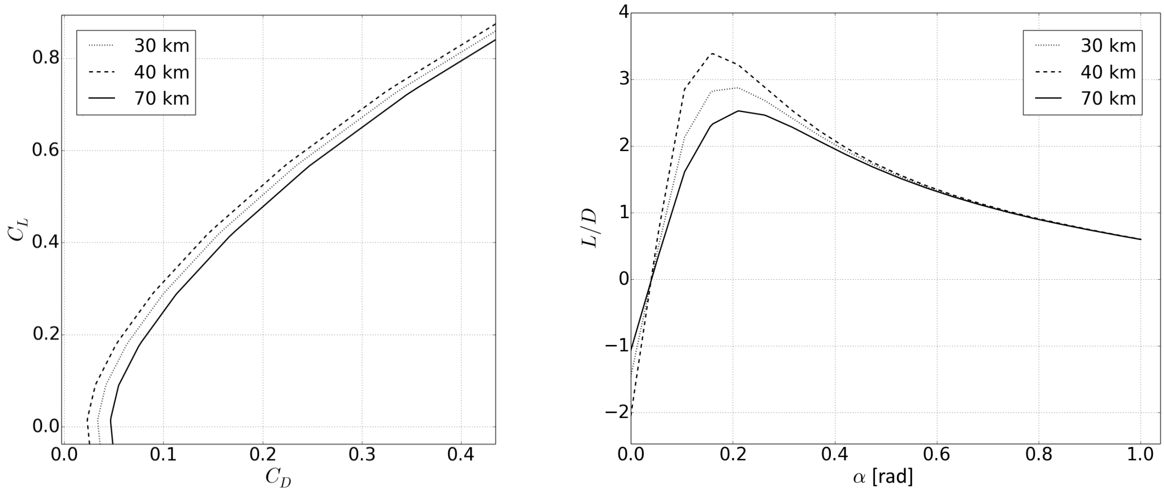

Figure 9.8: Drag polar and corresponding glide ratio for 30, 40, and 70 km altitude at $M = 10$

9.8 Interfacing with Other Departments

The trajectory model, covered in the next section, requires aerodynamic forces and moments to be available for a large range of angles of attack at various Mach numbers and altitudes. Aerodynamic data from the hypersonic model was generated at approximately 4,000 discrete points in the three dimensional domain. The code was parallelized to allow for simultaneous calculation of several data points. The output data can be conveniently imported and subsequently tri-linearly interpolated at any condition in between 20 and 80 km, at Mach numbers bounded by 5 and 35, and angles of attack ranging from 0 to 1.0 rad. No data was generated for negative angles of attack due to the failure of the thermal protection system when the upper surface is exposed to the impacting flow.

10 Guidance Design

This chapter contains the description of the model in use to compute the flight trajectory. First of all, the requirements on the trajectory will be shown. After, the three-dimensional equations of motion in the Earth-centred Earth-fixed reference frame (C-frame) are discussed. Then the reentry corridor will be presented, directly followed by the development of guidance software for the different flight phases. This contains a PID controller and multiple analytical solutions for the different phases in flight. Finally the results are shown, verification and validation is performed and finally sensitivity is discussed.

10.1 Requirements on Trajectory

The main trajectory constraints can be derived directly from the user requirements. The ones that were used as a starting point for the current system are reported hereby.

- **SYS.F.2** The vehicle shall follow a suborbital trajectory.
- **SYS.F.4** The landing site shall be within 100 km from the launch site.
- **SYS.F.6** The trajectory shall ensure a constant Mach > 10 and a variable Re of 5e5 < Re < 2e6.

From these, it was possible to derive more subsystem requirements. The downrange requirement spins off requirement **SYS.F.4**, and the value of 40,000 km is taken because it coincides with Earth's equatorial circumference. This range includes the possible range generated by launcher. Furthermore, requirements **GNC.REQ.05** and **GNC.REQ.06** are spin off requirements imposed by the execution of the experiments in flight and the recovery conditions, respectively.

- **GNC.REQ.01** The vehicle shall have a downrange of at least 40,000 km.
- **GNC.REQ.02** The trajectory shall not fly at a heat flux higher than 4 MW/m^2.
- **GNC.REQ.03** The trajectory shall minimize the integrated heat flux experienced by the vehicle.
- **GNC.REQ.04** The trajectory shall minimize the g-loads experienced by the vehicle during flight.
- **GNC.REQ.05** The vehicle shall reach an altitude of 12 km at subsonic conditions.
- **GNC.REQ.06** The vehicle shall reach a target Mach number of 10 at an altitude of 40 km.

10.2 Flight Mechanics Model

Given the requirements, it is then necessary to create a model to simulate the trajectory of the vehicle with. To simulate the reentry trajectory and analyze the behaviour of the vehicle during the descent, a simulator based on the non-linear equations of translational motion in the Earth-fixed, Earth-centred reference frame (the C-frame) was developed. These equations include summation of forces and kinematic relations to fully model the dynamic behaviour of the vehicle. The final equations of translational motion are summarized in Equations (10.1) to (10.3), as elaborated in Mooij (2017a).

$$\dot{V} = -\frac{D}{m} - g\sin\gamma + \Omega_t^2 R\cos\delta(\sin\gamma\cos\delta - \cos\gamma\sin\delta\cos\chi) \tag{10.1}$$

$$V\dot{\gamma} = \frac{L\cos\mu}{m} - g\cos\gamma + 2\Omega_t V\cos\delta\sin\chi + \frac{V^2}{r}\cos\gamma + \Omega_t^2 R\cos\delta(\cos\delta\cos\gamma + \sin\gamma\sin\delta\cos\chi \tag{10.2}$$

$$V\cos\gamma\dot{\chi} = \frac{L\sin\mu}{m} + 2\Omega_t V(\sin\delta\cos\gamma - \cos\delta\sin\gamma\cos\chi) + \frac{V^2}{r}\cos^2\gamma\tan\delta\sin\chi + \Omega_t^2 r\cos\delta\sin\delta\sin\chi \tag{10.3}$$

with γ the flight path angle, Ω_t the rotation of the Earth, δ the latitude, χ the heading, τ the longitude,V velocity and r the distance to the center of the earth. The corresponding kinematic relations are given by Equations (10.4 - 10.6).

$$\dot{r} = \dot{h} = V\sin\gamma \tag{10.4}$$

$$\dot{\tau} = \frac{V\sin\chi\cos\gamma}{r\cos\delta} \tag{10.5}$$

$$\dot{\delta} = \frac{V\cos\chi\cos\gamma}{r} \tag{10.6}$$

The equations of motion and the kinematic relation mentioned above represent a system of six non-linear time varying ordinary differential equations.The numerical scheme in use the Runge-Kutta 4 scheme, accurate to order 5. This applies to an initial value problem defined as:

$$\dot{y} = f(t, y) \tag{10.7}$$

$$y(t_0) = y_0 \tag{10.8}$$

The four constants required by this propagation method are listed in Equations (10.9 - 10.12) (being dt the time step in use for the propagation).

$$a = dt\, f(t_n, y_n) \tag{10.9}$$

$$b = dt\, f(t_n + \frac{dt}{2}, y_n + dt\, \frac{a}{2}) \tag{10.10}$$

$$c = dt\, f(t_n + \frac{dt}{2}, y_n + dt\, \frac{b}{2}) \tag{10.11}$$

$$d = dt\, f(t_n + dt, y_n + dt\, c) \tag{10.12}$$

Then, the update equation is given by the relation shown in Equation (10.13).

$$y_{n+1} = y_n + \frac{1}{6}\,(a + 2\,b + 2\,c + d) \tag{10.13}$$

$$t_{n+1} = t_n + dt \tag{10.14}$$

The simulation includes modules to simulate the atmospheric properties as a function of altitude and sea level conditions. Furthermore, the aerodynamics of the vehicle are integrated into the simulation and the program interpolates between the available data points of the database. Moreover, the tool integrates guidance equations (elaborated on in Section 10.4), the outputs of which are fed to the control module, consisting of a PID controller.

Extra modules in the program include the calculation of the heat flux. This is based on the computation of the stagnation point heat flux according to Scott's or Detra's three-dimensional model, as mentioned in Chapter 14. The termination criteria of the simulation is attained when the vehicle the necessary recovery conditions.

10.3 Reentry Corridor

Given the requirements on the maximum attainable g-load, the heat constraint and the equilibrium glide condition, it was possible to derive the range of possible combinations of altitudes and velocities that the vehicle can fly safely. The constraints were derived from analytical equations from Mooij (2017a) and reported in the foregoing chapters. All equations rely on the computation of the density or speed at which the constraint is located, from which the Figure 10.1 shows the altitude-velocity plot and the constraints imposed on the trajectory.

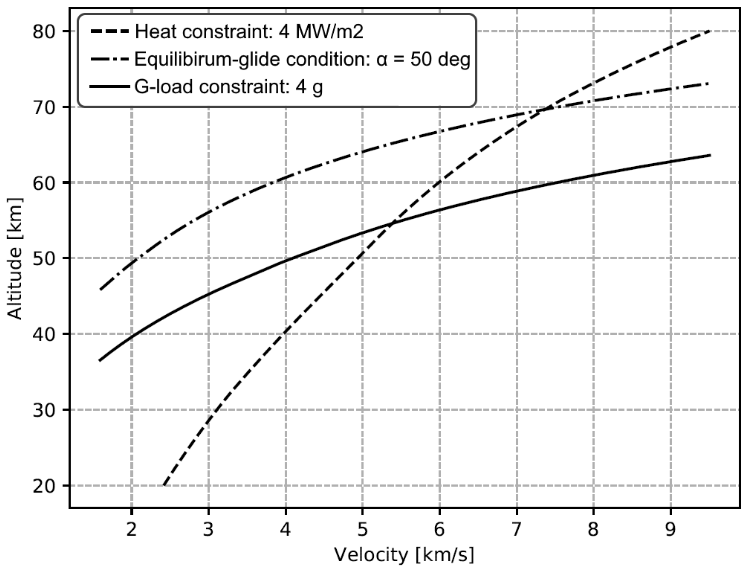

Figure 10.1: Altitude versus velocity plot showing the reentry corridor constraints

The heat constraint is derived using Detra's model and imposing a target constraint, set to 4 MW/m^2. The constraint density is computed with Equation 10.15. The constraint is shown with a dashed line in Figure 10.1.

$$V_q = \left(\frac{q_{target}}{\frac{11030}{\sqrt{R_n}}\left(\frac{\rho}{\rho_0}\right)^{0.5}\sqrt{2}\sqrt{\frac{1+K}{2}}}\right)^{\frac{1}{3.15}} V_c \tag{10.15}$$

Furthermore, the equilibrium glide condition was computed using Equation (10.16).

$$\rho_{eq} = 2\,\frac{W/S}{C_L}\left(\frac{1}{V_{eq}^2} - \frac{1}{V_c^2}\right) \tag{10.16}$$

Finally, the maximum load factor was set at a value of 4, and utilized in Equation (10.17) to compute the load constraint.

$$\rho_g = 2n_{g,max}\,\frac{mg_0}{V_g^2 S\sqrt{C_L^2 + C_D^2}} \tag{10.17}$$

10.4 Guidance

Now that the constraints are known, the actual trajectory can be evaluated. Several phases are identified, those are: skipping, heat flux, g-load constraint and experiment. In general, the strategy is to first skip such that the range requirement can be met, then follow the heat flux constraint for minimum integrated heat flux, which leads to minimum TPS mass. When approaching the g-load constraint, the vehicle switches to the g-load tracking mode as it should not violate this constraint. Finally, a Reynolds sweep at Mach 10 is performed. It is important to note that the upcoming computations are tools to show that a trajectory is feasible and they are not a finalized GNC software package. Limitations are evaluated, such that future development goals can be established.

10.4.1 Skipping

The first phase to consider is the skipping phase, meant to increase the range of the vehicle. The idea is to launch the vehicle in low-density atmospheric conditions with velocity lower than circular velocity and a negative or zero flight path angle. When descending and the density increases and consequent increase in lift makes the vehicle climb again and perform a skip.

This is particularly useful for Hyperion IV, as a trajectory around the world is challenging for a vehicle with limited L/D performance. Flying around the earth is necessary for requirement SYS.F.4 (landing 100 km from launch site) as a sub-orbital trajectory will not be able to make this requirement otherwise. Only a skipping trajectory can attain this range with this vehicle, so no other options (i.e. fully gliding flight or ballistic flight) were considered to be viable for the mission at hand.

Table 10.1: Vehicle entry conditions

Condition	Amount
V_e	7.3245 km/s
h_e	120 km
γ_e	-1 deg

The initial entry conditions are visible in Table 10.1.Values have been optimized such that the range is met with one single skip. The vehicle is given a fixed attitude during this maneuver: zero bank angle and an angle of attack of 50 degrees. Those properties are chosen as they are close to the maximum lift condition and will therefore promote skipping.

Limitations

From Table 10.1 it can be noted that the launcher separation accuracy required with the current GNC software is extremely high and as the system is highly non-linear and extremely sensitive it is hard to handle this only with changing launch conditions. Therefore, in further development, the angle of attack and banking angle will have to be made variable. For example, if entry velocity is too high, a banking angle or lower angle of attack can be used to make sure the vehicle still performs a similar skipping maneuver. Such a compensating maneuver is unfeasible when entry velocity is too low and therefore the target velocity for the launcher will be slightly higher than strictly needed.

10.4.2 Heat Flux Tracking

When the skip is performed, the vehicle will follow a heat flux constraint of 4 MW.This is done by the means of a PID controller, initiated at an altitude of 70 km.

Heat flux PID control

During the heat flux following phase, both angle of attack and bank angle are modulated using a PID controller. Both angles have to be modulated, as more accurate control can be obtained over the aerodynamic forces. Also, with a fixed angle of attack there is no measure in place to further increase lift when σ is zero. The general layout of the PID controller is visible in Figure 10.2 and the result of this control is visible in Figure 10.3. To make the system stable and predictable not only the gains had to be tuned, but also a limiting bank angle had to be selected. Without this, the vehicle would exceed the maximum allowable heat load on the upper surface. A maximum bank angle of 95 degrees was chosen as similar constraints have been imposed in other heat-following trajectories (Mooij, 2017b).

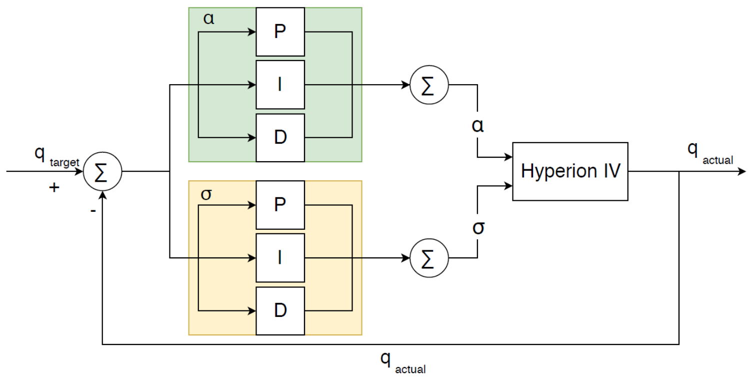

Figure 10.2: Heat flux control system layout

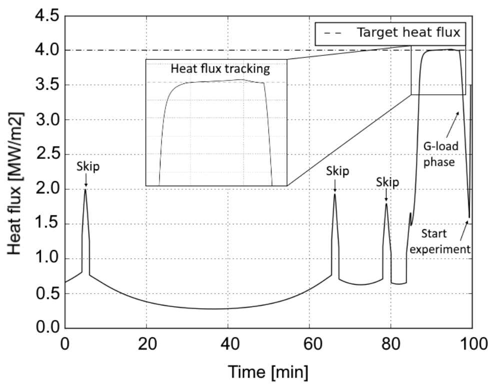

Figure 10.3: Heat flux in trajectory

Figure 10.4 shows the modulation of angle of attack and bank angle to follow the heat constraint. The initial (max) 95 degrees phase is the transition between skipping and heat-flux following. The vehicle has to lose altitude for an increased density and heat flux. The zoomed in part is where it approaches the heat-flux constraint, and the bank angle is modified such that it stays close to the 4 MW/m^2 heat flux constraint.

Limitations

The heat flux following is not perfect, with a maximum heat-flux of 4.0123 MW/m^2. This is due to non-perfect PID-control, as there is some overshoot (best visible in Figure 10.3). Also, this system does not account for disturbances yet, which will introduce extra errors. Also, to compute the heat constraint, the analytical expression by Detra as introduced in Chapter 14 is used. This model contains inaccuracies and therefore, in reality, measurements will be taken during the flight instead. If the difference between measurements and predictions are too inaccurate, the PID system might not be able to follow the constraint.

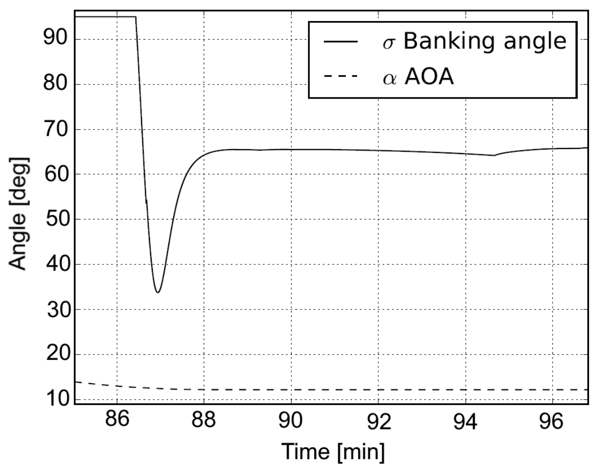

Figure 10.4: AOA and bank angle modulation for heatflux following

10.4.3 G-load Tracking

To follow the g-load constraint, an analytical formula was used from Mooij (2017b) which keeps ρV^n constant. For constant g-load (i.e. constant force), constant ρV^2 is desired (so n=2). This method makes use of Equation 10.18 for dγ/dV.

$$\frac{d\gamma}{dV}\mid_c = \frac{c_n}{\cos\gamma_c}\left\{\frac{2n^2KH_s\left(V^{n-1}+gH_s(n-2)V^{n-3}\right)}{\left(2KV^{n-2}(V^2+gnH_s)\right)^2}\right\} \tag{10.18}$$

Here γ is flight path angle, V velocity, $c_n = \rho V^n$, K $= \frac{m}{C_d S}$, $H_s = 7,050$m, g is the gravitational acceleration. With this, the g-load constraint was followed successfully as dV/dt is known and therefore $d\gamma/dt$ could be computed with $d\gamma/dt = d\gamma/dV \; dV/dt$.

Limitations

Limitation of this approach is that no optimization and integration of a control system was done. A similar approach to the heat-flux following can be implemented later, with PID and a more physical result.

10.4.4 Reynolds Sweep Experiment

The main experiment investigated here is the Reynolds sweep. This experiment keeps the vehicle's Mach number constant at 10, while decreasing the altitude. At every altitude the speed of sound is different. Now, this is solved with a time-marching method. The requirement is to have at every point the necessary drag to maintain Mach 10. This requires the computation of the necessary drag at point n to arrive at point n+1 still at Mach 10. First of all, the altitude at point n+1 is computed with Equation 10.19.

$$h_{n+1} = h_n + V_n \sin(\gamma_n)\, dt \tag{10.19}$$

Here h is altitude, V velocity and γ flight path angle. Now, the speed of sound at the next time step can be computed. With this, Equation 10.20 arrives at the required change in velocity.

$$dV = M_{Target}\sqrt{\gamma RT(h_{n+1})} - M_n\sqrt{\gamma RT(h_n)} \tag{10.20}$$

dV is now known, and with dt the acceleration is too. With Newton's elementary equations and the equations of motion, Equation 10.21 can be derived.

$$D_{req} = -m\left(g\,\sin(\gamma) + dV/dt\right) \tag{10.21}$$

With this, the drag at every point can be computed.

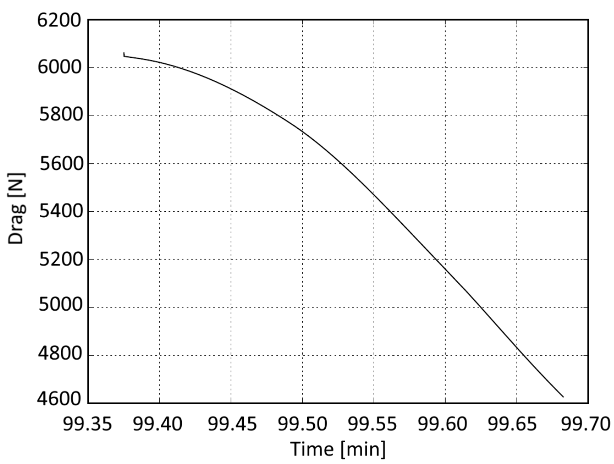

Figure 10.5: Drag during Reynolds sweep

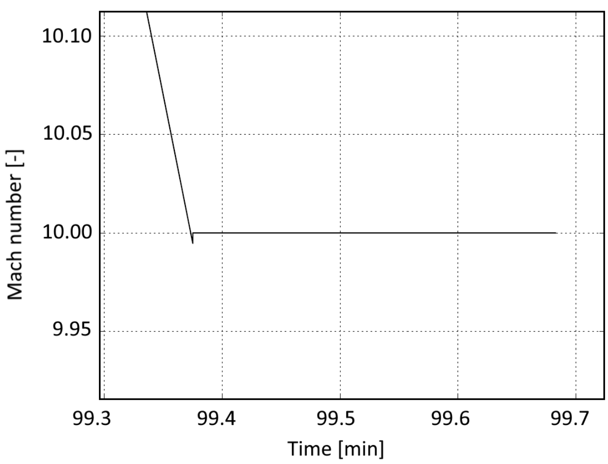

Figure 10.6: Mach number during Reynolds sweep

Initiating the experiment at the right moment is an optimization problem and can be further optimized. With the current parameter, Figure 10.5 shows the required drag over time during the experiment. The result of the imposed drag is visible in Figure 10.6. Then, the angle of attack comes from an interpolation of aerodynamic data. From drag and a zero bank angle, the angle of attack is derived and shown in Figure 10.7. A Reynolds sweep experiment is performed between 215,000 and 1,700,000.

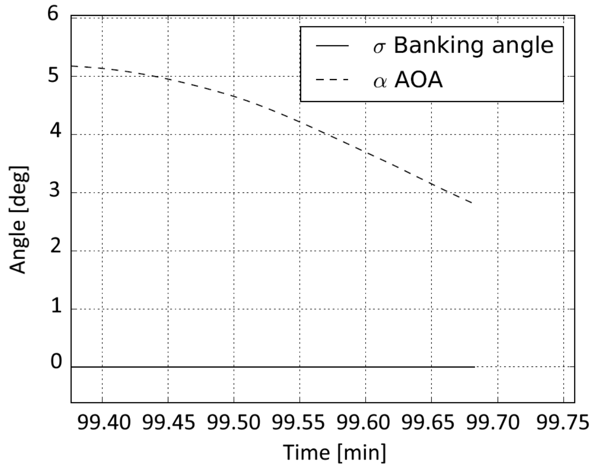

Figure 10.7: Angle of attack during experiment

Limitations

The way the experiment phase was initialized is to find the Mach number at which 6100 N of drag would be necessary, to ensure a continuous and thus more physical drag curve. The drag curve is now close to continuous, but this causes a peak in mach number. The initial mach number of the experiment is 9.998 and this is where the small spike originates from. Finally, the disturbances are not modeled and aerodynamic properties are assumed.

10.5 Trajectory Overview

After the specific phases have been discussed, an overview of the trajectory can be provided. In Figure 10.8 the flight path angle, altitude and mach number over time are visible together with altitude over velocity, latitude over longitude and finally α and σ over time.

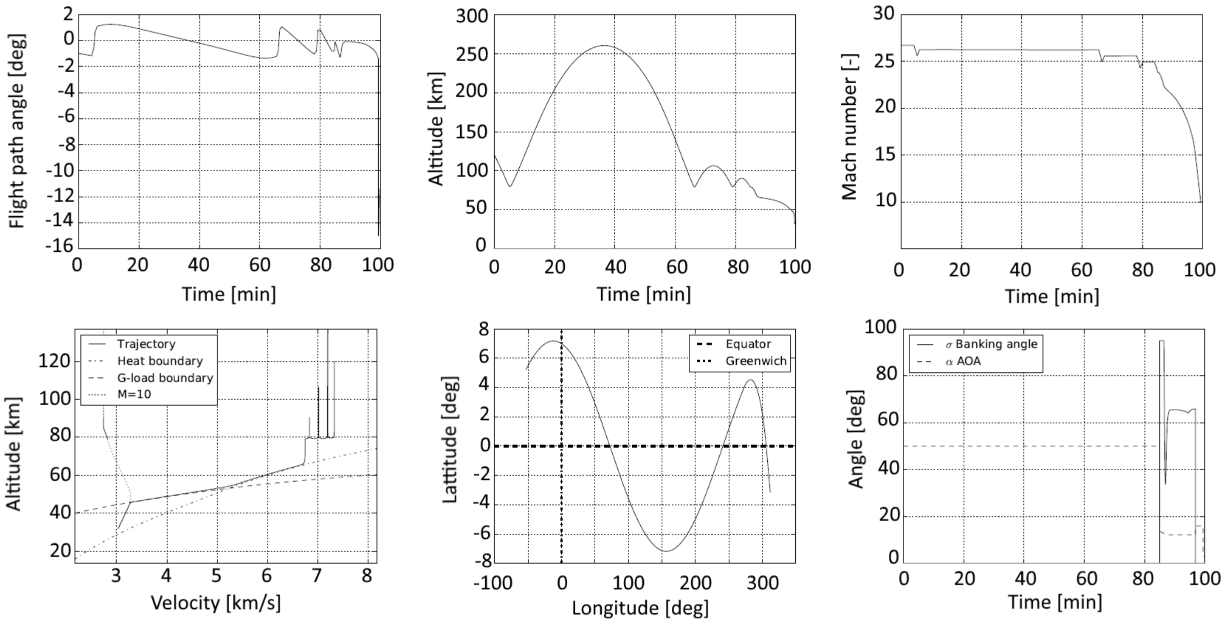

Figure 10.8: Trajectory overview

To draw conclusions from the results, assumptions and limitations should be taken into account. They include potentially erroneous aerodynamic data, discretization error and non-physical control commands. Non-physical control commands consist of sudden changes of attitude, which in reality would be a less abrupt process. Anyhow, even though shortcomings are present, satisfying performance can be achieved with the vehicle at hand. Most essential performance parameter are present in Table 10.2.

Table 10.2: Trajectory performance

Variable	Value
Downrange	41,694 km
Flight time	99.7 minutes
Maximum heat flux	4.0123 MW/m^2
Integrated heat flux	5,909.7 MJ/m^2
Reynolds sweep experiment time	18.46 sec

10.6 Model Verification and Validation

This section covers the procedures for verification and validation for the entry simulator that was developed and coded as described in Section 10.2.

10.6.1 Verification

Verification of the simulator was performed by comparing running a simulation of a free-falling point mass with no aerodynamic forces acting on it. The initial velocity was set to 0 km/s, at an altitude of 110 km and an initial flight path angle of -90 degrees (i.e. directed towards the center of the Earth) in a constant gravity field with an acceleration of -9.81 m/s^2. For this simple scenario, the analytical kinematic relations in Equations (10.22) and (10.23).

$$v(t) = V_0 + g\,t \tag{10.22}$$

$$h(t) = h_0 + v\,t + \frac{1}{2}\,g\,t^2 \tag{10.23}$$

The results of this verification process are shown in Figures 10.9 and 10.10.

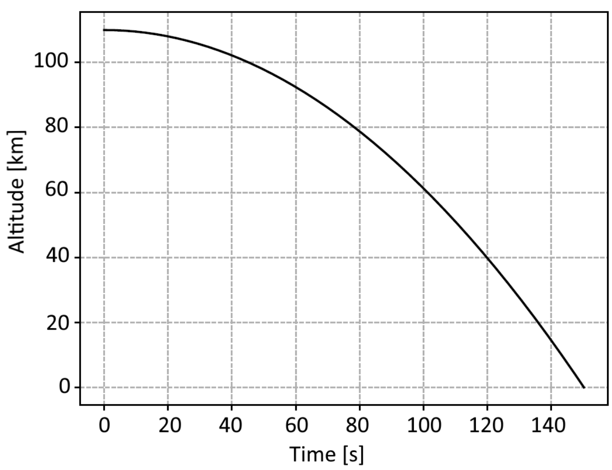

Figure 10.9: Plot of altitude versus time with no aerodynamic forces, initial altitude of 110 km, initial velocity of 0 km/s and flight path angle of -90 degrees with a constant g = 9.81 m/s^2

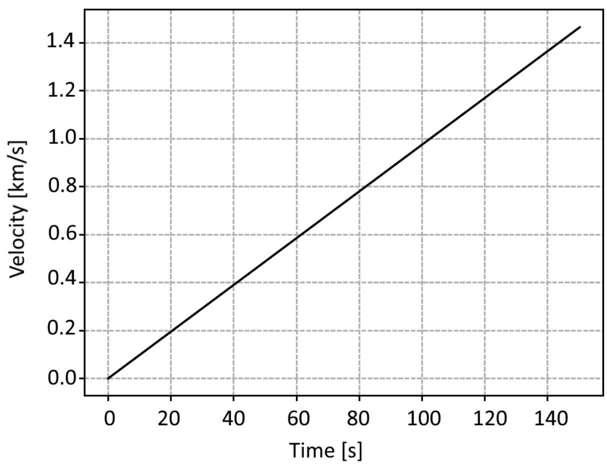

Figure 10.10: Plot of velocity versus time with no aerodynamic forces, initial altitude of 110 km, initial velocity of 0 km/s and flight path angle of -90 degrees with a constant g =9.81 m/s^2

10.6.2 Acceptance

Validation of the entry simulator is accomplished by comparing to the simulation of the Apollo reentry performed by Hirschel and Weiland (2009). Two profiles were analyzed, namely the altitude versus flight time and the load factor versus time profiles. The comparison with the simulator implemented in-house is shown in Figures 10.11 through 10.14.

The curves for the altitude versus time plot show consistency with the simulation produced in literature. For instance, for an initial flight path angle of -0.75 degrees, the simulation shows the vehicle levelling off approximately 400 seconds into the flight for a period of 100 seconds, which is confirmed by validation data. Furthermore, for an initial angle of -1.5 degrees, the vehicle starts descending after a the pseudo-leveled flight about 400 seconds into flight, which is again confirmed by the validation data.

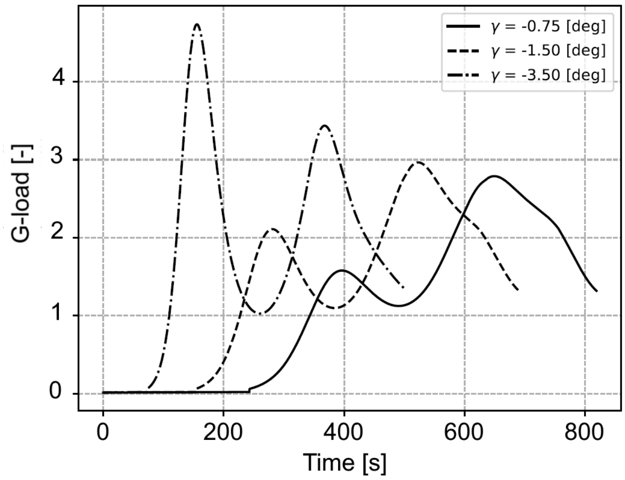

Figure 10.13: Altitude versus flight time profile for various initial flight path angles

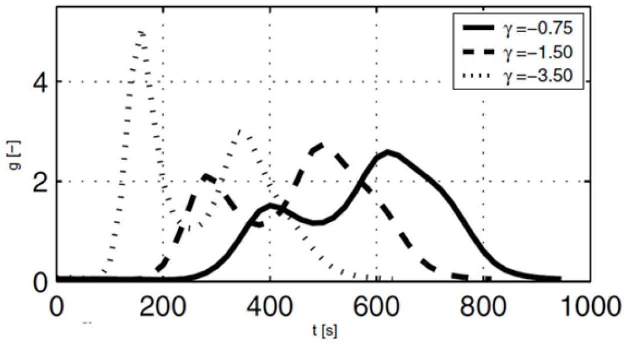

Figure 10.14: Altitude versus time profile from Hirschel and Weiland (2009)

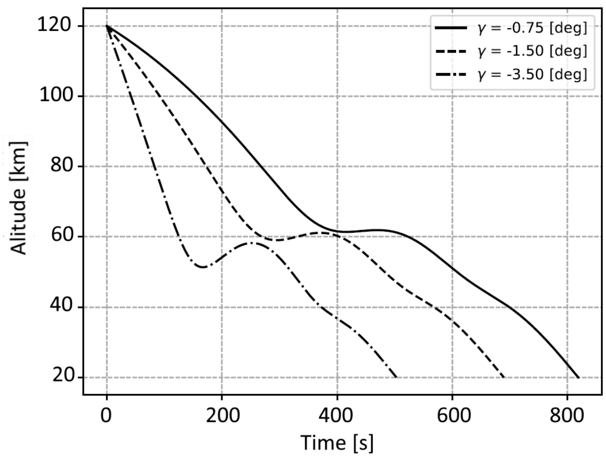

Figure 10.11: Altitude versus flight time profile for various initial flight path angles

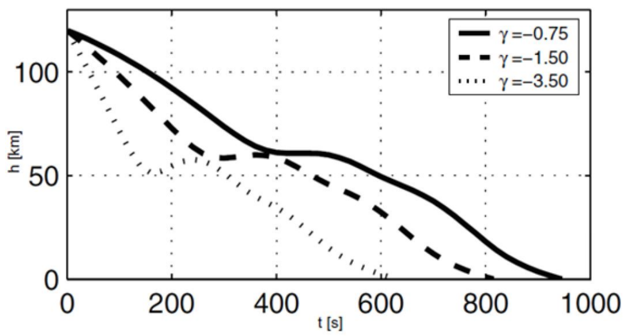

Figure 10.12: Altitude versus time profile from Hirschel and Weiland (2009)

Next, the load factor profile will be analyzed and compared. The entry trajectories for different initial flight path angles is plotted versus time. For an initial angle of -3.5 degrees, the the maximum load factor is experienced about 180 seconds into flight, which agrees with the result of Hirschel and Weiland (2009) displayed in the figure on the right.

Validation was also performed by using ASTOS 9.2.0. Using this software, it was possible to replicate the reentry trajectory computed as explained in the previous sections of this chapter. The vehicle was modelled as a ”Winged spacecraft” with an ”Auxiliary mass” corresponding to the mass of Hyperion IV. The atmospheric model was set to the *US Standard 1976* standard atmosphere and the Earth was modelled with the standard package from the ”Celestial Bodies” section in the ”Environment” menu. The initial dynamic state of the vehicle was set to the design initial conditions. The reference frame in use is the PCPF Planetocentric Frame (i.e. the C-frame). The simulation is terminated when the vehicle reaches sea level altitude or when the elapsed time exceeds two hours. The guidance profile of the current vehicle was also loaded on the software. With these settings, it was possible to produce data to compare the in-house simulation to. The first, shown in Figure 10.15 shows the ground track of the vehicle, demonstrating the vehicle can make the requirement of flying once around the Earth.

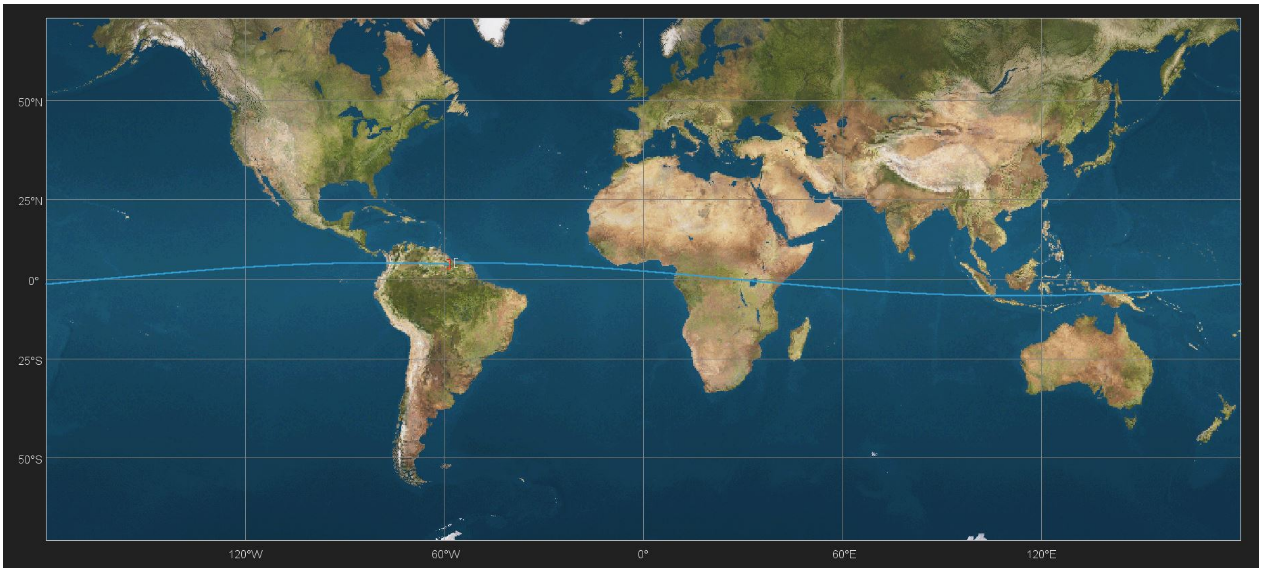

Figure 10.15: Ground track of the vehicle reproduced by ASTOS 9.2.0

The second results to be shown in the design the current is the altitude versus time profile, shown in Figure 10.16.

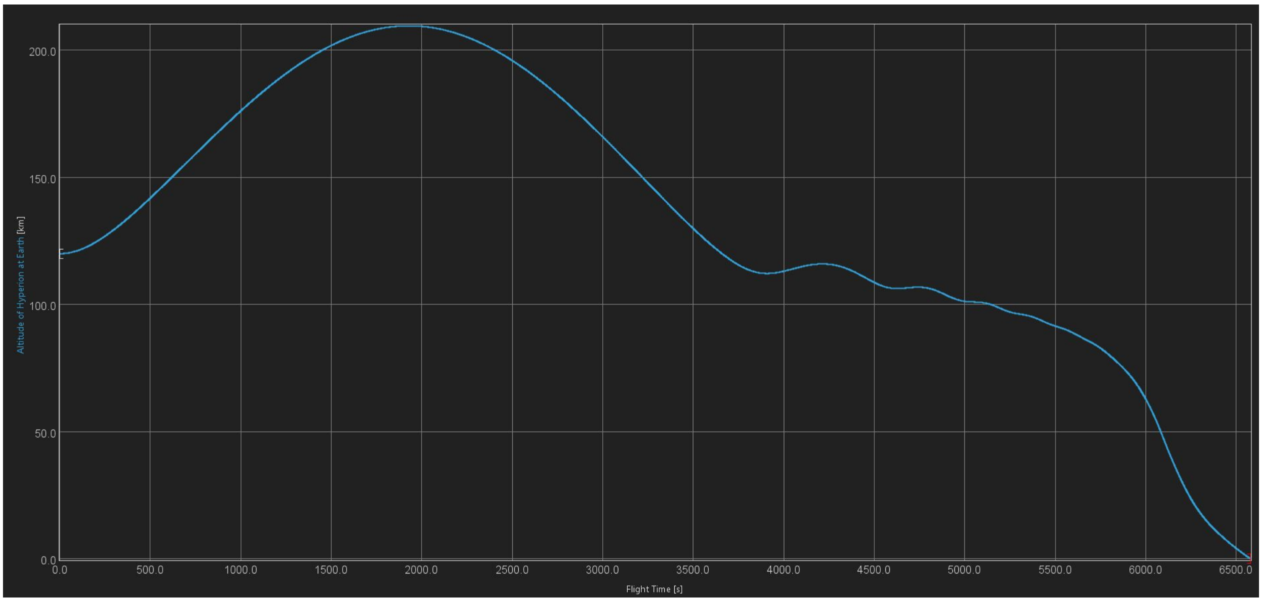

Figure 10.16: Plot of altitude versus flight time, reproduced with ASTOS 9.2.0

It can be seen that the altitude profile does not entirely correspond to the one presented in Figure 10.8. There, the apogee of the skip was arounf an altitude of 260 km, whereas the validation plots present a maximum altitude of 210 km approximately. Furthermore, according to ASTOS, the vehicle immediately enters a skipping trajectory, when according to the in-hourse simulation the vehicle first descends, to then enter the largest skip. These cause for this difference is believed to reside one of the following aspects.

- **Numerical error.** Numerical errors in the code are believed to be unlikely, due to the verification and validation performed with the Apollo data.
- **Guidance profile.** Tracing of the g-load was accomplished by using the analytical guidance equation introduced in Equation 10.18. This effectively changes the equations of motion, which is not taken into account by ASTOS.

10.7 Sensitivity Analysis

Sensitivity analysis is of great use to asses the robustness of the developed tool at hand. As stated before, the GNC software is extremely sensitive as the system is non-linear. It has been observed that small alterations in initial conditions can have a very substantial effect on the trajectory.

The question is now to which extend a sensitivity analysis should be performed for the GNC software. It was chosen to modify four parameters and evaluate their impact : varying density, varying launch velocity, varying initial flight path angle and varying aerodynamic properties.

Table 10.3: Trajectory performance with 10% less density

Variable	Value
Downrange	38,552 km
Flight time	93 minutes
Maximum heat flux	4.1220 MW/m^2
Integrated heat flux	4,633.30 MJ/m^2
Reynolds sweep duration	17.14 sec

Table 10.4: Trajectory performance with 10% less lift

Variable	Value
Downrange	30,343 km
Flight time	76 minutes
Maximum heat flux	2.0099 MW/m^2
Integrated heat flux	3,612.35 MJ/m^2
Reynolds sweep duration	0 sec

Ordered on increasing sensitivity, the impact of different alterations are visible in Tables from 10.3 to 10.6, the effect of different alterations are present. A 10% change in density has a marginal influence: both constraints have a small overshoot, but the experiment is performed properly and the vehicle should not have a problem to survive the flight. Nevertheless, a change in lift has significant influence as it changes the skipping. The issue with this is that the end of skipping phase is based on a timer in the GNC software. Because the time of skipping is reduced in time now, the skipping will be ended too late and following the constraints is no longer feasible. Therefore, no Reynolds sweep can be performed. The initial conditions from the launcher are most sensitive, as a 7.3 km/s launch velocity or a -3 degrees flight path angle.

Table 10.5: Trajectory performance with 7.3 km/s launch velocity

Variable	Value
Downrange	28,055 km
Flight time	71.04 minutes
Maximum heat flux	2.0065 MW/m^2
Integrated heat flux	3,323.33 MJ/m^2
Reynolds sweep duration	0 sec

Table 10.6: Trajectory performance with a -3 degrees launch flight path

Variable	Value
Downrange	7500 km
Flight time	22.7 minutes
Maximum heat flux	2.6416 MW/m^2
Integrated heat flux	988 MJ/m^2
Reynolds sweep duration	0 sec

10.8 Recommendations

Guidance, Navigation and Control is one of the most critical systems of any reentry mission, as it is the subsystem in charge of safely guiding the vehicle from the upper atmosphere down to the recovery area without violating any requirement on thermal and mechanical loading imposed by the design and the mission profile. In this project, a preliminary guidance design of the Hyperion IV vehicle was proposed. This section contains some ideas that can be implemented for a more sound design of the GNC system.

- **More robust control**: with the current design, active PID control is only integrated in the heat flux tracking phase. It would be recommended to implement the controller for more, if not all, phases of the flight.
- **TAEM guidance**: Terminal Area Energy Management guidance was not implemented for the in-house guidance model. Therefore, an accurate simulation of the approach and recovery phase was not implemented in the simulator.
- **Optimization**: complete trajectory analysis and design would require optimization of the control and guidance profile to achieve higher range or longer experiment time.

Now, Chapter 11 will go deeper into the hardware necessary to fly the computed trajectory. With this, it will also present the budgets.

11 Control System

Considering the trajectory determined in Chapter 10, Hyperion IV maintains a high angle of attack and later experiences drastic maneuvers to stay within the reentry corridor. The control system on-board must guarantee a safe and stable trajectory considering various flight conditions. To achieve this, Hyperion IV will be equipped with two main attitude control systems, namely the Reaction Control System (RCS) and aerodynamic control surfaces (body flaps). In this chapter, the design flow and its analysis of these control systems will be presented.

11.1 Requirements on Control System

The control system design decisions followed the main requirements presented earlier in Chapter 3, and the most relevant will be noted here again.

- **SYS.CR.5 The vehicle shall provide means of control**: due to various system requirements, the vehicle will need means of maneuvering. This requirement implies the 3-dimensional movement of the vehicle by various means. However, more specific requirements will be set by subsystems themselves.

From this requirement, further specific requirements were derived to set a focus in design decisions, and these are listed in the following.

- **CTRL.REQ.01**: the vehicle shall be stable with two degrees disturbance of angle of attack.
- **CTRL.REQ.02**: the RCS shall be optimally designed to minimize its mass.
- **CTRL.REQ.03**: the body flap shall be designed to be able to conduct the maneuvers.

Note that the angle requirement of two degrees described in the **CTRL.REQ.01** was derived from the analysis in Subsection 11.5.2.

11.2 Trade-Off Summary

In the Midterm Report (Amend et al., 2018b), a trade-off was perform to design the most optimal vehicle shape for the mission. Following from this decision, the control surfaces on the vehicle were concluded to be two body flaps on the back side of the vehicle. Furthermore, RCS is also equipped to ensure controllability in higher altitudes. Further design decisions will be described in detail in this Chapter.

11.3 Longitudinal Control System Design

The longitudinal control system was designed by using two main simulation tools: the optimal control theory and the angle of attack change simulation. The latter verifies the former simulation to see if the calculated controller gains can truly sustain the angle of attack disturbances. If not, iterations were taken by changing the parameters such as control surface dimension or maximum thrust. This analysis supported the designing of the control systems and will be presented in detail.

11.3.1 Optimal Control Theory

Optimal control theory is used to analyze control problems for a system represented by state space equations, generally described in the form as Equation (11.1).

$$\dot{\mathbf{x}} = \mathbf{A}\mathbf{x} + \mathbf{B}\mathbf{u} \tag{11.1}$$

Furthermore, the state feedback equation is given as in Equation (11.2)

$$\mathbf{u} = -\mathbf{K}\mathbf{x} \tag{11.2}$$

The linearized longitudinal equation of motion of Hyperion IV can be expressed in state space form as seen in Equation (11.3). Note that the this equation solely accounts for the analysis of the attitude control and neglects any asymmetric motion.

$$\begin{bmatrix} \Delta\dot{q} \\ \Delta\dot{\alpha} \end{bmatrix} = \begin{bmatrix} 0 & \frac{1}{I_{yy}}\frac{\partial C_m}{\partial \alpha}\bar{q}S_{ref}c_{ref} \\ 1 & -\frac{1}{mV}\frac{\partial C_L}{\delta \alpha}\bar{q}S_{ref} \end{bmatrix} \begin{bmatrix} \Delta q \\ \Delta \alpha \end{bmatrix} + \begin{bmatrix} \frac{1}{I_{yy}}\frac{\partial C_m}{\partial \delta_f}\bar{q}S_{ref}c_{ref} & \frac{1}{I_{yy}} \\ 1 & 0 \end{bmatrix} \begin{bmatrix} \Delta\delta_f \\ \Delta M_{Ty} \end{bmatrix} \tag{11.3}$$

Here, δ_f is the body flap deflection and M_{Ty} is the pitching moment induced by the thrusters. Furthermore, the corresponding state feedback equation can be expressed as Equation (11.4).

$$\begin{bmatrix} \Delta\delta_f \\ \Delta M_{Ty} \end{bmatrix} = \begin{bmatrix} K_{fq} & K_{f\alpha} \\ K_{yq} & K_{y\alpha} \end{bmatrix} \begin{bmatrix} \Delta q \\ \Delta\alpha \end{bmatrix} \tag{11.4}$$

An indirect method to solve the feedback matrix **K** for this state space equation will be used. As Mooij (2017a) suggests, Quadratic Optimal Control will be used, in which a mathematically defined cost criterion equation, seen in Equation (11.5), is minimized.

$$\mathbf{J} = \int_0^\infty (\mathbf{x}^T\mathbf{Q}\mathbf{x} + \mathbf{u}^T\mathbf{R}\mathbf{u})dt \tag{11.5}$$

The term $\mathbf{x}^T\mathbf{Q}\mathbf{x}$ represents the control deviation and the term $\mathbf{u}^T\mathbf{R}\mathbf{u}$ represents the control effort. Adjusting the **Q** and **R** will alter the speed of the controller response and the effort, and therefore they will follow an iteration process. These weighing matrices seen in Equation (11.6) are first constructed with the use of Bryson's Rule (Murray, 2010).

$$\mathbf{Q} = \begin{bmatrix} \frac{1}{\Delta\bar{q}^2_{max}} & 0 \\ 0 & \frac{1}{\Delta\alpha^2_{max}} \end{bmatrix} \quad \mathbf{R} = \begin{bmatrix} \frac{1}{\Delta\delta^2_{fmax}} & 0 \\ 0 & \frac{1}{\Delta M^2_{Tymax}} \end{bmatrix} \tag{11.6}$$

Where $\Delta\bar{q}^2_{max} = \infty$, $\Delta\alpha^2_{max} = 2°$, $\Delta\delta^2_{f_{max}} = 40°$ and $\Delta M^2_{Tymax} = 100$ N were selected as the initial input. These values will be altered as the design process proceeds, especially when the actuators of the body flaps or the thrusters are selected, leading to recomputation of these values.

Based on the activation of different controls of the space shuttle mission (Mooij, 2017a), the entry control modes were defined. Due to their effectiveness, the thrusters will be activated only when the dynamic pressure is less than 1,000 N/m^2. On the other hand, the body flaps will be activated once the dynamic pressure reaches 100 N/m^2. Therefore there will be a hybrid phase when both these controls are active, which ranges from dynamic pressure of 100 to 1,000 N/m^2.

With the use of these inputs mentioned above, the Linearized Quadratic Regulator (LQR) function in Matlab ®was used to find the optimal control gain **K** at all points of the trajectory provided in Chapter 10. This result will be discussed in Section 11.5.1.

11.3.2 Angle of Attack Change Simulation Model

The optimal gains were later analysed by simulating a step input of α to see if the system is stable or not and how agile the control system is. This has been simulated in Simulink and the control structure can be seen in Figure 11.1. Looking at this structure from left to right, each segment will be explained briefly. First, the pitch rate was assumed to have a constant 0 input while the angle of attack has a certain angle of step input. The selection of the angle will be discussed in Subsection 11.5.2. These input values go through the controller, which gets multiplied by the gain that has been calculated optimally by the LQR equation. Then, each input signal is saturated by the specified maximum deflection or maximum thrust. Finally, these inputs enter the state space equation, producing an output. Note that this structure represents a closed loop PD controller.

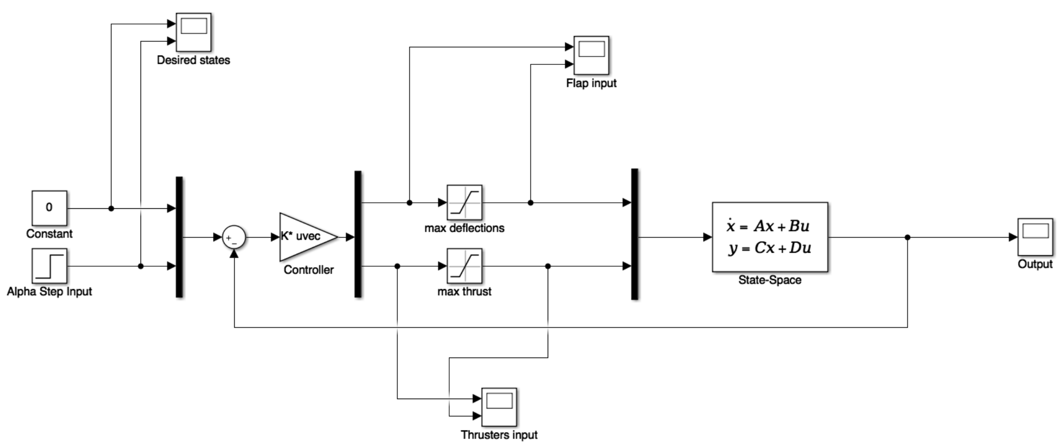

Figure 11.1: Simulink model for angle of attack change simulation

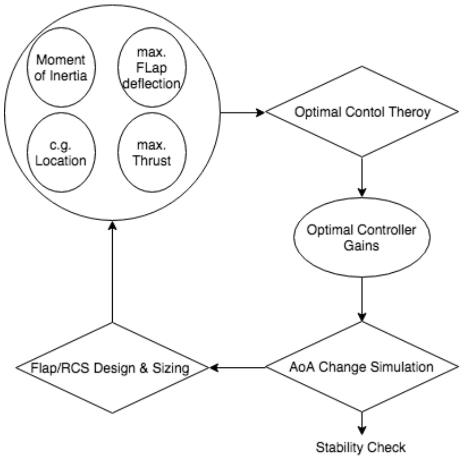

Figure 11.2: Control system design iteration

This angle of attack simulation model and the optimal control theory were the main tools to design a stable control system. Numbers of iterations were taken and this top level flow of parameters and simulations can be seen in Figure 11.2.

After a number of iterations, successful final body flap and RCS design were achieved while maintaining a stable control system. These results will be described in the upcoming sections.

11.4 Model Verification and Validation

Before the analysis of the simulation results, the simulation models must be verified to confirm their accuracy and validity.

11.4.1 Verification on Optimal Control Model

Verification of the optimal control model is conducted through a series of unit and zero input testing. Furthermore, the stability of the control system was analyzed by looking at the characteristics of full state feedback, namely the eigenvalues of the $\mathbf{A}^*$ matrix. Inserting the feedback (Equation (11.2)) into the state space equation (Equation (11.1)), Equation (11.7) can be obtained.

$$\dot{\mathbf{x}} = (\mathbf{A} - \mathbf{BK})\mathbf{x} \tag{11.7}$$

$\mathbf{A}^*$ is defined as $\mathbf{A}^* = (\mathbf{A} - \mathbf{BK})$. The real part of the eigenvalues of the $\mathbf{A}^*$ matrix were negative, indicating a stable control system at all points of the trajectory. This confirms the validity of the simulation as it is successfully outputting a stable and optimal gain.

11.4.2 Verification on Angle Disturbance Analysis Model

The angle disturbance analysis model is verified by a procedure similar to the one used to verify the optimal control model. Unit testing was conducted throughout the simulation. One example for the zero input testing is setting the angle of attack input to zero. Both the deflection of the body flap and the thrusting moment (seen in the "Flap input" and "Thrusters input" block in simulink model, Figure 11.1) showed a null response. This result is reasonable due to the fact that there is no disturbance and therefore it doesn't need to be counteracted. Together with many other zero and unit testings, this model was confirmed to be outputting a valid response.

11.5 Results

In this section, the outcomes of the two simulation tools described in Section 11.3 will be presented.

11.5.1 Longitudinal Controller Gains

As the input parameters were finalized after a number of iterations, the controller gain over the mission time can be plotted. This can be seen in Figure 11.3 for body flap controller gains K_{fq} and $K_{f\alpha}$ and Figure 11.4 for pitch thrust controller gains K_{yq} and $K_{y\alpha}$. What is interesting to notice is that there is a clear distinction between the thruster phase, hybrid phase and the body flap phase. Also, the skipping phenomena can be seen clearly three times, when the body flap gets activated and the thruster has a large drop in the gain. The thruster gain does not reach zero, which represents a hybrid phase during the skipping phase. After the final reentry at around 5100 seconds, it is clear that the thruster is disactivated and the body flap solely takes over the control.

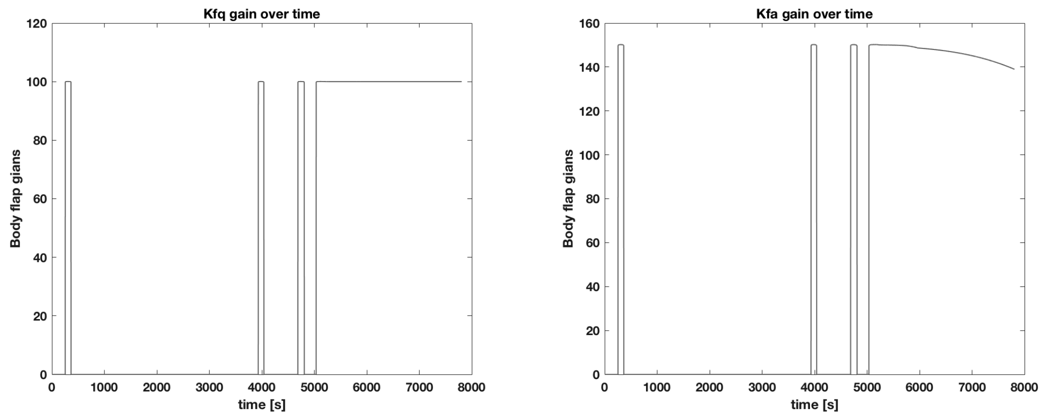

Figure 11.3: Body flap controller gain over mission time

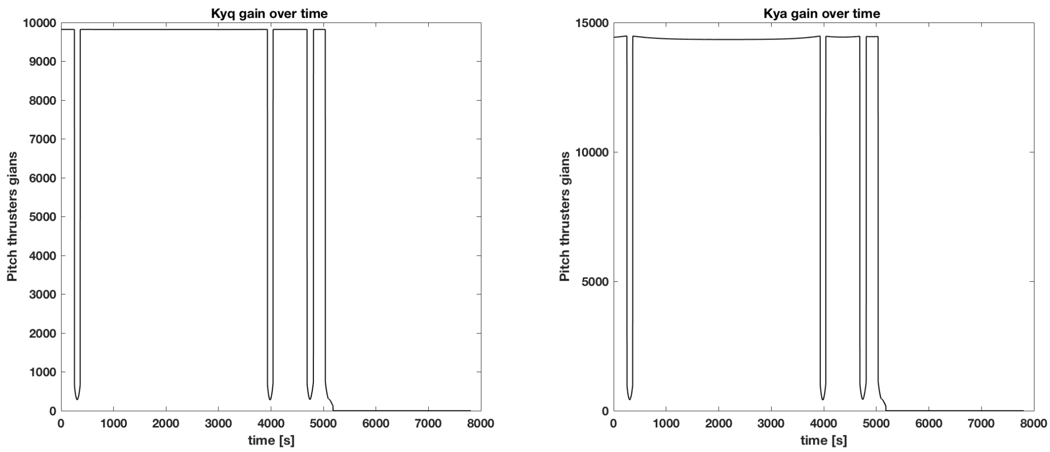

Figure 11.4: Pitch thruster controller gain over mission time

11.5.2 Controller Response to Angle of Attack Change

It is also important to analyse whether the calculated controller gains together with selected iteration parameters can produce a stable output when there is a required change or disturbances in angle of attack. This was done using the simulation presented in Figure 11.1. This analysis was conducted for all three controller phases: hybrid phase, body flap phase and thruster phase, such that at any time of the mission, the controllers are ensured to produce a stable output. First, the source of angle of attack change will be described and later the controller response for each phase will be analyzed.

Sources of Angle of Attack Change

In a nominal trajectory, the vehicle maintains a constant angle of attack until the final reentry as seen in Figure 10.8. However, due to the fact that the vehicle is going around Earth, the shift in angle of attack must be taken into consideration. A simple mathematical approach was taken to calculate this angular shift. The vehicle will have its final reentry at 85 minutes after the separation, at the range of 36,464 km. This range corresponds to 90.96 % of the Earth circumference and therefore the total angle of attack shifts by 324 °. Assuming that the angle shifts at a constant rate, the angle of attack shifts 0.0635 ° per second. This shift in angle of attack must be modified by the attitude control systems.

In addition, perturbations and disturbances during the flight can cause further change in angle of attack. These can be caused by sudden change in atmospheric condition such as density and pressure, unexpected gust, non-uniformity of the gravitational field and many more. In this analysis, the perturbations and disturbances as described above will be neglected. This is a fair decision because the resultant disturbance will be very small compared to significantly high velocity vector vehicle experiences. In addition, due to their random nature of appearance, accurate analysis would require heavy and expensive computation.

Also considering the output of sensitivity analysis conducted in Section 11.8, conclusion was drawn to conduct these analyses with 2° angle of attack input.

Hybrid Phase

The hybrid phase will be expected to have the most stable and fast response because there will be two controllers available. A disturbance of 2° angle of attack was inputted, while maximum flap deflection and maximum thrust moment was selected to be 30° and 30Nm, respectively. The output of this simulation is shown in Figure 11.5a. The angle of attack is stable at 2° (0.0349 rad), from around 4 seconds.

Thruster Phase

The system must still be stable when the body flap is dis-activated and the thruster is required to solely provide the attitude control, which is actually the majority part of the mission, as seen in Figure 11.4. This analysis has been conducted in another Simulink structure, which included a PID controller to acquire more stable responses. This system response can be seen in Figure 11.5b. The output of this analysis was important for the RCS design decision, since it required a lot of tweaking. The conclusion from this simulation was to have a maximum thrust moment of 30 Nm to have a stable response. The thruster phase response was very sensitive and this is further discussed in Section 11.8.

Body Flap Phase

The same analysis must be made when the body flap is the only means of attitude control. The response for the body flap phase was almost identical to the hybrid phase. Further analysis on the body flap can be seen in Section 11.6.

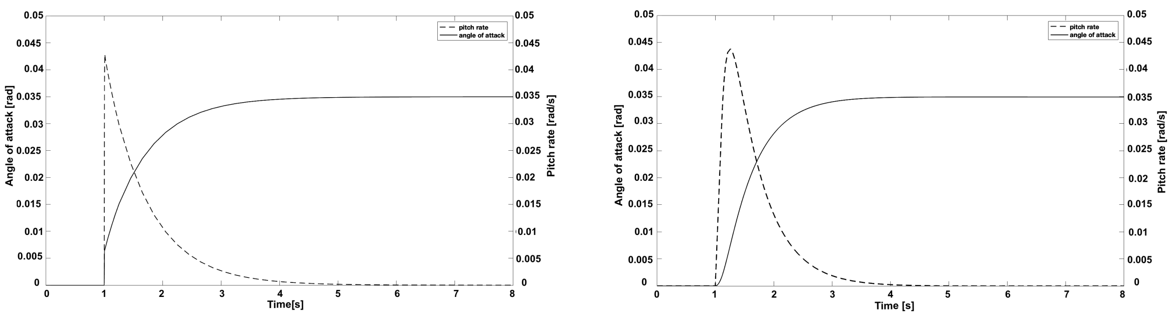

(a) Hybrid phase

(b) Thruster phase

Figure 11.5: System response to angle of attack change

11.6 Body Flap Design

The general body flap design was inspired by the IXV vehicle (Fumo, 2017), due to its simplicity, and how it can be integrated to the Hyperion IV vehicle design easily and efficiently. The sizing of the body flap was part of the iteration process as the desgin would change the center of gravity position and mass moment of inertia. Once the iteration parameters were frozen, body flap performance was analyzed by comparing the moment the vehicle experiences and the moment the flaps can generate during the mission.

The moment of the vehicle was simply computed by the use of aerodynamic coefficient C_{m_α} to compute the moment given by $M_v = C_{m_\alpha} \alpha \bar{q} S_{ref} c_{ref}$. The C_{m_α} was an output from the aerodynamic model, where $\bar{q}$ and α were taken from the trajectory model. On the other hand, the moment that can be produced by the body flap was calculated as following. First, the aerodynamic forces acting on the body flap was calculated with

$$F_f = \bar{q} S_f C_{p_f} \tag{11.8}$$

where S_f is the surface area of the bofy flap and the pressure coefficent on the body flap C_{p_f} is given by

$$C_{p_f} = C_{p_{max}} sin^2(\theta) \tag{11.9}$$

where θ is the flow deflection angle which approximately $\theta = \alpha + \delta_f$. From the given flight condition and the CG location (which the moment arm can be calculated), the moment induced by the body flaps on the CG can be computed.

The body flap dimensions and attachment location were iterated until the body flap moment can generate larger moment than the moment vehicle experiences. This is to ensure that the vehicle is always able to be trimmed and controlled. The result can be seen in Figure 11.6. Note that the flap moment is shown as the absolute moment. In addition, this plot presents the flap moment at 7° deflection. Lower angle of flap deflection did not ensure the trimmable condition for the whole mission. This does not mean that the body flap must be deflected at 7° at all times, but it is an indication that at some deflection, the vehicle is completely trimmable and controllable.

The final design of the body flaps can be seen in Figure 11.7. The actuator system includes the actuator, Y-lever and the flap rod, which transfers the force efficiently to the body flap. The electro-mechanical linear actuator can be ordered from ROLLON Linear Revolution [1], where variety of size and specifics of the actuators can be chosen.

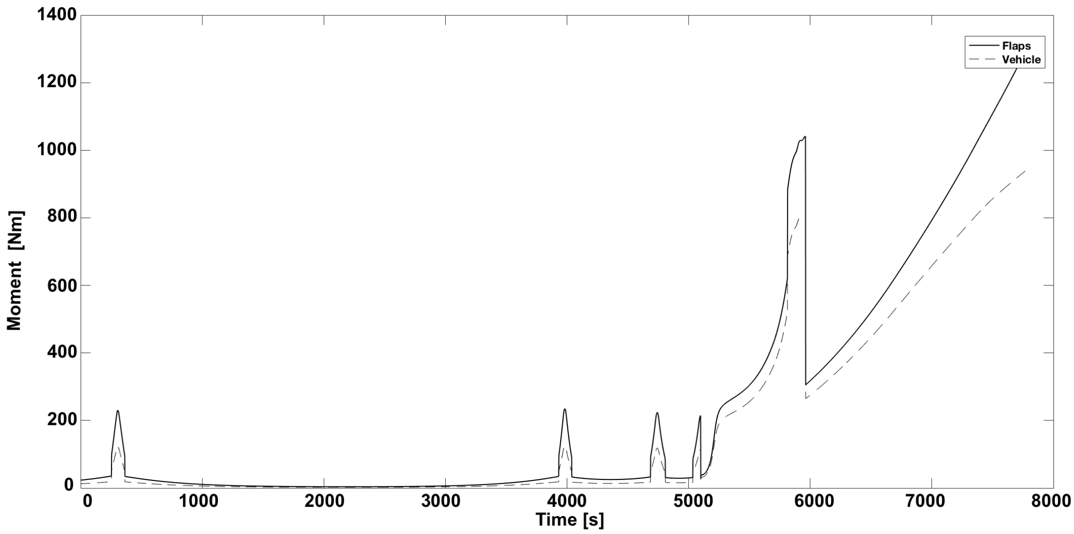

Figure 11.6: Moment experienced by the vehicle and absolute moment the flaps can generate at 7° deflection throughout the mission

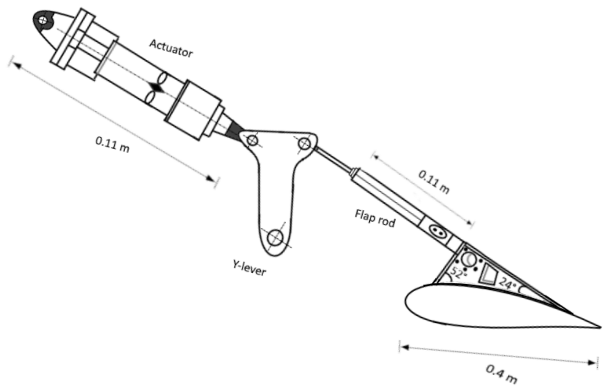

(a) Side view of body flap and actuator system (not to scale)

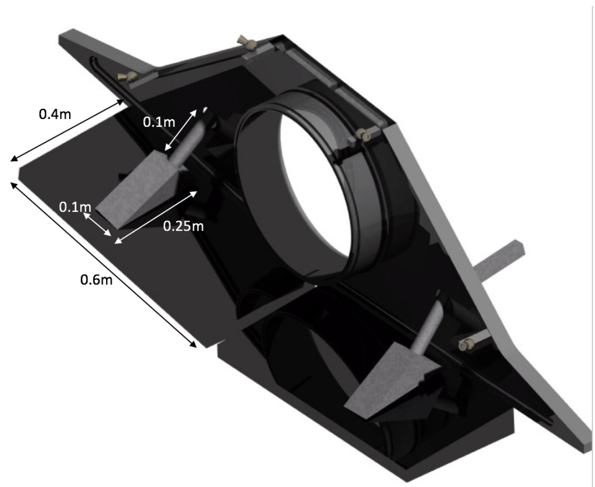

(b) Isometric view of the body flap and the back plate

Figure 11.7: Body flap design

[1] http://www.rollon.com/GLOBAL/en/ last accessed on 24/06/2018

11.7 Thrusters Design for the Reaction Control System

For the preliminary design of the RCS, inspiration was taken from the EXPERT vehicle; this is due to the similarity in both the mission profile and mass. Similar thrusters were chosen (5.6 N model 58-103 by Moog) with the weight of the valves and fastening scaled to 6 thrusters and the tank (GN2 fuel) scaled to the difference in wet mass. After a more detailed study about the controlability as described in Section 11.5.1, it turned out that a minimal thrust of 30N in longitudinal direction was needed. To minimize costs an off-the-shelf thruster was desired. After studying multiple options the Triad model 50-820 was chosen, which would need minimal adjustment and is illustrated in Figure 11.8. The thruster is able to produce a minimal thrust of 5 N up to a maximum of 52 N longitudinal and 105 N directional.

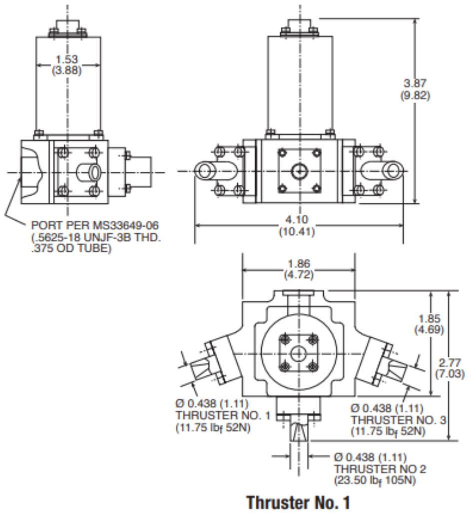

Figure 11.8: Unmodified triad RCS thruster by Moog (model 50-820) (Moog, 2017)

The nozzles of the thruster can be altered to reach higher or lower maximum thrust levels. As is illustrated in figure 11.8 thrusters 1 and 3 are angled, however for Hyperion IV they will be orthogonal to thruster 2. The thruster block will be placed on the back of the vehicle next to the body flap, such that the bottom thrusters do not thrust into the back of the body flap. Unfortunately the yaw thrusters are not put on the horizontal axis of the CG, therefore the pitch thruster of the other thruster have to fire to compensate the roll. The alternative would be to put the thrusters on the horizontal axis of the CG with the bottom thrusters angles. However it turned out that this was a heavier solution than the one chosen. The tanks were sized based on a directional or longitudinal disturbance of 1 degree every ten seconds. This resulted in a total thrust time of 5.2 s at 30 N. Using Standard rocket equations, the thruster characteristics provided by Moog Moog (2017), and a 30% margin a propellant mass was found to be 5.08 kg. From the propellant mass the tank volume was scaled to that of the Expert vehicle, form which the dry tank mass could be derived. For the piping and valves the Expert mass budget was used again, since Expert was using similar RCS systems from Moog this was deemed detailed enough. the piping and fastening was based on the estimated length and scaled to Expert resulting in roughly 0.9 kg. For the valves and filters the same were taken as for expert minus the once needed for the thrusters since those are integrated in the chosen thruster block. A better overview of all the masses is given in the mass budget in Figure 11.1. An overview of the Layout of the tank, the thrusters, and the piping can be seen in figure 11.9

11.8 Sensitivity Analysis

Sensitivity analysis must be conducted to understand how sensitive the system is to various parameters. This has been checked by changing different input parameters in different simulation models. It has been noticed that the effect of angle of attack change on the thruster phase has shown a very sensitive results, especially compared to the other phases and therefore will be the focus of this analysis.

The angle of attack was varied from 1° to 7° and the results can be seen in Figure 11.10. As it can be seen, the system response above 5° is unstable and at 7°, the angle of attack completely diverges. This is because there is not enough thrust to induce the required pitch rate to meet the requested angle of attack. This can be deemed as a large risk, if there will be an angle of attack change larger than 6°. The disturbances and perturbations are not expected to induce such large change in angle of attack, but this risk can be

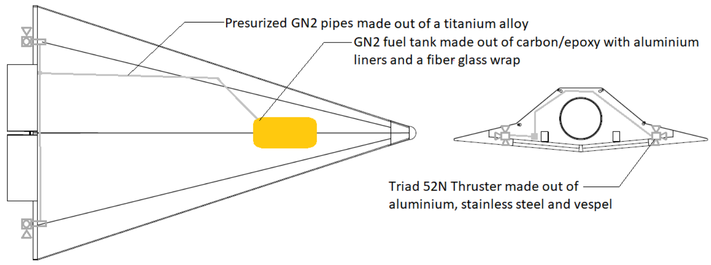

Figure 11.9: General layout of the RCS thruster, fuel tank and fuel pipes with respect to Hyperion IV.

applied during maneuvers. During the maneuvers, the angle of attack varies significantly as seen in Figure 10.8. Obviously, these maneuvers will not require instantaneous change in attitude, but the system can be prone to larger instantaneous angle disturbances than other phases of flight. However, fortunately during the thruster phase of the nominal trajectory, no attitude maneuvers are expected. Therefore all the maneuvers are taken care of by the body flaps, which showed no diverging or unstable response at larger change in angle of attack.

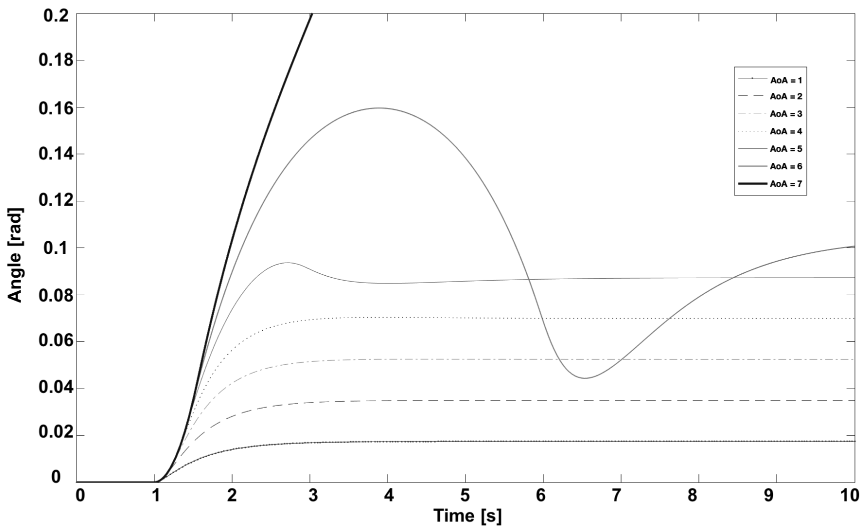

Figure 11.10: different alpha sensitivity on thruster

11.9 Control System Budget Summary

The summary of the mass and power budget of the control system is shown in Table 11.1.

Table 11.1: Control system budget summary

Item	Mass [kg]	Power [W]	Volume [m^3]
2 Body flaps	20	-	0.018
2 Actuator systems	5.45	200	-
Triad thruster	2 X 0.43	6-12	-
Fuel Tank (dry)	15.25	-	0.022
Monopropellant	5.08	-	*
piping and fastening	0.90	-	-

∗ propellant volume is included in the volume of the fuel tank.

11.10 Recommendations

In this chapter, the control system was designed and analyzed extensively. However, there are still many elements that can be improved for a better design, and better stability and control. This will be set as future recommendation, and these elements will be discussed briefly in this section.

The control system analysis was done solely for longitudinal system due to the time constraint. Therefore the analysis on lateral and directional has not been done. However, as the flaps provide very stable and robust control for longitudinal direction, it can also be expected to do so for the lateral direction. The only problem lies on the directional stability. The body flaps cannot solely control the yaw moment, but only by inducing it from the roll moment. Therefore, the directional stability must be analysed thoroughly and thrusters shall be designed to provide enough control in the yaw. If this is deemed impossible due to the fuel mass constraint, the directional stability can also be achieved by the placement of a fin. However, this will cause such a drastic change in the design, and will be preferred to be avoided.

The RCS belonged to the final step of the design since it is designed based on the position and size of all the other subsystems. It is for this reason that after every iteration of the design when subsystems are re-sized or re-positioned, the RCS should be redone. Given the current design the thrusters are able to be modified to produce 105 N each, it is therefore very unlikely that another thruster has to be found in future iterations. However, if such high levels of thrust are desired the tank will be too large, thus one might opt to use chemical or bipropellant thrusters due their higher I_{sp}.

12 Recovery System

A Descent and Recovery system is needed to bring the vehicle from a high speed flight regime to a steady state descent needed for the retrieval. Minimal damage to the vehicle is implied in the recovery purpose, and therefore it is needed to determine a method for which the ground impact velocity is the least. In general literature, the definition of recovery is a sequence of events which usually includes, but is not limited to, deceleration, stabilization, steady descent, landing and retrieval. Most if not all of these aspects will be discussed in the following section.

12.1 Trade-Off Summary

In the Midterm Report (Amend et al., 2018b), a trade-off was performed for various recovery and retrieval systems. As a recovery system it was decided to use an aerodynamic descent system, specifically an inflatable parachute. For retrieval system, a Mid-air Recovery System (MaRS) was chosen due to its outstanding cost, mass and reusability characteristics.

12.2 Requirements on Recovery

In Sections 3.2 and 3.4 it became clear that further subsystem requirements need to be derived to fulfill the top user and mission requirements.

- DRS.REQ.01 The recovery system shall provide the vehicle with a terminal velocity of 7.6 m/s.
- DRS.REQ.02 The recovery system shall have oscillations under 1 degree per second to allow for Mid-air Retrieval.
- DRS.REQ.03 The recovery system shall have a mass lower than 35 kg.
- DRS.REQ.04 The recovery system shall have a volume lower than 0.05 m^3.
- DRS.REQ.05 The recovery system shall impose loads on the structure no higher than 68.67 m/s^2 (7g).
- DRS.REQ.06 The recovery system shall allow the vehicle to reach terminal velocity at an altitude higher than 3000 meters.

12.3 Recovery Sequence

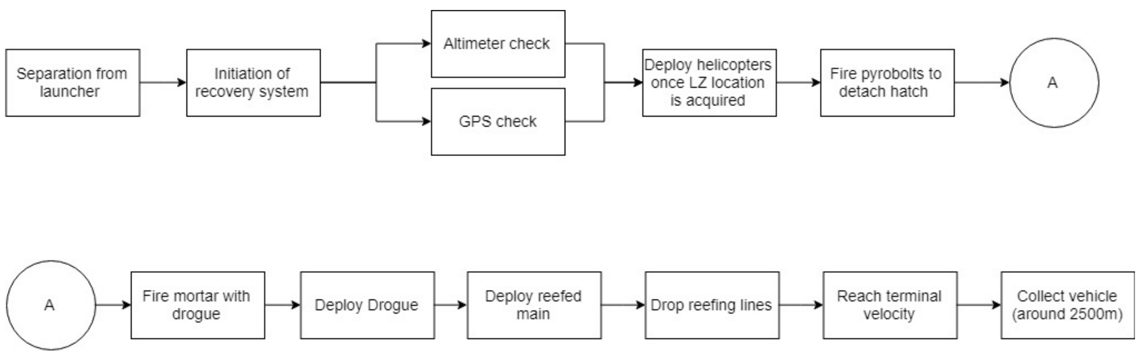

Figure 12.1: Recovery Sequence

12.4 Launch and Initiation

Due to the high acceleration and vibration loads, it is necessary to guarantee that the recovery system will not falsely deploy before the correct time.

To do this, the computers will be kept in a deep sleep state until the system is mechanically initiated, after which they will be able to operate nominally. Computer and sensor initiation will be performed with a mechanical switch and a lanyard. The lanyard will be connected between said mechanical switch and an appendix in the launcher, guaranteeing that the system will be initiated after separation is successful.

12.5 Deployment

To simulate the velocity and acceleration of the parachute-body system, a numerical tool based on non-linear equations of motion in a body frame was developed. These equations include summation of forces and kinematic relations to accurately model the dynamic behaviour of the vehicle, and are summarized in 12.1 and 12.4, as elaborated in Mooij (2017a).

$$m\dot{V} = -(D_p + D_v) + mg \tag{12.1}$$

with

$$D_p = \frac{1}{2}\rho V^2 S_p C_{D_p} \tag{12.2}$$

$$D_v = \frac{1}{2}\rho V^2 S_v C_{D_v} \tag{12.3}$$

and the kinematic equation

$$\dot{h} = -V \tag{12.4}$$

where the subscripts p and v represent the parachute and the vehicle respectively, and where the density ρ is calculated using the International Standard Atmosphere.

A script was written that numerically integrates the equations of motion above. Due to the simplicity of the model, the numerical method in use to solve the non-linear relations is an explicit time-marching Euler method, whose update formula is shown in Equation (12.5).

$$u_{n+1} = u_n + \Delta t f(t_n, u_n) \tag{12.5}$$

After a first run concerning only the main parachute, it became clear that even by minimizing the dynamic pressure at opening, the g-loads would be too high for the structures to support them.

It was then decided that the equations of motion would be solved in various altitude (time) steps. Considering that the free fall part of the trajectory is taken care of by the Guidance, Navigation and Control group, the simulation starts as soon as the drogue parachute opens, at an altitude of 10000 meters.

The simulation had three separate parts: first the drogue would be deployed to slow down the vehicle to an acceptable velocity, then the main parachute would be deployed in a reefed condition to minimize opening loads and finally the reefing lines would be dropped and the system would continue its descent until the steady state condition of 7.6 m/s defined in Section 12.7 would be reached.

The initial conditions of the model would be an altitude of 10000 meters and an initial velocity of 180 m/s. A flight path angle of 90 degrees was assumed for the simplicity of the model, and later confirmed by the terminal area energy management analysis performed by the GNC subsystem.

The model was ran and optimized with the various areas and coefficients found with CATIA and the aerodynamic simulation. The resulting reefing ratio was 0.2, with the reefed parachute deployed at 5000 meters and the reefing lines being dropped at 4000 meters. All the deployments will be coordinated by a dedicated flight computer, with hot redundancy in the sensor input provided by a radar altimeter and the GPS receiver. The graphs below show the velocity and acceleration profiles with respect to time and altitude, as well as showing that a maximum g-load of 5g (49 m/s^2) will be experienced by the vehicle.

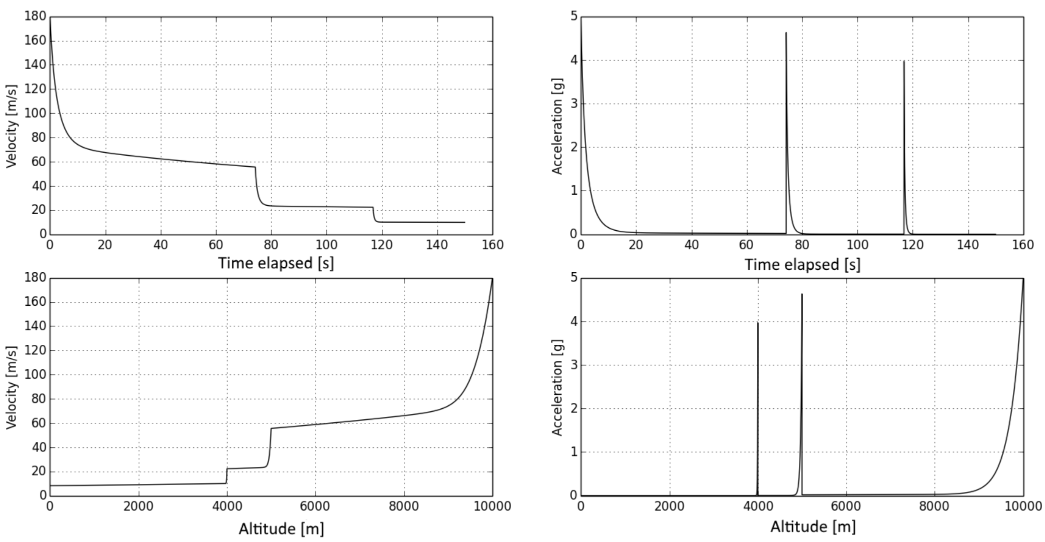

Figure 12.2: Velocity and acceleration profiles wrt. time and altitude

12.5.1 Deployment Device

Whether a pilot chute or mortar is used to deploy the various parachutes, it is necessary to calculate the minimum ejection velocity needed to clear the vehicle. This velocity, defined by Deweese and Schultz (1978), is expressed as follows, and will be used to calculate the pilot chute dimensions or the mortar ejection power and therefore its size.

$$\Delta V_j = \sqrt{2g\big(\bar{q}\frac{(C_D A)_b}{W_b} + \sin\theta_j\big)l_{sl}} \tag{12.6}$$

This results in an ejection velocity of 30 m/s, resulting in a pilot chute size of 1.34 m^2, calculated with a force equilibrium between the parachute weight and the drag generated by the pilot chute. Due to ease of design, however, a mortar supplied by Irvin Aerospace (Berry, 2007) will be chosen with an ejection velocity of 115 fps, a nominal diameter of 12.4 cm and a mass of 11.3 kg. This design was previously commissioned by the US Air Force and used in the F-16 Fighting Falcon, validating its effectiveness.

12.5.2 Model Verification and Validation

This model is based on two units, and they will need to be verified independently. The two units and respective verification procedures are as follows:

- Atmospheric interface unit: this unit provides the density at all altitudes considered. It was validated using an online ISA calculator[1], and it was shown that its results do not deviate more than 1% from the nominal results.
- Dynamics unit: this unit simulates the actual translational motion of the vehicle. The simulation was verified by 0-input tests as well as simulating each opening step independently.

Validation related to the parachute sizing and method was taken from Rossman et al. (2017). Their model was replicated with the given parameters, and the same values were obtained. The sizing therefore can be considered validated.

Validation of the design parameters was also done using the method from Gerundo (2010). The same initial parameters were used in the calculator, and the final result varied no more than 1%. This discrepancy is most likely due to the rounding of the number of gores, and therefore the model is considered to be accurate enough and validated.

Validation of the simulation tool was done using the commerical software Simulink ®[2] from Mathworks . A block diagram was created, as shown on Figure 12.3, and the initial condition as for the python simulation were given. A more simplified simulation was used, in which the drag area (the product of drag coefficient and surface) considered would double from 2 at 10000 meters to 4 at 5000 meters. The result of the validation is shown on Figure 12.4, where the red crosses represent the validation simulation while the continuous line shows the output of the simulation model. In the Simulink structure, the 1-D Lookup Table is the while-loop equivalent where the different drag areas are stored, while the ISA Atmosphere Model is a built in function that returns the density for every given height.

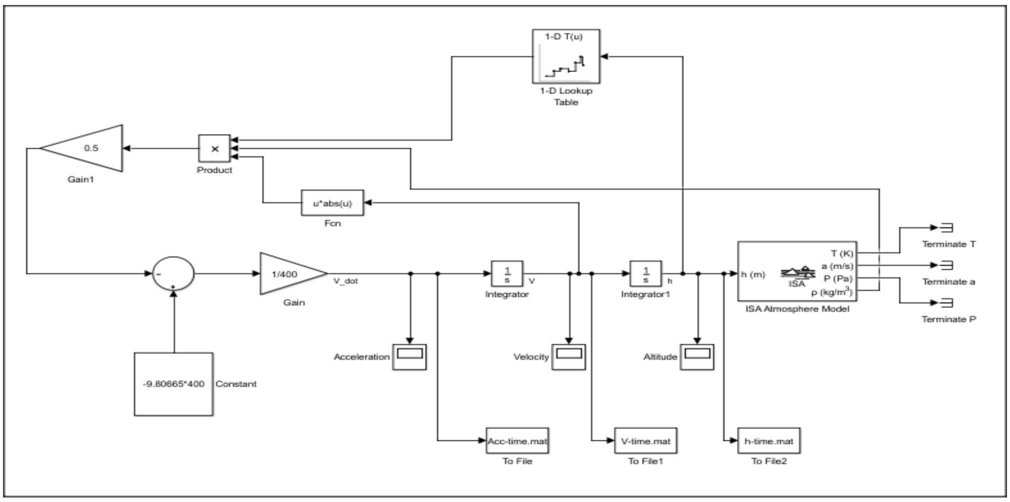

Figure 12.3: Simulink model used for validation

[1] https://www.digitaldutch.com/atmoscalc/, last accessed on 17-06-2018
[2] https://www.mathworks.com/products/simulink.html, last accessed on 17-06-18

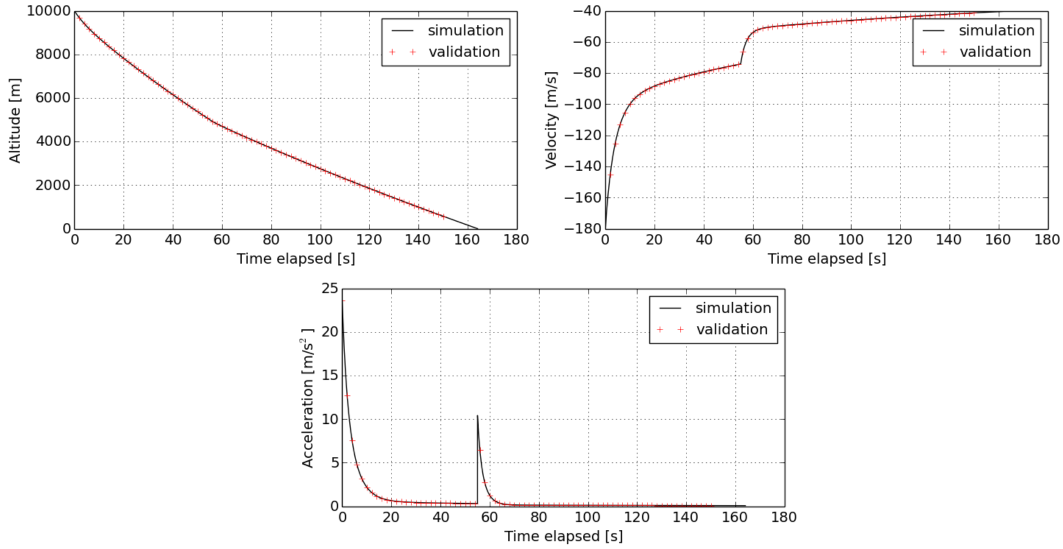

Figure 12.4: Validation data generated with Simulink

12.5.3 Sensitivity Analysis

The model proved to be fairly sensitive, especially with respect to the initial deployment altitude. Simply changing this value by as little of 5%, while keeping reefing ratio and drogue area constant, resulted in g-loads exceeding 5.5g. Similarly, changing the reefing ratio by the same amount leads to over 6g loads. While this is still tolerable by the internal structures, it means that the model is rather dependant on the trajectory simulation to deliver the appropriate initial conditions.

12.6 Recovery and Retrieval

MaRS operation will be terminated by connection with the main parachute, which will collapse apex first and will be reeled inside the recovery aircraft using the so-called "Trapeze Method"(Knacke, 1991); this consists of extensible poles and cables extended behind the aircraft, which will catch the parachute.

To accomplish this, relatively high system stability is necessary. To check the compliance with this this, and to formally meet the requirement set, another simulation was created to simulate a pendulum, with the vehicle as the suspended mass and the parachute canopy as the fulcrum of the motion. The equation of motion used was a non-linear differential equation, shown in Equation (12.7), with a damping coefficient introduced as the drag created by the vehicle, also shown below (Eq. 12.8).

$$\ddot{\phi} = -g/l_{sl} \sin\phi + D\dot{\phi} \tag{12.7}$$

$$D = \frac{1}{2}\rho(C_{D_v}S_v)(\dot{\phi} \cdot l_{sl})^2 \tag{12.8}$$

The simulation was ran over a 300 seconds time with a 5 degrees initial offset angle, and it showed the vehicle damp its oscillations down to ± 0.55 degrees with an angular velocity of 0.081 deg/s.

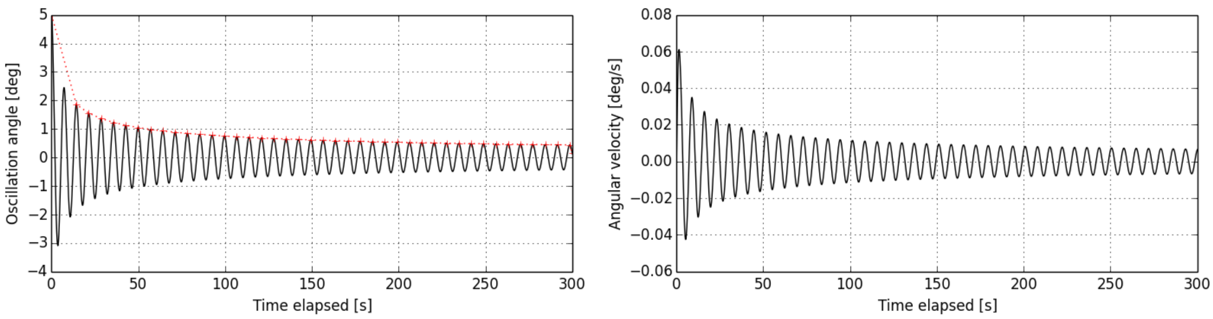

Figure 12.5: Oscillation angle and velocity wrt time

This oscillation is low enough that the model can be considered acceptable for MaRS.

The retrieval, as mentioned, will take place in mid air. Using a simple conservation of energy equation, and assuming that the helicopter after collection will slow down to 77 m/s (from 83 m/s), results in 26 KJ of work being done. Assuming this happens over a distance of 100 meters, the MaRS will experience around 2g of force. Due to the structures being sized for lateral g loads only along the z-axis, it will be necessary to keep this in mind while retrieving the vehicle.

12.7 Parachute Sizing

Using equilibrium of gravity and drag force, and a desired descent velocity of 7.6 m/s, a preliminary canopy sizing of 107.5 meters was found.

To provide accurate information related to mass, volume and power needed, it is necessary to size the actual parachute first. The information in this section was taken from Gerundo (2010) and Deweese and Schultz (1978).

In this calculations, a ringsail parachute was considered for the aerodynamic properties. Its characteristics are a relatively high drag coefficient (~ 0.8) and moderate to good stability.
The nominal diameter of the canopy is given by:

$$D_0 = \sqrt{\frac{4S_0}{\pi}} \tag{12.9}$$

The number of gores being equal to the number of suspension lines (N_{sl}) is

$$N_{\text{gores}} = 0.88D_0 \tag{12.10}$$

with the result rounded to the nearest integer. The length of the suspension lines is then:

$$l_{sl} = 1.15D_0 - 1 \tag{12.11}$$

The number of slots and gore height will not be calculated, as it goes beyond the scope of the project. However the suspension line strength is needed for the final mass budget:

$$F_{sl} = \frac{F}{1.5N_{\text{gores}}} \tag{12.12}$$

and the radial strength

$$F_{rt} = 0.9F_{sl} \tag{12.13}$$

Once these parameters have been estimated, the mass of the parachute can be calculated with the following formula from Knacke (1991). In the code, imperial units are used and then the result is converted into metric.

$$M_p = S_0 w_c + \frac{D_0}{2} N_{gores} w_{rt} \frac{F_{rt}}{1000} + N_{sl} l_{sl} w_{sl} \frac{F_{sl}}{1000} \tag{12.14}$$

where
w_c (Kevlar-281®): 0.105 lb/ft^2
w_{rt} (Kevlar®): 0.0035 lb/ft/1000
w_{sl} (Kevlar®): 0.0035 lb/ft/1000

Assuming a high pressure packing method will be used, it is possible to approximate the volume of the system. Pressure packing combined with suction of entrapped air can result in a packing density of almost 800 kg/m^3 (Knacke, 1991).

Drogue design was limited to its area, which the simulation returned as 5.5 m^2. Due to the mission specific design of drogue parachutes, it was decided that a contractor would be able to generate the needed design parameters. However, a conical ribbon-style parachute is recommended.

The results of the above calculations are summarized in the below table, Table (12.1).

Table 12.1: Main parachute parameters

Item	Nominal Diameter [m]	Number of gores [-]	Length of suspension lines [m]	Suspension line strength [N]	Radial tape strength [N]	Parachute mass [kg]	Volume [m^3]
Value	11.7	28	12.54	93.75	84.375	18.578	0.0232

12.8 Budget and Recommendations

Based on the analysis above, the descent and recovery subsystem budgets are presented in the Table 12.2.

Table 12.2: Descent and recovery subsystem budgets

Component	Volume, m^3	Mass, kg
Main Parachute	0.023	18.58
Drogue Chute	0.001	1.2
Mortar	0.011	11.3

There are various recommendations to be made about the simulation models used. First and foremost, it would be ideal to model the opening shocks not as instantaneous events but as continuous ones. A preliminary model for this was created using the following "fill-time" equation (Eq. 12.15), but it was found to be extremely time consuming to add into the current altitude-based model.

$$t_{fill} = \frac{8D_0}{V} \tag{12.15}$$

Another recommendation would be to model the parachute-vehicle system as two independent solid bodies each with its own mass moment of inertia and physical characteristics. This would provide much deeper insight into the dynamics of the system, elaborating on factors such as non-vertical reentry or the presence of unexpected wind gusts. Lastly, one of the main disadvantages of the parachute design method, is that the equations used are semi-empirical and therefore generated based on real parachute data. The problem with this is that parachutes are usually created on a mission-by-mission basis, something that could possibly hinder the accuracy of the sizing. For this reason, conservative estimates were chosen so that, at worst, the sizing would lead to an overestimation.

13 Structural Model and Design

To support the vehicle shape, provide support for the TPS and to carry all loads that can be experienced during the lifetime of the vehicle, a solid structure is needed. This chapter contains the description of the model used to size and analyze the structure of Hyperion IV.

13.1 Requirements on Structures

The main requirements on the structures subsystem have been defined in Chapter 3. These requirements are listed following.

- **SYS.CR.1**: The vehicle shall withstand any loads imposed on it during the mission.
- **SYS.CR.2** The vehicle shall be designed such to protect the internal subsystems.
- **SYS.CR.3** The vehicle shall be designed to ensure reliability and reusability.
- **SYS.CR.9** The vehicle shall allow for dis-assembly.

From this set of requirements, more specific requirements to the structural subsystem are introduced below.

- **STRC.REQ.01** The maximum von Mises stress in the structure shall not exceed 250 MPa.
- **STRC.REQ.02** The maximum compressive stress shall not exceed 160 MPa.
- **STRC.REQ.03** The cold structure shall allow for accessibility of the interior of the vehicle from the outside.
- **STRC.REQ.04** The cold structure of the vehicle shall have a total mass no higher than 52.0 kg.
- **STRC.REQ.05** The cold structure shall allow interfacing with the Vega LV.
- **STRC.REQ.06** No natural frequency for lateral vibration of the vehicle shall be lower than 15 Hz.
- **STRC.REQ.07** No natural frequency for axial vibration of the vehicle shall be lower than 60 Hz.

13.2 Trade-Off Summary

In the midterm phase, no actual trade-off had been performed on the structural subsystem due to the strict correlation between the vehicle shape, the actual concept of the structure and the choice of material. Since the highest temperature reached at the interface between the windward TPS and the supporting structure is 700 K, as stated in Section 15.4, the material chosen for the structure is grade 5 Titanium (Ti-6Al-4V Annealed). Titanium is an excellent material for high temperature applications, and is currently used in jet engines and high temperature airframes, with excellent properties at high temperature and a comparable density with respect to other metals. The properties of Ti-6Al-4V [1] vary with temperature [2]. A comparison between the material's properties at room temperature and 700 K is provided in Table 13.1.

Table 13.1: Variation of Ti-6Al-4V properties with temperature

Ti-6Al-4V Properties	At 290 K	At 700 K
E [GPa]	113.8	86 29
σ_{yield} [MPa]	880	600
ρ [kg/m^3]	4430	
Thermal expansion coefficient [1/K]	9.1 10^6	

While a structural concept for the vehicle was already proposed in the Midterm phase (Amend et al., 2018b), further analysis proved it to be unsuitable to support the TPS, and with limited volumetric efficiency. A new structural concept has been developed, shown in Figure 13.1. The structural concept features seven longitudinal beams located at the kinks in the core structure. These beams run along the full length of the structure, converging to the base of the nosecone. A total of 11 frames are placed at equal intervals along the vehicle's length, enhancing the overall stiffness of the structure. Not shown in the figure for clarity, is the skin, which ensures the ability to carry torsional loads and provide support for the TPS. The limiting factor for the sizing of the vehicle is its stiffness in the x direction. As explained in Section 13.6, the current dimension of the booms is enough to meet the natural frequency constraints imposed by the launcher, with a margin of 17.9 Hz. Bearing in mind that the vehicle may fly different trajectories to the one presented

[1] http://asm.matweb.com/search/SpecificMaterial.asp?bassnum=mtp641, retrieved 20-06-2018
[2] http://www.kobelco.co.jp/english/titan/files/details.pdf, retrieved 20-06-2018

before, which may impose higher loadings on the structure, the design of the structure is performed by taking a safety margin of 3 for buckling, and a safety margin of 5 for yielding.

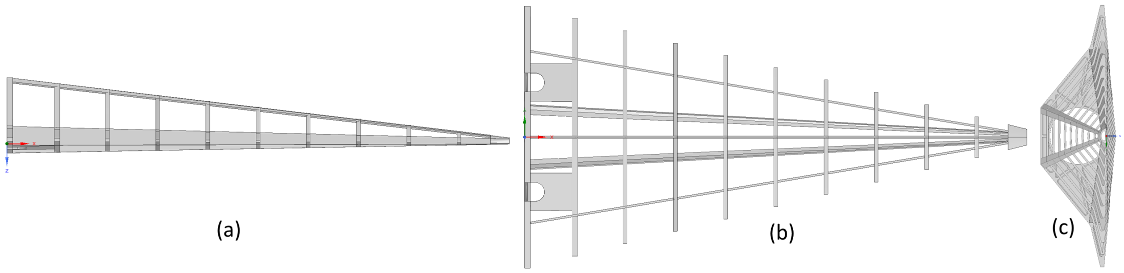

Figure 13.1: Structural concept: side view (a), top view (b) & front view (c)

13.3 Model Theory

The theory presented in Megson (2012) is used as a starting point for developing the structural model. The central simplifying assumption is the division of the continuum structure, with the ability to respond to direct and shear stresses, into discrete elements each capable of carrying only shear or axial stress. This method has the benefit of vastly reducing the dimensionality of the problem, whilst maintaining sufficient accuracy for the present analysis of the structure. Figure 13.2 displays the aforementioned division, with the longerons carrying only axial forces and the shear webs only effective in shear. Subsequent superimposition of the stresses allows for separate analysis of the axial, bending and shearing stresses. The frames, though not strictly involved in the calculation of the stress in the structure, ensure that the the booms do not buckle under compressive loads by decreasing the maximum column length. As such, by preventing buckling they also guarantee the validity of the assumption of an un-deformed cross section, which is necessary for application of the underlying theory.

Table 13.2: Boom location and dimensions

Boom	0&6	1&5	2&4	3
h [m] × w [m]	0.01 × 0.01	0.01 × 0.01	0.01 × 0.01	0.01 × 0.01
A [m^2]	0.0001	0.0001	0.0001	0.0001
z (x = 0) [m]	-0.350	-0.092	+0.009	+0.05
y (x = 0) [m]	± 0.150	± 0.454	± 0.454	0

The structural model includes eleven such frames, placed at constant intervals along the length of the vehicle. Each frame is connected to its neighbors using seven booms (Figure 13.2), placed at the corresponding geometrical locations of the longerons. In between the booms, shear webs are employed to transfer shear loads throughout the structure. The dimensions and positioning of the booms can be found in Table 13.2, while the thickness of the webs is 0.5 mm except for web 2 and 5, which have a thickness of 2 mm.

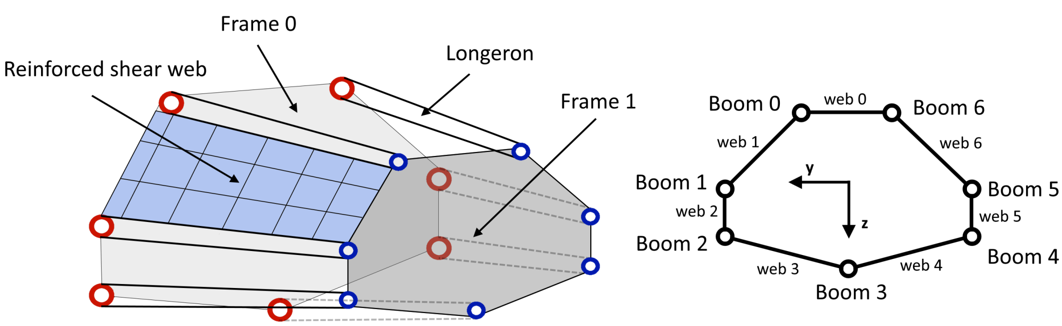

Figure 13.2: Discretization of the structure

13.3.1 Cross Sectional Properties

Each boom in Figure 13.2 is assigned a finite area, and all shear webs have their geometric thicknesses set. It is evident that due to symmetry, the centroid location only needs to be determined in terms of its z coordinate (relative to an arbitrary datum). The shear webs are assumed to have zero direct stress carrying capability, such that the shear stress is constant in between two booms.

As no lateral analysis is performed, only I_{yy} needs to be determined. The shear webs, previously assumed to carry no axial stresses, do not contribute to the second moment of area. It is important to note that the cross-sectional properties vary as a function of lengthwise position, both as a result of the tapered geometry and the taper of the booms themselves.

13.3.2 Axial & Bending Loads

Instead of assuming that under axial loading the stress throughout the cross-section is constant, which only holds true if the booms all have the same area, the compatibility of deformation is used to calculate the stress in each boom. Setting the displacement, $\epsilon_x L$, equal for all booms, the system of equations shown in Equation (13.1) is obtained. Symbols B_n and L_n represent the area and length of the n^{th} boom, respectively.

$$\begin{bmatrix} B_0/L_0 & -B_1/L_1 & 0 & 0 & 0 \\ 0 & 0 & \ddots & \ddots & 0 \\ 0 & 0 & 0 & B_5/L_5 & -B_6/L_6 \\ 1 & 1 & 1 & 1 & 1 \end{bmatrix} \begin{bmatrix} F_{x_0} \\ \vdots \\ F_{x_5} \\ F_{x_6} \end{bmatrix} = \begin{bmatrix} 0 \\ \vdots \\ 0 \\ F_x \end{bmatrix} \tag{13.1}$$

Solving the system of equations yields the x-component of the normal force in the each boom. The stresses resulting from bending moments were computed using Equation (13.2). The term M_y is the internal bending moment about the local y axis, z_n the z-coordinate of the n^{th} boom, and I_{yy} the second moment of area about the y axis.

$$\frac{F_{x_n}}{B_n} = \frac{M_y z_n}{I_{yy}} \tag{13.2}$$

$$\sigma_{n_n} = \frac{F_{n_n}}{B_n} = \frac{F_x}{B_n \frac{dx}{dn}} \tag{13.3}$$

Finally, following the superimposition of axial and bending load contribution to F_x, the definition of the geometry can be used to determine the associated stresses in each boom, as shown in Equation (13.3).

13.3.3 Shearing Loads

In addition to the actual cross-sectional internal shear force as a function of the lengthwise location, the taper of the booms contributes to (or provides relief of) the forces which need to be carried by the shear webs. As illustrated in Figure 13.3, a boom of which the axis is not orthogonal to the shearing plane has a force component in the y and z directions, depending on the local geometry.

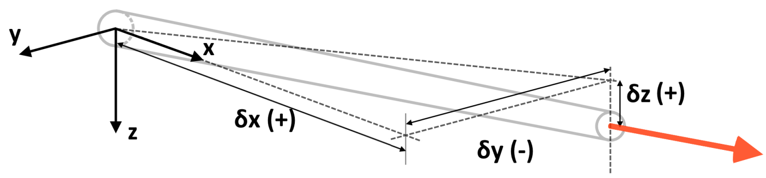

Figure 13.3: Axial force contribution to shear

Equation (13.4) was used to calculate the net contribution of the booms to the cross-sectional shear force, with $S_{z,w}$ the shear force carried by the web, F_{x_n} the x-component of the n^{th} boom's normal force.

$$S_{z,w} = S_z - \sum_{n=0}^{6} F_{x_n} \left(\frac{dz}{dx}\right)_n \tag{13.4}$$

$$q_s = -\frac{S_{z,w}}{I_{yy}} \left(\int_0^s t_D z ds + \sum_{n=0}^{s} B_n z_n \right) \tag{13.5}$$

The calculation of the shear stress is straightforward: the symmetry of both geometry and the loading guarantees a zero shear flow in the upper-most shear web, offering a convenient location to begin the summation (Equation (13.5)). It should be noted that the integral term falls away due to the zero effective direct stress carrying thickness of the webs, t_D. The shear stress is obtained by dividing the local shear flow by the geometrical thickness of the web.

Yielding under shear may be evaluated using the von Mises yield criterion (Megson, 2012), shown for the case corresponding to pure (single plane) shear in Equation (13.6). When the von Mises stress, σ_v is equal or greater than the material yield stress, the material will deform plastically. Under uniaxial loading, as is the case for the booms, the normal stress is equivalent to the von Mises stress.

$$\sigma_v = \sqrt{3}\tau \tag{13.6}$$

13.3.4 Buckling Model

Buckling is a phenomenon caused by asymmetries of the beam with the loading axis, resulting in an unstable development of bending moments. To simplify the analysis, Euler buckling is used, assuming each boom to be double-cantilevered in between frames (with one end allowed to translate). Whether a certain boom has buckled is ascertained using Equation (13.7),

$$P_{crit} = \frac{\pi^2 EI}{(kL)^2} \tag{13.7}$$

where P_{crit} is the load at which buckling begins, I and L are the second moment of area and length of a single boom respectively, and E is the material's Young's modulus. The column effective length factor, k, is used to specify the clamping conditions.

Effectively, the booms in between frames are clamped at one frame, with the adjacent frames restricting moments but not translations. However the shear webs provide support to reduce this translation such that the buckling is delayed. The column effective length factor is set to 0.65, to capture the combined effects of the booms and webs.

13.3.5 Vibration Model

During flight, the vehicle is subject to vibrational loads along with quasi-static loads. A proper analysis of the vehicle's natural frequencies is necessary to verify that each vibrational mode of the vehicle is above the required natural frequency. This becomes critical in the launch phase, where there are strict constraints on the allowed natural frequency of the payload.

The vehicle, including the custom made adapter, is modelled as a Multiple Degrees of Freedom (MDF) multi-mass system. The system is clamped at one end, in correspondence of the attachment between the PLA937VG standard payload adapter and the custom made payload adapter, which is included in the analysis.

Equation (13.8) below shows the equation of motion of the spring-mass system, where $\mathbf{M}$ is a diagonal matrix containing the mass at each frame, distributed according to the configuration layout. $\mathbf{K}$ is the so-called stiffness matrix, which contains the values for the stiffness of the springs.

$$\mathbf{M\ddot{x}} + \mathbf{Kx} = \mathbf{0} \tag{13.8}$$

The elements in the stiffness matrix change depending on the axis along which the vibration is analyzed. In axial direction, the stiffness of the LVA and vehicle booms is calculated using Equations (13.9) and (13.10).

$$k_{LVA_{ax}} = \frac{E_{LVA} A_{LVA}}{h_{LVA}} \tag{13.9}$$

$$k_{n_{ax}} = E_{boom} \frac{\left(\sum_{i=0}^{6} A_i\right)_n}{d_{frame}} \tag{13.10}$$

In lateral vibration analysis, the LVA is modelled with Equation (13.11) both for vibration in y and z direction. The vehicle booms are instead modelled using Equation (13.12) for y axis vibrations and Equation (13.13) for z axis vibrations.

$$k_{LVA_{lat}} = \frac{E_{LVA} I_{LVA}}{h_{LVA}^3} \tag{13.11}$$

$$k_{n_y} = \frac{3E_{boom} I_{yy_n}}{d_{frame}^3} \tag{13.12}$$

$$k_{n_z} = \frac{3E_{boom} I_{zz_n}}{d_{frame}^3} \tag{13.13}$$

Since the total of 11 springs are present in the model, 11 vibrational modes are expected to occur. Applying the modal analysis method (Turteltaub, 2015), the natural frequencies of these modes are the square root of the eigenvalues of the $\tilde{\mathbf{K}}$ matrix, which is derived in Equation (13.14). The eigenvalues are numerically found using the numpy.linalg Python module. The natural frequencies will be checked against the limits imposed by the LV in Section 13.6.

$$\tilde{\mathbf{K}} = \mathbf{M^{-1/2}KM^{-1/2}} \tag{13.14}$$

13.3.6 Thermal Expansion Model

In Section 13.2 the conditions at the interface between the TPS insulation and the cold structure have been defined, with temperatures reaching 700 K at the maximum heating point on the windward side. It is therefore necessary to take into account thermal effect in the design. Table 13.1 mentioned how the properties of Ti-6Al-4V are affected by the temperature at the interface. Thermal expansion phenomena are addressed with a top level estimate on the overall elongation of the vehicle assuming linear thermal expansion of a single beam under uniform heating. This top level estimate outputs an elongation of 9.5mm at the highest structural temperature. While the ceramic nature of the TPS surface does not allow deformation, the insulation which separates the ceramics from the structure is flexible, which would allow for small expansions of the structure. Therefore, based on this assumption, the phenomenon of thermal stresses will not be analyzed further, and the main focus of the structural analysis is on the mechanical loads on the structure. It is, however, highly recommended to perform detailed thermal analysis and design in detail the interface between cold structure and the thermal protection system.

13.3.7 Introduction of Forces

Though the equations and assumptions used to arrive at the stresses have been extensively outlined above, all require as input the cross-sectional internal forces or moments. It is important to distinguish how the structure is supported during flight and during launch or recovery.

Throughout the flight, the vehicle's structural analysis requires splitting the vehicle in two parts: one aft of the CG and the other ahead of it. Both are modeled as a cantilevered beam, with constraints in all degrees of freedom. During recovery and launch the vehicle is effectively cantilevered at the back-frame. Though arguably only the launch vehicle adapter (LVA) is capable of resisting moments, the parachute's bridle is assumed to effectively counteract the moments at the back of the vehicle.

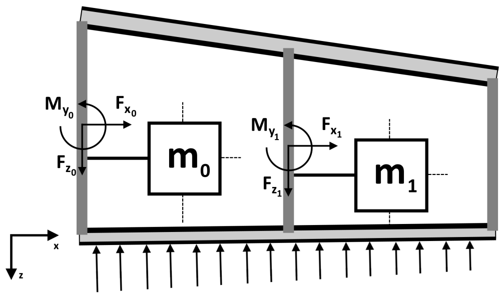

Figure 13.4: Load introduction model

The only forces considered are the distributed pressure loads on the vehicle's exterior surface and the forces caused by the acceleration of masses inside of the vehicle. Viscous forces on the exterior surface are neglected. Furthermore, to simplify the generation of the loading diagrams, all loads are assumed to be introduced at the frames only.

The total mass in between two frames is assumed to be transferred through a cantilever beam to the frame directly behind it (see Figure 13.4), resulting in an equivalent force and moment at the frame centroid.

$$F_{x_n} = \big(-a_x - g_0\sin(\theta)\big)m_n \qquad F_{z_n} = \big(-a_z + g_0\cos(\theta)\big)m_n \tag{13.15}$$

Equation (13.15) was used to calculate the forces the acceleration of mass m_n introduces into its supporting frame. The pitch angle θ and the vehicle's acceleration in body-frame as well as the gravitational acceleration, g_0, are required. The moment introduced at each frame as a result of the misalignment of the forces follows from the location of the mass with respect to the cross-sectional centroid at the frame. Table 13.3 displays the assumed mass attached to each frame. This mass is estimated from the configuration layout of the vehicle and it includes the mass of each spacecraft item in directly in front of the frame, up until the following frame.

Table 13.3: Assumed mass associated to each frame

m_n	m_0	m_1	m_2	m_3	m_4	m_5	m_6	m_7	m_8	m_9	m_{10}
mass [kg]	70	60	50	45	40	35	25	20	16	16	15

The aerodynamic loads are similarly distributed among the frames: to satisfy moment and force equilibrium of the panel, the two frames to which the panel is attached need to each supply a force in the direction of the normal of the panel. The taper of the panel, which in reality results in a line of action which is not exactly at the center of the panel, is neglected in this instance such that both frames supply the same reaction force. The pressure on the vehicle's lower surface is calculated according to the modified Newtonian local inclination method whereas the upper surface is shadowed during nominal operations and is hence not factored into the calculations. If the vehicle were pressurized then the skin in the shadow zone would also experience a net force, depending on the interior and exterior pressure. However, the interior of the vehicle is set to ambient pressure, an assumption justified by the placement of venting holes at the back of the vehicle. Finally, in addition to the shear forces which cause bending moments in conventional beams, the shift in the z-location of the cross-sectional centroid allows axial forces at one frame to induce bending moments at another.

13.3.8 Definition of Load Cases

During launch, the vehicle experiences a maximum acceleration of 7g in the axial direction as well as lateral vibrations around 0.95g (Perez, 2014). The accelerating forces are introduced into the vehicle through a fixed support (the launch vehicle adapter). Moreover, the payload fairing shields the vehicle from aerodynamic loads, such that it is only acceleration of masses which causes stress in the structure.

Throughout the flight a large variety of load conditions are experienced by the vehicle through different combinations of pressure distributions on the surface, the resulting deceleration, and pitch angle. To capture the most critical conditions, the structural model sweeps through the entire trajectory, using the relevant parameters as input to identify the most critical load condition and the associated stresses.

Upon deployment of the parachute, the primary force on the structure is an axial force acting on the rear-most frame into the negative x-direction. Contrary to the load scenario corresponding to the launch, the aerodynamic forces are not switched off during this analysis.

13.4 LVA Sizing and Design

Two standard LVAs are available for the Vega LV: PLA937VG and PLA1194VG, with a diameter at the payload interface of 937 and 1134 mm respectively (Perez, 2014). Given the dimensions of the vehicle, introduced in Sec 6.2, none of these two adapters are suitable for the mission, as their diameter is larger than the height of the vehicle. It is then necessary to size and analyze a custom made adapter. It was chosen to design and analyze an adapter which would connect the PLA937VG payload interface with the back frame of the vehicle. This choice was mainly driven by the availability of data for vibrations load constraints, which are only available for standard payload adapters of the Vega LV.

The modelling of the custom LVA design is a simple truncated cone, loaded in axial direction at launch, with minor quasi-static loads in lateral direction. The custom adapter is analyzed for vibrational loads in Section 13.3.5. The thin walled nature of the custom LVA makes the modelling resource intensive, and it was chosen to prioritize the analysis of the vehicle structure instead. Since the main failure mode can be expected to be buckling under axial compression, sizing of the custom LVA is done through Equation (13.16). The equation shows the classical buckling load of non stiffened cones under axial compression on the basis of shallow shell theory and assuming asymmetric buckling modes (Seide, 1956).

$$P_{cr} = \frac{2\pi E t^2 cos^2\beta}{\sqrt{3\left(1-\nu^2\right)}} \tag{13.16}$$

In the above equation, E is the Young's modulus of the material, t is the thickness of the conical shell, β is the angle between the diagonal side and the horizontal plane, measured towards the inside of the cone, and ν is the Poisson's ratio of the material. The Vega user manual imposes constraints on the material to be used at the connection between the PLA937VG and the connected element, specified to be AL7075. To simplify the design work, this will be the material used for the whole custom adapter. Table 13.4 summarizes the custom LVA dimensions, mass and loading conditions.

Table 13.4: Custom made LVA specifications

h [m]	d_{lower} [m]	d_{upper} [m]	t [m]	P_{cr} [kN]	$P_{estimated}$ [kN]	m_{LVA} [kg]
0.700	0.937	0.300	0.002	5.26 10^8	94.6	7.5

13.5 Model Verification and Validation

Verification and validation procedures are necessary in order to ensure that the model is implemented correctly, and that it captures the physical phenomena with sufficient accuracy. Due to limited resources, validation is not performed, but a strategy is proposed in Section 13.8.

13.5.1 Verification of Launch and Recovery Models

Verification of the launch and recovery model is done through a series of unit and zero input tests. Firstly, setting null accelerations and null aerodynamic forces does result in zero stresses on the structure. Following, setting null accelerations only at launch would result in zero stresses, since at launch no aerodynamic forces are present. For the reentry model, zero stresses are reached when both accelerations and aerodynamic forces are set to zero. If aerodynamic forces only are present during recovery, the vehicle would be in compression, however the shear forces would not be null. This is due to the fact that aerodynamic forces are only modelled for the windward side of the vehicle, which combined with the 90 degrees nose down attitude of the vehicle with a nonzero, yields a shear force in negative z direction.

13.5.2 Validation of Structural Model In-Flight

The flight model is accepted by following the same procedure used to verify the launch and recovery model. To verify if the model is correctly implemented, setting ambient pressure to zero and setting the gravitational acceleration to zero results in null stresses in the extra-atmospheric phase, as expected. Figures 13.5a and 13.5b show the boom stresses at maximum loading condition for null accelerations and null atmospheric forces respectively. With no atmospheric force, the vehicle is only decelerating, and the structure would deform in a upside-down U shape, setting boom 3 in tension. With only aerodynamic loads pointing in negative z direction, the vehicle instead deforms in a U pattern, setting boom 3 in tension. A further verification method is a zero input test, where no accelerations and no atmosphere did lead to zero stresses as expected. The results of these tests provide enough evidence to consider the model as verified.

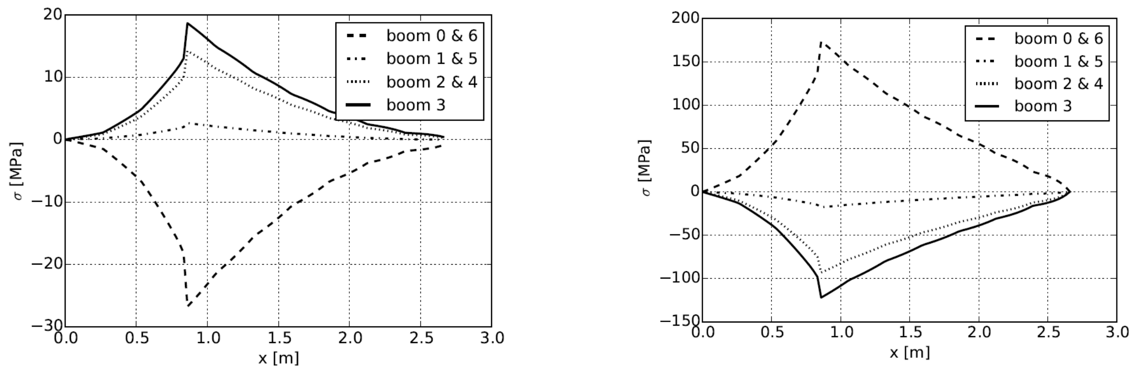

(a) Verification plot for accelerations set to 0

(b) Verification plot for atmospheric forces set to 0

Figure 13.5: Results of the verification process for the flight model concerning the booms

13.5.3 Verification of Vibrational Model

verification of the vibrational model is performed via a zero input test and a unit test. The zero input tests consists in inputting a zero stiffness matrix **K**. The obtained results matched the expectations of null natural frequencies for each vibrational mode. The unit test instead inputs unit mass for each body in the system, and a unit stiffness matrix. This will lead to unit natural frequencies for each vibrational mode. No further verification procedure is needed for the vibrational model.

13.6 Results

Figure 13.6 summarizes the internal load and moment distributions used to assess structural performance during launch, flight and recovery.

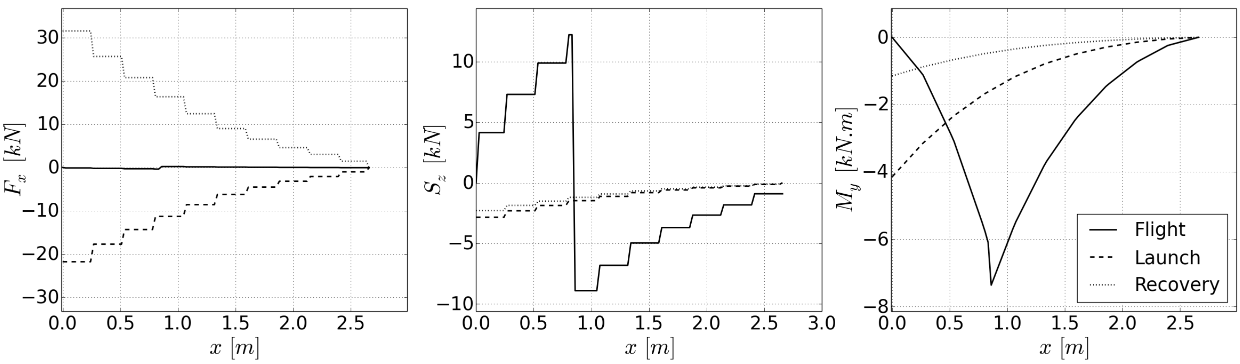

Figure 13.6: Loading diagram of most critical situation during launch, flight and recovery

As a result of the assumption that loads and moments are introduced at only the frames, loads display a stepwise behavior whilst a linear behavior can be witnessed for the internal moment distribution. In the S_z and M_y plot the consequences of the model are evident, with a change in sign of the shear force and a consequent change in slope for the bending moment.

In Figure 13.7, the stresses attained during flight and reentry are shown. In the two left plots, boom 3 is constantly under compression throughout the entire flight, which highlights the fact that acceleration loading is the dominating load case during flights. While it can be argued that during the flight conditions in space no stresses should be present, the loading condition during out of atmosphere flight can be imputable to a constant nonzero ambient pressure in the input file generated by the trajectory simulation. A total of 4 spikes can be visible in the timewise stress plot, indicating the atmospheric skipping phases of the flight.

According to the buckling model introduced in Subsection 13.3.4, the buckling stress is calculated to be 236.61 MPa. The maximum compressive stress in the booms is attained at 86.75 minutes into the flight, at the center of gravity of the vehicle, and it reaches -77.73 MPa, which is close to being half the value of the buckling failure. This is in line with the design safety factor used, which has a value of 3. The highest tensile stress is 112.61 MPa, which is well below the yield failure stress presented in 13.1. When looking at the webs, the maximum von Mises stress is attained at 70.32 MPa.

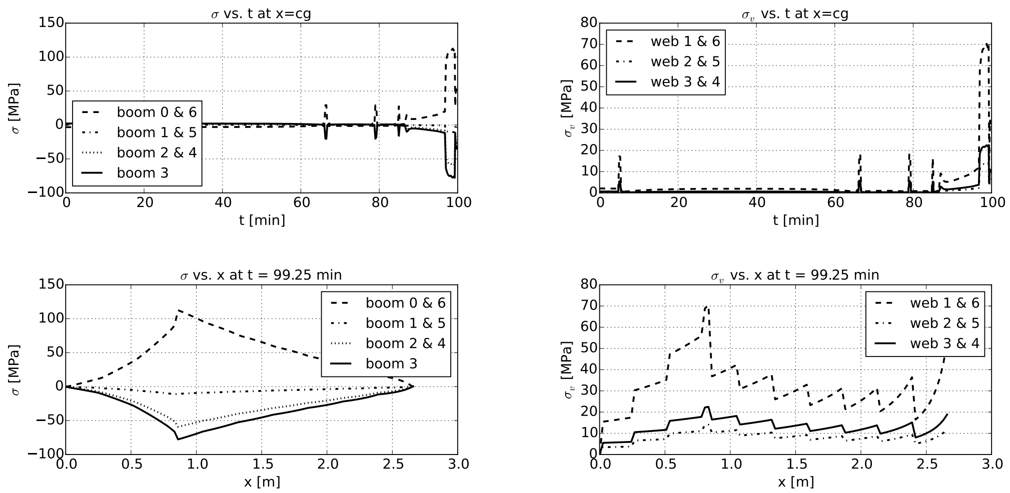

Figure 13.7: Results for structural model in flight condition

Figure 13.8 shows the lengthwise stress distribution at launch and at parachute deployment. At launch, all booms, except for the booms 0 and 6, are loaded in compression. This is expected, since only booms 0 and 6 are located above the centroid of the cross-section, and thus the misalignment between the launcher force vector and the centroid location generates a moment, which is the dominating load on the upper booms.

The loading gradually decreases with the distance from the back frame, reaching 0 stress at Frame 11. Steps present at each frame location are mainly due to the acceleration of the masses located at each frame. At those points, the loads are introduced, causing a small step in the force diagram, thus reflecting in the stress diagram. Looking at recovery, all booms are loaded in tension, as expected. Steps are also present.

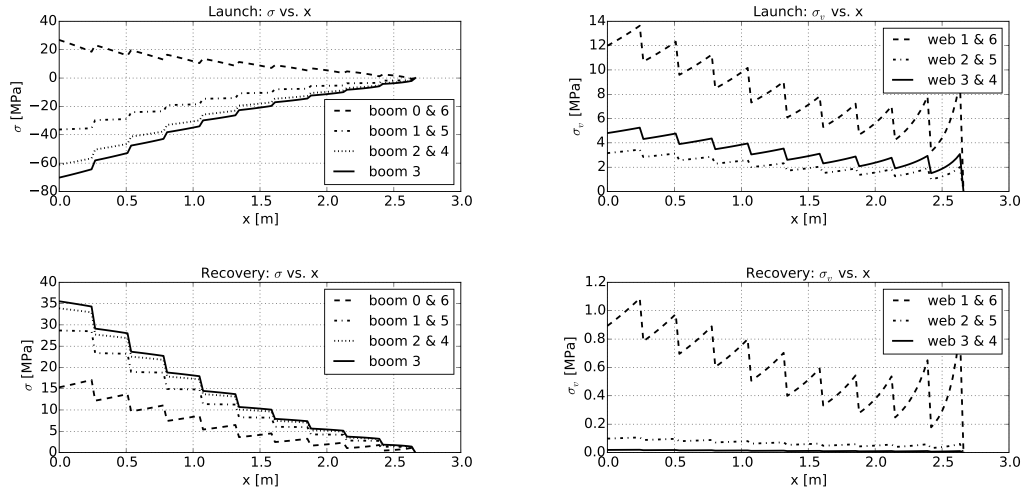

Figure 13.8: Results for structural model in launch and recovery conditions

After analyzing the stresses on the structures, results from the vibrational model introduced in Subsection 13.3.5 are presented in Table 13.5. It shows the natural frequency of each vibrational mode along the three vehicle axes.

Mode	Limit	1	2	3	4	5	6	7	8	9	10	11
ω_x	60	1282.4	1070.1	897.1	788.4	702.3	621.7	538.6	**77.9**	200.9	317.2	434.7
ω_y	15	641.2	558.8	501.0	442.4	377.3	311.9	245.4	183.4	128.7	**27.5**	73.4
ω_z	15	1451.4	1264.7	1133.8	1000.7	853.0	704.8	553.9	412.9	287.8	**28.9**	161.9

Table 13.5: Natural frequencies for undamped free vibrations at launch conditions

The lowest natural frequencies do remain above the lower limit imposed by launcher constraints, that are mentioned in the second column. The vehicle will therefore not resonate with the LV, and is deemed safe for launch conditions. While the two lowest lateral modes are mostly influenced by the dimensioning of the adapter, the dimension of the booms greatly impacts the lowest mode in axial direction. For this reason, stiffness is to be considered the limiting factor of the structural design, as decreasing the boom cross sectional area reduces the value of the natural frequency of the lowest axial mode.

13.7 Sensitivity Analysis

To verify the robustness of the structural model, a sensitivity analysis is required.

13.7.1 Buckling Failure Sensitivity Analysis

In Table 13.6, buckling stresses and buckling margins corresponding to the different assumptions on the boundary conditions mentioned are shown. The buckling margin is to be considered as the margin between actual stress in the booms and buckling stress, expressed in percentage of the buckling stress.

Table 13.6: Buckling stress variation for different column effective length

Design value of k [-]	0.65	0.80	1.0	1.2
Buckling critical stress [MPa]	236.61	156.19	99.96	69.42
Buckling margin [%]	67.14	50.23	22.24	-11.96

Only the three lowest values of k were analyzed. It is shown that a value higher than 1.1 will cause the booms to buckle in compression. The sensitivity analysis of the buckling model shows that if the underlying assumption made for the value of the column effective length should prove to be untrue, the vehicle would likely fail.

13.7.2 Flight Loads Sensitivity Analysis

The sensitivity analysis performed on the trajectory introduces uncertainties in the loads experienced by the airframe through the flight. A small deviation from nominal launcher performance could result to increased deceleration upon reentry, and could increase the aerodynamic loads. To analyze this type of occurrence, an increase of 30%, 50% and 100% in the accelerations sustained by the vehicle at all times during flight will be applied. The aerodynamic loads however will remain unscaled. This type of assumption however does not account the coupling of aerodynamic forces and accelerations, which are strictly correlated by the trajectory followed by the vehicle. Nevertheless, this assumption is valid enough to analyze the vehicle structural response to increased loads. The results of this analysis are summarized in Table 13.7.

Table 13.7: Maximum stresses in the structure for increased accelerations during flight.

	Nominal condition	30%	50%	100%	σ_{yield}
max σ tensile in booms	112.61	153.68	181.07	249.54	600.0
max σ compressive in booms	77.73	106.14	125.07	172.41	236.6
max σ_v in webs	70.32	96.04	113.19	156.06	600.0

The calculated stresses never exceed the yield limit, nor the buckling limit in compression. This highlights the importance of the safety factors applied in the sizing of the structure, which account for the uncertainties correlated to the trajectory of the vehicle.

13.8 Budget & Recommendations

The cold structure only impacts the mass budget of the vehicle. In the midterm report, the structural subsystem was assigned a budget of 52 kg. The mass of the structural subsystem has been modelled in CATIA, amounting to a total mass of 51.8 kg. A detailed breakdown of the subsystem mass is provided in Table 13.8.

Table 13.8: Detailed mass budget for the structural subsystem.

Element	Mass [kg]	Element	Mass [kg]	Element	Mass [kg]
Frame 0	12.337	Frame 6	1.149	Boom 3	1.112
Frame 1	3.846	Frame 7	0.931	Boom 4&5	3.785
Frame 2	2.566	Frame 8	0.653	Boom 0&6	2.224
Frame 3	2.272	Frame 9	0.391	Skin	9.262
Frame 4	1.710	Frame 10	0.935	**Budgeted**	52.000
Frame 5	1.610	Boom 1&2	3.785	**Total**	51.801

For future phases, validation of the model shall be performed. This can be done by analyzing the model with a commercial software using FEM, or by application of the same model to structural concepts with results available in literature. The first method would be the most accurate, however it would be too intensive, both time wise and from a computational point of view. Due to time constraints, validation by means of a FEM software will not be performed. It is however highly recommended to perform this type of validation in the beginning of the detailed design phase. The second proposed method is not as accurate as the first, but it can provide a good indication whether the model chosen does indeed reproduce reality to a certain degree of accuracy. However, while being less computationally intensive with respect to FEM, it would require to remodel the whole structure to the case presented in literature. It is therefore proposed to perform this analysis in the next phase. Furthermore, a more detailed analysis of the thermal stresses induced in the structure shall be performed in the next phase, to properly validate the assumption that the low thermal expansion coefficient does not induce relevant thermal stresses.

The next chapter will cover the aerothermodynamic model, used to determine the hearing and temperatures on the surface of the vehicle.

14 Aerothermodynamic Model

An aerothermodynamic model was developed such that a prediction of the temperatures on the vehicle surfaces could be performed. This was necessary both prior to the trade-off to set the minimum temperature that the material had to withstand as well as later during the development process to iterate the temperatures according to the new trajectories and to estimate the required amount of coolant to prevent overheating. Firstly, the theory of the model is presented. Secondly, verification and validation activities are performed. Thirdly, the results of the model are discussed.

14.1 Model Theory

The prediction of wall temperatures of the vehicle is a crucial step to ensure that the heat shield materials can withstand the thermal environment.

Firstly, the model computes the heat flux at the stagnation point, using the freestream conditions and the geometry of the nose. Since this is the most crucial step and has to be thus performed with high reliability, two separate models are used for the heat flux prediction and compared. The first model is a model proposed by Scott et al. (1985):

$$q_{Scott} = \frac{18300\,\rho^{0.5}}{\sqrt{R_{nose}}}\left[\frac{u}{10000}\right]^{3.05} \tag{14.1}$$

and the second by Detra et al. (1957):

$$q_{Detra} = \frac{11030\,\rho^{0.5}}{\sqrt{R_{nose}}\,\rho_0^{0.5}}\left[\frac{u}{V_c}\right]^{3.15} \tag{14.2}$$

In the equations above, R_{nose} is the nose radius, ρ and ρ_0 the freestream and reference (sea level) densities respectively, u the vehicle velocity and V_c a reference circular orbit velocity. According to Bertin (1994), the fluxes were then converted to 3D fluxed by multiplication by $\sqrt{2}$ and by a term of $\sqrt{(1+K)/2}$ in case of asymmetric geometries, where K is the ratio of the nose radii in the two axes.

During the trajectory, based on the angle of attack, two types of shocks can be present; a detached shock for high angles of attack and an oblique shock for small angles of attack. Both of them should be analyzed to impose thermal requirements on the material.

14.1.1 Detached Shock Predictions

From Tauber and Meneses (1986), using the stagnation point heat flux, the heat flux over the rest of the surface can be derived in the case of a detached shock. The heat flux at the wall is computed with:

$$q_w = \rho^n\,u^m\,C \tag{14.3}$$

where the constants n, m and C depend on the type of flow, u is the velocity and ρ the density. The equations for the laminar and turbulent flow modes for planes at an angle of θ with x the distance from the stagnation point are as follows, first for the laminar flow, with $m = 3.2$, $n = 0.5$:

$$C = 2.53 \cdot 10^{-9}\,\frac{sin(\theta)}{\sqrt{x}}\left[1 - \frac{h_{w,current}}{H_{t,current}}\right] \tag{14.4}$$

in which $h_{w,current}$ is the wall enthalpy and $H_{t,current}$ is the total enthalpy:

$$h_{w,current} = c_p\,T_{w,current} \tag{14.5}$$

where $T_{w,current}$ is the wall temperature. The total enthalpy is a property of the flow, and with u_θ being the component of the velocity in direction of the wall, the total enthalpy can be approximated as:

$$H_{t,current} = 0.5\,u_\theta^2 \tag{14.6}$$

Proceeding with the same definitions further through the analysis, for a turbulent flow at speeds below 4 km/s, the coefficients can be determined as follows, with $m = 3.37$ and $n = 0.8$:

$$C = 3.89 \cdot 10^{-8}\,sin^{1.6}\theta\,cos^{1.78}\theta\,\frac{T_{w,current}}{556}^{-1/4}\,x^{-1/5}\left[1 - 1.11\,\frac{h_{w,current}}{H_{t,current}}\right] \tag{14.7}$$

While in case of speeds higher than 4 km/s, the following relations hold, with $m = 3.7$ and n of 0.8:

$$C = 2.2 \cdot 10^{-9}\, sin^{1.6}\theta\, cos^{2.08}\theta\, x^{-1/5} \left[1 - 1.11\, \frac{h_{w,current}}{H_{t,current}}\right] \tag{14.8}$$

From the local flux at the wall, finally, the wall equilibrium temperature can be derived. This is not a straightforward process. In fact, since wall temperature stems from flux equilibrium, which includes the radiative flux (dependent on the wall temperature), iterative process has to be used to reach convergence. Thus, at first a cold wall with negligible enthalpy is assumed, giving rise to:

$$T_{w,current} = \left[\frac{(q_w - q_{cool})}{\sigma\epsilon}\right]^{1/4} \tag{14.9}$$

Where q_{cool} is a term added in case a cooling mechanism with a known heat flux decrease is included in the design. From this temperature, the wall enthalpy is estimated using $h_{w,current} = T_{w,current}\, c_p$. The new enthalpy is inserted for a new estimation of the actual wall temperature, as seen below.

$$T_{w,current} = \left[(q_w - q_{cool})\left[1 - \frac{h_{w,current}}{H_{t,current}}\right]\frac{1}{\sigma\epsilon}\right]^{1/4} \tag{14.10}$$

The process is repeated until convergence within a tolerance of 1 K is reached. In case the surface can radiate in two directions (outwards and inwards, if a cavity from inside of the TPS is used for enhanced radiative cooling), the radiative flux is double the original one.

The question arises regarding which model from the two (turbulent or laminar) shall be used. While transition of hypersonic boundary layer is not thouroughly understood, an estimation method for the transition Reynolds number, Re_T, as a function of the freestream Mach number, M, was defined by Bowcutt and Anderson (1987). The relation is as stated below:

$$Re_T = 10^{6.421\ \exp\left(1.209\, 10^{-5}\ M^{2.641}\right)} \tag{14.11}$$

The Reynolds number is then solved for at every point of computation, and the mode of the flow at that wall is determined based on whether it is higher or lower compared to Re_T.

However, the above mentioned results hold at high angles of attack only. If the angle of attack decreases and the shock becomes oblique, the wall temperature has to be computed using an estimation of the Stanton number.

14.1.2 Oblique Shock Predictions

In the case an oblique shock is present, according to Dittert et al. (2015), the wall temperature can be computed using the following radiative flux equilibrium equation:

$$\epsilon\sigma T_w^4 = St_\infty u_\infty \rho_\infty c_{p_\infty}(T_r - T_w) \tag{14.12}$$

in which the freestream Stanton number, St_∞, can be approximated by:

$$St_\infty = 0.332 Pr^{-2/3} Re^{-1/2} \tag{14.13}$$

for laminar flow, where Pr is the Prandtl number, assumed to be 0.71, Re is the Reynolds number, and:

$$St_\infty = 0.176(\log_{10} Re)^{-2.45} \tag{14.14}$$

for turbulent flow. The recovery temperature, T_r is given by:

$$T_r = T_\infty\left[1 + r(M_\infty)^2\frac{\gamma - 1}{2}\right] \tag{14.15}$$

with the recovery factor r being defined separately for laminar and turbulent flow, $r = Pr^{\frac{1}{2}}$ and $r = Pr^{\frac{1}{3}}$ respectively. Iteration until a difference of 1 K was then applied to find the temperature of the wall.

Due to time constraints, this temperature was only evaluated independently of the streamwise coordinate. The temperatures resulting from the detached shock and oblique shock assumptions near the stagnation point were compared at the highest stagnation point heat flux condition, and this temperature was taken as the worst case scenario for the design of the material. Since the oblique shock is partially attached to the body, it was expected that these temperatures will be higher compared to the detached shock predictions.

14.1.3 Leading Edge and Body Flap Adjustments

To predict the temperature on the leading edges, the approach of Kumar and Mahulikar (2016) was adopted, where the heat flux is proportional not to V_∞^3 but to $V_{\Lambda,\infty}^3 = [V_\infty \cos(\Lambda)]^3$ in which Λ is the sweep angle of the wings, leading to:

$$q_{sp,\Lambda} = h_{sp}(T_r - T_w) \tag{14.16}$$

in which h_{sp} is the heat transfer rate as a function of the freestream conditions and $V_{\Lambda,\infty}$. The recovery temperature for swept back leading edges can be computed as follows:

$$T_{r,\Lambda} = T_\infty \Big[1 + r[aV\sin{(\Lambda)}]^2 \frac{\gamma - 1}{2}\Big] \tag{14.17}$$

The recovery factor r depends on the nature of the flow. As mentioned in the previous section, it is either $Pr^{\frac{1}{2}}$ in case of laminar boundary layer or $Pr^{\frac{1}{3}}$ for turbulent boundary layer. Thus, the transition Reynolds number equation was again used. The variable a is the speed of sound and γ the ratio of the specific heats.

As far as the temperature distribution on the body is concerned, it was modelled as a separate plate with an additional body flap deflection angle with respect to the main vehicle:

$$\theta_{total} = \alpha_{vehicle} + \theta_{flap} \tag{14.18}$$

using the same model as described for the rest of the heat shield. The required body flap deflection, θ_{flap} and angle of attack, α combinations were derived from the trajectory. The initial body flap heat flux was adjusted down to the expected heat flux at the given longitudinal position on the vehicle, and then recomputed for the new total deflection angle.

14.1.4 Inclusion of Transpiration Cooling Effects

It was important to include the effect of cooling on the wall temperature, with the design shown in Chapter 16. The effects of transpiration cooling are, unlike film cooling, not well defined and cannot be computed using the convective properties and pipe geometry. Thus, wind tunnel measured data were interpolated and used for the estimation of the resultant temperature. The experiment closest to the current design of a cooling system for Hyperion IV is shown in Sudmeijer et al. (2007b), as it holds for small nose radii, and as it was performed at conditions similar to what is expected during the Hyperion IV mission.

Since the measurement points were not specified, to perform the interpolation of the temperature drop as a function of the distance from the tip, an equivalent CATIA model of the sample was matched with the original picture from the paper. With this, it was possible to estimate the measurement locations.

Using the estimated measurement locations, a quadratic model was developed to match the temperature data. It should be noted that once the nose tip reached thermal equilibrium, the entire tip reached the boiling point of water at approximately 290 K.

According to Sudmeijer et al. (2007b), a simple estimation of the required mass flow is by considering the latent heat of the coolant l and the stagnation point heat flux. Thus, to estimate the total amount of coolant needed for such a cooling performance, the following equation was used:

$$\dot{m} = \frac{\dot{q}\, A_{nose}}{l} \tag{14.19}$$

This cooling model was thus implemented in the code. The code would thus output temperature drop as a function of streamwise position and the required water mass flow to create such a temperature drop. To estimate the required mass flow of other gasses, such as Helium used for the cooling while the dynamic pressure is insufficient to prevent water from solidifying, scaling for the current design was used based on the mass flow of the water and based on the mass flow of Helium from the paper.

14.1.5 Upper Wall Temperature Estimation

For the upper walls, the estimations were much more challenging to generate since semi-empirical models are unreliable due to the large variations in the upper surface geometry. Thus, for an estimation of the upper wall temperatures, comparison to legacy missions was carried on. From Figure 14.4, it can be seen that temperatures on the upper surface reach from 150 up to 500 °C, which translates to 770 K, excluding leading edges. The lower surface temperatures of Hyperion IV are 1.25 times higher than those of Buran. Using this scale to adjust the temperatures at the top, 1000 K is derived as a requirement for the upper surface. Safety factor for these values shall be applied due to large uncertainties in the estimation method.

14.2 Model Verification and Validation

The code was made in two separate parts; the stagnation point heat flux estimation for the nose and leading edges, and the heat flux and temperature distribution estimation. Both parts were validated separately.

14.2.1 Stagnation Point Heat Flux

The stagnation point heat flux is determined using two independent models, which were validated separately in Scott et al. (1985) and Detra et al. (1957). Both values are calculated and compared, and in case of a large difference between them (> 15%), a warning message indicating that the results have a low reliability is generated. This has, however, not happened during any of the runs (besides extreme conditions at the edge of the atmosphere), and the error typically is smaller than 10 %.

14.2.2 Heat Flux and Temperature Distributions

Firstly, the detached shock model is validated using the data from Space Shuttle and Buran. The validation of this model was the most extensive since it was this model that was used to predict the temperature distribution over the lower plate. Afterwards, the oblique shock model is accepted. This model is significant since the maximum temperatures that the material has to withstand will likely be derived from the oblique shock assumptions.

Detached Shock Model

For the validation of the model, it was decided to use the Space Shuttle as a reference mission, since a lot of data is available. During the STS-1 flight, heat flux was measured and temperatures were obtained over the wings of Space Shuttle at different locations. The corresponding heat flux and temperature data is shown in Figures 14.1 and 14.2. In the graphs of the surface temperatures, the dashed line corresponds to the laminar flow and solid line to the turbulent flow. In both figures, the leftmost of the graphs refers to the measurements towards the leading edge of the wing. More data on the location of these points can be found in W.L.Ko et al. (1986).

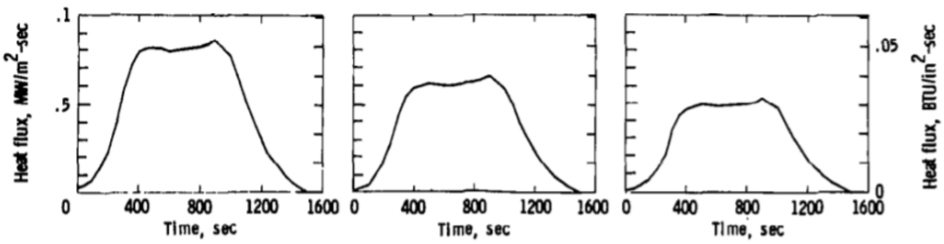

Figure 14.1: The expected surface heatflux on the wing box of Space Shuttle during its trajectory (W.L.Ko et al. (1986))

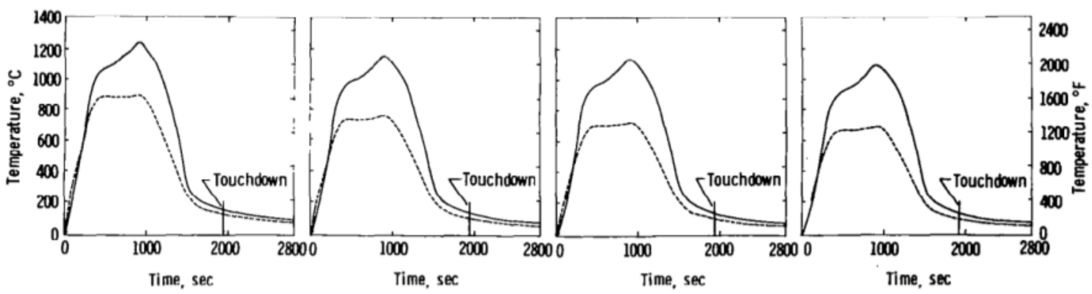

Figure 14.2: The expected surface temperature on the wing box of Space Shuttle during its trajectory, dashed for laminar flow and solid assuming turbulent flow (W.L.Ko et al. (1986))

The most critical part of the trajectory from the thermal perspective was taken into account, which is 1000 seconds into the flight. From the data, it is apparent that for a turbulent boundary layer, the surface temperature is approximately 1570 K (1300 °C) and for a laminar flow, it is 1130 K (850 °C). The heat flux is approximately 0.09 MW/m^2.

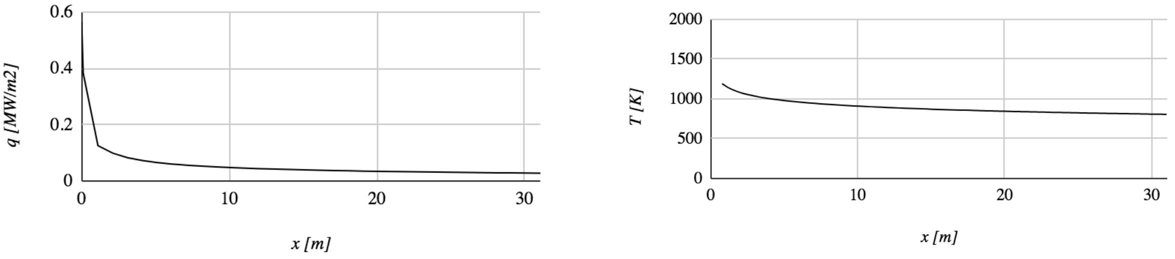

(a) The heatflux predicted by the model at 1000 seconds into the trajectory

(b) The surface temperature predicted by the model at 1000 seconds into the trajectory

Figure 14.3: Results for the Space Shuttle by the developed software for validation purposes

Angle of attack, altitude, Mach number at the given conditions, along with the emissivity, dimensions and wall temperature history were taken from W.L.Ko et al. (1986). Laminar analysis was run for validation, due to the higher confidence the authors of the paper had in those, and this model was used in the simulations of Hyperion IV. As it can be seen in Figures 14.3a and 14.3b, the model temperature at 25 meters (approximately the distance of where the temperature was taken in the Space Shuttle experiment) is 1180 K and the model heat flux is 0.10 MW/m^2. The respective errors are thus 11 % in heat flux and 5 % in temperature, which is deemed reasonbly accurate for such a simple model. Both temperature and heat flux were overestimated, which is beneficial for inherent safety of the design.

Having confidence in the stagnation point estimates, a second validation was performed using data from Buran. Using information about its trajectory, dimensions, and the temperature distribution from the Buran shuttle [1], the temperature at the stagnation point at the nose was matched such that the approximate flight condition of Figure 14.4 could be determined.

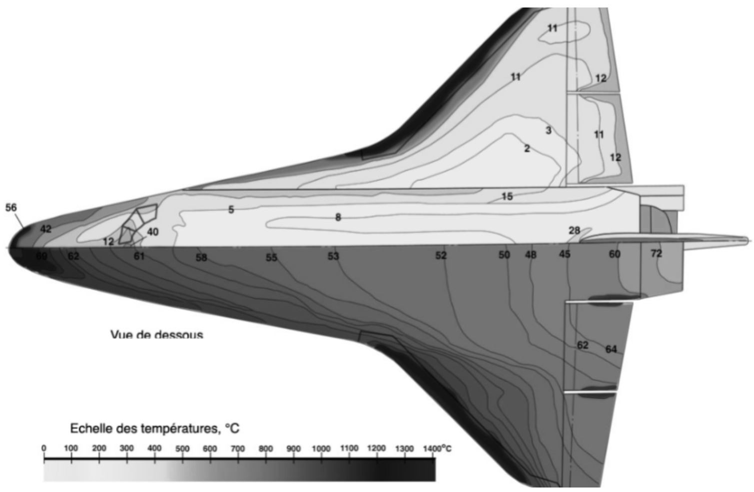

Figure 14.4: Upper and lower surface temperature distribution of the Buran vehicle

Matching the stagnation point temperature and knowing the flight conditions, the model temperature distribution was derived, as can be seen in the Figure 14.5. Emissivity was taken to be the same the one as in case of Space Shuttle (0.85) and a laminar flow regime was assumed.

The model temperature at the end of the vehicle is 800.9 K, corresponding to 528 degrees Celsius. This matched with the prediction for Buran, even though due to the scale, an exact number is hard to obtain. It is thus shown that the model agrees with predictions.

Oblique Shock Model

The acceptance of the oblique shock model was easier to perform since the temperature distribution was not solved for. The model was validated by using simulation data of SHEFEX III from Dittert et al. (2015),

[1] "http://www.buran-energia.com" Buran data. Last accessed 15/06/2018

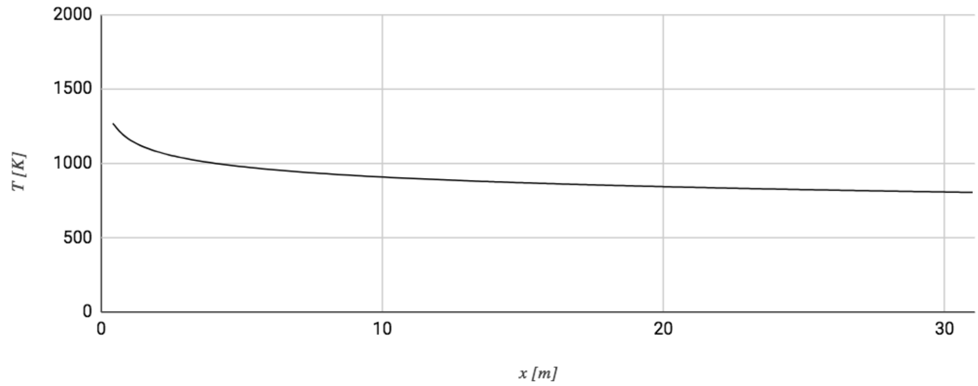

Figure 14.5: Simulated temperature distribution along the lower surface of Buran for validation purposes

where the method is used to predict worst case scenario oblique shock heat fluxes along the trajectory. For the same stagnation point heat flux, the oblique shock heat flux was compared with the paper, resulting in errors below 10%. This error is likely due to imprecise extrapolation and estimation of the freestream conditions used while attempting to reproduce the SHEFEX III trajectory in the code.

Leading Edge Model

The leading edge temperature model was validated using the results of Kumar and Mahulikar (2016). The freestream conditions and geometry were reproduced by the code and compared. Four wing sweep angles (40, 50, 50 and 70 degrees) were evaluated in total. The same trend of decreasing of the heat flux with increasing sweep back angle was found with the results matching quantitatively within 15%, which was the worst case error for 70 degrees of wing sweep. Most of the errors likely again resulted from uncertainties in the freestream conditions. Since all of the errors were below 15%, the model was accepted.

14.3 Code Limitations and Recommendations

There are several limitations to the above mentioned models. One of the main disadvantage is that they are semi-empirical and thus developed to fit real flight data, typically derived for blunt bodies and in general for bodies with a different geometry. The constants used to predict aerodynamic coefficients might not be accurate for Hyperion IV, and can be only verified after either wind tunnel testing or the actual flight. For example, it is expected that the injection of water will contaminate the boundary layer and might lead to transition sooner than expected. Such factors cannot be modelled using simple semi-empirical formulas.

Moreover, due to the difficulty in predicting the behaviour of the active cooling system, only a very simple interpolation formula was used to show the effects of the water transpiration on the surface temperature. Due to the fact that more advanced models could not be developed, temperatures estimations used for the design had to be very conservative, leading to an overdesign.

As was already mentioned, it is challenging to predict whether the shock is oblique or fully detached without CFD simulations. Designing for the upper temperature estimate resulting from the oblique shock relations will thus likely lead to additional overdesign, and thus more advanced numerical methods should be used to determine the aerothermodynamic environment around the vehicle.

Finally, catalycity and other surface chemistry was not taken into account due to time constraints. However, since the selected ceramic materials are almost completely non-cataltic according to Chapter 15, this assumption should not have a major effect on the results.

14.4 Temperature Estimation

After the materials were selected for the nose tip, TUFROC for heat shield and SPFI for the rest of the skin as described in Chapter 15), the emissivities were inputted into the code described above. The highest estimated temperatures during the trajectory at different Mach numbers were extracted and were plotted on the left side of Figure 14.6, with active cooling neglected. It can be seen that without active cooling, the nose temperature would reach 3000 K. This is above the design temperature of C/C-SiC, and thus active cooling has to be implemented. This prediction is based on the stagnation point heat flux equilibrium calculation of the aerothermodynamic model.

Using the leading edge part of the model, it was found that even at the worst case scenario heat flux condition, the leading edges stay at 1725 K, which is below the design temperature of TUFROC.

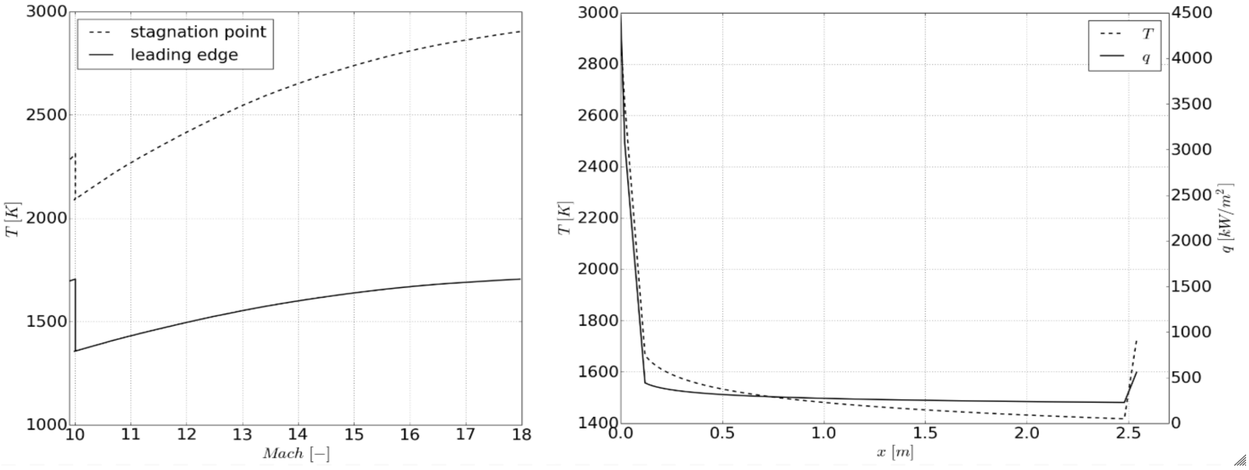

Figure 14.6: Wall temperature distributions (only single surface radiative cooling included) at different flight conditions including the nose cap temperatures and the temperatures of the body flap

For the maximum heat condition, the heat flux and temperature distributions along the lower surface are shown on the right side of Figure 14.6. As for the distribution along the lower heat shield, it is apparent that at the maximum heat flux condition, the maximum temperatures of the heat shield are below 1600 K assuming detached shock and no active cooling effects. For the highest heat flux condition, it was found that the temperature difference between the oblique and detached shock assumptions was approximately 500 K, with this difference changing along the trajectory since the models are proportional to the freestream conditions raised to different exponents. Since the angle of attack is kept relatively high, especially during the thermally most critical part of the trajectory (Mach 17), it is not expected that the shock will be fully attached and reach the oblique shock model temperatures. However, even if that happened, active cooling would still be responsible for decreasing the temperatures to at least a certain extent. Thus, an estimate for the maximum temperatures on the heat shield even in case of shock attachment is 1800 K- 1900 K.

14.5 Sensitivity Analysis

The main concern regarding the temperature analysis is the possible disturbance of the stagnation point heat flux. The maximum temperature from the stagnation point heat flux based on the nominal trajectory of 2900 K. If the maximum heat flux is increased by 10%, the maximum temperature increases by approximately 50 K, which stems directly from its dependence on the fourth root of the heat flux. Since transpiration cooling was shown to initially decrease the temperature by more than 1500 K Sudmeijer et al. (2007b) at the given mass flow, the heat flux would have to be 3 times as high for the nose to still fail. Under such conditions however, the nose could not be considered fail safe. Due to the fact that active cooling effects are neglected for the rest of the heat shield, it is this component that will fail first in case of heat flux variations. Since the heat flux drops rapidly behind the stagnation point and since the cooled nose is relatively long (14 cm), the heat flux of 2.4 times higher than the maximum heat flux predicted would need to occur on the trajectory for the TUFROC material to fail. At lower angles of attack resulting in the shock being oblique, the failure would happen much sooner, but due to the lack of detail of the code, the sensitivity could not be estimated.

This leads to another parameter which could unpredictably change due to perturbations: the angle of attack. It was modelled as a change to the flow incidence angle θ of the vehicle. It was found that at 15 degrees angle of attack which is approximately predicted for the trajectory, 2 degrees change in angle of attack would lead to temperature difference of 68 K at the beginning of the heat shield down to 59 K at the end. Therefore, perturbations to angle of attack could be critical to the heat shield only at the maximum heat flux condition when the expected temperature is close to the design temperature of TUFROC and only if these perturbations were significant.

The next chapter will elaborate on the selected materials for TPS and how they can deal with the above described thermal environments in more detail.

15 Vehicle Skin and Heat Shield Materials

Based on the trade-off, the SPFI and TUFROC materials were selected for the design of the vehicle. WHIPOX will be used to provide a radio-transparent window. This chapter summarizes the performance of these materials and how these materials will be integrated with the rest of the vehicle structure.

15.1 Requirements on the Heat Shield

From the requirements of Chapter 3, the following requirements on the heat shield were derived:

- **SYS.CR.1 The vehicle shall withstand any loads imposed on it during the mission**
- **SYS.CR.2 The vehicle shall be designed such to protect the internal subsystems**
- **SYS.CR.3 The vehicle shall be designed to ensure reliability and reusability**

Based on these requirements, the following sub-requirements have to be met by the TPS:

- TPS.REQ.1 The heat shield and skin shall withstand temperatures of up to 1500 K on the bottom side, 1000 K on the upper side and 1725 K on the leading edges, as based on the aerothermodynamic model.
- TPS.REQ.2 The heat shield and skin shall be airtight.
- TPS.REQ.3 The heat shield and skin shall be at TRL of 5 or above to ensure reliability.
- TPS.REQ.4 The heat shield and skin shall be reusable at least 20 times.
- TPS.REQ.5 The heat shield and skin shall have an insulation to protect the inner vehicle structure.

How these requirements are met is presented in the following sections.

15.2 Summary of the Trade-Off

During the material trade-off, the following criteria were considered: temperature limit, degradation, emissivity, toxicity, availability, technology readiness, failure strength, fracture toughness, thermal conductivity and coefficient of thermal expansion. The materials assessed were: Ceramic matrix composites, Porous C/C ceramic, off the shelf ceramic tile designs (TUFROC and SPFI), Procelite 170, PM 2000, Vitreloy, Depleted Uranium and Tungsten.

PM 2000 was found to be unavailable, and thus not considered further. Depleted Uranium was toxic, and thus discarded as well. The criteria that led to further filtering were the fracture toughness and strength, due to which Procelite and porous C/C were removed. Finally, from the options, the highest scoring solutions were the off the shelf ceramic tile designs, TUFROC and SPFI. Based on the temperature limits and availability, it was decided to put TUFROC on the bottom of the vehicle as a heat shield and SPFI to the rest of the vehicle skin. The rest of the chapter will elaborate on the properties of these materials and integration.

15.3 Material Properties

Firstly, for the two selected materials, their properties and performance are discussed in detail.

15.3.1 SPFI

For the upper and back vehicle skin, where the temperatures are expected not to exceed 1000 K, Surface Protected Flexible Insulation, SPFI, was chosen due to its superior properties and availability in Europe. Its Technology Readiness Level (TRL) is 5.

General Information

SPFI is based on the Flexible External Insulation material covered in a protective ceramic oxidation-resistant layer to survive higher temperatures, to provide for pressure tightness, and to improve thermo-optical properties such as emissivity. The CMC layer allows for usage up to 1670 K (single use, maximum temperature) or up to 1470 K (multiple used, design temperature) and acoustic loads of up to 160 dB according to ECSS (2011).

Temperature Limits, Degradation and Catalycity

Several thermal and plasma tests were performed to prove the usability of SPFI, as described in ECSS (2011). A thermal test on SPFI under the temperatures of up to 1400 K for 50 cycles showed that the material can be used as a reusable insulation for reentry vehicles. Plasma erosion and catalycity tests showed that due to oxidation, the weight loss is below 0.04% under maximum temperature conditions for 9 minutes, and that the surface shows non-catalytic behaviour which makes it suitable for the mission. Six cycles at design temperatures were also studied in an arc-jet reentry facility, and showed no degradation and only a minor flaking of the surface coating of the CMC layer.

Thermal Expansion

The load carrying layer of CMC has a very low thermal expansion coefficient, of 6E-6 m/K or lower. This means that as long as the frames allow for marginal expansion (below 10 mm for the vehicle), the thermal stresses induced by the thermal expansion of SPFI can be neglected.

Emissivity

As mentioned in ECSS (2011), in case of a pure CMC cover, the emissivity degrades significantly at elevated temperatures, which means that only heat fluxes of up to 100 kW/m^2 (T = 1200 °C) could be withstood. An external emissivity coating system was thus developed, with an excellent adhesion to the CMC cover, which increases the emissivity and decreases catalycity. This coating ensures a hemispherical emissivity of 0.8, which means that the allowable aero-convective heat fluxes can exceed 200 kW/m^2, which is sufficient for the upper skin of the vehicle. Next, the TUFROC material for the heat shield is discussed.

15.3.2 TUFROC

Toughened Uni-piece Fibrous Reinforced Oxidation-Resistant Composite, TUFROC, was selected for the heat shield with temperatures above 1000 K with a TRL of 7. If not stated otherwise, the information below is based on Stewart and Leiser (2006) and Leiser et al. (1989).

General Information

TUFROC is made out of ROCCI (Refractory Oxidation-resistant Ceramic Carbon Insulation) on the upper side for dimensional stability and a fibrous based insulation on the lower side. The composite withstands temperatures of 1970 K and is applicable to wide surfaces as well as sharp leading edges of vehicles.

Temperature Limits, Degradation and Catalycity

Extensive testing of the material took place as described in Stewart and Leiser (2006) during which the material was exposed to heat fluxes from 182 W/cm^2 up to 315 W/cm^2 for over 600 seconds. These conditions larger than expected heat flux during the mission since the heat flux further down from the nose decreases significantly. Pre- and post-test photographs showed no degradation after first two testing rounds of 120 seconds. During the 3rd and 4th test, the estimated temperatures were as high as 2770 K, yet only a very small change in the leading edge radius was observed. This indicated that TUFROC is highly resistant even over its design temperatures for short duration of time. The temperature measurement of the tiles also indicated that the material is fairly non-catalytic, since the measured temperatures were at last 200 K below than they would have been for a fully catalytic wall.

Thermal Expansion

Just like in case of SPFI, since thermal expansion is one of the primary sources of stresses in hypersonic missions, the TUFROC cap and the cap insulator base have initial depressions which allow for expansion during the heating and following reduction of stresses.

Emissivity

The ROCCI cap can be treated with a High Efficiency Tantalum-based Ceramic Composite (HETC) formulation for improved hemispherical emissivity. It was shown that below 1978 K, the total emissivity was above 0.9, while above these temperatures, it decreased to 0.87. This makes TUFROC superior to other materials in terms of emissivity.

15.4 Material-Structure Structural and Thermal Interface

According to ECSS (2011), the SPFI layer can be bonded to the substructure using an adhesive. Since this adhesive cures at the room temperature, this leads to straight-forward integration and maintenance of the TPS. SPFI is not a load carrying structure, since it is mostly composed of the flexible external insulation. Thus, the structure underneath must be designed to be load carrying.

Tests on SPFI mentioned in ECSS (2011) showed that at the design temperatures, the temperature of the structure underneath does not exceed operational temperatures of Aluminum. Thus, if Titanium with a higher melting point is used for the load carrying substructure, these limits will not be exceeded.

In case of the TUFROC interface, all the demonstration articles contain an aluminum mounted ring that is bonded to their bases for easy assembly and disassembly. Thus, they can be attached to a strut that is cooled if needed, and no adhesive is required. Tests from Stewart and Leiser (2006) showed that the interface with the substructure does not exceed 722 K, which is well below the operating temperature limit of the Titanium substructure. Thus, no additional insulation is needed.

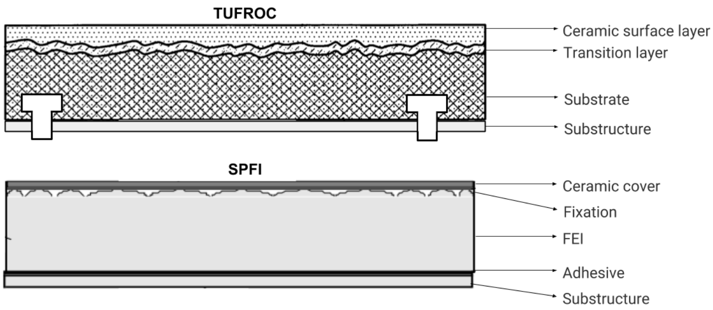

Figure 15.1: Design of material attachments adjusted according to ECSS (2011) and Leiser et al. (1989)

15.5 Passive TPS Redundancy

To increase the reliability of the TPS and survive the flight even in case of the primary TPS failure, redundancy should be applied. Both the TPS tiles and the SPFI will be attached to a Titanium plate holding the structure, which has a melting temperature of almost 2000 K. It is not oxidation resistant, however, the pressures and temperatures typically driving the oxidation rates will not be significantly large unless the broken section is located near the nose or at the leading edges. Thus, this Titanium plate provides redundancy provided that the failure does not happen on the leading edges or near the nose tip.

15.6 WHIPOX for Radio-Transparency

To generate radio transparent windows for communication purposes, a tile from WHIPOX, from Kunz and Goering (2014) will be used under the antenna and above the GPS receiver. This WHIPOX tile will have the same area size as the antenna and receiver. According to Kunz and Goering (2014), WHIPOX is resistant to temperatures up to 1500 K and is also reported to be resistant to oxidation and corrosion. Since this material is a part of the heat shield and not as reliable as TUFROC, inspection of this piece will be crucial to ensure the safety of the mission. It will be placed to the back of the vehicle, since based on the aerothermodynamic model, the temperatures there should not overshoot 1500 K even in case of oblique shock thermal conditions.

15.7 Active Cooling Budgets and Recommendations

Based on the analysis of the materials above, the volume and mass budgets for the TPS are summarized in Table 15.1. WW stands for the windward side, LE for the leading edges and LW for the leeward side.

Table 15.1: TPS budgets

Component	Volume, m3	Mass, kg
TUFROC WW	0.092	36.8
TUFROC LE	0.038	15.2
SPFI LW	0.087	17.54

More research has to be performed on the analysis of the transient heat transfer from the heat shield to the inner structure. Moreover, in the next design phase, it is also important to consider the interfaces between the separate ceramic structures and ensure that the manufacturing costs are not too high due to the required geometry. Since the nose tip will become much hotter compared to the heat shield, the next chapter elaborates on the design of this part separately.

16 C/C-SiC Nose Tip Material and Design

This Chapter discusses the design of the nose tip.

16.1 Requirements on the Nose Tip

For the design of the nose tip, the following requirements from Chapter 3 were mainly considered:

- **SYS.CR.1 The vehicle shall withstand any loads imposed on it during the mission**
- **SYS.CR.2 The vehicle shall be designed such to protect the internal subsystems**
- **SYS.CR.3 The vehicle shall be designed to ensure reliability and reusability**
- **SYS.CR.7 The vehicle shall have an active cooling system**

From the requirements above, further main subsystem requirements can be derived, presented below.

- NST.REQ.1 The nose tip shall include active cooling system.
- NST.REQ.2 The nose tip shall be airtight.
- NST.REQ.3 The nose tip shall not fail in case of active cooling system failure.
- NST.REQ.4 The nose tip shall have an insulation to protect the inner vehicle structure.
- NST.REQ.5 The nose tip including the active cooling system effects shall withstand temperatures of up to 3000 K, as based on the aerothermodynamic model.

The design to comply with the requirements above is described in the sections below.

16.2 Summary of the Trade-Off

During the trade-off, similarly to the heat shield design, the following weighting criteria were considered: temperature limit, degradation, emissivity, toxicity, availability, technology readiness, failure strength, fracture toughness, thermal conductivity and coefficient of thermal expansion. The materials assessed were: Ceramic matrix composites, Porous C/C ceramic, Tungsten, Diamond, off the shelf ceramic tile designs (TUFROC and SPFI), Procelite 170 and PM 2000.

The only materials that were not discarded due to insufficient properties were Carbon Matrix Composites (CMC), Porous C/C, Tungsten with coating and Diamond. The best score was found with Porous C/C, again due to the easiness of the application of transpiration cooling through it, and thus this was selected as a first choice. Specifically, C/C-SiC matrix was chosen due to its superior degradation resistance and higher technology readiness level.

16.3 Nose Tip Material Design

The following sections describe the general properties of the porous C/C-SiC ceramic.

General Information

A porous C/C-SiC ceramic nose tip was selected, since its operating temperature is up to 2000 K, but it can withstand temperatures up to 3300 K for a few minutes (Patel et al. (2012)) in case of active cooling failure. Carbon carbon ceramic was optimized for the use of transpiration cooling in Stuttgart, resulting in the development of a so called OCTRA material, presented in Dittert and Kütemeyer (2016). Due to its optimized permeability, it is this material that was chosen in particular for the use in the Hyperion IV design. Unless stated otherwise, the information below is taken from Dittert and Kütemeyer (2016).

Temperature Limits, Degradation and Catalycity

OCTRA is designed to withstand the temperatures of 2000 K on a long term basis. While ceramic materials are generally non-catalytic, the main problem is oxidation, and thus recession when exposed to atomic oxygen. As long as the transpiration cooling mechanism works, oxidation is prevented by the thin layer formed out of water vapour on the surface, as discussed by Dittert et al. (2015). However, in case the cooling mechanism fails, the oxidation of the C/C-SiC ceramic results in an average recession rate of 0.0057 mm/s, as shown by Xie et al. (2013). The mitigation for this risk will be discussed in Section 16.5.

Thermal Expansion

The thermal expansion coefficients of the C-C and SiC ceramic materials are very small, resulting in the expansion of less than 1% for 2000 K temperature rise ($5 \cdot 10^{-6}$ per K), according to Osgood et al. (1956).

This means that the thermal stresses are minimal. Moreover, since the material is porous, it can also partially expand into the space in its pores, which means that negligible stress will be created due to the small thermal expansion. This also indicates that the pores should be slightly oversized.

Emissivity

The emissivity of C/C-SiC is very high with values up to 0.8. If necessary, it can be increased even above 0.9 if special coatings are used on the surface, such as in case of ROCCI.

The selection of the porous C/C-SiC directly leads to the conclusion that transpiration cooling is the method chosen. The proposed design of this cooling system is discussed in Section 16.4.

16.4 Active Cooling Design

It is obvious from Figure 14.6 that cooling has to be used such that the nose tip can survive the mission, as C/C is designed for 2300 K and the temperatures can reach almost 3000 K. It was also for that reason that the OCTRA material was selected. Transpiration cooling will be provided first by Helium when the pressure is below the point at which water can remain liquid. Once the dynamic pressure and temperature exceed this point, water will be used instead due to its superior heat capacity and latent heat.

The pump power for the active cooling has to be estimated such that the system can be accommodated for in the vehicle power budget. The maximum required mass flow estimated for the trajectory was extracted and designed for. This means that even at the highest pressure conditions, the pumps need to provide enough power to deliver this amount of water or Helium per second to the nose, including pressure losses in the porous material, $P_{out} = P_{stag,max} + P_{loss}$. The pressure losses for the maximum mass flow are, according to Dittert and Kütemeyer (2016) estimated to be below 20 MPa. For a given pipe radius, from $\dot{m} = vm/L$ the velocity of the water and Helium can be estimated. To achieve such water velocities, a certain pressure has to be achieved in the tank, for which the Bernoulli equation can be used. From the tank pressure, the pump power can be estimated using:

$$P_p = 1/\eta \frac{\dot{m}}{\rho} \Delta P \tag{16.1}$$

which results in 110 W including 30% contingency if the pump efficiency, η, of 0.7 is assumed.

The mass of the water and Helium for the entire trajectory are 1.37 kg and 0.35 kg, respectively. According to Akin (2016), with V being the coolant volume, the tanks can be then sized by $m_{tank} = 299.8V + 2$, leading to 6.77 kg. The 110 W will be enough for both pumps, since they will not operate at the same time.

The design can be seen on Figure 16.1. Two separate cooling tanks for water and Helium are used, both connected to pressure reducers and solenoid valves for mass flow control. Based on the current predictions from the preliminary trajectory, the estimated speed of the coolant across a 5mm thick pipe to achieve the desired cooling is approximately 4.6 cm/s. While the diagram shows only two pipes, there will be at least 4 pipes, if not more, to deliver the water more evenly. This can only be designed however, once more advanced transient heat transfer simulations are employed to optimize the cooling effect and coolant dispersion.

After delivery to the C/C-SiC material, the coolant propagates through the pores to the surface, where it evaporates. The regression rates and the presence of the Carbon phenolic layer indicated on the figure will be discussed in Section 16.5.

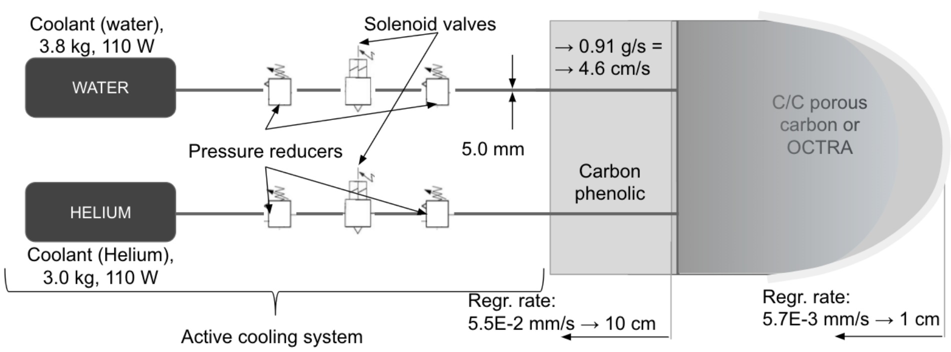

Figure 16.1: Active transpiration cooling system of the nose tip

16.5 Passive Ablative Nose Tip Redundancy

Since nose is a critical system, loss of which will result in an immediate failure of the mission, it was decided to apply several layers of redundancy to its design. The three distinguished stages of failure are:

1. Failure of the transpiration cooling system leading to C/C-SiC oxidation
2. Braking of, or significant damage to the nose tip after transpiration cooling failure
3. Penetration of hot flow inside the vehicle after transpiration cooling failure and nose tip damage

It was decided to mitigate all of these risks in the design. Since failure of the nose tip is not regarded as a nominal condition of the flight, these backup mitigation systems were not made to satisfy the user requirement of 20 times reusability. Should their use be required, they guarantee that the vehicle can safely return back to the Earth without failure, but the nose will have to be completely replaced.

16.5.1 Failure of the Cooling System Leading to C/C-SiC Oxidation

In case the cooling fails and thus the water vapour cannot protect the C/C-SiC nose from oxidation, the material will start to recess at the rate of 0.0057 mm/s (Xie et al. (2013)), as shown on Figure 16.1. This means that approximately a centimeter will be lost in total during a nominal mission in case the failure happens at the beginning of the reentry phase. For that reason, the C/C-SiC thickness is at least a centimeter in every direction, and 4 centimeters at the front, such that sufficient amount of material is available before the insides of the vehicle are exposed.

It should be also noted that the trajectory might be affected due to the changing nose radius in case such failure happens, leading to even more extreme temperatures reached. However, the TUFROC material is capable of short term exposure to temperatures of up to 2700 K Stewart and Leiser (2006), so this will likely not affect the integrity of the rest of the vehicle.

16.5.2 Breaking of or Significant Damage to the Nose after Cooling Failure

Ceramic materials are typically brittle, so although the material could in theory still protect the vehicle even in case of the cooling failure as described above, this does not hold if the nose tip gets punctured or damaged during the flight. This results in a second stage failure - loss of the vehicle in case of damage to the nose after the failure of the cooling mechanism.

Under nominal conditions, as long as the cooling mechanism works, the material can withstand the temperatures even in case of a damage to the nose, since the hot flow will not penetrate inside the nose due to the presence of water. However, in case the cooling mechanism fails, this no longer holds, and the hot plasma will penetrate the C/C-SiC down to its attachment structure and melt the adhesive. This means that the nose tip will start detaching from the structure underneath, which would result in the loss of the vehicle.

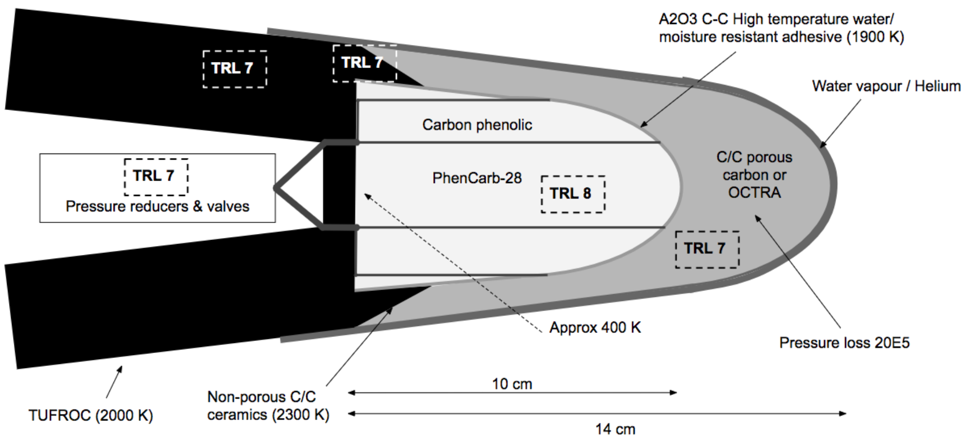

Figure 16.2: The geometry and composition of the nose

To mitigate such risk, a layer of carbon phenolic is applied inside the nose as insulation, the geometry of which can be seen in Figure 16.2. The original NASA carbon phenolic is no longer available, but a similar version, known as PhenCarb-26, was created and is available by NASA's Ablative Laboratory (ARA), with a similar recession rate (NASA (2004)). Firstly, this material acts as a perfect insulation to the connection with the rest of the vehicle. Secondly, even if the adhesive fails and the C/C-SiC material detaches, this material starts to slowly ablate away at the average rate of 0.055 mm/s (Sutton (1970)) as indicated on Figure 16.1, resulting in the total loss of 10 cm during a nominal flight if such a failure happens at the beginning of the reentry. This protects the vehicle until the recovery, and further damage is not expected since carbon phenolic has a much higher fracture toughness compared to C/C-SiC. On the sides, the non-porous ROCCI material will be used that can withstand up to 2300 K, and 3000 K for a short period of time. Even during the ablation, the insides of the carbon phenolic layer with the original virgin material will not reach temperatures of above 400 K according to Sutton (1970). Should the entire layer melt away at the end of the flight, the nose is sealed with a piece of TUFROC ceramic, which can sustain up to 2700 K for a short period of time until recovery, as mentioned above.

16.5.3 Penetration of Hot Flow after Cooling Failure and Tip Damage

Finally, the last concerns are related to the pipes, through which the plasma could penetrate inside the vehicle in case of a malfunction of both the cooling mechanism and the C/C-SiC material.

Nominally, this would be prevented by a valve in the feed system. However, in case of a malfunction of the nose tip material and the cooling system, the valve could be melted due to the inflow of the very hot airflow. Fortunately, the pipes will be mounted through the carbon phenolic, which, while ablating, create a strong layer of char on its surface, as described by Sutton (1970). This char will clog the thin pipes and prevent significant inflow into the feed system and rest of the vehicle. This is one of the reasons why the pipes were proposed to only have a diameter of 5 mm.

16.6 Material-Structure Structural and Thermal Interface

The connections to and the insides of the nose will be provided by a high temperature (up to 2000 K), moisture resistant adhesive for ceramic-ceramic bonds based on Al_2O_3 by Ceramabond™ [1].

Due to the presence of the insulating carbon phenolic, the temperatures behind the nose tip are not expected to exceed 400 K. The structure will be bonded to non-porous ceramic on the sides and a TUFROC ceramic in the back.

16.7 Integration of the Active Cooling Pipes

The pipes will be made of Tungsten and as shown on Figure 16.2, they will adhere to the phenolic attached to the edges of the sealing ceramic plate. The Tungsten pipes will be further split using a junction into two at the attachment to the phenolic. The split up pipes will be separately inserted into the phenolic and upon reaching its surface, they will spray the coolant into the porous C/C-SiC.

16.8 Nose Tip Budget and Recommendations

Based on the analyses of the previous sections, the active cooling subsystem budgets are presented in the Table 16.1.

Table 16.1: Active cooling subsystem budgets

Component	Volume, m^3	Mass, kg
Helium tank + coolant	0.0026	3.0
Water tank + coolant	0.0012	3.8

More in-depth research has to be conducted to obtain further data about the materials and the active cooling system. Moreover, the transient heat transfer analysis has to be done to verify that the insulation, which is currently in use behind the nose, is sufficient to protect the inner vehicle structure. The design of the active cooling system also still has to be developed further. For that, tests have to be performed to better estimate the required mass flow of the water and Helium coolants to potentially lead to volumetric and mass reductions.

One major disadvantage of the ceramics for reentry applications is the fact that it is easily damaged, thus requiring very good maintenance. It could also result in drastic increase in operational cost. Thus, another possibility of using a Tungsten nose tip with a anti-oxidation coating was considered, and a feasibility study for possible future applications was developed, as presented in Chapter 18.

[1] "https://www.aremco.com/wp-content/uploads/2015/04/A02_15.pdf"

17 Thermodynamic Model for a Metallic Nose Tip

To determine feasibility of the metal tip two factors had to be considered, namely the thermal expansion and the deterioration. Before any of such analysis could be made, the temperature of the materials must be know. To model temperatures properly, a mesh study would be desired, however, due to time constrains, a more simplified model was developed. This model divides the nose into 4 parts, namely the plasma formed on the nose, the outer skin/coating, the tungsten core, and lastly the water in the film. The script calculates the energy flows across all those part, which results in the total energy per part. From this the temperature per part can be computed by dividing by mass and by the specific heat. Since only the temperatures of the coating and core must be known, some assumptions for the other two parts were made. It is assumed, that for every step the old plasma and water have been flushed away, this is such that energy can not accumulate and so they will only focus as heat well or heat sink. these assumptions hold as long as the air stream velocity is higher than 12 m/s. For the water it depends on the exposed area, stream velocity, and mass flow, therefore, it must be kept in mind that at least one must be scaled such that the water leaves the tip as a vapor.

17.1 Heat Flows

Every energy flow was studied, modeled and put in a function. Each energy flow will be mentioned and discussed separately below, ordered from the flows interacting with the alumina coating to the flows interacting with the tungsten core.

17.1.1 Heat Flows for Alumina

Heat Flux To model the heat flux imposed by the air colliding with the vehicle Detra's model was used. Detra was chosen to stay consistent with the other thermodynamic model for the porous c/c ceramics.
Dissociation Heat When temperatures reach above 2000 K a fraction of water starts to dissociate, as is described in Tsutsumi (2010). The amount of the H_2O to dissociate is denoted by n, for the model a value of 0.01 was chosen. The article gives a value of 0.035. It was opted to reduce this in order to give a more conservative estimated, since due the high speeds the H_2O(g) might not have enough time to reach the 0.035 fraction. The dissociation will only have an effect when a mass flow is present.

$$Q_{dissociation} = nmE_{dissociation} \tag{17.1}$$

Boundary Layer Heat Transfer Reduction
As a object moves through any fluid a boundary layer is formed. This boundary layer reduces the effective heat transfer. Luckily Detra's approach is on data rather than theory and therefore takes this effect already in effect. However, when the mass flow is injected the boundary layer is expanded and this is not corrected by Detra. Due to time constrains it was opted not to construct an entire boundary layer simulator but rather to use a heat transfer effective coefficient. The coefficient was set at 0.9 during mass flow. This value was based on the cooling effectiveness of nitrogen with a flow of 2 g/s (minimal flow in the created model) Sudmeijer et al. (2007a).

Emissivity
The primary heat loss is due to the emissivity computed using Equation (17.2). Where the emmisivity (ϵ) is a material property and has a value between 0.9 to 0.94 for alumina, σ is the Boltzman's constant, and T is the temperature in K.

$$Q = \epsilon\sigma T^4 A \tag{17.2}$$

17.1.2 Heat Flows for Tungsten

Conductivity
The temperature difference between the alumina and tungsten causes a heat flow. This heat flow was calculated using Fourier's law (17.3). Where dx was set to be the alumina thickness and the dT the temperature difference between the alumina and tungsten. k and A are the thermal conductivity and area respectively. k was found to be 35 J/Km. For A the nose area was taken since the difference is negligible.

$$Q = kA\frac{dT}{dx} \tag{17.3}$$

Boiling and latent heat

The pipes inside the core are conducting heat and transporting it outside. This is done in two steps. First the water boils, computed using equation 17.4. Second, the latent heat which was computed by multiplying the mass flow times the latent heat.

$$Q = UdtA \tag{17.4}$$

U is the heat transfer and depends on a couple of factors, namely the mass flow, the amount of pipes, and the distribution of the pipes. For the nose a value of 5678.26 W/m^{2}K was taken [1], which is at 40% of what industrial film cooling devices can achieve maximum with most being at values between 60% to 70% and is therefore a conservative estimate. The area was linked to the mass flow, since a efficient film design requires a full mesh study to find the best configuration.

17.2 Operational Procedure

The model will have 3 inputs, provided by the GNC department, namely altitude, the speed, and the atmospheric density. two additional inputs were given, namely the atmospheric temperature and the Mach number, but these were only used to create graphs. For every set of data points the system iterated the flows times a small time step, set at 0.01 s, and computes the new temperatures by dividing the total energy accumulated in a specific part by its heat capacity cp. The program was originally written to do this until a stable state was achieved, before moving on to the next set of data points. This was latter changed, to reduce computation time and due to the fact that every data point represents a 0.2 s time step. Every iteration of data points got only 20 steps of 0.01 s. With the temperature of the coating and core a couple of design analysis could be made, each will be described in its own subsection.

17.2.1 Flight Conditions

To understand the abilities of the nose TPS not only the temperature had to be studied but also the pressure at the stagnation point. The stagnation pressure was calculated using methods provided in both the books Anderson (2006) and Mooij (2017a). Both provided Equation 17.5.

$$P_{stag} = \rho_{\inf} u_{\inf}^2 \tag{17.5}$$

The pressure data was used to study the severity and critical points of the trajectory. Which included the maximum temperature, minimal pressure and critical combinations, visually represented in a variety of graphs.

17.2.2 Coolant Mass

When the skin temperature of the alumina coating reaches a temperature close to a set risk temperature, the cooling system starts pumping water through the film to cool the nose until it reaches a safe temperature after which it is turned off again. The temperatures are set at 2300 K and 2200 K respectively. The scripts is allowed to increase or decrease the mass flow by 0.5 g/s for every iteration. After every iteration it is checked whether the mass flow was neither to high not to low.

17.2.3 Oxidation Levels

To determine whether the metallic TPS is a fail safe system, a most severe failure study had to be preformed. This case assumed that both the coating and the AC fail. For this particular case it is desired to know the degradation levels of the tungsten. To determine the degradation levels the article by Bartlett (1964) was used. The article provides a variety of graphs which display the oxidation for various conditions. For each of these conditions equations were established.

Oxidation for T<2273 K

$$X_w = C P_{O_2}^{n_P} n_T^{T_{surf}} \tag{17.6}$$

Where P_{O_2} is the pressure at the surface, the n's and C are material property constants, and T_{surf} is the temperature at the surface. The n_T was derived from the slope in Figure 17.1. The n_P was similarly derived from the slope in Figure 17.3. The C was set such that the curves had the right magnitude.

Oxidation for T>2273

At temperatures above 2273 K oxidation is independent of temperature as can be seen in figure 17.1, therefore,

[1] http://www.hcheattransfer.com/coefficients.html,last accessed: 18-6-2018

all oxidation levels above 2273 can be predicted using equation (17.7), which is similar to equation (17.6) but without the T term.

$$X_w = C P_{O_2}^{n_P} \tag{17.7}$$

However, this was not as straight forward as one might think.For pressures below 10^{-5} atm the constants were found similarly to the method described above. However, for pressure above 10^{-5} atm a boundary layer forms reducing the surface pressure. The boundary layer is formed by the evaporating WO2. To determine this reduction again would require a full boundary study/model which is beyond the given time constrain. Instead a reduction of ten was chosen which was similar to that observed in the experiments in Bartlett (1964). As can be seen in Figure 17.2, a curve is shown with $P_{tot} = P_{O_2}$, from this curves new negatively straight curves form for different surface pressures. From the latter the n_p was found for conditions $10^5 < P_{tot} < 10^{-3}$ and $P_{tot} > 10^{-3}$. The C is than found using the formal graph and the given total pressure reduced by a factor of ten, after which the total pressure is used to calculate the oxidation levels. All oxidation levels are appended and multiplied by a time step, the sum results in the total oxidation for a given trajectory under failure.

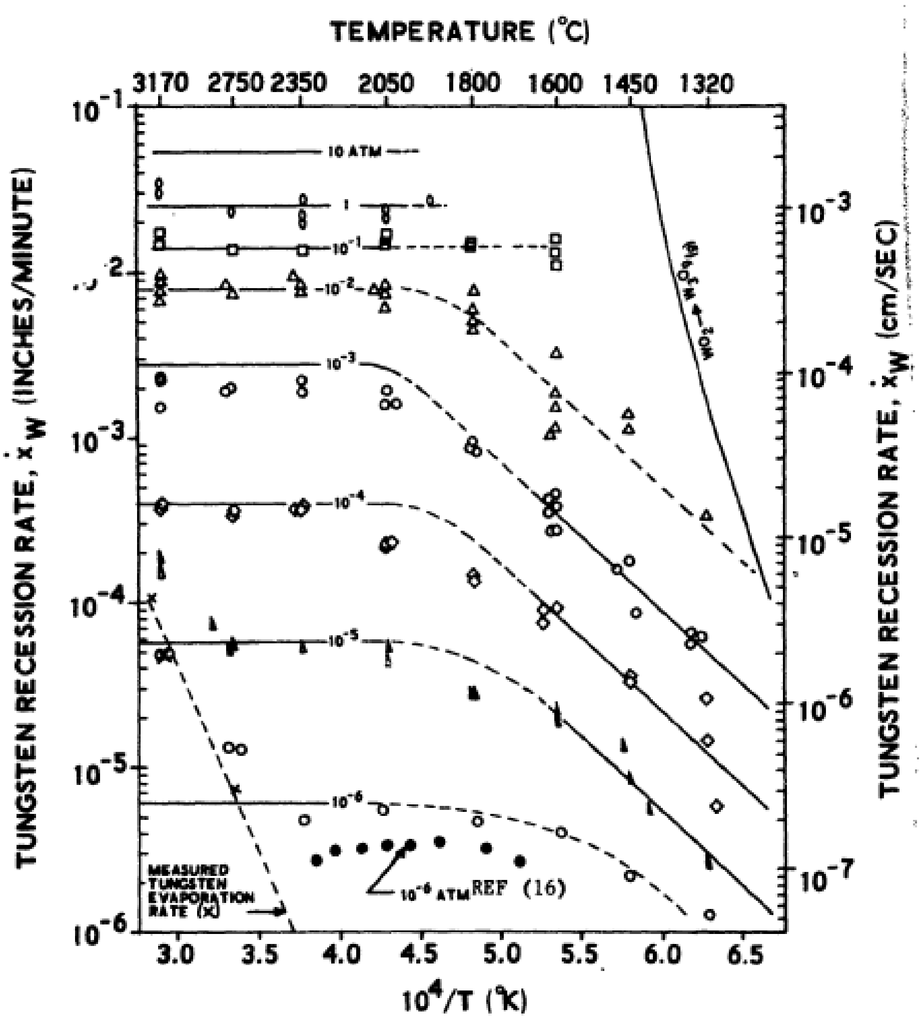

FIGURE 6. ARRHENIUS PLOT OF TUNGSTEN RECESSION RATE VERSUS RECIPROCAL ABSOLUTE TEMPERATURE IN OXYGEN: HORIZONTAL LINES OF LEFT HAND SIDE ARE BASED ON THEORETICAL PREDICTIONS. SEE FIGURE 10

Figure 17.1: Shows regression rates dependency on temperature for various constant pressures (taken from Bartlett (1964)).

17.2.4 Thermal Stresses

The thermal stress could not be computed in stress units, this was simply due the fact that the E-modulus and other mechanical properties of alumina are unknown. It was therefore decided to look at the area difference between the W-core and the Al_2O_3-coating. This was done by using the method presented in the book Callister and Rethwisch (2015). Where the volumetric increase and area increase can be estimated by 3α and 2α, where α is the linear thermal expansion coefficient. The subscript would take two data points from the thermodynamic model, the maximum temperature reached and the point where the temperature difference was the largest. It would than calculate the volumetric increase of the W-core of the very tip of the nose (so the half sphere with partly the cone) and the area increase of the alumina. From the volumetric increase it would calculate the new radius and from that determine the area increase. The one with the largest area difference was then given.

17.3 Model Verification and Validation

17.3.1 Thermal Stresses Unit Test

To test the functionality of the thermal stress subscript, it was developed in its own model before being added in the main model. The model was tested by using two made up materials, for which a radius increase was chosen from this increase a particular temperature was chosen and with those two the thermal coefficients were found. The subscript was given the thermal coefficients and the temperatures from which it had to find the previously chosen radius within a accuracy of 1%. The iterative steps were reduced until the desired level of detail was achieved.

17.3.2 Oxidation Equations

As has been described before the equation used were based on the experimental data presented in the article by Bartlett (1964). So this provides a perfect method of testing the accuracy of the equations, since the graphs produced by the subscript should provide the similar results as the once provided in the article. For the high temperature and high pressures the following graph was produced with the graph from the paper in the same Figure 17.2. Further more a blue end a red cross is shown. These were values not used to compute the orange curves but used to verify the accuracy of the model.

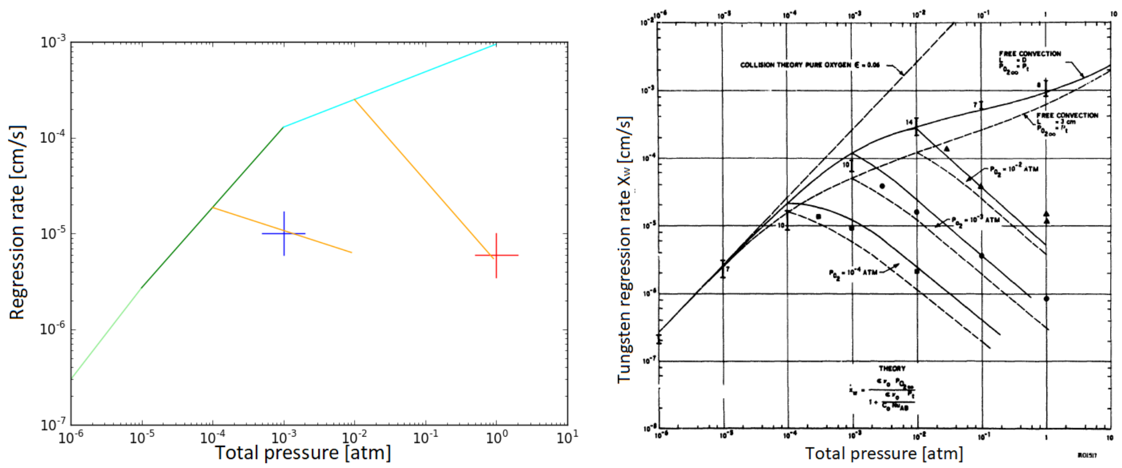

Figure 17.2: Shows the created graph against the experimented graph for T>2000k, right graph taken from Bartlett (1964).

For temperatures below 2000 K another graph was used to computed oxidation levels, the results are illustrated in Figure 17.3. Now one might notice that the curve is relatively accurate at higher pressures but as the pressure goes down the inaccuracy increases. This has to do with which points one constructed the curves. It was chosen to chose points that resulted in more accurate data during higher pressures, since only a small portion of the flight is preformed under these conditions, further more the impact of the oxidation at these pressure levels is so small compared to the higher levels that it had minimal effect on the design.

To make a more accurate prediction individual curves would have to be constructed for different temperature and pressure regions, but given the time constrains and insignificant effect it was chosen not to do this. One explanation why the curves do not follow the physical models could have to do with the fact that at these condition the oxide does not evaporate but rather forms a coating which could prevent other oxygen molecules form reaching the tungsten. As the temperature and pressure go up more coalition happen between the oxygen and tungsten resulting in a higher change of oxidation, thus the regression rate increases.

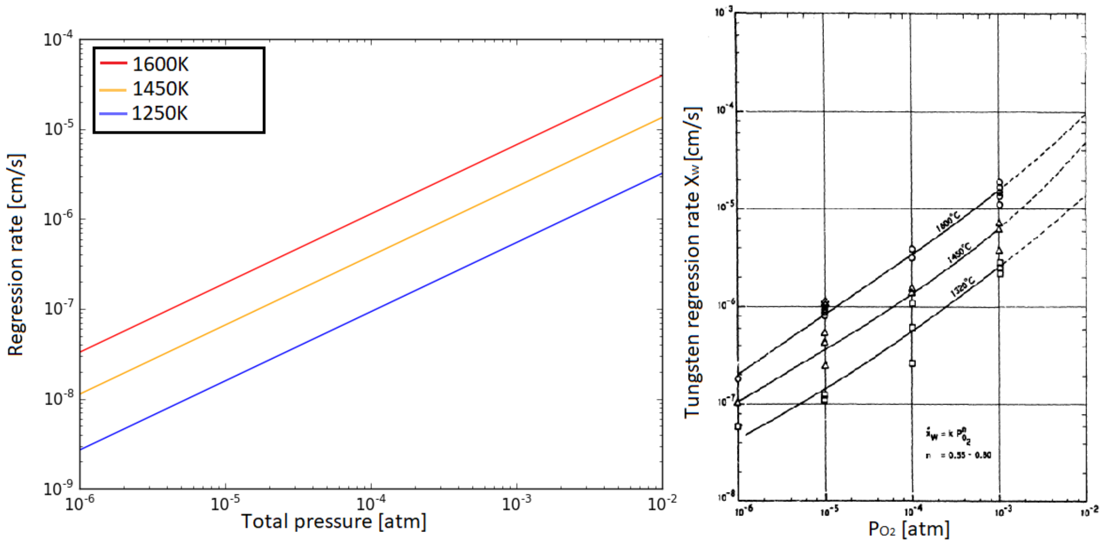

Figure 17.3: Shows the created graph against the experimented graph for T<2000K, right graph taken from Bartlett (1964).

18 Feasibility and Design of the Tungsten Alumina Coated Nose Tip

Hyperion IV will have to fly Through most extreme reentry conditions and on top of that, the vehicle has to be fully reusable. This posed a major problem for the nose tip thermal protection system design. Most conventional materials would not survive this mission, because given the conditions, the ablative heat shield is not reusable and can therefore not be used, which only leaves the design team with the option of C/C ceramics. C/C ceramics have a long history concerning reentry vehicles. Therefore, sufficient amount of information is available on the characteristics of these materials. The problem found by the design team is that C/C ceramics are very brittle and porous, which implies that after every flight thorough inspection has to take place, which may end up in replacements. Given that the Space Shuttle had similar problems, it was found that C/C ceramics do not have the required characteristics to achieve the reusability requirements of the Hyperion IV project. The lack of desired specifications can be explained by noting that all TPS designs are currently designed for single use only. Therefore, less conventional options had to be considered as well. Of all less conventional options considered, an alumina (Al_2O_3) coating with a tungsten(W) core seemed most promising, known as W-Al_2O_3. The reason for being the best option had to do with the fact that the technique of combining W with an Al_2O_3 coating has been used for over many years. Also, this technique has a high failure temperature and requires minimal development compared to other design possibilities. Other options included Super alloys, metallic matrices, metallic glass and crystals. Due to its low TRL and first impression of simplicity, it was decided that a detailed feasibility study had to be done for the W-Al_2O_3 TPS. The feasibility concerned the following: manufacturing, thermal stresses and oxidation. Furthermore, budgets for weight and TRL have been studied as well, however these were not seen as killer constraints like the former three feasibility constraints.

18.1 Feasibility Study on the Killer Constrains

From the feasibility study, it was concluded that the W-Al_2O_3 should be considered in the TPS design if ESA opts to develop a fully reusable vehicle. The porous C/C ceramic nose tip should be chosen for a vehicle only to be used once. All vehicle analyses, such as the risk, will be done based on this last design, as it was found that for this design a more complete analysis can only be done when more research has been done about the W-Al_2O_3 concept.

18.1.1 Production Processes

Currently three production methods exist for a Tungsten structure. The most common one is sintering, after which the film pipes are drilled. This method is not recommended though, as sintering is not optimal for manufacturing complicated structures, implying much machining which could compromise the structure. Another common practice is plasma flame-spray, which can be seen as an additive manufacturing process, usually performed in a vacuum or noble-gas environment. This process has limitations in terms of precision, as the film pipes cannot be made small enough when drilled. Also, grinding is necessary to ensure the proper shape, as this method is commonly used for oil drills. The last production method is centrifugal casting. This method is unfortunately not commercially viable, due to the fact that the entire cast has to be constructed out of graphite after which all the exposed parts have to be plasma coated by tungsten to prevent the creation of tungsten-graphite (WC). Centrifugal casting is capable of achieving the highest level of precision with minimal compromises (Calver and Beall, 1966). Similar techniques are currently used on titanium parts and vary in mass from 10 kg to 1000kg (Hiodge and Maykuth, 1968). Hence, the centrifugal casting method is recommended. ESA will most likely have to build the production facility themselves, however the upside is that they will be the only producers of this fully reusable heat shield. They can use this position to be a unique TPS provider which has an incredible market potential, which could possibly make the production method commercially viable.

After the construction of the W core, an aluminum coating is applied. First, holes are drilled in the aluminum to free the film piping. Finally, the whole structure is oxidized in the an O_2 enriched environment at a temperature of 823.15 K for two hours. This process ensures the best Al_2O_3 coating (Boratto et al., 2013). The reader should take note that the uncoated tungsten will be covered with a proxy to prevent oxidation. The oxidation process will also reduce thermal stresses when the nose is heated to temperatures up to 2300 K. For this study, plasma 3D printing was considered as well, which allows for the 3D printing of metallic structures in an argon environment. This method might be applicable for tungsten, however this has not been developed yet. Companies or organizations that are willing to invest in detailed tungsten production might be more interested to look into this production process as it offers a faster and more flexible production line.

18.1.2 Thermal Stresses

To determine the thermal stresses in the structure, a coding script was written to compute the difference in area expansion of the W and Al_2O_3. Due to both the complexity of the nose tip design and time constraints, only the outermost tip could be considered for analysis, which was modeled as a curved cone. The script computes the expansion for two scenarios, being the case of maximum temperature difference between the coating and core and the case of the maximum temperature of 2300 K. It was found that the latter case was the most critical one. An area of 0.00015 m^2 was found to expand on a total area of 0.02716 m^2. This increase was due to the tungsten expanding more, even though Al_2O_3 was expected to expand more due to its larger linear expansion coefficient. The thermal coding script was a smaller part of the larger thermodynamic model script, which was written for the metallic nose to identify the two cases mentioned above. The reason that no stress values are given is that because of the high temperatures, changes are found for the E-modulus, yield load and fracture load. This change was well studied for Tungsten, but is largely unknown for aluminum. Tungsten appears to lose about 25 GPa of E-modulus for every 800 K in temperature increase. The yield modulus decreases to around 70-80 MPa for 2300 K (Dodge, 1971). However similar numbers are unknown for Al_2O_3 at 2300 K. Assuming a linear relation is not feasible, given how close 2300K is to the melting point of Al_2O_3, which results in non-linear relations that cannot be modeled. Given the fact that the area changes are very small and that the alumina coating with a tungsten core is used in lamp wires, where temperatures are high due to high electrical resistance, it can be assumed with high certainty that the coating will not fail due to thermal stresses. To get this certainty higher, the design team recommends studying the E-modulus dependency on temperature.

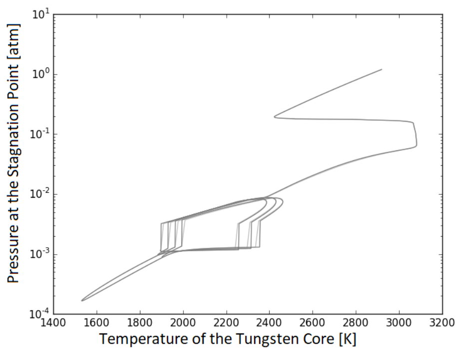

(a) Pressure in the stagnation point over the temperature of the tungsten core in case the AC fails.

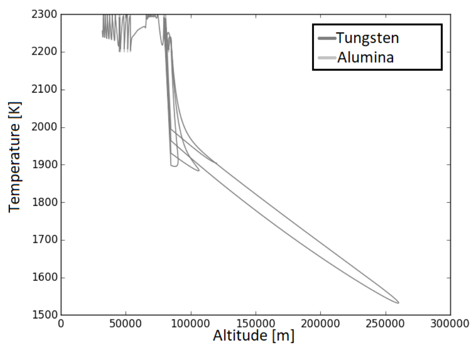

(b) Temperature of The W-core and Al_2O_3-coating over altitude

Figure 18.1: Temperature and pressure analysis of the Tungsten with alumina coating

18.1.3 Oxidation of the W-Al_2O_3 ose Tip

One of the biggest concerns when working with metallic TPS is the oxidation phenomena. Most metals at high temperatures turn into a metallic-oxide. Normally, this oxide forms a protective layer, but at very high temperatures the oxide evaporates. The removal of metallic oxide is increased when an airstream is present. It was thus that this posed the biggest killer constraint for the W-Al_2O_3 concept. Due to the mid-air retrieval, the vehicle is not able to significantly change its flight path to have a less hazardous reentry in case of failure of the nose tip. Such failure can occur when the active cooling system fails, which causes the coating to melt. In such a scenario the tungsten tip must be able to survive the complete trajectory. In the thermal model it was assumed that the AC failed and that the coating was damaged during separation. For every data point provided by the GNC department, the oxidation levels were computed using the surface pressure and the temperature of the tungsten core, which can be seen in figure 18.1a. The model gave as output a total oxidation of 1.27 cm over the entire trajectory. The oxidation levels were extrapolated from the article Schneider and McDaniel (1967). The total oxidation level is only the oxidation at the outermost tip where the flow is orthogonal to the surface.

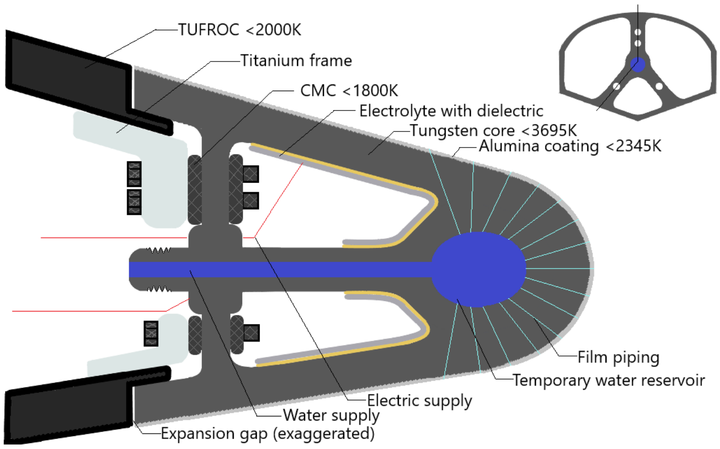

Figure 18.2: A layout of the W-Al_2O_3 nose tip design.

By sizing the thickness of the nose to meet the oxidation needs, it was found that the front needed a thickness of 1.5 cm and 1 cm for the remaining sides. The latter was based on off the shelf calculations and assumptions on how much lower the oxidation would be. It is therefore recommended that for the next iteration, the oxidation levels over the entire area of the nose are computed, such that a better required thickness can be obtained. Furthermore, a proper stress study must be done such that the internal layout of the nose tip is sufficiently sized. Using the current sizing, a total weight of 20.7 kg for the entire nose tip design was estimated. Given this mass budget it was concluded that the oxidation is no killer requirement since the tungsten nose is a fail safe system without too much compromise in the mass budget. The W-Al_2O_3 design is therefore deemed a fail-safe system and does meet the subsystem requirements. Note that the the thermodynamic model assumed that the tungsten is non-reactive with other gasses. This was due to the fact that the article Perkins and Crooks (1961) concluded that W is non-reactive with N_2 as well as that during plasma-spray production hydrogen is often added to the gases to reduce oxidation.

18.2 The Conceptual Design of the W-Al_2O_3 ose Tip

The design of the metallic nose tip was not only driven by killer constraints, but also by the budgets. It was thus decided that a solid tungsten tip could not be chosen since the design would weigh more than 57.25 kg. In the final design it can be seen that besides from the very tip, the majority of the design is empty, as seen in Figure 18.2. As can be seen as well, the nose tip is attached to three points, which is the minimum. Three points were chosen such that it is easier to install the electrolyte and dielectric. The electrolyte and dielectric are installed to make the nose tip a capacitor. This is done such that when the nose operates in environments where the pressure is low enough to allow the O_2 and O^- to penetrate the alumina, the excess of electrons present in the tungsten react with the O_2 and O^- rather than with the W molecules. It must be stated that such a system can only operate briefly before reentry as due to the high temperatures the electric resistance prevents the negative charging of the tungsten. Unfortunately, the materials that should be used for the electrolyte and dielectric together with the power required were not determined yet. This was due to the time constraints. A more detailed explanation about the capacitance coupling will be given in Section 8.8.

The thermal expansion is also a problem when concerning the TUFROC ceramic to which it is attached. To prevent any damage to other parts due to the nose expansion, some measures were taken. The nose is attached to the structure such that the majority of the expansion happens at the front and therefore does not press against other parts. For the attachment, a simply screw system was chosen such that it can easily be removed for maintenance. For the screw system, the same system as in SHEFEX II was used, namely a CMC made out of C/C-SiC, which is a composite consisting of carbon fibers with a matrix of carbon and silicon carbide Weihs et al. (2008). The CMC screws have a very small expansion which prevents the nose from getting loosened when heated. The last measure taken to prevent expansion damage, was by using the same method applied for the SR-71 Blackbird, namely leaving small expansion gaps, illustrated in figure 18.2, to allow the material to expand during normal operations. The expansion gaps imply that the back of the nose has to be air-sealed from the rest of the craft (not shown in the Figure 18.2), which has the advantage that heat can less easily conduct from the nose to the rest of the craft.

For the film cooling different methods and designs were considered. Water has three primary ways on cooling the design, which are conducting heat, evaporation and dissociation of the water. The location where which cooling method was used defined the different designs. Multiple combinations were tried in the thermodynamic model and eventually it was found that when both heating and evaporation happen inside the nose and the dissociation occurs outside the nose, this is the most efficient case. This is due to the fact that water is more likely to dissociate Tsutsumi (2010) and increases the boundary layer when it comes out as a vapour. The increase of the boundary layer is considered a secondary effect, due to the difficulty of modeling the increase in boundary layer.

For the film piping, many small pipes expand in diameter when the water evaporation is most efficient. However, this poses major challenges for the manufacturing process and was thus abandoned after two iterations. Instead it was opted to have a large pipe followed by a temporary water reservoir, which would ensure evaporation of the water. For the amount of cooling liquid, H_2O in the Hyperion IV case, the thermodynamic model was used which turned on the active cooling in case a temperature of 2300K was achieved and turned off when a temperature of 2200K was reached. This resulted in a total use of roughly 6.7 kg, however this value is most likely a major overestimation due to the many conservative estimations used in the thermodynamic model. This would also explain why the cooling effect in the thermodynamic model is less effective than what was found in the paper of Schneider and McDaniel (1967). In Figure 18.1b, the temperature of both the coating and the core can be seen as a function of altitude for when the AC is operational.

The W-Al_2O_3 nose tip uses the same pumps as for the porous C/C ceramic nose tip design. The reader should note that the W-Al_2O_3 does not use Helium in the early stages of the mission, but rather relies on its active anti-oxidation system (AAOS) as mentioned before. A final remark about the oxidation of tungsten, since the affected areas turn yellow after service, visual inspection becomes a viable option.

18.3 Budget and Recommendations

In table 18.1, an overview of the mass budget can be found. Even though this is significantly large, it must be stated that the nose will also act as both ballast as well as its own structural component, also known as a hot structure. The battery needed for the AAOS still has to be determined due the uncertainty in required voltage. It is important to note that it might turn out that Hyperion IV's own EPS can be used, resulting in no extra battery mass. For the mass of the tank, the similar reasoning can be followed, due to limited research in film cooling, as it is difficult to find proper validation data to validate the H_2O consumption.

Table 18.1: Active cooling subsystem budgets

Component	Mass, kg	Volume, m^2	Power, W
Nose material	20.7	0.002	-
Water tank + coolant	10.7	0.0068	-

As has been described before, the fracture coefficient of tungsten at lower temperatures could be problematic considering damage tolerance. Luckily, industry has already found a solution, namely by adding a bit of steel up to 4%, which is able to significantly increase the ductility and thus increasing the damage tolerance. However, the type of steel and the exact percentages are trade secrets and given the needed centrifugal casting production method, no company can provide a nose tip of this particular alloy. ESA most likely will have to research and develop their own alloy for this material.

Another disadvantage is that steel contains carbon molecules and with high temperatures, these molecules might switch from iron to tungsten which could compromise the tungsten core. This phenomenon has to be researched well before any such alloy can be implemented. For the coating, ESA might want to consider an alumina-silicon carbide (Al_2O_3-SiC) coating. As was described in the article by Johnson et al. (2014), there are internal stresses between the the Al_2O_3 and the SiC such that when cracks appear and the material is heated up, the cracks are compressed and closed. This is a form of self healing and would significantly increase the damage tolerance and promote reusability. However, the test documented in the article was done in an argon environment, thus ESA would have to reproduce the same results in atmospheric conditions to investigate the advantages. After reproducing the self healing characteristics, it must be checked whether these will also happen during reentry conditions, thus lower pressures and under the presence of molecular gases. Another advantage of Al_2O_3-SiC besides the self healing phenomena, is the fact that it can be produced at higher temperatures, thus reducing the thermal stresses during reentry.

19 Telemetry and Tracking

Telemetry and tracking are crucial part of the vehicle to ensure that the data can be down linked before retrieval and thus not loss in case of a potential vehicle damage. Moreover, GPS tracking is required such that the vehicle can be guided and the trajectory re-created post flight.

19.1 Requirements on T&T

The main derived requirement from Chapter 3 on T&T is:

- **SYS.CR.10 The vehicle shall transmit data through communication link**

Based on SYS.CR.10, the following requirements can be drawn:

- TT.REQ.1 The SNR at any point to the nearest station while transmitting shall be at least 15 dB.
- TT.REQ.2 All the data shall be transmitted while in flight to prevent data loss upon retrieval.

where the 15 dB SNR results from an acceptable bit error rate discussed below. The design satisfying the main requirements is shown in this section.

19.2 Summary of Trade-Off

Due to the communications blackout, it was decided that the signal will be down linked only once outside of the hypersonic regime. Communication during the hypersonic regime through the plasma will be a part of the on board experiments and thus not an integral part of the design.

Based on availability and proximity to the preliminary trajectory, 9 ground tracking stations were selected for the transmission. They are described in more detail in the following sections, along with a preliminary design of the T&T architecture.

19.3 Telemetry and Tracking Design

To analyze the Signal to Noise ratio (SNR), the link components have to be identified. The expression of the SNR can be written in dB, as in Equation 19.1 (Cervone, 2016):

$$SNR = P + L_l + G_t + L_a + G_r + L_s + L_r + 228.6 - DR - T_s \tag{19.1}$$

where P stands for the transmitter power is denoted as P, cable loss from the transmitter to antenna as L_l, vehicle antenna gain G_t, space loss L_S, atmospheric attenuation L_a, ground station antenna gain G_r, cable loss from the ground station antenna to the receiver L_r, T_s is the system noise temperature and finally, DR is the data bit rate. The following subsections elaborate on the values of the components.

19.3.1 Ground Segment

To obtain the information of the receiver and the ground station antenna, candidates for ground stations must be analyzed. Constant coverage of the vehicle is required to have a constant down link stream of data. Given the equatorial orbit selected for the vehicle, ground stations located at latitudes between +20 and −20 degrees of latitude have to be identified. Suitable ground stations for tracking have been identified using AGI STK software's repository for ground stations. The found stations are: Guiana Space Center tracking station (French Guiana), Cayenne tracking station (French Guiana), Malindi (Kenya) belonging to the ESTRACK network (Muller, 2008). Stations not under ESA direct control are Libreville (Gabon), Diego Garcia tracking station [1] (Diego Garcia Island, Indian Ocean), Malaysia Space Center [2] (Malaysia), Kwajalein atoll [3] (Marshall Islands). Kiritimati (Kiribati) and Cotopaxi (Ecuador). Since the final phase of the flight is crucial, constant tracking by ground station is required. Kiritimati and Cotopaxi tracking stations are not able to track the vehicle at the same time, therefore it would be beneficial to use a floating tracking station mounted on a ship, positioned in the Pacific ocean at a longitude of −120 deg.

It was not possible to retrieve complete data for dish diameter and gain to noise temperature for all ground stations. It follows the assumption that antennas of the same diameter have the same gain to noise temperature ratio. This was the case for Kiritimati, Cotopaxi and the support vessel.

[1] http://jat.sourceforge.net/jat/data/core/groundstations/DBS_NDOSL_WGS84.txt Ground station data repository. Last accessed 25/05/2018

[2] http://www.angkasa.gov.my/?q=en/node/198 Malaysia ground station data. Last accessed 25/05/2018

[3] https://www.smdc.army.mil/KWAJ/RangeInst/TM.html Kwajalein ground station antenna details. Last accessed 25/05/2018

Table 19.1: Data of the ground station antennas

Parameters	Guiana & Cayenne	Libreville, Malindi, Diego Garcia	Malaysia, Kiribati, Support Vessel, Cotopaxi	Kwajalein
Dish diameter	15	20	5	7
G / T_s	29.1	21.3	19.0	20.0

From the Table 19.1, the receiving gain and the system noise temperature can be calculated. For the calculation of the link budget and sizing of the transmitter the smallest antenna diameter of 5 m is used chosen. The antenna efficiency $\lambda_r$and the cable loss factor were assumed to be 0.8.

19.3.2 Transmission Segment and Link Closure

Based on heritage, the Aydin Vector T-300 S/L transmitter was selected, with 10 W radiated power at 84 W power consumption [4]. The antenna gain is programmable, and in case the gain is insufficient, amplifiers can be introduced into the circuit, increasing the gain by up to 13 dB. Based on preliminary market search, a power of 10 W for such a gain increase can be expected, as shown in Drews et al. (2017).

A simple patch antenna was selected. Based on research of small explosive delivery systems, for a frequency of 2.4 GHz, to achieve a gain of at least 10 dB, 186 mm long strip is required Saratayon et al. (2013). From Monthasuwan et al. (2013), the length of the strip is indirectly proportional to the frequency of the transmission. The antenna copper patches are attached to a PVC substrate, as shown on Figure 19.1.

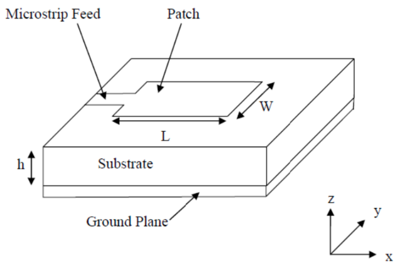

Figure 19.1: Antenna copper patch attached to a PVC substrate according to Monthasuwan et al. (2013)

If 13 dB gain is achieved using the programmable transmitter, amplifier and the antenna, with the power of 10 W, the expected SNR at all stations for the distance of 100 km is at least 15 dB, which is acceptable. Assuming an additive white Gaussian noise channel, a 10 MHz bandwidth and 15 Mbps data rate, 15 dB SNR implies the $\frac{E_b}{N_0}$ of approximately 14 dB for every station, indicating that the bit error rate is below 10^{-8} in case BPSK is used, based on Heegard and Wicker (1999). This is deemed sufficient. For this figure, the frequency of 1.4 GHz must be used, otherwise the the SNR decreases below 15 on some of the stations. Frequencies below 1.4 GHz cannot be used due to the specification of the transmitter, in which case additional radio frequency converters are required, increasing the volume and mass.

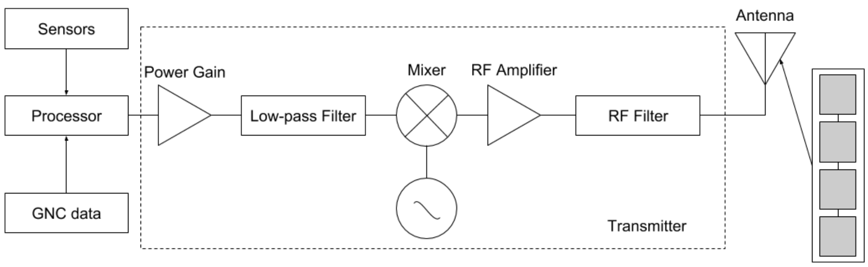

Figure 19.2: Preliminary high-level transmitter architecture

Since 1.4 GHz is required and the length scales with the frequency, the length of the antenna has to be at least 319 mm. Based on Monthasuwan et al. (2013), the height of the strip is 1.8 mm, and the width is 25 mm. The 15 Mbps data rate indicates that if the data can be transmitted during at least 5 minutes in flight, 36 GB of data can be sent, which directly translates into the ceiling of the data budget. This figure could be further increased by more advanced data compression techniques.

[4] "https://www.flightglobal.com/FlightPDFArchive/1995/" Aydin Vector T-300. Last accessed 20/06/2018

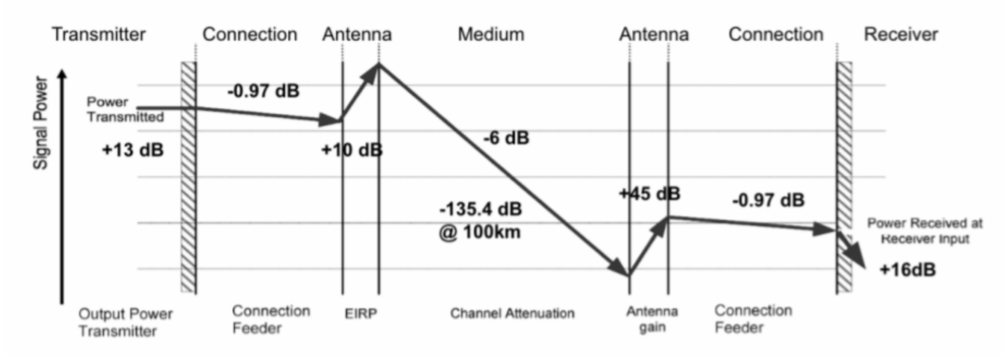

Figure 19.3: General Link Budget

The architecture of the transmitter is shown on Figure 19.2. The link budget was computed for every ground station to ensure satisfactory signal. A generalized, average link budget is shown on Figure 19.3.

In addition to the transmitter, a Phoenix GPS receiver will be installed on board for tracking. For a good quality of the GPS signal, the Phoenix receiver will be connected to an amplifier similarly to the receiver. According to Markgraf (2007), the Phoenix receiver has dimensions of 7 cm x 5 cm x 1.5 cm, operating power of 0.85 W and a mass of 20 g.

19.3.3 Communication Flow Diagram

A simplified communication flow diagram is shown on Figure 19.4. The two main external communication subjects are the GPS satellites and the ground stations. Data from the GPS satellites is received using the Phoenix GPS receiver. The communicated data is transferred to the flight computer. From experiments and other system measurements, the data is transmitted to the ground stations using T-300 transmitter.

In addition to these two major communication parties, after the flight, the vehicle directly communicates with the operation staff, which downloads the data and upgrades the software. Finally, the data can be also transferred from the ground stations if it was received in a satisfactory condition during the flight.

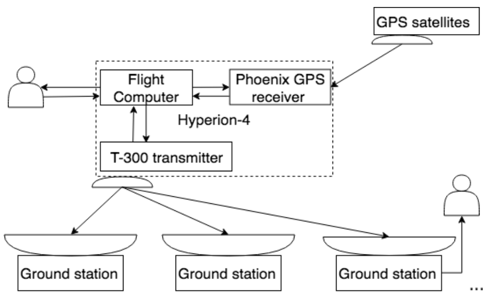

Figure 19.4: Communication Flow Diagram

19.3.4 T&T Budgets and Recommendations

Since the vehicle has no up link, the total budgets are shown in Table 19.2. Once the trajectory is precisely determined, the link budget shall be revised and designed in more detail. The next sections elaborate on the rest of the on board instruments.

Table 19.2: Budgets for the T&T subsystem

Component	Volume, cm^3	Mass, kg	Power, W
Transmitter	4 x 6.5 x 2	0.113	10.00
GPS Receiver	7 x 5 x 1.5	0.020	0.85
Amplifier 2x	2x (5 x 3 x 3)	0.100	20.00
Antenna	31.9 x 0.18 x 2.5	0.232	10.00

20 Command, Data Handling and Avionics

Command and data handling units are necessary to perform all of the control tasks required for the operation of the vehicle. Avionics and other instruments are added to provide input into the control sequences. The design of the Avionics, Command and Data Handling subsystem is described below.

20.1 Requirements on Command, Data Handling and Avionics

From the derived requirements in Chapter 3, the following two mainly concern the design of avionics:

- **SYS.CR.11 The vehicle shall be able to store data on board**
- **SYS.CR.12 The vehicle shall be able to transfer data upon vehicle retrieval**

Both of these requirements can be directly translated to subsystem requirements:

- CDH.REQ.1 The command and data handling system shall be able to store all the sensor and processed data on board with n+1 redundancy
- CDF.REQ.2 The command and data handling system shall have such an interface that a complete data transfer without any loss can occur upon vehicle retrieval

How these requirements are intended to be satisfied is described in the sections below.

20.2 Summary of Trade-Off

The instrument selection was mainly based on the heritage mission data without a formal trade-off process. Afterwards, if an incompatibility between instruments was found, or in case it was discovered that the unit was either too heavy or large in volume, other options were explored and the instrument was replaced. This iterative process finally led to a convergence in design that both has a low mass and can physically fit into the vehicle, while accommodating to the rest of the subsystems and experiments.

20.3 Command, Data Handling and Avionics Instruments

In addition to the sensors for experiments and telemetry, position and attitude sensors as well as data handling units have to be included on board for proper function of the system. The system is responsible for the following tasks:

- acquiring data from the sensors and other measurement units
- data processing and storage
- transmitting of the data through telemetry
- flight path tracking and determination of the attitude
- control of the actuation systems

The instruments and handling units that are responsible to perform the above mentioned tasks are discussed below. At this stage of the design, it is most important to select the instruments to perform subsystem sizing. Thus, the selection of the components can be changed during the next iteration of the design.

20.4 Data Links

All data links will be designed to satisfy the RS-422 technical standard. For data exchange, several high speed interfaces from the payload handling unit are required, connected to the following components: all sensors through dedicated interfaces, telemetry and memory banks, position and attitude sensors (GPS and IMU) and the flight computer for guidance and navigation.

The high speed interface between the payload sensors and the main computer can be realized through a common sensor data bus with synchronous parallel ports.

20.4.1 Fault Tolerant Flight Computer

As a flight computer, Fault Tolerant Computer was selected for this mission, produced by Astrium, Airbus D&S for space applications and nominal power consumption up to 40 W. Its mass is 6.5 kg and the dimensions are 295 mm x 160 mm x 250 mm [1]. It was standardized by ESA SCC specifications and developed for applications such as the ISS. It has 6 MIL-STD 1553B ports, 6 discrete ports and 2 reset ports. Since the interface of the Astrium FTC is the protocol standard MIL-STD-1553, a converter to RS-422 is necessary for

[1] "http://cs.astrium.eads.net/ftc/tech.html" Astrium FTC. Last accessed 20/06/2018

communication. In case a customary LEON-4 based computer is developed that can match the performance of the Astrium FTC with a RS-422 interface, the converter does not have to be included.

20.4.2 Protocol Converter

Sizing of the protocol converter was based on Astronics products from Ballard Technology [2]. The example converted from AB3000 series includes 4 I/O ports to RS-422 and 4 I/O ports to MIL-STD-1553. Its mass is 2.3 kg and size 135 mm x 195 mm x 71 mm. Power consumption is estimated to be 10 W.

The converter might not be needed in case a different flight computer is chosen or developed for the mission that will communicate using the RS-422. In that case, the above mentioned budgets can be saved for other subsystems. However, as soon as there is any component not compatible with the communication protocol, a protocol converter must be used.

20.4.3 Payload Data Handling & Acquisition System

Payload Data Handling System VPDHS produced by Vetronic Aerospace was selected as the payload data handling unit. The mass of the computer is 2.3 kg, with the dimensions of 290 mm x 192 mm x 34 mm and power consumption of 15 W [3]. The data handling unit is capable of receiving and filtering the data from sensors as well as from the camera, either by the RS-422 interface or by MDM-25, which agrees with the ESA standards. It also contains an RS-422 interface to the GPS receiver and is capable of receiving and compressing imaging data, and thus the PHOENIX receiver and the IR camera can be connected to it directly. Five of these units are needed, since above 220 sensors are used on board and each of VPDHS can cater to 54 ports.

20.4.4 Inertial Measurement Unit

In addition to the Phoenix GPS sensor, HG1700 SG Honeywell inertial measurement unit developed for weapon and drone systems will be used to provide data to the navigation subsystem. The GPS sensor is 0.7 kg with the dimensions 87 mm x 87 mm x 54.5 mm and power consumption of below 5 W [4].

20.4.5 Radar Altimeter

As an altimeter, the HiAlt45K Altimeter from United Instruments was preliminary chosen, since it is FAA approved and can measure heights up to 13.7 km (recovery begins at 10 km). The altimeter has mass of 0.2 kg power consumption of less than 1 W [5].

20.5 Software & Hardware Diagrams

To analyze the software and hardware connections within the vehicle, software and hardware diagrams were developed, which are shown in Figures 20.1 and 20.2.

The software diagram shows the preliminary top level data and signal flow. Figure 20.1 indicates that most of the links lead to or from the Flight computer and the memory banks.

The data from the experiments are collocated and gathered using 5 payload data handling units using the RS-422 and MDM-45 communication protocols. This data is processed, filtered and compressed, directly saved to the memory of the payload data handling units (32 GB x 5) and sent to the flight computer. The overall storage space including the storage of the flight computer is 224 GB. The same is done with the output data of the other sensors such as GPS sensor, IMU, radar altimeter, IR camera and other sensors monitoring the health of the subsystems.

In case the Astrium FTC is used, the data has to first flow through the communication protocol converter. This is not necessary if the selected computer is capable of communication in RS-422.

The fight computer processes this data to provide inputs back to the subsystems. During such operations, it can use a vehicle database with specifications on the vehicle aerodynamics, planned trajectory and other vehicle specifications. This database can be replaced or updated in between the flights. The database can also be an internal part of the computer, which will increase the speed of data transfer as no conversion is necessary. All the data is saved in memory banks of the computer in case of the failure of the payload data handling units.

[2] "http://www.ballardtech.com/products.aspx/dir/protocol/" Protocol converter. Last accessed 20/06/2018
[3] "https://www.vectronic-aerospace.com/space-applications/" VPDHS data. Last accessed 20/06/2018
[4] "https://aerospace.honeywell.com/en/products/navigation-and-sensors/" Phoenix data. Last accessed 20/06/2018
[5] "http://www.perfectflitedirect.com/products/HiAlt45K-Altimeter.html" Altimeter data. Last accessed 20/06/2018

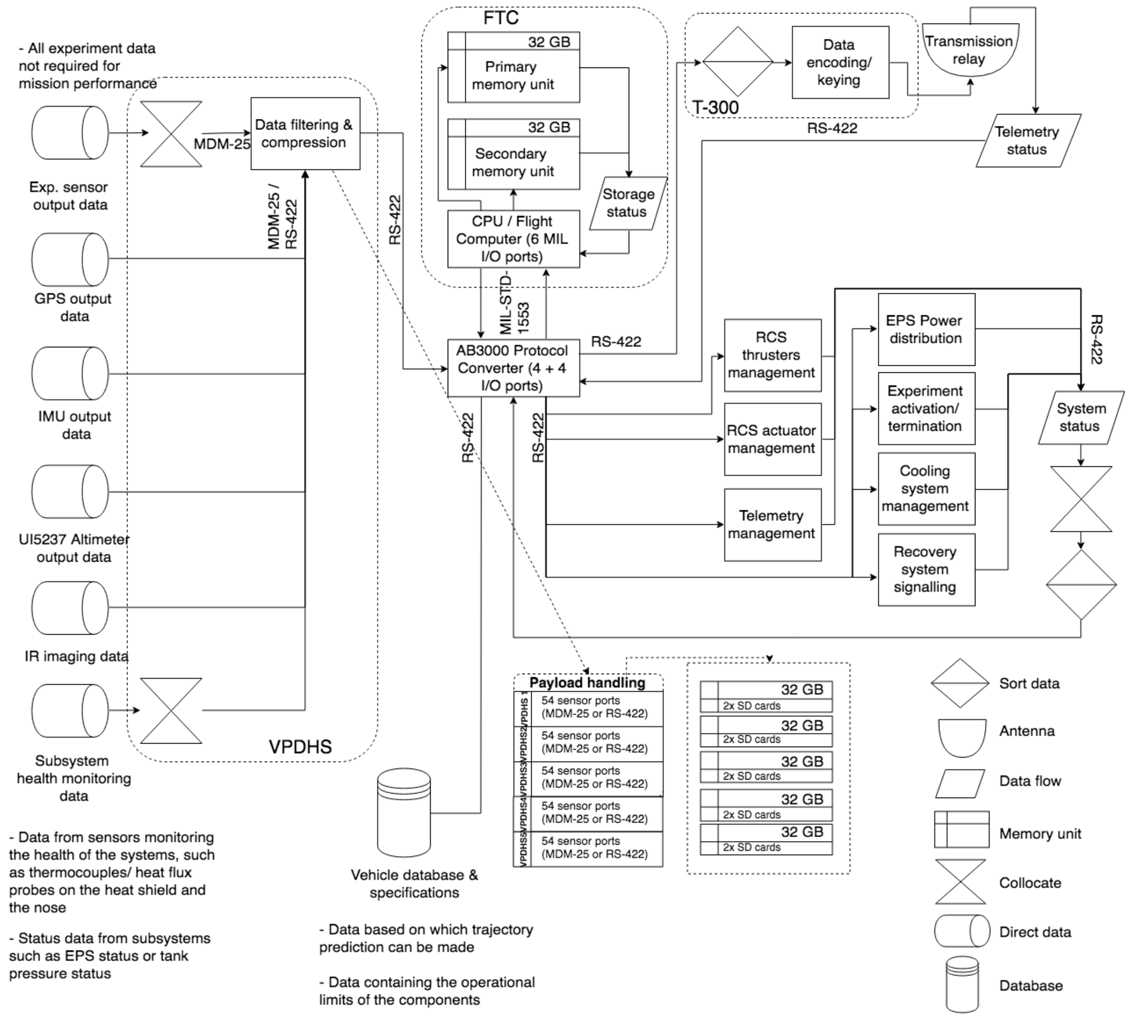

Figure 20.1: Software Diagram

Two types of inputs are sent into the flight computer; firstly, the actual data from sensors or from the database, and secondly, the operation statuses of the subsystems to indicate their health. Three types of output data is distributed by the computer; the processed measured data either sent to the memory banks or to the communication subsystem for transmission; the desired configuration or operation settings to the subsystems such that proper functionality of the vehicle is ensured; and finally, simple switch on and switch off triggers to subsystems such as recovery or the active cooling subsystem to initialize or terminate their operations. Since these data signals result in a physical activity of the subsystems, they are also included in the hardware diagram. The explanations to the symbols used are included in the diagram legend.

The top level hardware connections are far more simple, as can be seen on Figure 20.2. The hardware diagram shows only links that should translate into physical movement or other type of mechanical activity of the subsystems. Since the electrical connections are shown in the electrical block diagram in Chapter 21, they are not considered in hardware diagram anymore.

Signalling from the FTC is sent to the RCS thruster interface, where it is converted in the movement of valve actuators regulating the tank pressure and thrust levels. Similar operation is done with the active cooling subsystem, where the valve actuators operate the settings of the helium and water tanks for cooling.

In case of the recovery subsystem, the recovery system firing circuit initiates the firing of the pyro bolt using a pyrotechnic charge to release the parachute. To activate the recovery system in the first place, a mechanical switch is needed triggered by the separation of the launcher. The mechanical switch signals to the FTC that the recovery is active only once separation is performed to prevent opening of the parachutes while inside the launcher.

For the telemetry, the gain can be controlled directly by the FTC. Otherwise, if automatic gain control is programmed, which is possible for the current transmitter and amplifiers, it can be automatically optimized between the transmitter, amplifiers and the antenna. Thus, the voltage or current pulse to trigger the gain change can propagate either from the FTC, or between the telemetry instruments themselves.

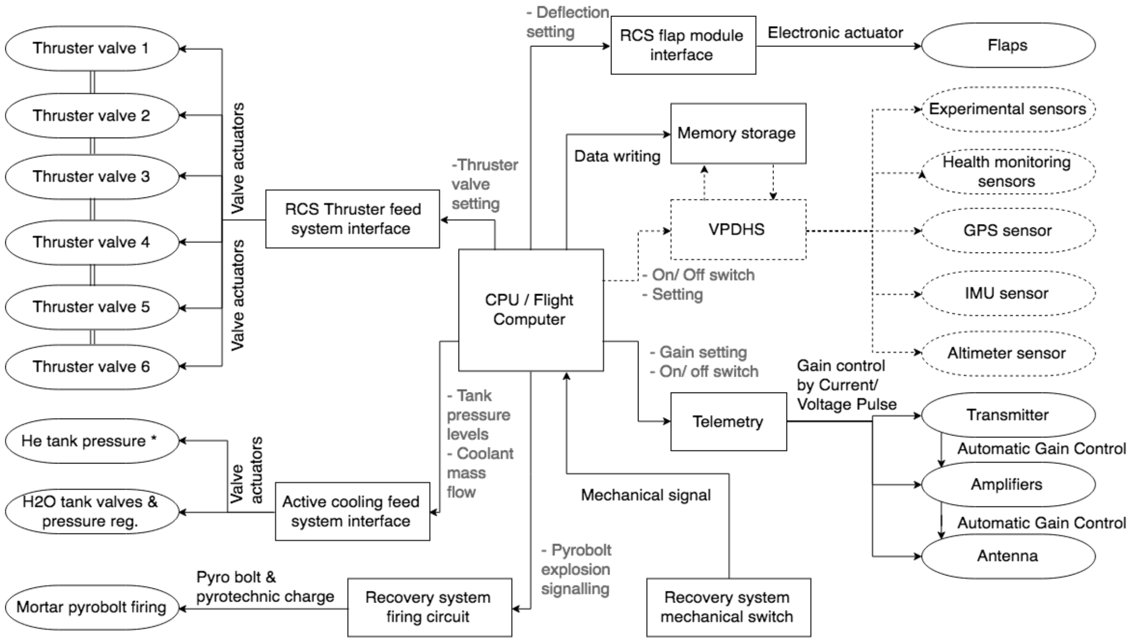

Figure 20.2: Hardware Diagram

The FTC can also initiate writing of the memory storage, which is composed both of the VPDHS memory cards and of the cards within the FTC itself. Finally, control of the data sensors is possible if such sensors are included later in the design. At this design phase however, no such sensors were suggested in the vehicle, and thus the lines are dashed.

20.5.1 Possibilities for Customer Payload Integration

With the current number of sensors, in the fifth VPDHS unit, there are still 40 sensor connections available. Since the data budgets are still not filled completely, storage for a possible customer payload is also available. The additional sensors of the customer shall be able to communicate through either RS-422 or MDM-25, with 4 interfaces still open for imaging data sources such as cameras. Optionally, also a MIL-STD-1553 payload can be considered, since the converter is currently included on board. This might, however, decrease the speed of data reading and data writing. The biggest limitation on the customer payload is thus not the data connection, but rather the power, discussed in Chapter 21, and volume.

20.5.2 Command and Data Handling Budget and Recommendations

From the configuration above, the budgets are summarized in Table 20.1. Contingency of 1.5 to both mass and power budget was included to compensate for the components that were not considered, such as simple I/O modules for the subsystems or excessive cabling.

Table 20.1: Command, data handling and avionics budget breakdown

Component	Volume cm^3	Mass, kg	Power, W
Payload data handling unit (VPDHS), 5x	29 x 19.2 x 17	11.5	75
Fault Tolerant Computer (FTC)	29 x 16 x 25	6.5	40
Inertial Measurement Unit (IMU)	8.7 x 8.7 x 5.45	0.7	5
Altimeter	8.4 x 0.3 x 0.2	0.012	<1
Protocol converter	13.5 x 19.5 x 7.1	2.3	10
Contingency 1.5	1.5	1.5	

Even though the communication protocols and data storage were considered during the design, during the next iteration phase, the data rate between the separate units and the frequency of the communication links have to be analyzed. Additional components might be necessary to account for the possible discrepancies or low data rate, which is another reason for the 50% added contingency to the budgets.

The reminder of the on board instruments not yet mentioned belong to the electric power system vital for power generation and distribution, described in the next chapter.

21 Electric Power System

As all modern aerospace vehicles are known to consume electrical power, the Hyperion IV vehicle forms no exception. Carefully providing a breakdown of the electrical power usage of the vehicle is important from multiple perspectives, such as cost, mass and volume. A bottom up approach was conducted per department to establish a complete breakdown, in which is shown how much power is consumed in total per department as well as per device. This allows in turn to provide information on how much power the vehicle consumes as a whole, but also on how heavy the EPS subsystem is going to be, how much space is occupied by the EPS subsystem and how much the EPS subsystem is going to cost on a total basis.

Hence, based on the method applied in designing the EPS subsystem no trade-off was performed.

21.1 Requirements on EPS

Based on the critical user requirements presented in Section 3.4, the following requirements were derived regarding the EPS subsystem to assure proper design

- EPS.REQ.1 **The means for guidance & navigation, as well as the means for control, shall together consume 350 W of power at most**: This requirement originates from the requirements SYS.CR.4 and SYS.CR.5.
- EPS.REQ.2 **All the means contained in the platform for experimental testing shall consume at most 40 W of power**: This requirement originates from the requirement SYS.CR.7
- EPS.REQ.3 **The means for transmitting data through communication link and upon vehicle retrieval shall consume together at most 200 W of power**: This requirement follows from the requirements SYS.CR.9 and SYS.CR.11.
- EPS.REQ.4 **The means for storing data on board the vehicle shall consume at most 130 W**

21.2 EPS Budget Breakdown

The complete EPS breakdown for the Hyperion IV is shown in Table 21.1.

Based on the estimated maximum power which is needed for running all hardware on the Hyperion IV as shown at the bottom of Table 21.1, it was decided to use two DC-DC converters which together are capable of providing up to 1000 W of power. The reader should not get surprised by the fact that the maximum total power of the EPS subsystem is actually higher than the 1000 W of power, as the maximum total power will never be achieved (otherwise this would imply that all EPS devices are operational at the same time, which will never occur during service). These converters are fed by a voltage input in the range of 180 - 420 V DC. This voltage input is provided by a power supply made out of 100 Li-Ion polymer batteries, each providing a voltage of 4.2 V DC.

A complete outline for the EPS is provided with the Electrical block diagram shown in Figure 21.1.

21.3 Meeting the Requirements

In this section, a brief discussion is provided on how each of the subsystem requirements established in Section 21.1 were met.

- EPS.REQ.1: This requirement was met. Power consumption has been estimated to be 338.7 W.
- EPS.REQ.2: This requirement was met. Power consumption has been estimated to be 36.11 W.
- EPS.REQ.3: This requirement was met. Power consumption has been estimated to be 160 W.
- EPS.REQ.4: This requirement was met. Power consumption has been estimated to be 115 W at maximum.

21.4 Recommendations

Based on the design performed in this chapter, the design team has no clear recommendations on the EPS subsystem other than to establish contacts with ESA-affiliated companies to guarantee the provision of recognized off the shelf electric devices and sensors.

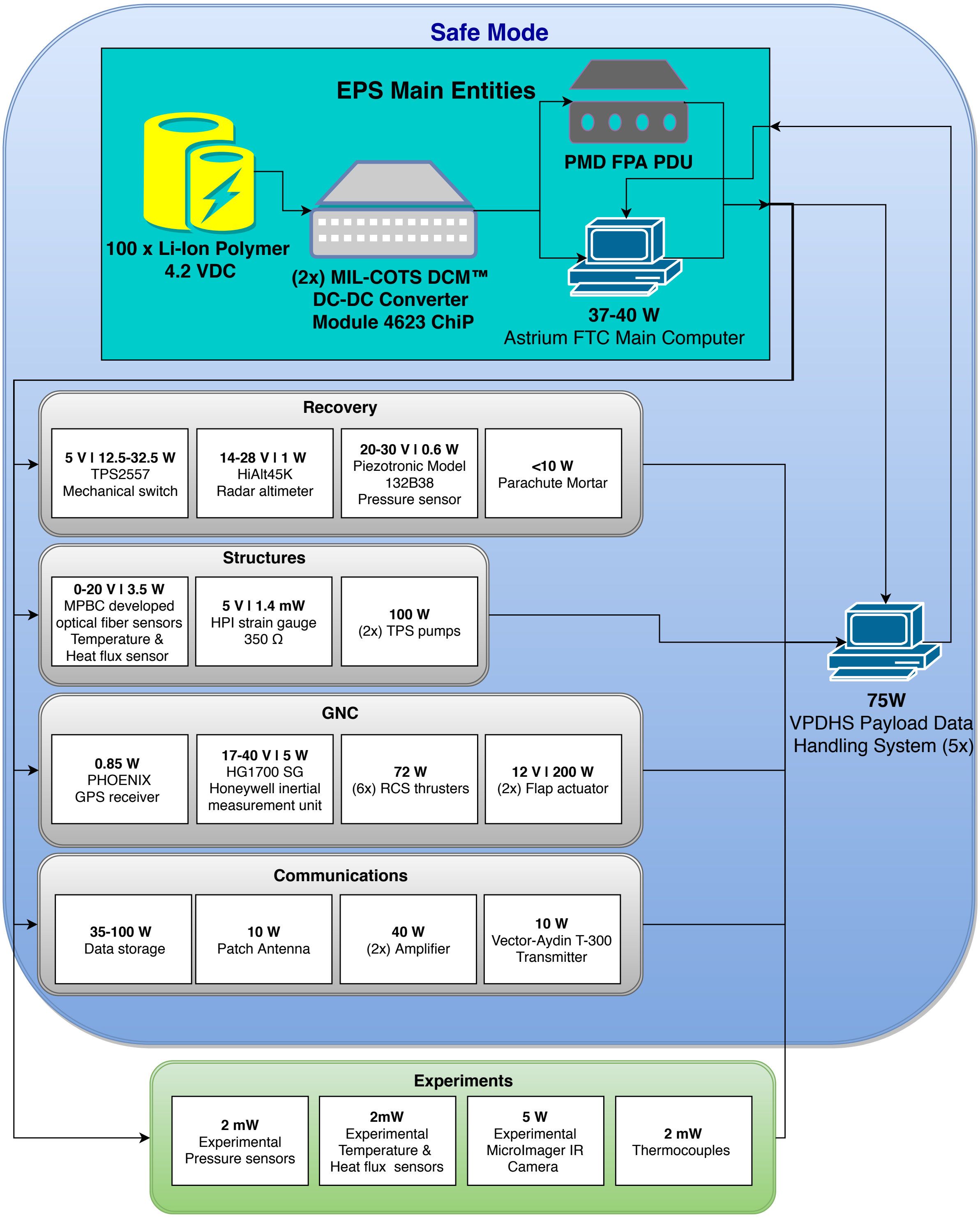

Figure 21.1: EPS Block diagram of the Hyperion IV

Table 21.1: Power budget breakdown for Hyperion IV

Department	**Min. Power usage (W)**	**Max. Power usage (W)**
Main EPS entities		
Astrium FTC main computer	37	40
VPDHS payload data handling system (5x)	-	75
Protocol converter	-	10 W (total)
Harness	-	70.1 W (total)
Total	**37**	**199.9**
Launch & Recovery		
TPS2557 mechanical switch	12.5	32.5
HiAlt45K radar altimeter	-	1
Parachute mortar	-	<10
Pyrobolt	-	33
Total	**12.5**	**76.5**
GNC		
PHOENIX GPS receiver (2x)	-	1.7
DMARS-R attitude sensor	-	5
RCS thrusters (6x)	0 (non-active)	72 (nominal)
Flap actuator (2x)	-	200
Total	**0**	**278.7**
Communications		
Data storage	35	100
Antenna	-	10
Amplifier	-	40
Vector-Aydin T-300 Transmitter	-	10
Total	**35**	**160**
Materials & Structures		
MPBC developed optical fiber sensors - temperature & heat flux sensors	-	33.6
TPS pumps (2x)	-	100 W (total)
Total	**0**	**133.6**
Experiments		
Instrumentation's	-	0.11
IR camera	-	36
Total	**0**	**36.11**
Contingency		**66.35**
Total EPS power	**84.5**	**946.35**

22 Project Design & Development Logic

This chapter is going to describe the project design and development logic, as well as operations and logistics of the Hyperion IV project. The activities mentioned are classified into the project management phases used by ESA described in Puech (1996) and shown by Figure 22.1. The overall schedule is described by Figure 22.2. The design reviews and their respective dates are shown in the Gantt Chart as milestones as defined in Amend et al. (2018a). The milestones in chronological order are: Critical Design Review (CDR), Qualification Review (QR), Acceptance Review (AR), Operational Readiness Review (ORR) and Flight Readiness Review (FRR). Activities and milestones before the start of phase C, starting with the Project Design Review (PDR), are not shown, as they are already completed. The milestones represent beacons of the validation and verification activities occurring consistently over all phases until phase F. Phase C mainly regards management activities to ensure a pass of the CDR, like requirement verification, and a smooth transition into production activities. Qualification and verification models have to be produced followed by the start of qualification testing. The bulk part of phase D are the concurrent activities of production, assembly, and acceptance testing. The qualification testing, the verification of the subsystem requirements, has to be completed in phase D. Phase E mainly includes the functional and flight testing of the manufactured vehicle, as well as the ground operations, concluded by the ORR and FRR. As seen by the Gantt charts below (Figures 22.1 and 22.2), the whole project highly relies on effective concurrent engineering, typical for space projects on a European scale.

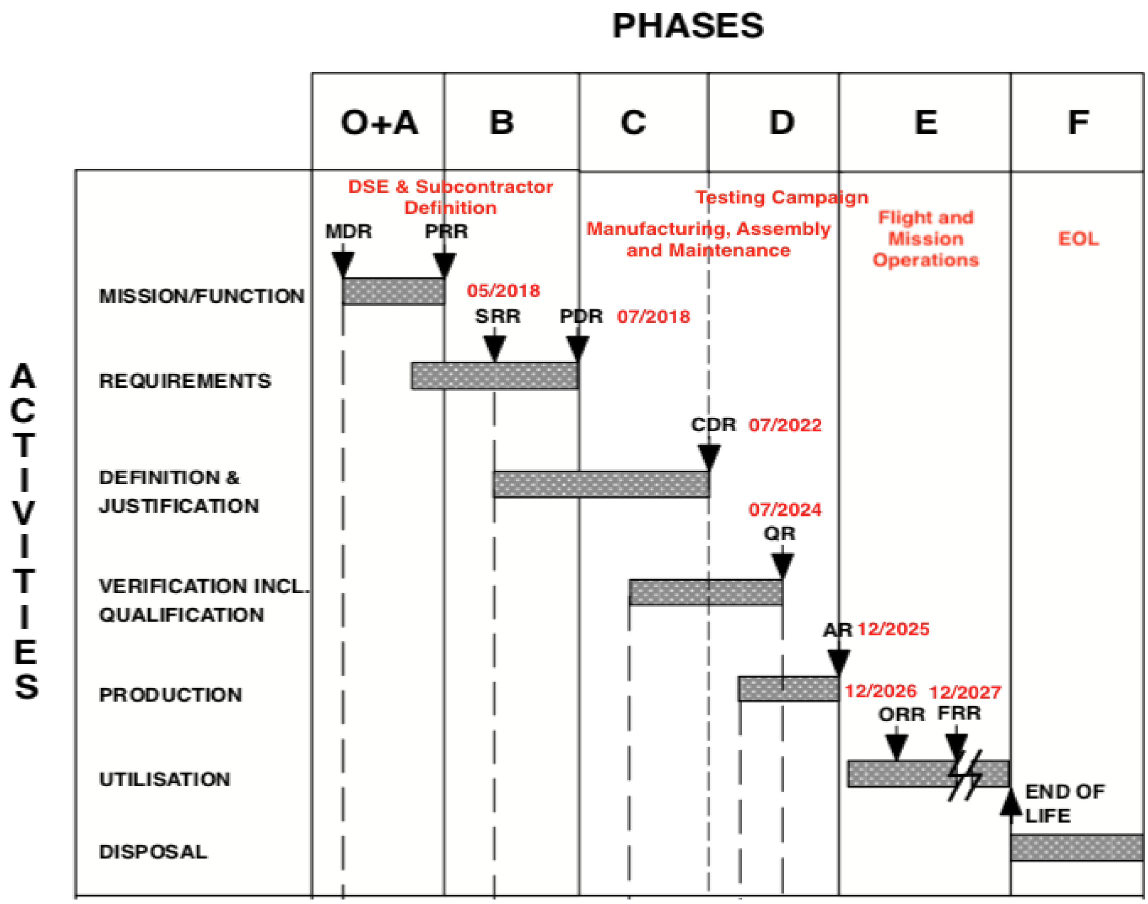

Figure 22.1: ESA project management phases and activities

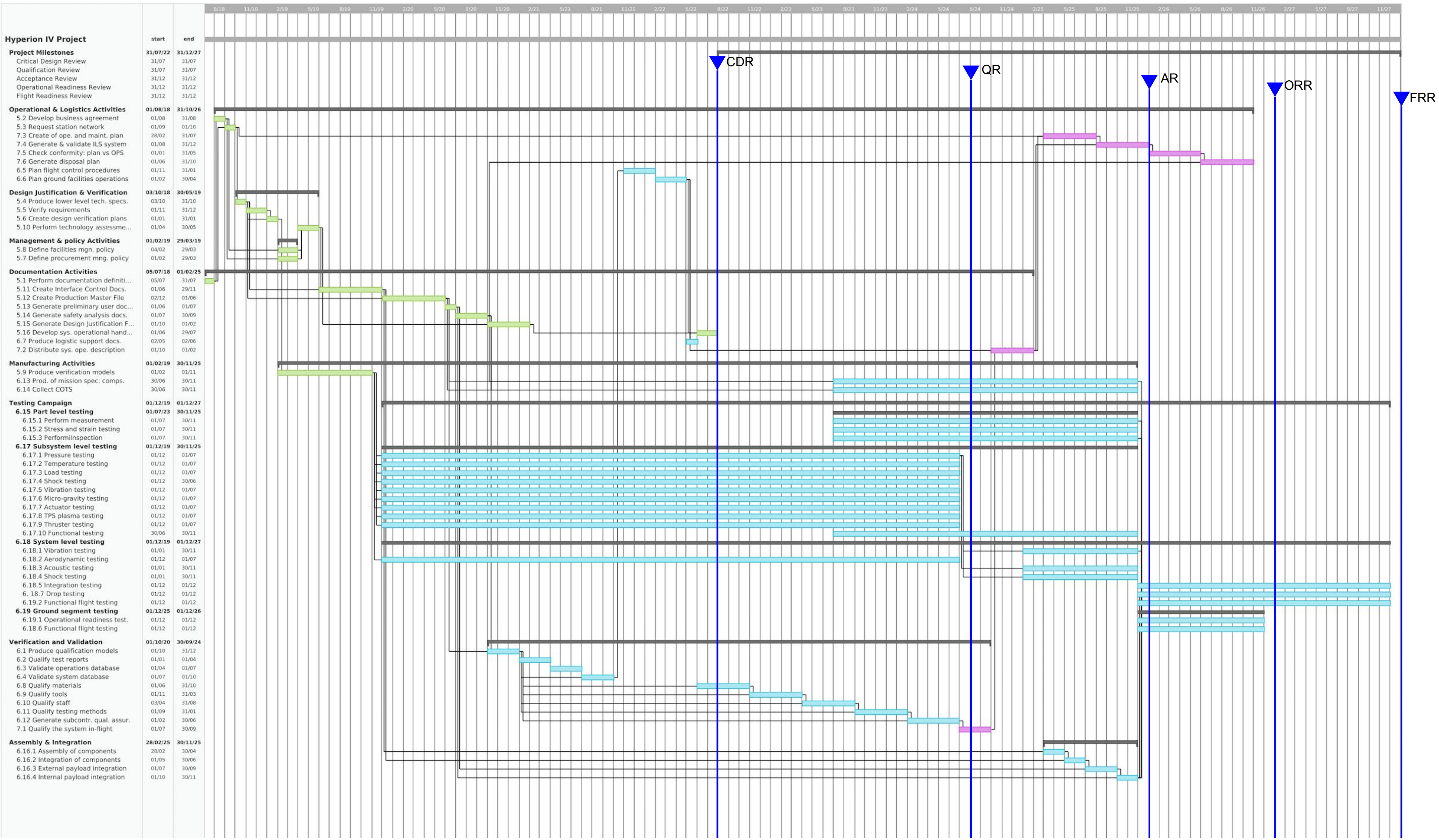

Figure 22.2: Gantt Chart

22.1 Phases 0 + A & B: DSE

This phase happens during the nominal DSE project. Here the vehicle will be designed using a systems engineering-centered approach, and a certain level of detail will be reached for all subsystems. This report is the presentation of the mentioned design, and with its submission this phase comes to an end.

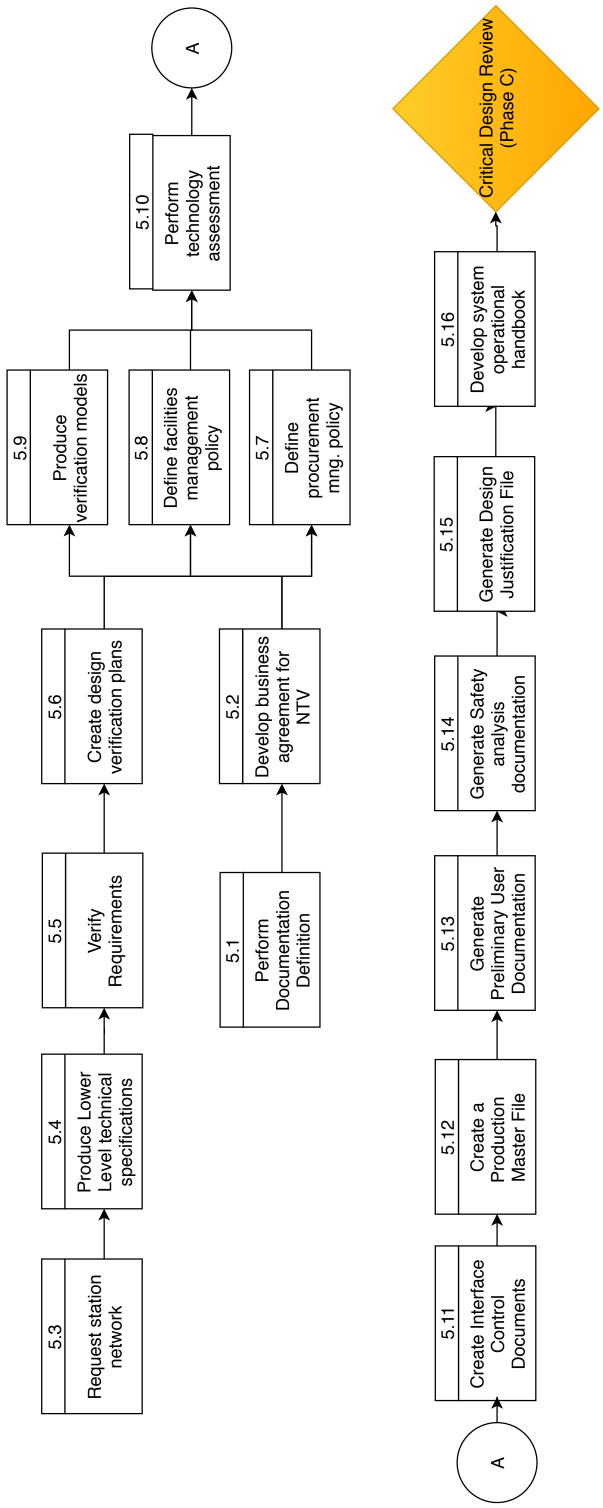

Figure 22.3: Work flow until CDR

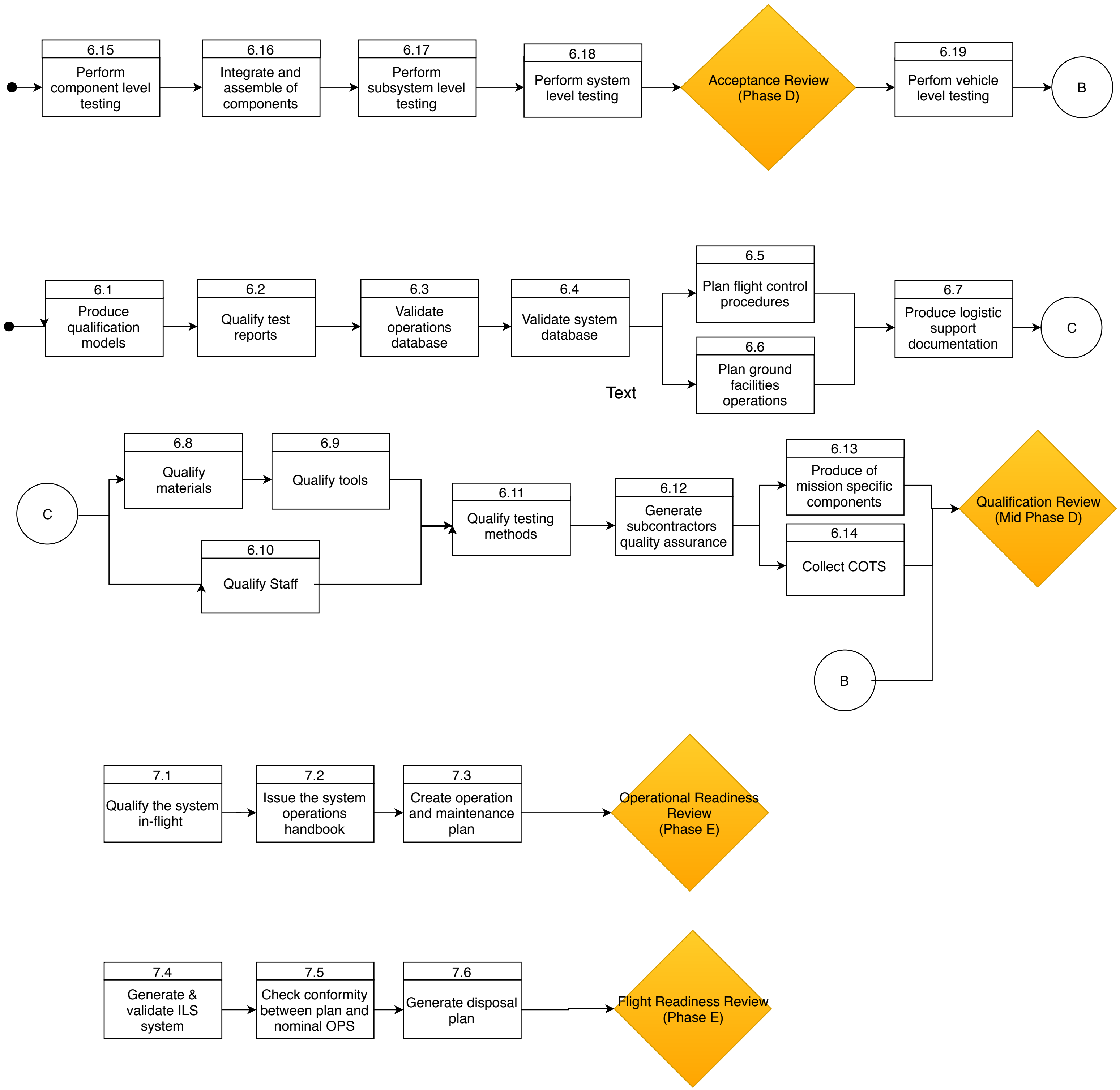

Table 22.1: Work Flow Diagram for phases D and E

22.2 Phases 0 + A & B: Subcontractor Definition

Based on the analysis of the mission elements and subsystems, and based on the analysis of past missions, subcontractors for the separate work packages were proposed. The proposed contractor work distribution is shown on Figure 22.4.

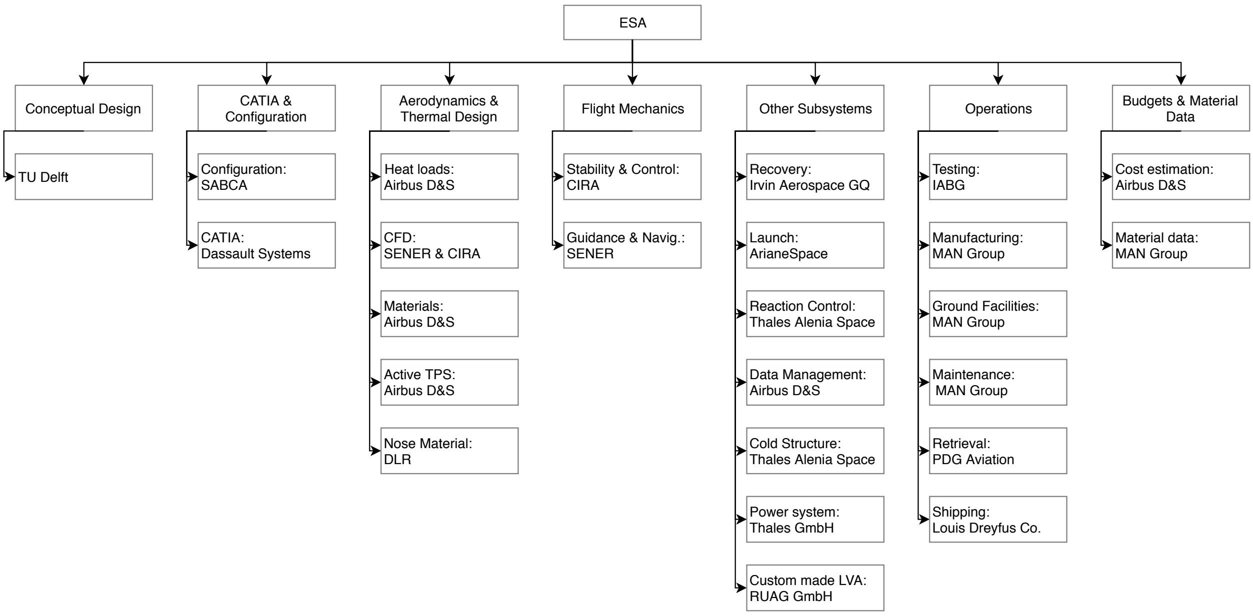

Figure 22.4: Suggested ESA subcontractors for selected mission elements and subsystems

The conceptual design is done in this report by Delft University of Technology. SABCA Aerospace and Dassault Systèmes will be responsible for the CAD design and configuration layouts. Since the material used for the nose tip is developed within DLR, this organization is suggested as the subcontractor for the nose material design. Due to their past experience, Airbus D&S can take the responsibility of predicting the rest of the heat loads, including the rest of the material and TPS design. The guidance and navigation subsystem can be designed by SENER as in case of previous reentry vehicles, and the stability and control design for ESA is typically done by CIRA in Italy.

The resulting design of the RCS and data management systems, including TT&C, will be produced by Thalen Alenia Space. Since mid-air retrieval is chosen as a method of recovery, PDG Aviation is proposed to take over the recovery operations work package, and as the Vega launcher is selected for launch, the launch work package can be shifted to ArianeSpace. Based on the previous missions, the rest of the subsystems, such as the cold structure and the power subsystem is suggested for Thales Alenia Space. The custom made LVA is produced by RUAG GmbH.

Shipping of the vehicle to French Guiana is proposed to Louis Dreyfus Company, which have already experience in transportation of satellites across the Atlantic. Handling of the tests is proposed to IABG. The rest of the operations, including ground facilities, maintenance and manufacturing can be handled by MAN Group in the United Kingdom. Due to their vast manufacturing experience, MAN group can also provide material databases for budgeting. Finally, the cost estimation is typically carried out by Airbus D&S.

22.3 Phases C, D & E: Testing Campaign

This section elaborates on the testing actions as described in the Gantt Chart. The testing activities are split up into subsystem and system tests, both including tests necessary to pass the QR, AR, ORR, and FRR. Therefore, the testing campaign is a concurrent activity present during the whole project guiding the validation and verification activities. The proposed testing campaign spans from phase C to phase E of the ESA project management framework. In phase C all testing conditions for the overall system, each subsystem, and even parts have to be fixed. This enables the project team to develop and manufacture the parts and models needed for the ground-based testing. In phase D the ground-based testing is completed. The technical compliance with the requirement is checked during QR. Additionally, the testing is accompanying the production of the vehicle, leading up to the AR. Flight system level tests on the produced vehicle are conducted in phase E and being summarized at the FRR (Puech, 1996). This includes all verification tests for the Vega launcher. To sum up, all needed specimen and test dummies have to be specified and produced between August 2018 and November 2018. Qualification testing to assure compliance with the technical

requirements has to be conducted between December 2019 and July 2024. This includes subsystem and system ground testing. The final product testing accompanying the production has to be conducted from July 2023 to December 2025. Functional operations and logistics testing is conducted between December 2025 and July 2026. Functional flight, drop, and integration testing is conducted between December 2025 and December 2027.
The following testing locations were deemed practical to conduct all following described tests.

1. Vibration testing: Hydraulic Multi-axis Shaker at ESTEC, the Netherlands[1]
2. Small scale wind tunnel testing: GHIBLI Plasma Wind Tunnel in Italy and Von Karman Institue Plasma Wind Tunnel[2] [3]
3. Large scale wind tunnel testing: SCIROCCO Plasma Wind Tunnel and High Enthalpy Shock Tunnel Göttingen (HEG), in Germany [4]
4. Drop testing: Biscarrosse range in France, Salto di Quirra range in Italy, Kiruna range in Sweden
5. Acoustic testing: Large European Acoustic Facility (LEAF) at ESTEC, The Netherlands[5] and the Industrieanlagen-Betriebsgesellschaft (IAGB) test center in Ottobrunn, Germany.
6. Shock testing: ESTEC, the Netherlands
7. Static and dynamic characteristic testing: IABG test centre in Ottobrunn, Germany[6]
8. Measurement and simple stress tests: Directly at the manufacturing company.
9. Integration test: at ESTEC, the Netherlands
10. 0 g-load test: European Altered Gravity Aircraft [7]

22.3.1 Subsystem and Component Testing

As explained, subsystem and component testing are mostly present in phase C and D, assuring a qualified design and production. First the most important general subsystem tests concerning all subsystems are outlined, followed by subsystem tests specific for the most important subsystems of the Hyperion IV vehicle.

During the production each part and assembly has to be measured to pass the AR. It has to be assured that the measurement instruments are sufficiently calibrated. A respective quality assurance process has to be implemented at the manufacturing site. This also applies for off-the-shelf products. Certain parts, like the structural components, can also undergo stress and strain tests directly after production.

A general subsystem level testing cycle to assure the compliance with the technical requirements is explained by Moreau (1995). The most important subsystem tests of it, dictated by the mission constraints and the mission environment at hand are pressure, temperature, acceleration, micro-gravity, and shock testing.

As not all of the vehicle interior will be pressurized, some parts are going to be exposed to a static pressure tending to zero. This is accompanied by a wider temperature range as compared to ground operations. Therefore, sub-assemblies should be tested under vacuum condition.

During launch and deceleration in the reentry phase substantial g-loads act on the vehicle and therefore on the single parts as well. Parts and sub-assemblies vulnerable to high loads, for example assemblies with loose parts, have to be tested for the acceleration. The predicted acceleration range was estimated to be 7g in x and z direction of the body frame reference system.

For a short time interval the vehicle will experience micro-gravity. This can impose a threat to assemblies and feed systems. Therefore, those subsystems should be tested under 0 g loads.

Especially during the separation from the launcher and the parachute deployment high shock loads act on the vehicle. Therefore, subsystems have to be tested for shock loads up to 7g, the maximum shock load occurring during launch.

One of the most important subsystems of the mission is the TPS. The TPS has to be tested in a high speed wind tunnel to assess its effectiveness at high temperatures. Additionally, tests in a plasma tunnel have to be conducted to account for the chemical reactions taking place at the present flight regime. Both tests have to be conducted for a TPS tile specimen of each type and the nose cone. The nose cone tests are conducted with and without active cooling in the respective temperature range. Additionally, ablation tests

[1] https://www.european-test-services.net/services-mechanical-Hydra-Vibration.html,lastaccessedon23/05/2018

[2] https://www.cira.it/en/research-infrastructures/plasma-wind-tunnels/Plasma%20Wind%20Tunnel%20Complex, last accessed on 22/05/2018

[3] https://www.vki.ac.be/index.php/research-consulting-mainmenu-107/facilities-other-menu-148/high-speed-wt-other-menu-158/69-mach14-free-piston-hypersonic-wind-tunnel-longshot, last accessed on 13/06/2018

[4] http://www.dlr.de/as/en/desktopdefault.aspx/tabid-190/391_read-49620/ last accessed on 25/05/2018

[5] http://sci.esa.int/lisa-pathfinder/43462-lisa-pathfinder-modules-ready-for-acoustic-tests/, last accessed on 22/05/2018

[6] https://www.iabg.de/en/business-fields/space/mechanical-tests/, last accessed on 23/05/2018

[7] https://www.esa.int/Our_Activities/Human_Spaceflight/Research/European_space_agencies_inaugurate_altered-gravity_aircraft

have to be conducted for the nose cone material. For each specimen 10 to 20 tests should be conducted. The temperature range for the tests without active cooling are 1000 to 1600 Kelvin, and for tests with active cooling 2300 Kelvin. All gathered data is used to validate the requirements as well as the used calculation software.

As the vehicle is only able to fly the required range by controlling its attitude precisely, reliable thrusters and body flap actuators are of high importance. The force delivered by the thrusters has to be tested in an ambient pressure range of 100 to 1 Pa, while he actuators need to deliver the required acceleration to move the body flap 25g.

To pass the acceptance tests, every subsystem present in the flight-ready vehicle has to be functional tested under the most possible realistic conditions. The tests represent a combination of the above mentioned, and are conducted on the actual subsystem used.

22.3.2 System Testing

System level testing is conducted during phase D and E, including ground and flight tests for both the flight model and the ground operations part. A base drive vibration test has to be conducted to assess if the vehicle can withstand the vibrations induced during the launch. The test has to be conducted with the final flight model for it to pass the ARR. The sine-equivalent induced vibrations that should be tested are shown in Table 22.2, based on Perez (2014). Stringer drive vibration testing should be used for modal vibration testing to validate used calculation software. Additionally, it is required to measure the natural frequencies of the vehicle. This is done by exciting the structure and measure its response. The Vega rocket imposes certain constraints to the natural frequency of the payload. Lateral frequencies should be larger than 15 Hz, and longitudinal frequencies either between 20 Hz to 45 Hz, or larger than 60 Hz (Perez, 2014).

Table 22.2: Sine-equivalent vibrations from Vega launcher

	Frequency Band (Hz)			
	1-5	5-45	45-110	110-125
	Sine Amplitude (g)			
Longitudinal	0.4	0.8	1.0	0.2
Lateral	0.4	0.5	0.5	0.2

High speed wind tunnel tests have to be conducted to validate the aerodynamic behaviour estimated by simulation. As even the larger high speed wind tunnel are not able to accommodate the full sized model, a dummy shape has to be used. The tests should be conducted at the whole Mach number and angle of attack range. Additionally, boundary layer transition and boundary layer shock wave interaction has to be tested to obtain data for comparison with the in-flight experimental data gathered.

Acoustic tests are carried out to make sure the system can withstand and survive the intense noise generated by the launch vehicle engines after ignition. A key aspect of these tests is to better characterize the vibration loads that the vehicle instruments withstand. Data obtained during acoustic testing will prepare the vehicle for mechanical testing; it will avoid exposing delicate instrument to unnecessary mechanical loads. The acoustic test has to be conducted with the final flight model for it to pass the ARR. The noise spectrum based on the lift-off noise generated by the Vega rocket ranges from 110 to 140.3 dB and 31.5 Hz to 2828 Hz deduced from Perez (2014).

The final flight vehicle has to be tested for shocks generated mainly during the launch and the parachute deployment. As the parachute system is tested during the drop test, the respective shock is not tested here again. Shock tests are conducted typically by initiating the device that will cause the shock loads during the flight. Those systems usually involve pyrotechnic devices firing. To demonstrate this situation and to be able to test it, the following procedure is taken. First, the spacecraft is suspended, and the separation charge is fired. Next, the launch adapter section below the separation plane drops a few inches to a soft cushion, as described in Roe (2014). The shock response curve for separation and staging of the Vega rocket can be retrieved from Perez (2014). Combined with the natural frequencies of the vehicle one can determine the maximum shock loads which have to be induced.

To be able to launch Hyperion IV and properly follow the trajectory, precise information about all static and dynamic characteristics is needed. This includes wet and dry mass, mass and area moment of inertia, exact centre of gravity, and the dimensions of the vehicle.

To pass the FRR an integration test with the Vega launcher has to be conducted. It is sufficient to use the adapter and launch envelope of the Vega rocket for this purpose only.

Additionally, a functional tests of the actual flight-ready vehicle is conducted. The functional tests should simulate the use of all systems, the connection with the operations and logistics concept, and the environmental conditions as accurate as possible. The mission sequence has to be followed precisely to detect possible flaws.

All Operational mission components have to undergo operational readiness and functional testing to pass the ORR. This should include all possible sub-contractors active in the operational sequence.

Finally, one of the most important tests to be conducted is the drop or flight test. A drop test has to be conducted to test the recovery and mid air retrieval system, as well as the control surface efficiency in subsonic flight. It is proposed to lift a dummy vehicle with the needed systems on board by a helicopter to around 4 km altitude, being a compromise between actual recovery altitude and altitude a helicopter is able to reach. After reaching the required altitude, the dummy vehicle is released and the parachute deployment triggered. Before triggering the parachute, data about the effectiveness of the control surfaces is gathered.

22.3.3 Testing Operations and Logistics Concept

The analysis of the testing phase from an operational and logistical point of view is performed in this subsection. All manufacturers and test sites, exception made for Salto di Quirra test range are located in continental Europe, while the latter is located in Sardinia. Ferry services are present, therefore road transportation is the preferred way of moving parts in this phase.

Test sites shall be arranged no later than 24 months before the test day. This is done to secure the test site and avoid having to reschedule the test.

22.4 Phases C & D: Manufacturing, Assembly and Maintenance

After the preliminary proposal of the subcontractors and identification of the Component off the shelf (COTS) components, the manufacturing, assembly and integration planning can take place.

Table 22.3: List of COTS and custom made components of the vehicle

Category	COTS	Supplier	Custom made
Structures	Assembly equipment	-	Titanium structure
Materials	PhenCarb	ARA	Overall TPS structure
	OCTRA C/C-SiC	DLR	TPS/TPS interfaces
	TUFROC	NASA	TPS/STRC interfaces
	WHIPOX	DLR	He tank & feed system
	Cerambond adhesive	Aramco	H2O tank & feed system
Telemetry	T-300 S/L transmitter	Victor Aydin	Patch antenna
	High gain amplifiers	-	Telemetry data links
	Phoenix GPS receiver	DLR	
Command & Data Handling	VPDHS payload unit	Vectronic Aerospace	Subsystem comm. links
	Astrium FTC computer	Airbus D&S	Subsystem I/O interfaces
	Protocol Converter	Ballard Technology	Subsystem data links
	HG1700 IMU	Honeywell	Subsystem switches
Launch			LVA & attachments
Recovery	HiAlt45K Altimeter	United Instruments	Firing circuit
	Canopy	-	Canopy
	Suspension lines	-	Drogue
	Pyro bolt	-	Mortar
	Radial tapes	-	Mech. initiation switch
Reaction Control	RCS fuel tank	VACCO	Nitrogen tanks
	RCS triad thrusters	Moog	Directional nozzles
Electric power subsystem	Li-Ion batteries	-	Power distribution unit
	DC-DC converters	MIL-COTS DCM	Subsystem power links
Instruments	Pressure transcuders	-	Specialized sensors
	Thermocouples	-	Customer experiments
	Strain gauges	-	
	Heat flux sensors	-	
	IR camera	Micro-Epsilon	

22.4.1 Manufacturing Activities

The manufacturing activities can be split into the activities related to the COTS (Component off the shelf) components that need to be collected and qualified only, and the components that have to be manufactured specifically for the mission. The latter is analyzed first, followed by the COTS component analysis. Based on the subsystem design, the summary of which COTS products can be used and which components have to be designed is shown in Table 22.3. If the components can come from several suppliers, or if the supplier was not yet selected, an "-" is placed to the supplier cell.

22.4.2 Structural Assembly

The assembly will be performed using dedicated assembly jigs. The proposed top level steps during the assembly are shown on Figure 22.5. The reason for this order is the fact that TUFROC windward shield is far more durable and fracture resistant compared to the relatively thin SPFI material. Thus, most of the assembly will take place using the windward shield as a support structure. The inner structure will be fixed to the TUFROC tiles using fasteners. Afterwards, since the inner structure provides interface for the subsystems, the subsystems will be placed around the inner structure. Once the subsystems are positioned, the vehicle will be closed using the SPFI insulation. TUFROC leading edges will be afterwards added to close the wings of the vehicle. Finally, since nose is material-wise the most sensitive part of the vehicle, it will be attached the last.

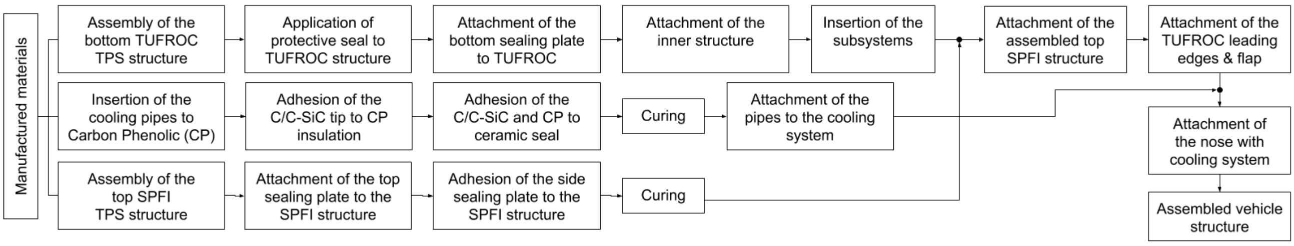

Figure 22.5: Top level assembly sequence

22.4.3 Payload Integration with the Vehicle

Payload integration is possible either inside or on the outside of the vehicle. In case of external payload, a platform of 15 x 15 x 7.5 cm is provided, where the payload is exposed to heat fluxes of up to 100 kW/m^2 and temperatures of up to 1900 K. The weight of 2 kg (estimated maximum mass of a test tile for the given platform) shall not be exceeded. Five thermocouples, one heat flux sensor and one pressure sensor are included to measure the conditions on the platform.

Internal payload can be a plate on which various items can be attached, of 30 by 30 cm in size. This has to be attachable to either the inner bottom sealing plate or to the structural frames. In case the payload has to be pressurized, the customer is responsible for providing the pressurization system.

The payload shall not pose any hazard to the rest of the vehicle. The attachment of the customer payload has to be detachable without damaging the structure or the platform. The integration of the payload takes place after maintenance activities, and after the payload is subjected to testing.

22.5 Phase E: Flight and Mission Operations

Phase E begins after the Acceptance Review. Once the vehicle is fully assembled, it will have to pass the Operational Readiness Review and the Flight Readiness Review. Phase E is divided in pre-flight mission operations, flight operations, recovery operations, maintenance operations and refurbishment operations.

22.5.1 Pre-Flight Operations and Logistics

The Vega launcher, operated by Arianespace, is launching from Guiana Space Center (Centre Spatiale Guiannais, CSG) in French Guiana. Its geographical location has consequences on the logistics and operations of the project. The vehicle will be shipped by sea from Rotterdam harbor to Cayenne Dégrad-des-Cannes international harbor. Louis Dreyfus offers a roll-on roll-off service, meaning that the vehicle can be directly loaded onto the vessel, inside a truck transporter trailer. The dimensions of the fully assembled vehicle allow it to fit within a standard shipping container, greatly easing the transporting operations. To comply with long water shipping times, the vehicle shall be shipped 4 weeks ahead of the launch window opening, along with all the ground systems.

22.5.2 Launch Campaign & Flight

The Launch service is provided by Arianespace for the whole sequence of 20 flights. Arianespace will handle the launch and flight from beginning of combined operations until separation from the LV.

The Vega user manual Perez (2014) explains in great detail all the operational and logistical aspects within the CSG. The launch campaign starts at the moment the vehicle arrives at the Kourou harbor and is unloaded from the vessel. As a requirement from Arianespace Perez (2014), no more than 21 days shall pass between the arrival in Guiana and the start of combined operations. This means that there are 21 days to prepare the vehicle on site for launch, before it is handed over to Arianespace. The vehicle shall also be handed over to Arianespace no more than 10 working days prior to launch.

Vehicle preparation will occur in a dedicated hangar for the mission. After start of combined operations the vehicle will be transferred to the Payload Preparation Facility in CSG. After which the vehicle will be connected to the LV, transferred to the launch pad and the final countdown will begin.

22.5.3 Tracking Station & Mission Control

During the flight phase, it is important to track the vehicle and ensure downlink of data. The tracking of the vehicle is important to validate the trajectory model and to have a constantly updated estimate of the landing zone of the vehicle. The usage of tracking stations is therefore an important operational and logistical aspect that needs to be taken into account from the early phases of the mission. To guarantee a constant tracking of the vehicle, GPS tracking can be used in the suborbital phase, in combination with the tracking from ground stations. The details of the ground stations are described in more detail in Chapter 19. For every flight, it must be ensured that each one of the tracking stations are operational and available for use. A team of engineers shall be sent, if necessary to the tracking stations to ensure their functionality.

Mission control will be located in European Space Operations Centre (ESOC) in Darmstadt, Germany, since Hyperion IV is a ESA supported mission. A permanent control room shall be set up and dismantled only at the end of phase F, described in Section 22.7. A permanent team of engineers for the mission will be stationed in French Guiana, to coordinate on-site operations and guarantee the correct functioning of the launch and landing operation. Launch operations will also be followed from the mission control center at CSG.

22.6 Vehicle Recovery

The recovery method has been chosen to be mid-flight recovery. This method requires to have a well thought logistical and operational structure, as the recovery operation involves more flying vehicles operating in a civilian airspace. Since the landing zone is within the borders and territorial waters of French Guiana, the operations would be subject to French and European air regulations. Mid air retrieval has been explained in Chapter 12, and PDG Helicopters has been indicated as the company that would provide this service. PDG Helicopters is based in the UK. However, the selected helicopter, the AS350, can be retrofitted easily on-site by engineers from the company. The helicopters will be rented from a local helicopter operator.

Helicopter operations will take off from Kourou Airfield. Since the area to be covered (100 km radius) is too wide for a single helicopter, due to its limited speed, a fleet of 3 helicopters will be required to cover the area. They are displaced based on the probability of landing site, and will be constantly updated and directed to the landing position by the tracking station and coordinated by the operations control in French Guiana.

The helicopter will return the vehicle at Kourou airfield, only 500 meters away from CSG payload preparation facilities. The helicopter will deposit the vehicle onto a tailor made rig, to avoid ground impact, and will be transported to a dedicated area in CSG, where the vehicle will be inspected post flight and refurbished for next flight.

22.6.1 Maintenance

The maintenance of the vehicle will take place after every flight. Different subsystems need different detail in maintenance, with the most critical ones requiring thorough inspection every flight. Table 22.4 summarized the preliminary plan for maintenance, indicating the subject, the type of maintenance and the frequency. TPS systems can be accessed externally, while most refurbishment and inspection of the inner systems will take place through the parachute door in the back side of the vehicle. However, if a system has to be replaced completely due to failure, the bottom side of the heat shield can be mounted away, since the TUFROC tiles and the lower inner sealing plate are attached by screws.

Inspection

The inspection phase spans from when the vehicle is delivered to the hangar till the data collection and processing. There are a few key reasons for inspection: firstly, it needs to be assured that the vehicle is safe to approach and handle; this is done mostly by visual and remote inspection. Secondly, it is imperative to determine whether critical or non-critical components of the vehicle are still functioning properly or need replacement: in this case the vehicle will be refurbished in the appropriate phase. Keep in mind that some subsystems such as the Active Cooling, will need refurbishing regardless, and as such will need minimum inspection.

Data Collection

Data collection happens once the internal hard drives have been retrieved, and the data is moved on to the ground station computers. There it will be checked against the cloud data for noise and discrepancies, and after proper verification the hard drive will be replaced within the vehicle.

Refurbishing

As mentioned in Section 22.6.1, the maintenance and refurbishment of the vehicle will take place after every flight. This phase includes, but is not limited to, the refilling of all propellant and water tanks, the recharging of the battery and the substitution of filled data drives. The parachute packing is a critical component of this phase. Suspension lines will be checked for possible burns due to contact with the lower surface of the vehicle and if necessary they will be replaced. The canopies of both the drogue and the main chute will be properly folded and packed in the respective bags, taking care to fold the radial tapes correctly. The pilot chute will be replaced every flight, as it will be ejected once the main is pulled out.

Table 22.4: Maintenance strategy

Item	Inspection / Refurbishment	Method	Frequency	Access point
Nose tip	Inspection	Visual	Every flight	External access
	Inspection	NDT	Every flight	External access
Heat shield + flap	Inspection	Visual	Every flight	External access
	Inspection	NDT	Every 3 flights	External access
Inner structure	Inspection	Visual	Based on T data	The back side
Active H2O tank	Refurbishment	Refueling	Every flight	The back side
RCS N2 tank	Refurbishment	Refueling	Every flight	The back side
Battery	Inspection	Visual	Every flight	The back side
	Inspection	Measurement	Every 3 flights	The back side
	Refurbishment	Recharging	Every flight	The back side
Memory unit	Refurbishment	Reformatting	Every flight	The back side
Flight Computer	Refurbishment	Updating	Every flight	The back side
Parachute	Refurbishment	Re-assembly	Every flight	The back side
Mortar	Refurbishment	Re-assembly	Every flight	The back side
Actuators	Refurbishment	Lubrication	Every 3 flights	The back side
All subsystems	Inspection	Visual	Every 3 flights	The back side
	Refurbishment	Replacement	If failure	The windward vehicle side

22.7 Phase F: End Of Life Operations

End of life operations span from the end of phase E to phase F of the ESA project management work. These operations are necessary between flights to assure that various sponsors and stakeholders are satisfied and that the vehicle is disposed of in an appropriate manner, according to the disposal plan. Some activities analyzed range from the immediate inspection of the vehicle from various expositions and sponsor events organized by the operation committee and other various mission partners.

Expositions and Sponsor Events

After all the nominal mission procedures have been completed, the vehicle will be brought to expositions and other sponsor events. Most of these activities will take place in the continental United States and Europe, and therefore the vehicle will need to be shipped from the operations base to around the world. As mentioned in the Midterm Report (Amend et al., 2018b), the vehicle fits within a standard shipping container, therefore greatly simplifying the logistical problems.

One of the expositions most likely to be interested in the vehicle is the Space Expo in Noordwijk, the Netherlands. This location is coincidentally the final assembly site, and as such it will probably be the last journey the vehicle will make before getting dismantled. This coincides with phase F of the ESA project management standards. Other expositions will include universities and research centers interested in displaying Hyperion IV.

Sponsor events will usually occur at the various companies that sponsored the project; this renders neigh impossible to determine before the production phase where the vehicle will have to be carried. Either way the setup will be similar to the expositions, where posters and critical team members will be shipped to sponsor companies for presentations. Other sponsor events might include active usage of vehicle subsystems such as body flap actuation. These will require vehicle power, and therefore the batteries will need to be recharged beforehand.

Control center dismissal and mission heritage

The last act of Hyperion IV operations is dismissal of the control center, reassignment of the workforce and collection of mission heritage. With the vehicle disposed, the data that has been collected through the whole duration of the mission shall be stored on the ESA internal server, as well as all the technical documents connected to the project. Due to the defense sensitive nature of the project, technical information which could be used for military applications will be classified. Furthermore, all paper copies of the technical reports will be stored in ESRIN, in Frascati, Italy.

In parallel, the workforce directly employed by ESA under the project will be reassigned to different projects. The management will be the last personnel to be reassigned, since it is their duty to oversee all operations and declare the end of phase F.

23 Risk Analysis

Now that a design on subsystem level has been established, risk analysis can be performed. This analysis helps to asses the overall risk of the concept and finally provide the risk mitigation strategy. The risk is separated into different categories: GNC, TPS, launch and recovery, and external risks.

A similar categorization is done for risk impact. The different categories are:

Catastrophic: Loss of vehicle during the flight
Critical: Violation of user requirement
Marginal: Cost or schedule overrun
Negligible: A flaw after which the vehicle can still operate

The risks presented in the next section apply to the current design and can be mitigated with further design iterations. Some of the risks exist due to limitations in this preliminary design and will certainly be mitigated with further iterations. At the end of the risk analysis, the risk map is shown and a risk mitigation strategy is proposed.

23.1 Risk Description

23.1.1 Guidance Navigation & Control

The current GNC software lacks robustness and is therefore a high-risk subsystem at this stage. Anyhow, sufficient risk mitigation strategies are in place to prevent a failure of the system. It should be considered that in case of a GNC failure, the vehicle might impact populated areas.

GNC1 **Solar radiation**: Radiation from the sun is hard to predict and can have significant impact on, among others, density. This may impact the range and the vehicle might land outside of the recovery area. Therefore, it is critical but unlikely, as solar activity is to be monitored before launch and accounted for.

GNC2 **Inadequate atmospheric conditions in trajectory**: This covers other uncertainties in atmospheric properties, mainly arising from weather conditions. Strong down- or side-winds can be locally present in the atmosphere are plausible, but very hard to predict and correct for. The impact of this risk is marginal.

GNC3 **Space debris**: Space debris is a major challenge for all types of space missions. Objects below 1 cm in diameter are challenging to detect and have enough energy to damage the TPS catastrophically. Anyhow, the flight time in space is minimal as a suborbital trajectory is flown and no space debris is expected in the atmosphere. Collision is very unlikely to occur.

GNC4 **Jammed control actuator**: Even though a properly designed actuator is used, the risk of a jammed actuator can never be excluded. It is plausible to occur and would have a catastrophic impact as the vehicle would become uncontrollable. One could argue the likelihood of this risk. Anyhow, the research team sees that the influence of the extreme environment has to be taken into account.

GNC5 **Boundary layer contamination and limited flap effectiveness**: Little is known about hypersonic aerodynamics, which is one of the main reasons this mission exists. It means there is a remaining uncertainty in aerodynamic performance and it is therefore plausible that flaps are not effective enough to follow the nominal trajectory. This has critical influence on the user requirements as the vehicle might not stay within the reentry corridor or not make the range.

23.1.2 Thermal Protection Systems

TPS1 **Critical nose damage**: Fracture toughness is low for the chosen nose, and so it is relatively brittle. This imposes a risk during transport and production as well as during flight. It has been observed earlier that small particles can critically damage the material and make replacement necessary. This is likely to occur and would have critical consequences as it would violate the user requirement on reusability of 20 times.

TPS2 **Valve failure and/or tank leak**: Even though these systems have been used extensively in the past, they still cause a substantial risk. Mission heritage shows that a failing valve or tank is plausible and its impact with the current design would be catastrophic.

23.1.3 Launch and Recovery

L&R1 **Launch failure**: The Vega launch vehicle is one of the most reliable launchers on the market, with a design reliability peaking off at 0.98. However, there is still, even though low, uncertainty on the success of the launch sequence. This places the probability of occurrence to very unlikely but its impact to catastrophic.

L&R2 **Launch delays due to weather or technical problems**: Delaying the launch can occur due to inappropriate atmospheric conditions, leading to missing the launch window and incurring into schedule overruns and hence, extra launch costs. This places this risk's impact to marginal and its probability of occurrence to unlikely.

L&R3 **Inaccurate launcher separation**: High accuracy in separation conditions is required for a proper reentry. It is known that the final stage of the Vega launch system injects payload with an accuracy of ± 15 km (Perez, 2014). Therefore, given the sensitivity of the Guidance system to initial condition, the impact of this factor on the mission is catastrophic, and the probability is likely.

L&R4 **Mid-air retrieval failure**: Mid-air retrieval of reentry vehicles has been performed for heritage missions, but still possesses a certain degree of uncertainty, given the fact that the helicopters need to be manually positioned in the terminal area of the trajectory and pilots need to perform the retrieval manoeuvre. Missing the vehicle will result in it splashing down in the Atlantic Ocean off the coast of French Guiana or landing in the nearby rain forest. In either case, loss of vehicle is probable. This places the risk at an unlikely probability of occurrence, but with catastrophic impact.

L&R5 **Failure to obtain a sponsored launch**: The current cost estimation is based on the chance of obtaining a sponsored launch from the Space Agency. The probability of obtaining funding for the launch operations is relatively low, placing the likelihood of this risk to plausible. Its impact would be critical for the project due to significant cost overruns with respect to the mission budget.

23.1.4 External Risks

EXT1 **Changes in taxation law**: Changes in taxation law can pose a threat to the financial budget breakdown of the mission. Changes with substantial impact are unlikely and the effect is marginal, as it is improbable to violate one of the user requirements.

EXT2 **Changes in regulatory law**: Changes in laws within the European Union can lead to shipping delays and/or cost overruns, depending on the severity of the change. The impact of such a change is marginal as it would affect the schedule of the project but not the flight capabilities of the vehicle. Its probability extremely low.

EXT3 **Unreliability from sub-contractors**: Being a project run in an international context, multiple systems will be outsourced to subcontractors. Failure by an external party to deliver the design and manufactured part in time results in schedule and hence, cost overruns, placing the severity of this to marginal and its probability to unlikely.

EXT4 **Delay in certification due to bureaucracy**: Certification procedures require a relatively large amount of time and cost resources to be completed. Being non-compliant with one procedure leads to delays in licensing and ultimately higher cost of the mission. Maybe failure to certificate the vehicle is a design flaw, but certification guidelines are changing constantly and unpredictable. The delay is very unlikely and marginal.

EXT5 **Mission delay due to ESA politics**: As happened for multiple programs within the European Space Agency, cancellation or delay of the program is plausible and the impact is catastrophic. Reasons can be a more valuable alternative project within the agency or a lack of budget from participating countries. This is plausible to occur (it has happened before) and critical.

EXT6 **Lack of public interest**: All space missions and comparable heritage missions were based on a scientific or commercial interest. Public interest might have changed after final design has been performed or even after the vehicle has been built. Reasons could be advancement in hypersonic wind tunnels or decreased interest in space flight in general. As hypersonic aerodynamics is of great interest to the scientific community, the interest is unlikely to settle down in this time span. The impact of this would be catastrophic though, as budgets would decrease dramatically.

EXT7 **Competition from other space agencies**: According to the market analysis, multiple parties are interested in performing a similar mission to Hyperion IV. Competition design can lead to a lower market value of the present mission. Given the amount of resources and development time required, the probability of this risk is extremely unlikely but its consequences critical.

EXT8 **External experiment causes decrease in vehicle performance**: External experiments such as new materials or GNC software can have significant and unknown consequences. Naturally, elaborate testing will be present but even then not all influences can be captured. The influence of this is critical, but with proper testing it is unlikely to cause problems.

EXT9 **Noise pollution over populated areas**: The vehicle will be flying relatively low and fast over Central America, leading to the possibility of generating sonic shock waves generating nuisance for overflown populated areas. The effect of this is marginal as it would violate sustainability requirements but with the current GNC design it is likely.

EXT10 **ATC failing to clear adjacent airspace**: The path of the vehicle will have to be cleared with a sufficient margin. The lower part of the trajectory is most critical and collision with an airplane is very unlikely but would be catastrophic.

EXT11 **Unavailability of test facility**: Hypersonic testing facilities are in high demand from various organizations and governmental space agencies, making their availability relatively restricted. There is therefore the chance that this would cause delays in the test campaign, placing the impact of this risk to marginal and the probability to plausible.

Considering all risks mentioned in the previous paragraph, a risk map was produced, with which the criticality of the risks could be visualized. This is visualized in Figure 23.1.

	Very unlikely	Unlikely	Plausible	Likely
Catastrophic	GNC3,L&R1,EXT10	L&R4,EXT6	GNC4, TPS2	L&R3
Critical	EXT7	GNC1,EXT8	EXT5, L&R5	TPS1,GNC5
Marginal	EXT2,EXT4	L&R2,EXT1,EXT3	GNC2,EXT11	EXT9
Negligible				

Figure 23.1: Risk map before application of the mitigation strategy

23.2 Mitigation Strategy

This Section elaborates on risk mitigation strategies for the most critical risks. That is, the risks in the orange and red boxes in Figure 23.1.

GNC4 Unfortunately the risk of a jammed actuator can't be fully mitigated. Once it happens, vehicle loss is certain. Anyhow, the research team can have influence on the probability of occurrence of a stuck actuator. A development plan for the actuator is written and carried out. Risk of the event is assessed afterwards and if not satisfactory another R&D cycle is performed. The risk is now unlikely to occur, but still catastrophic.

GNC5 This risk is related to hypersonic aerodynamics. First of all, the probability of an inaccurate estimation can be reduced by a hypersonic testing campaign of the separate parts as well as a (scale) model of the vehicle. Uncertainty remains however, as not all circumstances can be simulated. Therefore, an assessment of the flap sizing safety factor will follow. Previous missions have shown that computations and tests might not be an accurate estimate for flap effectiveness and therefore a separate risk assessment will be performed after the conceptual flap design is completed. With this, an appropriate safety factor for the flap sizing can be chosen. The probability of occurrence is now unlikely, but its impact still critical.

TPS1 The mitigation can be split up in two parts: on the ground and in-flight. On the ground, the nose is protected in a separately designed protecting rig. This can protect the nose during transport and in the manufacturing facility. Besides, a protocol will be written for everyone working in close proximity to the nose, reducing the chance of improper handling of the nose. In-flight there is less room for mitigation, as the vehicle can't stir around small particles. Anyhow, launch will be postponed if hail is expected and mid-air retrieval is designed to keep the nose in tact. This will not alter the impact of this risk, but the probability to plausible rather than likely.

TPS2 Unfortunately the risk of valve / tank failure can't be fully mitigated. Once it happens, vehicle loss is probable. Anyhow, the research team can have influence on the probability of occurrence of a failing valve or tank. A development plan for these part is written and carried out. Risk of the event is assessed afterwards and if not satisfactory another R&D cycle is performed. The risk is now unlikely to occur, but still catastrophic.

EXT5 It is generally challenging to influence politics, but it can have a meaningful effect. The main stakeholder governments will be convinced of Hyperion IV's purpose and if there is a schedule or cost overrun the involved parties will be notified as soon as possible. Unfortunately it is very hard to predict what influence this will have and this risk is therefore still plausible and critical.

L&R3 Given the sensitivity of the GNC system to the initial launch conditions (i.e. dynamic state of the vehicle at separation from launcher), high trajectory injection accuracy is desired. It is known that the injection accuracy of the Vega is ± 15 km for the nominal mission. Given that the GNC robustness is necessarily limited, a risk is remaining. It is known that if the vehicle is separates at a too low altitude, the total energy of the vehicle will be too low for the range requirement to be met, most likely resulting in mission failure. Therefore, it is desired to aim for a higher altitude and for a lower angle of attack at the skipping part of the flight to skip to a lower altitude. The vehicle can now still follow the nominal trajectory in the second part of the descent. This strategy will affect the impact of the risk, bringing it to critical instead of catastrophic, as most probably the vehicle will not be lost but the performance requirements will be violated. A more robust guidance system is also recommended, with PID along the entire flight range.

L&R5 Sponsored launch is desirable due to the significant reduction in cost it would bring to the project. However, this opportunity is certainly not granted. To reduce the impact of this event, it would be necessary to contact other launch and operation providers. This would require an alteration of the design mission profile to account for, eventually, a different launch site and different launch conditions. This would bring the impact to this risk to marginal, as it would affect the schedule of the project but not the actual flight.

The result of the application of the mitigation strategy is an updated risk map, where the most critical risks have been moved to a new location, according to their updated risk level, as displayed in Figure 23.2.

	Very unlikely	Unlikely	Plausible	Likely
Catastrophic	GNC3,L&R1,EXT10	L&R4,EXT6, GNC4, TPS2		
Critical	EXT7	GNC1,EXT8, GNC5	EXT5, TPS1	L&R3
Marginal	EXT2,EXT4	L&R2,EXT1,EXT3	GNC2,EXT11,L&R5	EXT9
Negligible				

Figure 23.2: Risk map after the application of the mitigation strategy

Design Weaknesses

At this design phase, it is not only the external risks which are a threat to the design. The design has also a number of weaknesses, some of which are discussed below:

- **Wind gusts and turbulence not considered in the design**: In the current GNC algorithm no disturbances have been taken into account. In reality, disturbances will occur and have an influence on the final trajectory and the trajectory requirements might not be met.
- **Non-ideal experiment environment**: Under-performing GNC software and disturbances can result in a non-ideal experiment environment. Even though extensive R&D can be done in the area of GNC, imperfections will remain as predicting all disturbances is infeasible. This will decrease the value of the experiments, as the nominal trajectory will not be followed exactly. This is likely to occur and critical with the current GNC software as it is not yet inventive enough.
- **Parachute packing**: Improper packing of the parachute canopy leads to faulty deployment of the recovery system, resulting in either greater shock loads upon opening or excessive descent rate.

- **Degradation of shape**: High heat- and aero loads degrade the shape of the vehicle and lead to alteration of aerodynamic performance, while no safe mode is available. This could be seen as a design flaw, but it is extremely hard to predict influence of these loads in a hypersonic regime and hence uncertainty remains. It is plausible and catastrophic.
- **Sudden AOA and/or sideslip change due to disturbances**: Disturbances can not be fully predicted and have substantial impact on TPS performance. This risk is most influential at low angles of attack, as the disturbance needed for decreased performance is smallest. A disturbance can change vehicle attitude such that the SPFI is exposed to hot flow, which would cause vehicle burn up. It is plausible as the experiment imposes low angles of attack and little disturbance is needed.
- **Active TPS under-performance**: The active TPS is an experimental system and performance is hard to predict. Failure can occur or more coolant mass flow might be required. Again, this partially comes down to a design flaw but this system is a risk even in a later phase of the design.
- **Unavailability of materials**: Since NASA is the manufacturer of TUFROC material, it might not be available on the European market. This is plausible as the TUFROC material was not part of a mission design before. Anyhow, the USA and Europe have collaborated extensively before. It is a critical risk, but another material can be manufactured with similar properties as TUFROC.
- **Exceeding design loads during transport**: Due to human error or unpredictable impacts, the vehicle might experience excessive loads during transportation between engineering, testing and launch facilities.

Now that the risks and weaknesses have been treated, the RAMS analysis will be performed in Chapter 24.

24 RAMS Analysis

To perform the RAMS study of Hyperion IV, more information regarding the components have to be obtained. This section discusses the approach that should be taken to conduct the RAMS analysis during the next design phase of the mission. The proper RAMS analysis will thus take place mainly during the Technology Assessment activity numbered as 5.10 in the Gantt Chart, Chapter 22.

24.1 Reliability

Reliability is an aspect of RAMS which is likely the most difficult to analyze and requires detailed knowledge about the possible failure modes of the components and the likelihood of occurrence of these modes. Afterwards, an analysis can be performed which yields the most likely reason of mission failure and further suggestions can be made for the design as means of failure risk mitigation. Failure Mode Effect Analysis (FMEA) will be conducted by the suppliers and subcontractors, where all possible failure modes will be identified and classified based on the severity of their consequences, similarly as done now in the risk analysis in Chapter 23.

From the preliminary design risk analysis in Chapter 23, it can be concluded that the most unreliable system of the vehicle is the thermal protection system including the active cooling subsystem, due to its low technology readiness level as discussed in Chapter 16. It has never been flown before on a hypersonic mission, and even though TRL development will be performed within the restrictions of the cost budget, the hypersonic conditions cannot be properly simulated using ground facilities only, as discussed in Chapter 22. Proper communication between the subcontractors working on the aerothermodynamic simulations, defined in Chapter 22, developing the actual TPS design and the material testing facilities has to be ensured to increase the reliability of the system as much as possible within the cost budget.

Another low reliability area is the mid-air retrieval method chosen for the recovery of the vehicle, as introduced in Chapter 12. Even though mid-air retrieval has been performed before, the particular method heavily restricts the possible landing area of the vehicle. Moreover, compatibility between the parachute system, vehicle stability and the retrieving helicopters has to be ensured. This places crucial importance on the communication between the subcontractors developing the parachute system, performing the aerodynamic simulations, and on the subcontractor actually providing the mid-air retrieval service.

These items will be regarded as critical and placed into the Critical Items List during the further design phases such as the aforementioned Technology Assessment activity. By doing so, it will be ensured that they are monitored constantly during design development.

24.2 Availability

Three types of availability can be recognized. First, it is the availability of the components and subsystems during the manufacturing, second, the vehicle availability for the customer, and finally, the availability of the operations services. All three types are discussed below.

24.2.1 Component Availability

The first aspect of availability analysis is the availability of the components required for the vehicle manufacturing. Specifically, it is mainly the availability of the components not manufactured or designed in Europe that is the most critical, such as the TPS material TUFROC, which could result in delays and cost overrun. Based on the current market analysis however, all the components should be available. Another, more detailed market analysis will be performed during the Technology Assessment activity prior to the generation of the Production Master File and prior to collection of the COTS, as discussed in Chapter 22.

24.2.2 Vehicle Availability

The vehicle availability is a function of reliability and maintainability. From the perspective of the vehicle, if maintenance plans are met, and if reliability of its critical subsystems is high enough to not cause significant failures during the mission requiring extensive operations, the availability of the mission will be as scheduled, approximately one to two flights per year. The maintenance plans are outlined in Chapter 22 and will be further defined in the system operations handbook prior to phase E, as shown in the Gantt Chart. In case of low reliability and frequent failures during the flights, more maintenance and repair activities will have to be performed, significantly reducing the vehicle's availability. In case of a major failure leading to the vehicle disintegration in flight, the availability will become zero since another vehicle will not be manufactured, and the project will be terminated.

24.2.3 Operations Services Availability

The availability analysis also concerns the operations facilities, primarily the ground stations and testing facilities. Prior to the flight, it has to be ensured that all ground stations are available for signal reception, as explained in Chapter 19. This will be properly communicated and planned with the ground stations during the creation of the station network activity, which will take place directly after the preliminary design review (for more information on scheduling, refer to the project Gantt chart in Chapter 22). In addition to the ground support system, since extensive testing is required for the technology development activities, availability of the testing facilities during design and manufacturing is also significant. Delays in the testing facilities availability might lead to schedule and cost overrun. Thus, to mitigate the risks of such overruns, advanced tools shall be developed to ensure availability of the operations services. These activities will be described during the operations planning in phase C of the design.

24.3 Maintainability

Maintenance plan of the vehicle was discussed in Chapter 22, proposing the activities to ensure continuous operation of the vehicle for 20 times reusability. The frequency of these activities and the method how the critical systems can be accessed were also discussed.

For maintainability assurance, it is crucial to ensure that the systems can be accessed for inspection and possible replacement. This is achieved by providing access through the back side of the vehicle and through the possibility of the detachment of the lower side if required.

Another aspect of maintainability is the proper training and qualification of the staff, the qualification of the inspection methods and the quality of the mission operations services in general. This will be ensured through extensive qualification activities and operational planning and documentation leading to the qualification and operational readiness reviews, as discussed in Chapter 22.

24.4 Safety

Safety of high speed aerospace missions is typically assured by trajectory abortion in case of failure in flight. However, due to the fact that mid-air retrieval was chosen as a recovery technique, it is not possible to land anywhere else outside of the region covered by the retrieving helicopters. Mission abortion thus cannot be performed, and if the trajectory deviates significantly from the nominal one, the vehicle will be lost.

Moreover, if the control of the vehicle is lost during the reentry phase, the vehicle will start to tumble, unable to further manipulate its trajectory. Such tumbling will likely result in complete disintegration of the vehicle since only the nose tip is designed to survive the stagnation point heat fluxes, as shown in the Chapters 15 and 16. It is thus likely that even if control of the vehicle is lost, its complete disintegration in-flight will mean that it will not pose large dangers to the areas below.

The risk of endangering populated areas in case of loss of control of the vehicle was further mitigated by planning the trajectory such that it is close to the equator, mostly above the ocean, as discussed in Chapter 10. There are, however, still several small cities which could be hit by the vehicle remnants. Further measures will be taken during testing and design analysis to explore and prevent possible modes of the failure of the control system for this reason. Hazard Analysis will be conducted to identify hazard scenarios by the subcontractor, and the outcomes will be documented in the Safety Analyses Report, as a part of the operations handbook generated in phase C.

In addition to safety during the flight, safety should be also ensured during pre-flight activities such as manufacturing, testing and assembly and during mission operations in phases D and vehicle disposal in phase F. The majority of the safety risks related to mission operations, manufacturing, testing and assembly can be mitigated by conducting the scheduled qualification activities and by the planning of and adherence to the safety and disposal methods, as defined in Chapter 22.

No toxic or hazardous materials were used in the design as mentioned in the material characteristics in Chapters 15 and 16, and the sustainability philosophy further described in 25 ensured that the safety is considered in all aspects of the mission. In addition, the project will adhere to national and international legal restrictions. All the above mentioned activities thus indicate that safety is one of the mission's highest priorities which will be considered at every stage of the project.

As mentioned above, the inclusion of toxic and hazardous materials and components is not only the concern of safety, but also sustainability. The measures to ensure the highest possible level of sustainability feasible for the mission requirements are described in the Chapter 25.

25 Sustainability Analysis

In this chapter, the sustainability analysis for the Hyperion IV project will be reported. This analysis will be supported by the sustainability checklist created in the baseline report (Amend et al., 2018a). This checklist has been filled by different departments and responsible members of the group and has been approved by the team as a whole.

25.1 Results of Sustainability Checklist

Sustainability checklist was filled in by the group and resulted in a successful outcome, which will be discussed in this section briefly. The completed checklist is given in Figure 25.1. As can be seen, many of the design aspects were considered to be excellently following sustainable design choices. "Excellent" grade corresponds to the score of over 80% of achievement, which are colored in green. This grade suggests that no human rights are violated, no labor rights are violated, no hazardous materials as predefined are used, the risk of laboratory accidents is minimal, and the process is either neutral or uses few natural resources. The aerodynamics, manufacturing process, TPS and material departments all scored this grade. The other departments RCS, GNC and Operations and Logistics scored a lower mark in this checklist, resulting in a yellow color suggesting a "good" grade. This grade suggests that the design did not fully follow the sustainability scheme or no mitigation actions were taken at this stage. The sustainability analysis for most relevant departments will be further discussed in the following sections.

Welcome to the gate review sustainability checklist. Please fill in the checklist for your subteam and the code of conduct, and hand it back to the sustainability manager 3 days before the gate review. If you encouter a red indication, please contact the sustainability manager.

Scale: On a scale from 0-100 %, how does your current design support/comply with the statement w.r.t. sustainability. Indicating 60 % would comply with the sufficient grade in the trade-off weight criteria for the DOT. The rest scales accordingly.

	% 0-100/N.A.
Aerodynamics	**82**
The current design minimzes the enclosed volume.	90
The proposed testing methods have minimum energy usage.	70
The L/D ratio is maximised	80
RCS	**80**
The current thruster design minimizes the total system mass.	70
The current thruster design minimizes the noise.	80
The thruster design support the reusability and end of life strategy.	70
The current design does not involve any hazarderous nor toxic materials.	100
GNC	**77.5**
The current trajectory is efficient w.r.t resource usage.	90
The trajectory does not conflict with so called social sustainability, for example does not fly over densely populated areas causing noise pollution.	70
The landing approach does not put the environment or society on risk.	85
The control system minimzes the use of power or fuel usage.	65
Manufacturing	**85**
The manufacturing process is not harmful the envioronment nor to humans.	80
The manufacturing process is optimized to use as small resources and energy as possible.	70
The manufacturing process does not violate the labour rights.	100
As many off-the-shelf materials and components should be used (to largen the manufacturing process and increase efficiency).	75
The manufacturing process is safe and is the risk of accidents is litttle.	90
TPS	**87**
The TPS design does not inolve any hazarderous materials.	100
The TPS desing does not exhaust large particles in the atmosphere.	100
TheTPS design does not invlove toxic coolants.	100
The TPS system is optimized to have minimum mass.	65
The TPS design is resistant to degradation.	70
Materials	**85.7**
The materials used support a minimal mass design.	70
The materials used are non-hazardous.	100
The degradation characteristics of the materials is minimum.	70
It is possible to reuse the materials and they comply with the EOL strategy.	85
The materials are safe to manufacture.	90
The testing methods proposed use minimum resources.	85
The testing methods proposed are safe to conduct.	100
Operations & Logistics	**75**
The ground operation facility must be optimized to use as small resources and energy as possible.	90
The total transportation footprint is minimized.	60
The assembly procedure supports a sustainable design (inspection and maintenance is of ease)	90

Figure 25.1: Sustainability Checklist

25.2 Material Analysis

The materials chosen are Tufroc, SPFI and Tungsten with Aluminium coating or Carbon-Carbon ceramics. The materials are not hazardous or toxic, proposed testing methods are safe to conduct and use relatively low resources, and they are safe to manufacture. They partly comply with the reusability requirement and are easy to integrate in an end of life strategy. The materials are only sufficient in the sense that they do not fully support a minimal mass design and might experience degradation. However, a fail safe design was made and therefore it can be said that measures were taken to achieve a sustainable design.

25.3 Logistics and Operational Concept Analysis

Logistics and operational concept can be divided into three main components and they will be briefly analyzed separately.

25.3.1 Manufacturing and Assembly Process

First, the manufacturing processes are generally in line with the sustainability concept. Of course, for such an experimental project, off-the-shelf products are not always available and more energy consuming processes have to be used. On the other hand, the assembly process was optimally designed such that inspection, maintenance, and dis-assembly (when necessary) can be conducted easily and efficiently. This will prevent any damages on the vehicle and ensures minimization of the waste. This results in encouragement of the vehicle reusability and consequently scored a high grade in sustainability aspect.

25.3.2 Transportation and Testing

Testing facilities and manufacturing locations were chosen and selected such that minimum transportation is needed. Although the design process still involves an intensive transportation scheme due to the required quality of testing facilities which are scattered all around Europe. Furthermore these testing procedures involve a great amount of resources, especially considering the manufacturing of qualification models. However, every test is vital for accomplishment of the mission and cannot be avoided.

25.4 Launcher Analysis

The Hyperion IV mission makes use of an expandable launcher, the Vega rocket. Consequently, the sustainability suffers compared to any reusable launchers. However, a reusable launch method such as the Falcon-9 rocket or the Pegasus were not optimum for this mission according to the trade-off. This trade-off involved a sustainability criteria and therefore this can be said to be an inevitable decision.

25.5 Trajectory and Recovery Analysis

The trajectory was optimally designed not to fly over densely populated area, reducing the impact of noise pollution as much as possible. This is plausible and can be achieved by the defined nominal trajectory. Considering the high sensitivity of the trajectory, this cannot be given an excellent grade. Mid-air retrieval is chosen as the recovery method. This method is not intrinsically less sustainable than other retrieval options, as the amount of vehicles and fuel used are not higher than normal. Furthermore, from a social sustainability point of view, this recovery method has a minimum impact on the population since it will be conducted close to a sparsely populated area in French Guiana.

25.6 Reaction Control System Analysis

Thruster design in the reaction control system (RCS) was defined in Chapter 11. A non-toxic cold gas nitrogen was selected as the fuel, therefore meeting sustainability requirements. The design of the RCS valves and feed system was done with sustainability in mind.

25.7 End of Life Strategy

Referring to Section 22.7, the end of life strategy of the vehicle has been well adopted for the sustainability scheme. The parts of vehicle can be reused and the EOL strategy will be designed for expositions and other sponsor events. This way, the waste can be kept minimum and the vehicle will remain valuable even long after the mission.

26 Requirement Compliance Matrix

With the preliminary design defined, it is possible to revisit the mission requirements on the mission from Chapter 3 to elaborate on whether they were mot or not. The requirements and their status are presented in Table 26.1.

Table 26.1: Requirements Compliance Matrix

Mission Requirement	Status	Verification method/ Evidence
SYS.F.1 The vehicle shall be reusable 20 times.	CANNOT BE VERIFIED	Cannot be verified without increased budget for testing.
SYS.F.2 The vehicle shall follow a suborbital trajectory.	MET	Preliminary trajectory simulation shows that orbital velocity is not reached at any point of the flight.
SYS.F.3 It shall be possible to reconstruct the trajectory post-flight with an accuracy greater than 1 m.	MET	GPS data is received and saved for post-flight analysis.
SYS.F.4 The landing site shall be within 100 km from the launch site.	MET	Preliminary trajectory simulation shows sufficient range to orbit the Earth at least once.
SYS.F.5 The vehicle shall be fully autonomous.	MET	The vehicle does not uplink any commands according to the design.
SYS.F.6 The trajectory shall ensure a constant Mach >10 and a variable Re of 5e5 <Re <2e5.	REVISED, MET	Preliminary trajectory simulation shows the given Reynolds sweep at Mach 10 with minor deviations.
SYS.F.7 The trajectory shall ensure a phase of constant stagnation point heat flux of 1 MW/m^2 <q <6 MW/m^2	MET	Preliminary trajectory simulation shows heat fluxes up to 4.4 MW/m^2.
SYS.F.8 Active cooling systems shall be included in the mission design.	MET	Active cooling is an integral part of the TPS design.
SYS.F.9 Material experiments shall be included in the mission design.	MET	A platform for material experiments is included in the design.
SYS.F.10 Aerodynamic experiments shall be included in the mission design.	MET	A platform for aerodynamic experiments is included in the design.
SYS.C.1a The cost of a single flight shall not exceed M€156.	~~REVISED, MET~~ CANNOT BE VERIFIED	Cannot be verified without better bottom up cost estimation tools.
SYS.C.1b The cost of a 20 times reusability shall not exceed M€267.	~~REVISED, MET~~ CANNOT BE VERIFIED	Cannot be verified without better bottom up cost estimation tools.
SYS.C.2 Safety shall be ensured throughout the project.	MET	The design does not contain any hazardous procedures or materials. In case of failure, the vehicle disintegrates before touching ground.
SYS.C.3 Use of toxic material shall be avoided.	MET	The design does not contain any toxic material.
SYS.C.4 All aspects of the project shall comply with national and international laws.	MET	The design does not contain any illegal procedures or materials.
SYS.C.5 Maximum mass of the wet S/C shall be below 400 kg.	REVISED, MET	Based on the CATIA model, the vehicle mass is 321.7 kg

As discussed in the cost breakdown, the reusability requirement **SYS.F.1** cannot be verified within the given budget. While the vehicle was designed such that it should be able to withstand 20 flight cycles, this has to be properly verified in wind and plasma tunnels once the technology readiness level (TRL) has been raised sufficiently. Since this cannot be concluded at this stage of the design, this requirement cannot be verified and thus cannot be concluded to be met.

From the discussions with the customer, the suborbital trajectory is followed as long as the vehicle does not reach orbital speed at any point on its trajectory. Since this is indeed the case based on Chapter 10, the mission requirement **SYS.F.2** is met.

The vehicle contains the Phoenix GPS receiver and a radar altimeter for precise position tracking, and also an IMU to estimate the position based on vehicles rotations and acceleration. All the data flows directly to the memory units and is thus saved instantly. Moreover, the data about position is also sent through an antenna after the communication blackout phase to back the data up on ground stations (refer to Chapter 19). Therefore, it is possible to reconstruct the flight trajectory even in case of recovery failure, which implies that the requirement **SYS.F.3** was also met by the design.

Requirement **SYS.F.4** concerns the fact that the vehicle has to land in the vicinity of the launch site, and thus perform at least one orbit around the Earth. While more advanced GNC software has to be used to confirm this requirement, current simulations indicate that the vehicle has sufficient L/D to perform the orbit using skips, as can be seen in Chapter 10. Thus, this requirement is for now considered to be satisfied.

The vehicle was designed without a pilot, and such that it does not need communication during the blackout phase, as proved in Chapter 19. This makes the vehicle fully autonomous, meeting the **SYS.F.5** mission requirement.

The requirement **SYS.F.6** concerns the Reynolds sweep at Mach 10, revised compared to the baseline. Even though small fluctuations around Mach 10 are still observed in the trajectory when the Reynolds sweep is performed, as shown in Chapter 10, these fluctuations can be removed using a more advanced software for GNC. This requirement is satisfied as well.

Similar situation exists for the **SYS.F.7** requirement. The requirement states only the possible range of the heat fluxes, and since the current expected heat fluxes along the trajectory do exceed 1 MW/m^2 and increase up to 4 MW/m^2 as seen in Chapter 10, this requirement is met.

The requirements **SYS.F.8, SYS.F.9** and **SYS.F.10** are related to the experiments on board. As explained in Chapter 8, platform for several material and aerodynamic experiments have been designed both on the upper and lower sides of the vehicle. In addition, since active cooling is an integral part of the thermal protection system as explained in Chapter 16, all of the above states requirements were satisfied by the design.

The next requirement, **SYS.C.1**, concerns the cost of the vehicle. After initial consultation with the customer, the requirement was changed from M€120 to M€156. This requirement cannot be verified until detailed design is made, during which the cost of the components as well as that of operations, manufacturing, testing and mainly the TRL development is known precisely. While the current cost breakdown in Chapter 28 does indicate that this requirement can be met, there are still too many uncertainties in the analysis to confirm it.

System constraints **SYS.C.2, SYS.C.3** and **SYS.C.4** are all related to the safety and legality of the mission. As discussed in Chapters 24 and 25, no toxic or otherwise hazardous materials were included in the design, and the current scheduling provides sufficient space for proper safety planning and sufficient training of the staff. Since the project is ran under ESA, it will be ensured automatically that international laws and legal constraints are being met, since otherwise heavy fines would be imposed. Thus, the three constraints are regarded as met.

The final system constraint, **SYS.C.5**, is the mass budget. The mass budget was, after consultation with the customer, increased from 250 kg up to 400 kg. Even though the current design does not extent to the highest level of detail, there is sufficient margin to add small components or slightly resize the subsystems if needed, while still adhering to the mass of under 400 kg. The mass budget is shown in Chapter 7. Therefore, the last mission system constraint is met as well.

To summarize, out of the basic mission requirements, two were revised after the discussion with the customer, and two cannot be verified at this stage of the project. The rest of the requirements was met, according to the current design, met. The compliance matrix results can however change if later during the detailed design phase it is found that significant changes have to made. Since not all subsystems are at the highest possible TRL, a TRL development plan is proposed next.

27 TRL Development Plan

In this Chapter, an explanation will be provided on how the Technology Readiness Level (TRL) of some of the systems and instruments mentioned in this report can be increased by means of future development plans. The possible obstacles that can prevent proper development will also be considered. The increase of TRL can raise the efficiency of future missions, lower the risk, and might even open the door to new missions. This chapter is closely linked to the experiments in Chapter 8, which explains the projects contribution to raising the TRL, the testings of Chapter 22, which explains general testing methods and the recommendations of Chapter 29, where the most important TRL development program is identified. The cost mentioned in this chapter is not included in the cost budget of the project (see Chapter 28), except for the cost of the TRL development of the active cooling system and the tungsten nose. They shall be understood as suggestions and predictions for further projects. The general increase of TRL by means of usual testing activities in the scope of the project are excluded here and represented in the testing activities in Chapter 22 and in the cost analysis in Chapter 28.

27.1 Aerodynamics TRL Development Plan

Improving the TRL of the aerodynamics implemented in the Hyperion IV implies deeming the vehicle ready to encounter any aerodynamic irregularities during service and perform better from an aerodynamic perspective, which is advantageous primarily in hypersonic regime. The subjects to be questioned in the associated development ranges from boundary layer (BL) transition prediction, over boundary layer shock wave interaction, to neutral point analyses considering hypersonic gas effects. Hypersonic aerodynamics are in general still afflicted with uncertainty, as described in Section 8.3, which lowers the efficiency of hypersonic aerodynamic design. In Table 27.1, the aerodynamic development analyses which can be conducted are shown, together with the related TRL development cost for each of the analyses. The TRL scale described in table 27.1 does not match the ESA definition, as it rather represents the current state of research. A TRL of 6 on this scale represents an understanding of single effects, but not an encompassing theory implementing all effects and their interdependence. A TRL of 8 would represent an advanced empirical model. The experiments proposed in 8.3, to be conducted during the mission, will aid the development program tremendously. The cost seen in table 27.1 is a rough estimation assuming that it would take 2 years of research with 15 employees, at least two flight tests, and 10 wind tunnel tests consisting of 10 to 15 legs of testing. The cost for a wind tunnel run are M€0.21, including labour cost. The cost for two flight tests validating the tests with hypersonic data amount to M€26, based on the estimated cost in Chapter 28 scaled down to two tests. The cost of conducting the research would come down to M€18[1]. It goes without saying that these numbers are rough estimations and that they are only presented to hint in the right direction. To sum up, to raise the TRL of hypersonic aerodynamic specifications, advancements have to be made in numerical simulation, advanced testing methods, and flight data extrapolation. Therefore, advanced ground-based testing with in-flight validation has to take place. The approximate total costs will be M€92.2, without offsetting the value of the experimental data to be gathered.

Table 27.1: Aerodynamic TRL development plan

Name	**Current TRL**	**Potential TRL**	**Development strategy**	**Development cost (M€)**
Aerodynamic BL transition prediction Boundary Layer shock wave interaction	6	8	New advanced testing methods (plasma actuators) (Kendall, 1975) (Parent et al., 2018)	46.1
Aerodynamic-Real gas effects on neutral point and control surface efficiency's	6	8	New wind tunnel insights (Muylaert et al., 2003), Flight extrapolation, Improved numerical simulations (Longo and Radespiel, 1996)	46.1
Overall Aerodynamics	**6**	**8**		**92.2**

[1] Internal communication with supervisors, 21.06.2018

27.2 TPS TRL Development Plan

The active TPS under a reusability aspect is still under development. As explained in Chapter 16, a ceramic nose is relatively refurbishment intensive, imposing challenges to reusability. Therefore, a Tungsten nose tip was suggested. Although being promising, it is lagging the TRL level.

Even though W-Al2O3 is the most promising concept presented in this report, in terms of reusability and damage tolerance, its TRL is below the desired level. Currently the TRL is in between 4 and 5 based on the article by Kostomarov et al. (2009). It is therefore that if ESA chooses to design such a fully reusable TPS, the following studies should be preformed, omitting the recommendations in Section 18.3. The first phase of research should consider, the regression rate of both the Al2O3-coating and W-core in a heated and high pressure environment. This research, if successful, should try to implement an airstream, preferably at hypersonic levels. It is important to analyze the change of mechanical properties of Al2O3 when heated close to its melting point, such that the thermal stresses can be better understood. Finally, film cooling testing should be performed under different cooling configurations, as described in Section 18.2, such that better models can be created to predict the effectiveness of the coolant and the amount of coolant needed. For the second phase, plasma wind tunnel tests should be conducted on the W-Al2O3 to see the regression rates. Also, the role of water should be studied here as well as performing a scratch test. The interaction between W and the CMC C/C-Sic when heated, should be studied to guarantee that fastening is not compromised during flight. In the end of the second phase, tests concerning the oxidation of tungsten at temperatures above 2,000K at varying total pressures and Mach numbers should be performed, such that the boundary layer (created created due to the evaporation of WO_2) can be estimated. This will lead to a more accurate prediction of oxidation of tungsten in case the alumina fails, thus resulting in more efficient designs. For the third phase, a W-Al2O3 nose-tip that uses AC is put in a plasma wind tunnel to be tested. If the budgets allow, a plasma-shock tunnel might be more desired to get more accurate data. If phase three is successful, the W-Al2O3 is at a TRL of 8 and is ready to be flown on an actual mission for validation. Given that Hyperion IV is a testbed, ESA might opt to stop at phase two, which would result in a TRL of 6 to 7, depending on the progression in Phase two. To determine which choice is more beneficial, a proper risk analysis for the cost should be performed, which is at the stage of this report beyond scope.// //

The current TRL development plan only extends to cover the metallic nose tip such that it fits within the mission budget. Based on a research of past missions, to raise the TRL level of all the vehicle subsystems to the sufficient level to prove their 20 times reusability, the costs could reach up to 1 B€. Such a TRL development analysis would be very extensive, and was thus regarded to be outside of the scope of this report.

28 Vehicle Cost Estimation

Like in every major project, the cost analysis forms an essential piece which largely determines the direction in which the project moves time-wise and performance-wise. Knowing precisely where every part of the budget is allocated has proven to be pitfall for most of the engineering projects done in the past. Therefore, after conducting a careful evaluation of all individual components, along with proper discussions with ESA, a solid and detailed cost breakdown of the Hyperion IV project was established.

28.1 Requirements on Cost

The requirements on cost are given by the adjusted top level mission requirements.

- **SYS.C.1 The cost in combination of a one time use or 20 times reusability shall not exceed the following:**
  a. M€156 for a vehicle flown once,
  b. M€267 for a vehicle that is 20 times reusable.

28.2 Trade-off Summary

As it was impossible to assess the cost for different vehicle concepts entering the trade-off, a cost-related trade-off was never realized at this stage. The launcher vehicle selection was conducted using a specific cost category. The costs for the winning launcher, being the Vega rocket, constituted M€37.1. However, the Hyperion IV group still preserves the proposal of negotiating a free launch.

28.3 Cost Breakdown

After scaling all the information down to the specifications and total available cost belonging to the Hyperion IV program, the cost breakdown shown in Table 28.1 was established.

In the first weeks of the project the target cost was changed from M€120 to M€156 for a one time use vehicle, and M€267 for a mission including 20 recurring flights as described in chapter 3. The breakdown of the target cost is based on mission heritage, incorporating as much detail as possible[1]. The cost breakdown was adjusted to fit the mission specific categories and focuses. The target cost was used as a systems engineering tool to monitor the cost development throughout the project. The target cost in table 28.1 represents the breakdown of the M€267 for a mission including 20 flights.

The structure of table 28.1 reflects the importance of certain aspects of the Hyperion IV mission with 20 recurring flights. Under development and production, the cost for each subsystem is shown including the cost for tests, if known. To achieve the requirement of designing a vehicle which is at least 20 times reusable, it was deemed necessary to raise the TRL of the TPS, especially of the nose tip design as described in Chapters 18 and 27. Therefore, the cost breakdown includes a category for TRL development cost, which only considers the nose tip design. Additionally, to emphasize its significance to fulfill the mission, most of the cost documented under the testing category is centered around the TPS subsystem. Due to a lack on information for all testing costs, a substantial risk margin was applied in the cost assessment.

To sum up, the cost breakdown shows in detail the additional cost required to conduct all the testing and TRL development necessary to fly a mission with a reusable vehicle for at least 20 times, as well as the costs for the nominal mission. However, the TRL related cost only include the cost for the nose tip development, with the the cost for an overall TRL development program being beyond the scope of this report.

The actual cost was established throughout the mission as far as possible. It has to be mentioned, that data was not available for every category, and most of the numbers should be treated with caution. This is reflected in the high risk margins for actual cost. Deviation from the target cost can be observed in the cost for development and production of the airframe and vehicle systems, both turning out to be cheaper. More cost was allocated to the TRL development, testing, and risk margins. The total actual cost come down to M€266.2.

28.4 Recommendation

As was already mentioned, it was not always possible to assess the cost for all subsystems and mission segments. Because the cost was only analyzed for a preliminary design, this cost breakdown should only be used as a guideline. A more detailed cost breakdown shall follow in phase C of the Hyperion IV project.

[1] Internal communication with supervisors

Table 28.1: Target and actual cost Hyperion IV

Category			Target cost (M€)	Actual cost (M€)
Development and Production			**157**	**110**
	Airframe (AF)		**77.8**	**48.1**
	Nose tip/Leading edges		20.7	12.8
	Remainder structure		38	23.5
	Final assembly/ System integration		5.8	3.6
	Wind tunnel testing		7.5	4.6
	Airframe technology I&T		5.8	3.6
	Vehicle systems (VS)		**45.5**	**28.3**
		General systems	**32.1**	**20.1**
	FCS Mission & Flight control		26.8	16.6
	EPS subsystem		0.8	0.5
	Environmental system		1.6	1.1
	Recovery system & helicopters		1.1	0.7
	Experiments		0.8	0.6
	General system integration		1	0.6
		Avionic systems	**13.4**	**8.2**
	FTI & Health monitoring		9.4	5.8
	Communication system		2.7	1.6
	Avionic system integration		1.3	0.8
	Hypersonic technology, FT engineering		**20.1**	**17.4**
	Aerodynamics		0.7	0.6
	Mission simulation		1.2	1.1
	FT-Operation Engineering & Planning		9.6	8.2
	FT-Support		1.1	1
	Project Management		4.5	3.9
	Hypersonic configuration		2.2	1.9
	ILS / RMT		0.8	0.7
	Other (O)		**13.6**	**16.2**
	TRL Development		11.7	15.5
	Workforce		1.9	0.7
TPS & Testing				
	TPS		**29**	**29**
	Testing		**24**	**20.4**
	Dropping test		12.7	10
	Plasma tunnel TPS test (specimen)		0.004 (30x)	0.004 (30x)
	Overall TPS test (incl. active cooling)		0.008 (10x)	0.008 (10x)
	Shock test ESTEC		0.03	0.03
	Mechanical / Loading test		10.9	10
	Vibration test		0.2	0.2
	Testing margin		**21**	**38.8**
Operations			**24**	**38.5**
	First mission		6.4	10
	Recurring operations		17.6	28.5
Risk margin			**12**	**30**
Total costs			**267**	**266.2**

29 Conclusions

This report has shown the progress of the Hyperion IV project up until the end of the fourth and last phase. Pursuing the project objective "To design an unmanned experimental hypersonic test bed within 10 weeks with a group of 10 students to win the Anthony Fokker prize."

In the beginning of this report, an outline was provided on the project objective & organization of the Design Synthesis Exercise for the Hyperion IV team. To support this further, it was followed by the complete mindset and system engineering methodology to provide a solid understanding of how the project was viewed by the project team. Afterwards, the full study of the requirements was provided and additional, but necessary requirements were derived to deem the project more qualified for a full analysis, both on a technical and non-technical basis. Moreover, an elaborate market analysis was conducted to look for potential markets which may have an advantageous share in the Hyperion IV project, for both the project team and the third parties themselves. After defining all potential markets, it was discussed how the Hyperion IV team planned on harvesting the financial benefit from this project through a return of investment approach. Next, the functional overview of the hypersonic vehicle itself was provided in the form of both, a functional flow diagram, and a functional breakdown structure. Here, a chronological and an overarching framework were provided, respectively, on all different functions of the Hyperion IV in the different mission phases. After defining the different functions of the vehicle, a brief discussion was provided on the Design Option Tree (DOT) with all different vehicle concepts, showing how the trade-off was performed and which concept was chosen. Additionally, the reader was provided with a complete and final overview of the specifications and various budgets belonging to the Hyperion IV vehicle, as well as a graphical layout of the configuration.

Furthermore, the variety of experiments were discussed in addition to the different subsystems implemented in and designed for the Hyperion IV vehicle. These subsystems were generally envisioned as models, used for simulating and predicting the behaviour of the vehicle with regards to the different aerospace disciplines, which are the aerodynamics, astrodynamics, GNC, DRS, structures, aerothermodynamics, TT& C, Avionics and EPS. It must be noted that significant emphasis was laid on the design of the materials subsystem, due to its criticality for meeting a large number of user requirements. After having seen the different subsystems, a general review was presented on how the vehicle performs during service. This performance overview was given with respect to the aerodynamics, thermal protection and trajectory of the Hyperion IV.

A chronological outline of all different mission steps starting from vehicle preliminary design up until the End Of Life was provided thereafter, based on the six standard mission phases as defined by ESA.

From a technical stance, a detailed risk analysis and a generic RAMS analysis were conducted for the vehicle at question. To realize a continuous and well-established project, a sustainability analysis was conducted to accomplish this goal.

At the end of this report, a compliance matrix was set up to provide the reader with an overview on whether the requirements were met by the project group. Also, a TRL development plan was introduced to highlight the potential subsystem fields were sufficient information is available to start new research on increasing the TRL of associated domains. Finally, this report provided the reader with an estimation of the overall cost of the Hyperion IV.

29.1 Recommendations

Throughout this report it was mentioned, that the complete analysis and development conducted throughout the project will not definitely fulfill the requirements given in chapter 3, as certain subsystems need further development. Further, uncertainty on whether a requirement can be met or not, has been expressed in chapter 26. Due to time and resource constraints, these have been formulated as recommendations to ensure a proper project development in the future. This section summarizes the most important recommendations.

Further useful experiments like an ablation experiment and gathering data on the chemical composition inside and outside the shock are suggested.

Regarding the trajectory, it is recommended to extend the use of PID control, to implement TAEM guidance to refine the recovery phase, and to further optimize the trajectory.

The analysis of the control system is lacking the analysis on lateral and directional control, which is beyond the scope of this report. A thorough analysis should be conducted, which might lead to a resizing of both the body-flap and thrusters.

The final phase of the trajectory, the recovery, uses an altitude-based model, which could be refined by modelling continuous shocks and events. Additionally, treating parachute and vehicle as separate systems, each with their own characteristics is recommended.

It is recommended to refine the structural analysis by adding thermal stresses, which are neglected due to large safety margins in this report, and validate the model by a commercial FEM software.

As the aerothermodynamic model uses semi-empirical models, it is recommended to conduct a more precise analysis using CFD, as at this stage the TPS is likely to be overdesigned. Also, the interpolation of the active cooling system behaviour can be expended. On the hardware side of the TPS it is mentioned that the transient heat transfer from the heat shield to the inside structure has to be improved, as well as the interfaces between different ceramics.

Regarding the C/C-SiC nose tip design, more research and testing should be done to ensure the fail safe mechanisms as well as to better understand the required mass flow for the active cooling. For proper use of the W-Al_2O_3 nose tip the described TRL development program as well as material testing is necessary.

The design and budgets for telemetry and tracking, Avionics, and the EPS should be revised and refined throughout the detailed design phase to incorporate the deeper knowledge at this stage.

Finally, a more detailed cost analysis shall be conducted during the detailed design phase.

To sum up, this report is an excellent base to be used at the beginning of the detailed design phase. If all recommendations proposed are followed, the vehicle should be able to fulfill all requirements and successfully deliver the important experimental data.

29.2 Acknowledgement

The group would like thank to Erwin Mooij for his guidance during the project, personal approach and extensive, yet very appreciated feedback. It would also like to express its gratitude towards Kees Sudmeijer and Christopher Teruna for consultations, and for providing literature and other information sources. In addition, the group would like to thank the staff of ESTEC for assisting with cost estimation, and specifically Alvaro Martinez Barrio for his supervision from the side of ESA. Project management and systems engineering teaching assistants Vlad Stefanovici and Sunayna Singh also helped to improve the overall quality of the report. Finally, the group also appreciates the attitude of the Flight Performance & Propulsion department for accommodating the group, and the cleaning staff for maintaining the group environment.

Bibliography

N.P. Adamov, A.M. Kharitonov, E.A. Chasovnikov, A.A. Dyad, M.I. Kazakov, A.N. Krylov, and A.Yu. Skorovarov. Aerodynamic characteristics of reentry vehicles at supersonic velocities. *Thermophysics and Aeromechanics*, 22(5), apr 2015.

D.L. Akin. Mass estimating relations, 2016.

J. Amend, B. Barsom, M. Brchnelova, G. Dacome, B. Duisterhof, A. Levoni, L. Lischwe, E. Matsuda-Martin, J. Sem, and D. Sonneveldt. *Hyperion 4 - Baseline Report*. Delft University of Technology, May 2018a.

J. Amend, B. Barsom, M. Brchnelova, G. Dacome, B. Duisterhof, A. Levoni, L. Lischwe, E. Matsuda-Martin, J. Sem, and D. Sonneveldt. *Hyperion 4 - Midterm Report*. Delft University of Technology, June 2018b.

J. D. Anderson. *Hypersonic and High-Temperature Gas Dynamics, 2nd edition*. AIAA, 2006.

J. D. Anderson. *Fundamentals of Aerodynamics, 6th Edition*. McGraw-Hill Education, 2017.

ANSYS. Ansys fluent user manual, 2017.

D. Arnal and J. Délery. Laminar-turbulent transition and shock wave/boundary layer interaction. Technical report, NATO, 2004.

R.W. Bartlett. Tungsten and molybdenum oxidation kinetics at extremely high temperatures, 1964.

D. Berry. Mortar deployed parachutes for spin stabilization and recovery, 2007.

J.J. Bertin. *Hypersonic Aerothermodynamics*. AIAA, TL571.SB47 629.132 '306-dc20 93-26658, ISBN 1-56347-O36-5, 1994.

M.H. Boratto, L. Vicente, and A. Scalvi. Deposition of al2o3 by resistive evaporation and thermal oxidation of al to be applied as a transparent fet insulating layer, Sept 2013.

K.G. Bowcutt and J.D. Anderson. Viscous optimized hypersonic waveriders, 1987.

K.G. Bowcutt, J.D. Anderson, and D. Capriotti. Viscous optimized hypersonic waveriders. *American Institute of Aeronautics and Astronautics*, 12(15), January 1987.

W.D. Callister and D.G. Rethwisch. *Materials Science and Engineering*. John Wiley & Sons, 2015.

E.D. Calver and R.A. Beall. Centrifugal casting of tungsten, Jan 1966.

A. Cervone. *AE2111-II Aerospace Design and Systems Engineering Elements II, Spacecraft Telecommunications, Lecture 09,*. Delft University of Technology, 2016.

R.R. daCosta, Q.P. Chu, and J.A. Mulder. Reentry flight controller design using nonlinear dynamic inversion, 2003.

R.W. Detra, N.H. Kemp, and F.R. Riddell. *Addendum to Heat Transfer to Satellite Vehicles Reentering the Atmosphere*. Jet Propulsion, Volume 27, No. 12, pages 1256-1257, 1957.

J.H. Deweese and L.R. Schultz. *Recovery System Design Guide*. US Department of Commerce, December 1978.

C. Dittert and M. Kütemeyer. Octra - optimized ceramic for hypersonic application with transpiration cooling, 2016.

C. Dittert, H. Bohrk., and H. Elsaesser. Design of a transpiration cooled shart leading edge for shefexiii, 2015.

H.L. Dodge. Young's modulus of drawn tungsten and its variation with change of temperature, including a determination of the coefficient of expansion, 1971.

S. Drews, F. Rautschke, D. Maassen, C.T. Nghe, and G. Boeck. A 10-w s-band power amplifier for future 5g communication, 2017.

ECSS. Space engineering: Structural materials handbook - part 6: Fracture and material modelling, case studies and design and integrity control and inspection, 2011.

M. Fumo. Aero-thermal post flight analysis of ixv control surfaces, 2017.

A. Gerundo. Parachute-system design for planetary landing, 2010.

C. Heegard and S.B. Wicker. Turbo coding, 1999.

A.K. Hiodge and D.J. Maykuth. Properties of new high temperature titanium alloys, 1968.

E.H. Hirschel and C. Weiland. *Selected Aerothermodynamic Design Problems of Hypersonic Flight Vehicles*. Springer, 2009.

O.T. Johnson, P. Rokerband, and I. Sigalas. Microstructure and properties of al2o3–sic nanomaterials, 2014.

L.H. Jorgensen. Prediction of static aerodynamic characteristics for space-shuttle-like and other bodies at angles of attack from 0 to 180 degrees. Technical report, Ames Research Center, January 1973. NASA Technical Note D6996.

J.M. Kendall. Wind tunnel experiments relating to supersonic and hypersonic boundary-layer transition. *AIAA Journal*, 13(3):290–299, 1975.

T.W. Knacke. *Parachute Recovery Systems Design Manual*. Para Publishing, March 1991.

D.V. Kostomarov, K.S. Bagdasarov, and E.V. Antonov. Oxidation of tungsten in the w–al2o3 system at temperatures from 2350 to 2500 k and pressures from 1 to 10e5 pa, 2009.

S. Kumar and S.P. Mahulikar. Aerothermal analysis for configuration design of swept leading edge hypersonic vehicle, 2016.

M. Kunz and J. Goering. Whipox, long fibre, all oxide ceramic matrix composite (ocmc) for industrial applications, 2014.

D.B. Leiser, M. Smith, R.A. Churchward, and V.W. Katvala. Toughened uni-piece fibrous insulation, 1989.

J.M.A. Longo and R. Radespiel. Flap efficiency and heating of a winged re-entry vehicle. *AIAA Journal*, 33 (2), Mar 1996.

J. Luo and E. Lan. *Fuzzy Logic and Intelligent Systems.* Kluwer Academic Publisher 85-124, 1995.

L.H. Mack. Boundary-layer linear stability theory. Technical report, Jet Propulsion Laboratory, 2010.

M. Markgraf. Phoenix spaceborne gps receiver, 2007.

T. H. G. Megson. *Aircraft Structures for Engineering Students.* Elsevier, 2012.

J. Monthasuwan, C. Saetiaw, and C. Thongsopa. Curved rectangular patch array antenna using flexible copper sheet for small missile application, 2013.

Moog. Cold gas thruster triad, 2017.

E. Mooij. *AE4870B - Re-entry Systems, Lecture Notes.* Delft University of Technology, 2017a.

E. Mooij. Re-entry guidance for path-constraint tracking, Jan 2017b.

D. Moreau. *Test Requirements for Space Equipment.* Office for Programmatics and Policy, ESTEC, 1995.

J. Mulaert, L. Walpot, H. Ottens, and F. Cipollini. Aerothermodynamic reentry flight experiments expert. Technical report, ESA-ESTEC, ATOS Origin, NATO, 2009.

P. Muller. *ESA Tracking Stations Facilities Manual.* European Space Agency, 2008.

R. Murray. Optimization-based control, 2010.

J. Muylaert, F. Cipollini, L. Walpot, H. Ottens, G. Tumino, W. Kordulla, G. Saccoccia, M. Caporicci, and C. Stavrinidis. In-flight research on real gas effects using the esa expert vehicles. *AIAA Journal*, Dec 2003.

NASA. Family system of advanced charring ablators for planetary exploration missions, 2004.

NASA. *Space Shuttle Tiles.* NASA & Aeronautics Research Mission Directorate, EP-2010-12-482-HQ, 2010.

J. Osgood, J.R. Whittemore, and N.N. Ault. Thermal expansion of various ceramic materials to 1500c., 1956.

B. Parent, M.N. Shneider, and S.O. Macheret. Large eddy simulation of boundary layer transition induced by dbd plasma actuators. *AIAA Journal*, Jan 2018.

A.A. Pasha and K. Sinha. Simulation of hypersonic shock/turbulent boundary-layer interactions using shock-unsteadiness model. Technical report, Indian Institute of Technology Bombay, 2012.

M. Patel, K. Saurabh, V.V. Prasad, and Subrahmantam. High temperature c/c–sic composite by liquid silicon infiltration: a literature review, 2012.

E. Perez. Vega user's manual, 2014.

R.A. Perkins and D.D. Crooks. Low-pressure, high-temperature oxidation of tungsten, July 1961.

G. Della Pietra, S. FLazini, E. Colzi, and M. Crisconio. Fuzzy logic controller for small satellites navigation, July 2005.

L. Prandtl. Bemerkung über die entstehung der turbulenz. *Zeitschrift für Angewandte Matgematik und Mechanik*, 1(6), 1921.

U.S. Prasad and G. Srinivas. Flow simulation over re-entry bodies at supersonic & hypersonic speeds. *International Journal of Engineering Research and Development*, 2(4):29–34, jul 2012.

J.M. Puech. Space project management, 1996.

Lord Rayleigh. On the stability or instability of certain fluid motions. *Proceedings of the London Mathematical Society*, s1-19(1), November 1887.

B. Reinatz and J. Ballmann. Computation of hypersonic double wegge shock/boundary layer interaction. Technical report, RWTH Aachen, 2016.

E. Reshotko. Boundary-layer stability and transition. Technical report, Case Western Reserve University, 1976.

R.R. Roe. *Spacecraft Dynamic Environments Testing.* National Aeronautics and Space Administration, December 2014.

G. Rossman, M. LeVine, S. Lawlor, T. Sloss, and P. Mishra. Conceptual design of a small earth reentry vehicle for biological sample return. *AIAA*, February 2017.

T. Rösgen, C. Pereira, S. Airaghi, and A. Vuilleumier. Temperature mapping of a re-entry vehicle flap in high enthalpy flow test. Technical report, ETH Institute of Fluid Dynamics and RUAG Space, 2012.

P. Saratayon, V. Pirom, and T. Saelim. Antenna subsystem for small missile, 2013.

H. Schlichting. *Boundary-Layer Theory.* Mc Graw-Hill Book Company, 1979.

S.J. Schneider and C.L. McDaniel. Effect of environment upon the melting point of al2o3, April 1967.

B. Scott, M. DiFulvio, K. Matthew, and K. Kowalkowski. Forced boundary-layer transition on x-43 (hyper-x) in nasa larc 20-inch mach 6 air tunnel. Technical report, NASA, 2000.

C.D. Scott, R. C. Ried, R.J. Maraia, C.P. Li, and S.M. Derry. *An AOTV Aeroheating and Thermal Protection Study.* Progress in Astronautics and Aeronautics, AIAA, Vol. 96, pages 198-229., 1985.

P. Seide. Axisymmetrical buckling of circular cones under axial compression. *Journal of Applied Mechanics*, ASME Transactions(23):625–628, 1956.

L. Shi, B.L. Guo, Y.M. Liu, and J.T. Li. Characteristic of plasma sheath channel and its effect on communication, 2012.

K.F. Stetson. Comments on hypersonic boundary-layer transition. Technical report, Wright Research & Development Center, 1990.

D.A. Stewart and D.B. Leiser. Lightweight tufroc tps for hypersonic vehicles, 2006.

K. Sudmeijer, A.v. Foreest, A. Gülhan, B. Esser, M. Sippel, and B.A.C. Ambrosius. Transpiration cooling using liquid water, 2007a.

K. Sudmeijer, A.v. Foreest, A. Gülhan, B. Esser, M. Sippel, and B.A.C. Ambrosius. *Transpiration Cooling Using Liquid Water*. AIAA, AIAA-2007-4034, 2007b.

K. Sutton. An experimental study of a carbon-phenolic ablation material, 1970.

M.E. Tauber and G.P. Meneses. *Aerothermodynamics of Transatmospheric Vehicles*. AIAA, AIAA-86-1257, 1986.

T. Thiele, F. Siebe, and A. Gülhan. *SHEFEX II Flight Instrumentation and Preparation of Post Flight Analysis*. NASA & Aeronautics Research Mission Directorate, EP-2010-12-482-HQ, 2011a.

T. Thiele, F. Siebe, and A. Gülhan. *SHEFEX II Flight Instrumentation and Preparation of Post-Flight analysis*. DLR Aerospace Center, 2011b.

A. Tsutsumi. Thermodynamics of water splitting, 2010.

S. Turteltaub. *AE2135-II Lecture slides*. Faculty of Aerospace Engineering, TUDelft, March 2015.

H. Weihs, J. Longo, and J.Turner. The sharp edge flight experiment shefex ii, a mission overview and status. Technical report, German Aerospace Center (DLR), May 2008.

C. Weiland. *Aerodynamic Data of Space Vehicles*. Springer, 83052 Bruckmühl , Föhrenstr.90 , Germany, 2014. E-mail: claus.weiland@t-online.de.

M.A. Wen-Tao, Z. Qing-Zhen, S. Bobo, and G. Chen. Robust control approach for re-entry vehicle based on inversion model, 2005.

W.L.Ko, R.D.Quinn, and L. Gong. Finite-element reentry heat-transfer analysis of space shuttle orbiter, 1986.

S.F. Wu, C.J.H Engelen, R.Babuska, Q.P. Chu, and J.A. Mulder. Intelligent flight controller design with fuzzy logic for an atmospheric re-entry vehicle, January 2000.

J. Xie, K. Lin, H. Li, Q. Fu, and L. Guo. Ablative property of c/c–sic–hfc composites prepared via precursor infiltration and pyrolysis under 3,000 c oxyacetylene torch, 2013.